DEVELOPMENT AND STABILITY ANALYSIS OF DEGRADABLE FRAC PLUG

A Dissertation

by

HIROAKI YOSHIDA

Submitted to the Office of Graduate and Professional Studies of
Texas A&M University
in partial fulfillment of the requirements for the degree of

DOCTOR OF PHILOSOPHY

Chair of Committee,	Nobuo Morita
Committee Members,	Jenn-Tai Liang
	Kan Wu
	Jaime Grunlan
Head of Department,	Jeff Spath

August 2020

Major Subject: Petroleum Engineering

ABSTRACT

Degradable frac plug (DFP) can eliminate mill-out of frac plug and reduce the operational time in multi-stage hydraulic fracturing in unconventional reservoirs. High mechanical strength and degradation rate are necessary for components of DFP to hold a high differential pressure during fracturing and disintegrate promptly after fracturing.

In this study, degradation behavior and mechanical property of fast-degrading rubber, alloy, and polymer were evaluated to examine their applicability to DFP. The effect of various factors such as temperature, salinity, additives, acid, and alkaline on the degradation were investigated. Mechanical tests and pressure tests of DFP and its parts composed of the fast degrading materials were performed. Stability analysis of the components by the finite element method was also conducted. Stability of various designs of plug components under high pressure was quantified with ABAQUS, a finite element analysis (FEA) software.

Degradation rate of all fast-degrading materials were in general increased with increase in temperature. In contrast, salinity concentration, acid, alkaline, and additives affected degradation rate differently for each fast degrading material. Mechanical tests indicated that plug parts composed of the fast-degrading materials had enough strength for frac plug. Designs of plug components were optimized by FEA and designs that reduce deformation of rubber downstream decreased stress and strain on other plug parts. The DFP with optimized parts showed improved pressure tolerance in the pressure tests.

In this paper, the degradation behavior and mechanical property of the new fast-degrading material in various conditions were discussed. Based on the results, the materials can be used for not only DFP but also other applications in oil and gas industry. The novel frac plug composed of

the new fast-degrading materials enables engineers to reduce the cost and time of the well completion process.

DEDICATION

To my wife and family

For their endless love and support.

ACKNOWLEDGEMENTS

I would like to express my sincere gratitude to my advisor, Dr. Nobuo Morita for guiding and supporting throughout my PhD study. I am always surprised by his broad knowledge and profound insight for research.

I would like to thank Dr. Jenn-Tai Liang, Dr. Kan Wu, and Dr. Jaime Grunlan for their service, valuable suggestions and advice. Their knowledge and wisdom helped me a lot throughout the course of this research.

I also would like to acknowledge my thankfulness to all the staffs of the Department of Petroleum Engineering and Texas A&M University High-Performance Research Computing Center for providing resources. I am thankful for Geomechanics JIP research program provided by Petroleum Engineering Department at Texas A&M University, for providing the financial support for this study.

Thanks also go to my friends and colleagues for making my time at Texas A&M University valuable and fruitful.

Finally, thanks to my beloved wife and family for their love and support.

CONTRIBUTORS AND FUNDING SOURCES

Contributors

This work was supported by a dissertation committee consisting of Professor Nobuo Morita from Petroleum Engineering Department, Professor Jenn-Tai Liang from Petroleum Engineering Department, Dr. Kan Wu from Petroleum Engineering Department, and Professor Jaime Grunlan from Mechanical Engineering Department. All work for the dissertation was completed independently by the student.

Funding Sources

This work was financially supported from Geomechanics JIP (Joint Industry Program).

Portions of this research were performed with High Performance Research Computing resources provided by Texas A&M University (https://hprc.tamu.edu)

NOMENCLATURE

DFP	Degradable Frac Plug
DI	De-Ionized
DTPMP	Diethylenetriamine Penta (methylene phosphonic acid)
f	Yield function
FEA	Finite Element Analysis
FEM	Finite Element Method
gpt	gallon per thousand gallons
$J_2{}'$	Second deviatoric stress invariant
NBR	Nitrile Butadiene Rubber
PAA	Poly(acrylamide/sodium acrylate)
PGA	Poly(glycolic acid)
PLA	Poly(lactic acid)
s_{ij}	Deviatoric stress
TMAC	Tetramethyl ammonium chloride
Y	Yield strength

TABLE OF CONTENTS

LIST OF FIGURES

Page

LIST OF TABLES

Page

1. INTRODUCTION

1.1 Background

Frac plug is widely used for multistage hydraulic fracturing in unconventional reservoirs. It is set in a wellbore by wireline tool followed by perforation of casing. Once a frac ball is dropped with fluid and it is seated on a ball seat of the frac plug, it blocks the well and isolates the downstream and upstream of the section in the wellbore and hold a high pressure so that fractures are created upstream of the plug when hydraulic pressure is applied. Conventional frac plugs are in general composed of cast irons, composite materials, and nitrile butadiene rubbers (NBR). All the materials have high mechanical strengths since the frac plug has to withstand high pressure during hydraulic fracturing in a wellbore. Figure 1 shows general components of a frac plug. Slips anchor the plug in the casing. Conventionally, cast irons and composite materials are used as a material of slip and other components except for the seal element. NBR is used as a material of sealing element that expands in the set position and isolate downstream of the casing. All the

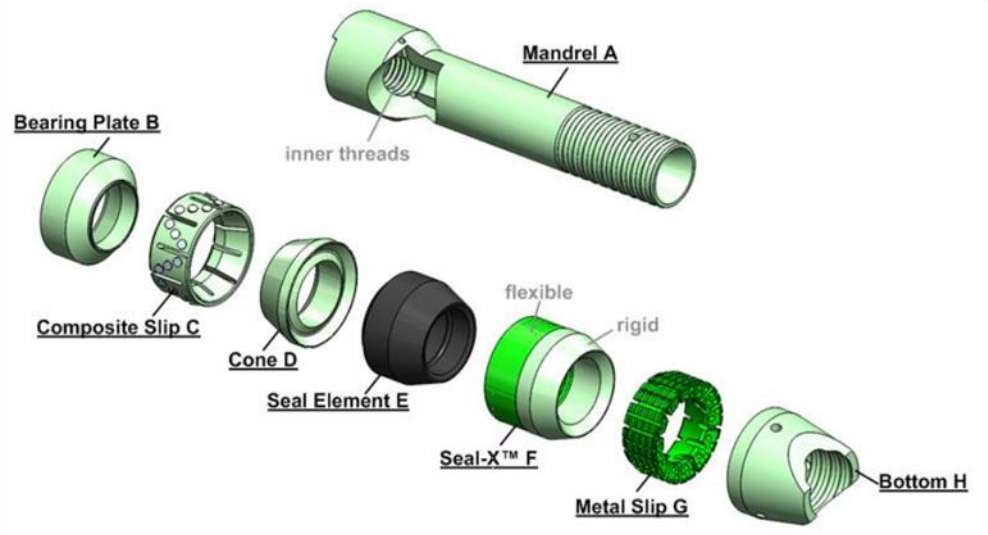

Figure 1 Components of a frac plug (Reprinted from Hou et al., 2014)

materials are non-degradable and remain in a wellbore after fracturing. Therefore, mill-out with coiled tubing is required after staged cluster fracturing prior to production. This process is time consuming and increases operational risks. Sometimes mill-out costs more than USD 200,000 and several days (Nichols & Eis, 2017). In addition, it is sometimes not possible to mill-out frac plugs at the toe section in long lateral wells due to limitation of the length of coiled tubing. Swor and Sonnefeld (2006) developed self-removing frangible plugs to eliminate the mill-out process. The plug can be removed by detonation after its use. However, it remains solid debris after the detonation in a wellbore and they can be stuck in the wellbore and cause production problem especially in horizontal wells. In addition, the detonation can damage the casing. Degradable frac plugs (DFP) can be a solution to eliminate the mill-out as they disintegrate by degradation in a wellbore after hydraulic fracturing and release the isolation of the section in the well. DFP needs to be degraded completely within several days to weeks after fracturing. Therefore, materials used for DFP are required to have a high mechanical strength and specific degradation rate under in-situ wellbore condition. There are several materials which have the proper strength and degradation rate, such as degradable polymers, degradable rubbers, and alloys. In the following literature review, these degradable materials and their application in oil and gas industry are discussed.

1.2 Literature Review

1.2.1 Degradable alloys

Degradable alloys used in current oil and gas industry can be divided into two categories: Mg base and Al base alloys. Degradation mechanism of these alloys is galvanic corrosion (Fripp, et al., 2017). Mg or Al is used as a base metal for the degradable alloy due to its low standard redox potential. The degradation reaction is shown in the equations below.

$$Mg \rightarrow Mg^{2+} + 2e^{-} \quad (1)$$

$$2H_2O + 2e^{-} \rightarrow 2OH^{-} + H_2 \quad (2)$$

$$Total\ reaction\ of\ Mg: Mg + 2H_2O \rightarrow Mg(OH)_2 + H_2 \quad (3)$$

$$Al \rightarrow Al^{3+} + 3e^{-} \quad (4)$$

$$3H_2O + 3e^{-} \rightarrow 3OH^{-} + {}^{3}/_{2}\, H_2 \quad (5)$$

$$Total\ reaction\ of\ Al: 2Al + 6H_2O \rightarrow 2Al(OH)_3 + 3H_2 \quad (6)$$

As a cathodic dopant of the alloys, a small amount of metals with high standard potential such as zinc, iron, copper, and nickel are added to Mg and Al alloys to accelerate the degradation. In addition, the degradation rate depends on physical conditions and chemistry of fluid. As shown in Figure 2, degradation rate of degradable alloys used in oil and gas industry generally ranges from 0 to more than 10,000 mg/cm^2/hour depending on parameters such as temperature, salinity, and pH (Xu & Zhihue Zhang, 2019). Therefore, it is crucial to understand the degradation behavior of each alloy under various conditions, since it is essential information to choose an appropriate degradable alloy for specific purposes based on wellbore condition and fluid. Degradation of Mg

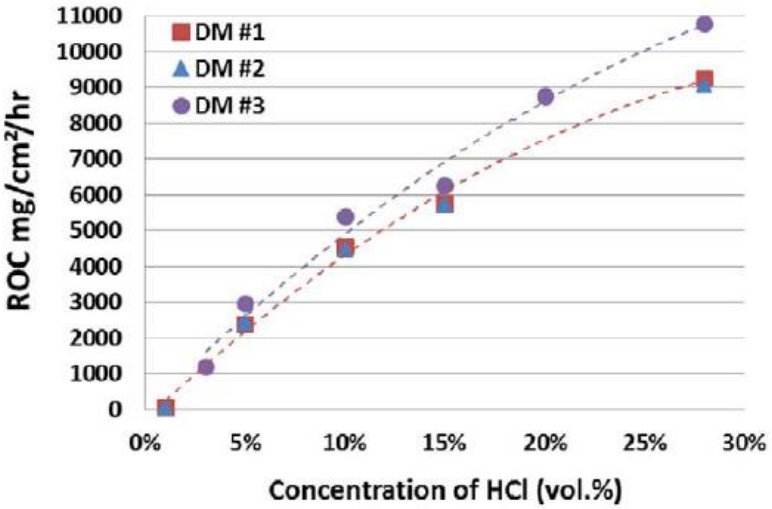

Figure 2 Rate of disintegration as a function of fluid HCl concentration (Reprinted from Xu & Zhang, 2019)

alloy proceeds via surface degradation (Takahashi et al., 2018). A relatively light density from 1.7 to 2.7 g/cm^3, which is close to the wellbore fluid density, is also required for degradable materials especially for horizontal wells as they are pumped with wellbore fluids (Xu & Zhang, 2019). In general, Mg and Al alloys are light metals and have density of 1.8-2.2 g/cm^3 and 2.4-2.7 g/cm^3, respectively (Tu et al., 2019).

Liu et al. (2008) investigated the effect of impurity elements on corrosion of Mg and Al alloys. They reported that corrosion rate of high-purity Mg in 1 M NaCl solution was as low as 1 mm/year. If the concentration of cathodic dopants in Mg or Al alloys is below a tolerance limit, the degradation rate of the alloy is significantly low. Fripp and Walton (Fripp & Walton, 2016) reported degradation rate of degradable alloy could be controlled by adding dopants such as zinc, nickel, and iron and changing dopant concentration. They conducted degradation test of alloys with different cathodic dopant concentrations in 3% brine at 200°F and reported increased degradation rates for the high dopant sample. However, applicability of the materials for DFP is

not clear as they did not show mechanical strength of the material. They also mentioned that degradation of Al alloy is slow as a strong passivation film formed on the surface retards its degradation. To overcome this problem, addition of a post-transition metal to Al alloy is required. Mg and Al alloys require salt or acid to accelerate the degradation where a higher concentration of salt increases the degradation rate. Xu and Zhang (2019) performed degradation tests of a dissolvable metal in KCl solutions with its concentration ranged from 1 to 20% and reported the rate of disintegration increased with increase in the concentration of KCl. In their result, the corrosion rate was as low as about 80 mg/cm^2/hour even in 20% KCl solution. Keerthivasan and Koløy (2019) investigated the effect of chloride ion concentration and temperature on the degradation of their degradable alloy and concluded that the dissolution reaction sped up with increase in chloride ion content and temperature. They also pointed out that temperature has more dominant influence on the degradation as it increases the kinetic energy of the reactant molecules. Degradation rate depends on not only salt concentration and temperature but also the type of salt. Murphy et al. (2019) studied the influence of type of ions on the degradation rate of their degradable Mg alloy. They found that divalent cations such as Ca^{2+} and Mg^{2+} in the solution affected negatively on the degradation rate and it dropped by 10% in a high concentration condition. They also reported that high concentrations of sulfate and carbonate ion decreased the corrosion rate of the alloy by 40%. Ning et al. (2015) investigated the influence of cations on degradation of Mg alloy with various salt solutions in two anionic systems which are chloride and phosphate. In the study, solutions of NaCl, KCl, $MgCl_2$, $CaCl_2$, Na_2HPO_4, K_2HPO_4, NaH_2PO_4, KH_2PO_4, and $Ca(H_2PO_4)_2$ were used. They concluded that corrosion of the Mg alloy by cations tested was decreased in the order of $K^+ > Na^+ > Ca^{2+} > Mg^{2+}$. Takahashi et al. (2018) conducted degradation test of Mg alloy with various salt solutions such as KCl, Na_2SO_4, and $NaHCO_3$.

According to Takahashi et al., the decrease in thickness of Mg alloy at their degradation test was greater in the order of $NaHCO_3 < Na_2SO_4 < CaCl_2 < NaCl < KCl$. They also reported degradation of Mg alloy is affected by additives such as biocide and friction reducer. As various factors such as temperature, salinity, and dopant influence the degradation profile of each degradable alloy, understanding of degradation behavior of each degradable alloy is significant depending on the application and its operation condition.

Mechanical strength is another crucial property for degradable alloys used in oil and gas industry as the pressure in wellbores is high and applied differential pressure can be several thousands of psi. Xu et al. (2011) reported that compressive stress of degradable alloy ranges from 40 to 100 ksi. Zhang et al. (2013) conducted compression test of degradable alloys and their maximum compressive stress were from 35 to 80 ksi. Due to its high mechanical strength, degradable alloy can be used for the slip material of DFP.

1.2.2 Degradable Polymers

Degradable polymer can be further classified as thermoplastic, thermoset polymer and polyurethane elastomer based on the mechanical property. In general, degradation of degradable polymers occurs via hydrolysis in the presence of water and they do not require any salts or other trigger chemicals to degrade. Polyglycolic acid (PGA) is a degradable thermoplastic polymer with ester units in the structure (Figure 3). The ester units in the backbone of PGA are hydrolyzed by water and decomposed to monomer units (glycolic acid). As shown in Figure 4, PGA has a high mechanical strength compared to other polymers (Okura, et al., 2015). Therefore, PGA is applicable to downhole tools or other applications which require a high mechanical strength. As the density of

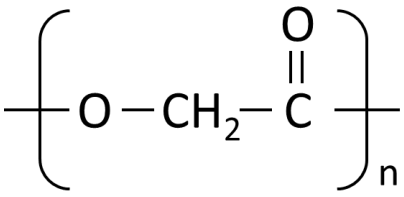

Figure 3 Polyglycolic acid

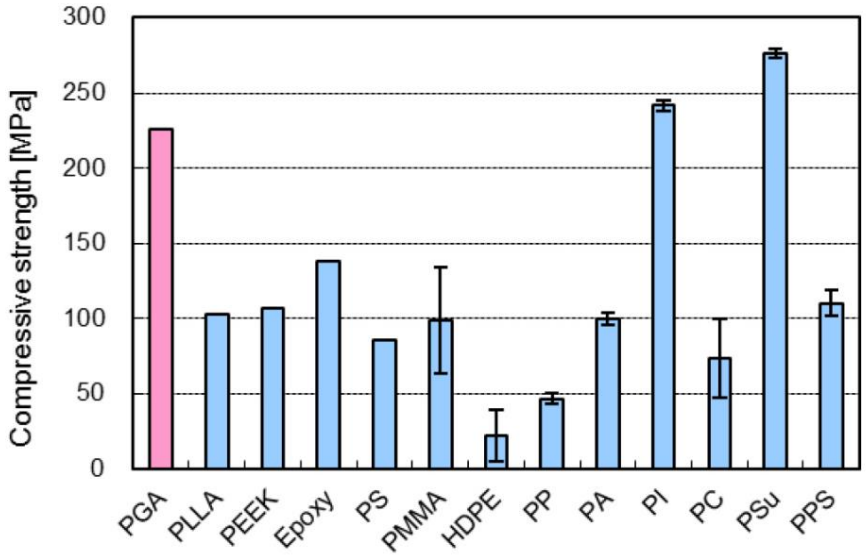

Figure 4 Comparison of the compressive strength of PGA with other ball materials at ambient temperature (Reprinted from Okura et al., 2015)

PGA is 1.5 - 1.6 g/cm^3, there should be no problem to pump it down with wellbore fluids. Similar to degradable alloys, PGA is degraded via surface degradation (Okura, et al., 2012). Degradation of PGA is not affected by salinity or other chemicals dissolved in wellbore fluids and the rate of degradation increases proportionally to temperature increase (Takahashi et al., 2018). Okura et al. (2015) reported the degradation profile at different temperature (Figure 5). At a high temperature above 100°C, PGA was completely degraded within 15 days. However, it takes more than 30 days to degrade completely in lower temperature conditions. Application of this PGA will be limited in some cases due to this slow degradation rate at a low temperature. Therefore, a higher degradation rate is required to widen the applicability.

Polylactic acid (PLA) is also a thermoplastic polymer and categorized as polyester. Degradation of PLA also proceeds via hydrolysis and the degradation rate depends on temperature, molecular weight, crystallinity, and pH (Willberg & Dismuke, 2009). It has a lower mechanical

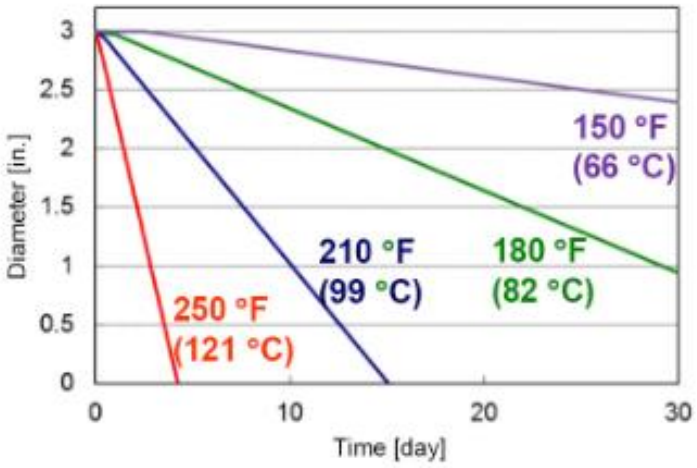

Figure 5 Change in the diameter of PGA frac balls in water at different temperatures over time (Reprinted from Okura et al., 2015)

strength and density (1.21-1.25 g/cm^3) and its degradation rate is slower than PGA (Yoshimura et al., 2014). Hence, application of PLA is limited compared to PGA.

Garza et al. (2017) developed a new thermoset degradable composite material derived from cyanate ester polymer mixed with glass fibers and proprietary additives for the frac ball application. The degradable composite material has a density of 1.18 g/cm^3 and compressive strength of 42 ksi (290 MPa). Its glass transition temperature is as high as 536°F and much higher than PGA (104°F) so that risk of fracture is low for the application. However, they did not conduct the degradation test with the material in the article. Khatiwada et al. (2017) conducted degradation test of the same composite material. The degradable composite material left 50 % of non-degradable filler by the original weight after the degradation test. As this non-degradable filler may cause formation damage or production problem, this degradable composite material is not feasible for DFP. Degradable polymer with a certain degradation rate and mechanical strength can be used as a substitute material of composite material for DFP.

1.2.3 Degradable rubbers

Polyurethane rubber is an elastomer and it is degradable. As it is an elastomer, it has a low Young's modulus and a high maximum strain. Figure 6 and Figure 7 show the structure of polyurethane elastomer and its degradation process, respectively. The reaction of diisocyanate and diol compound creates urethane bond. The degradation occurs in the presence of water by hydrolysis. The stability of urethane rubber in the presence of water depends on the chemical structure of the monomer unit. The hydrolysis stability of polyurethanes based on different polyester diol structure changes as follows: poly (ethylene adipate) diol based < poly (1,4-butylene adipate) diol based < poly(ε-caprolactone) diol based (Szycher, 2012). Krasowska et al. (2015) reported that degradation of conventional polyurethane rubber takes several months or years to complete under the atmospheric condition. They conducted degradation tests of two types of polyurethane which are poly (ethylene-butylene adipate) based and poly(ε-caprolactone) based in

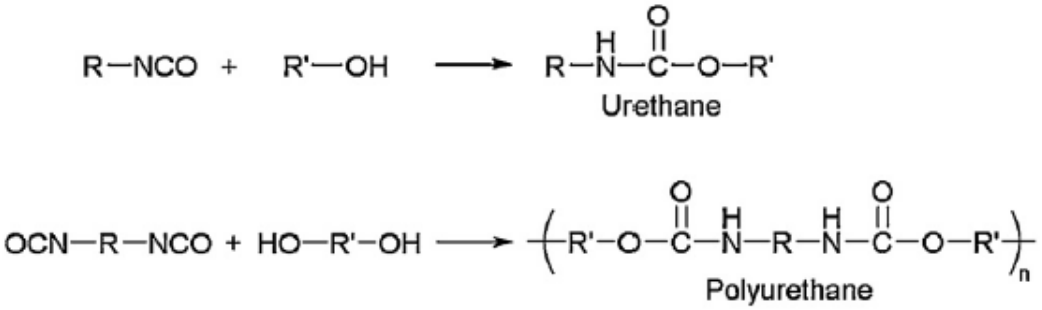

Figure 6 Structure of urethane and polyurethane (Reprinted from Xie et al., 2019)

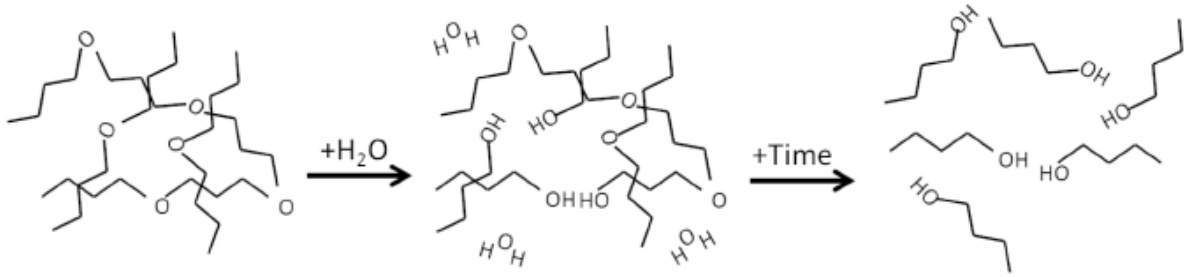

Figure 7 Hydrolysis reaction of polyurethane elastomer (Reprinted from Fripp & Walton, 2017)

the Baltic Sea water. The former degraded only 19% and the latter degraded as low as 4% after 12 months. Accordingly, degradation of polyurethane needs to be accelerated for DFP application. Unlike PGA or Mg alloy, polyurethane elastomer degrades via bulk degradation (Figure 8). Therefore, its mechanical strength of entire body is degraded equally with time. Polyurethane is relatively a light material compared to degradable alloys and PGA, and its density is 1.31 g/cm^3 (Duan et al., 2018).

Takahashi et al. (2016) reported that mechanical strength of degradable polyurethane elastomer is similar to the conventional NBR, which is widely used in oil and gas industry. They also concluded that acid accelerates the degradation reaction of polyurethane elastomer. Shore-A hardness of degradable elastomers decreases with time during the degradation process and once the hardness becomes below 20, the material is easily broken and fall apart into small pieces. Fripp

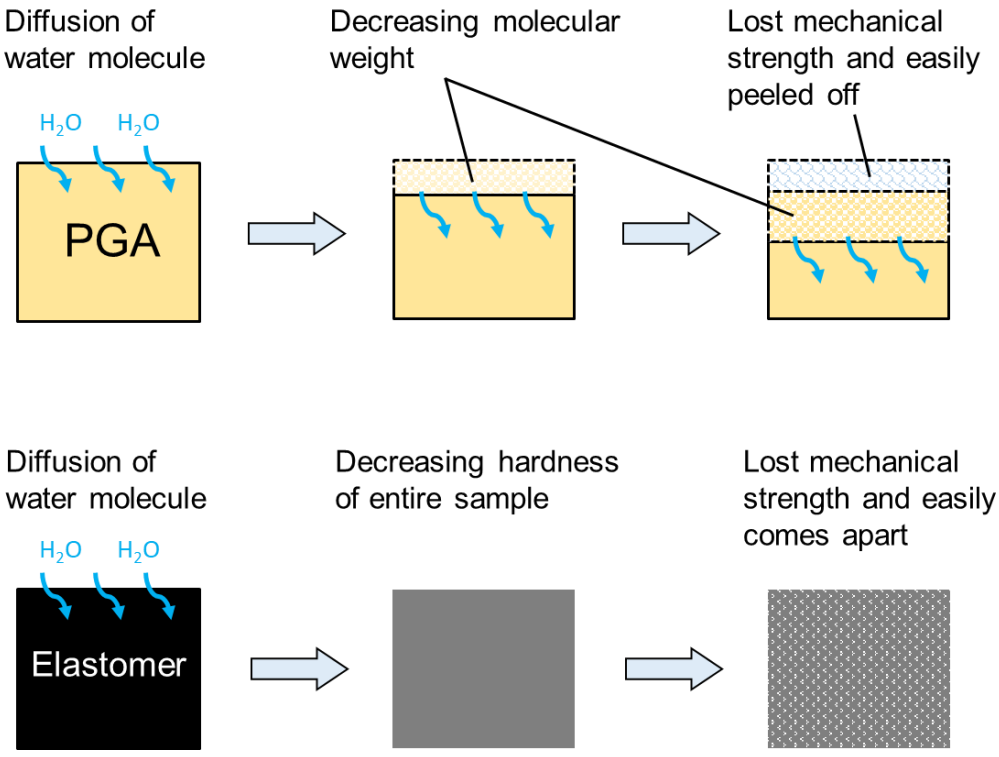

Figure 8 The difference in surface degradation and bulk degradation

and Walton (2017) developed a degradable elastomer and the degradation was completed within 10 days at 90°C but more than 40 days were required to degrade completely at 68°C. Therefore, application of the elastomers is limited to a high temperature environment. According to them, the rate of degradation reaction depends on temperature but it is not affected by the salinity of solution. Since polyurethane rubber has degradability and preferable elasticity, it is applicable to the seal element of DFP.

1.2.4 Application of degradable materials in oil and gas industry

Degradable polymers in fiber, powder, or flake shape have been used for diverter applications. Yoshimura et al. (2014) applied PLA and PGA to fluid loss control materials and concluded that PLA and PGA have similar capability for fluid-loss reduction to conventional silica flour. After certain time, the polymers are degraded in the fluid so that fracture can recover its permeability. Due to their light weight, they can be pumped in wellbore with fluid. The degradable polymers are pumped to wellbore and accumulated in high permeability zone and plug the zone. Therefore, they reduce fluid loss. After specific time in the wellbore fluid, the materials are dissolved via hydrolysis. Kim et al. (2019) conducted proppant transport studies using PGA and PLA fibers with three types of fracture slot equipment. The fibers reduced settling speed of proppant and they enabled proppants to be transported efficiently in the fracture. They also degrade completely within several weeks in wellbore fluids.

Xu et al. (2011) developed a frac ball made of dissolvable metal. It successfully held 10,000 psi at 150°F. However, according to their degradation test in 3% KCl at 200°F, it degrades as low as 0.005 inch per hour. It takes more than three weeks to dissolve the 3.5-inch ball completely and it is too slow. In addition, degradation profile of the material in other conditions is not clear since they performed their degradation test in only one condition. Keerthivasan and Koloy (2019)

conducted pressure test with their degradable metal ball in 5,000 psi maximum pressure at 70°C. Even though the ball withstood 5,000 psi, its performance in higher pressure such as 10,000 psi was not investigated. Kumar et al. (2018) investigated applicability of degradable alloys to gas lift valve. The degradable gas lift plug worked as temporary dummy valve and dissolved after certain time. In their study, mechanical test or pressure test were not performed. Hence, its applicability for DFP is ambiguous.

Jin et al. (2019) developed a degradable metal and studied the pressure tolerance for DFP applications at 52°C. The maximum differential pressure that the plug was able to hold was as low as 4,772 psi, which is too low for DFP application. Li et al. (2018) reported a result of the degradation test and field test of their dissolvable materials for DFP applications. The change in mass of the degradation material in fracturing fluid was significantly smaller than that in KCl solution. This indicates that the DFP requires addition of KCl to make it degrade in wellbores. Jin and Zeng (2017) performed a pressure test and a degradation test of their degradable Mg-Al frac plug. The plug held 7,200 psi for 13 hours and 10,000 psi for 20 mins in 200°F, and the plug dissolved completely after 200 hours at 200°F. However, their degradation test was conducted in a high chloride concentration (15,000 mg/L) and the degradation behavior in lower salinity concentration was not mentioned. Without degradation data of the degradable material in various fluid conditions, applicability of the material to DFP in actual well conditions cannot be discussed. Therefore, not only pressure tolerance of the downhole tool but also understanding of degradation profile of degradable materials in various fluid condition is crucial to the development of DFP.

1.3 Research Objectives

In this research, applicability of three fast-degrading materials to DFP was studied from the aspect of degradation profile and mechanical strength by the following tests and analyses.

Degradation test: In order to understand degradation profile of the materials, degradation tests in various conditions such as different temperatures (120, 150, 175, 200°F), different types of salts (KCl, NaCl, $CaCl_2$, KNO_3, K_2SO_4, $KHCO_3$), additives (scale inhibitor, friction reducer, surfactant, biocide, clay control agent, corrosion inhibitor, iron control agent), acid (HCl), and alkaline (NaOH) were performed. We also carried out degradation test with DFP assembly.

Mechanical test: Several mechanical tests including simple uniaxial tensile and compression test were conducted to investigate their mechanical strength. Loading tests of frac plug parts made of the degradable materials with universal testing machine were also performed to evaluate their strength and performance in casings.

Finite element analysis: A commercial finite element analysis software, ABAQUS was used for optimization of the shape of DFP components. Behavior of several new designs of seal element and socket under high pressure condition were simulated with ABAQUS. In addition, the deformation behavior of frac balls with various diameters under 10,000 psi were simulated to optimize the size. Several mandrels with different designs were modeled and the effect of design on the stress state under certain load was also analyzed.

Pressure test of DFP: In order to determine the pressure tolerance of DFP composed of the fast-degrading materials, pressure test of the DFP using a large pressure vessel with temperature capability was conducted.

2. DEGRADATION TEST OF FAST-DEGRADING MATERIALS

2.1 Degradation test of fast degrading PGA

2.1.1 Material and methods

PGA material used in this study was low temperature grade PGA (PGA-FD) with high molecular weight and it was provided by Kureha Corporation. A cubic specimen of PGA-FD with the dimension of 1 cm × 1 cm × 1 cm was put in a beaker with 50 mL of DI water and left in a thermostatic oven (Thermo Fisher Scientific, Heratherm OMH60) under specific temperatures (120°F, 150°F, 175°F, 200°F) without agitation. Thickness and weight of the samples were measured at a certain time interval. Before the measurement of PGA-FD samples, fragile layers on the surface was removed by a utility knife. The same degradation test with 10% KCl solution, 15% HCl solution, and 0.1 M NaOH solution were conducted at 150°F. All other conditions were the same as above at the tests. The pH of 0.1 M NaOH solution is around 12-13 and it represents pH of gel frac fluids. For the case of 0.1 M NaOH, fluid was replaced by new one every 24 hours to keep the pH of the solution. Degradation tests of PGA-FD in various types of salt solutions (K_2SO_4, KNO_3, $KHCO_3$, NaCl, KCl, and $CaCl_2$) were carried out in a solution with a concentration of 0.27 M at 150°F. All other conditions were the same as above for the tests. With the same protocol, degradation test with eight additives was also carried out at 150°F. Model chemicals were used to simulate the main components of each additive in slickwater. The additives, corresponding model chemicals used in the test, and their concentrations were shown in Table 1. The concentrations were chosen based on other literatures (U.S. Environmental Protection Agency, 2015; Takahashi et al., 2018; Sun, 2014; Koteeswaran et al., 2018; Mainier et al., 2018; Finšgar & Jackson, 2014; Balanaga karthik et al., 2014; Barati & Liang, 2014). The materials except for poly(acrylamide/sodium acrylate) were purchased from MilliporeSigma (Louis, MO, USA).

Poly(acrylamide/sodium acrylate) was purchased from Polysciences, Inc. (Warrington, PA, USA). All the tests were duplicated. The pH of solution was measured with a pH meter (OAKTON, pH 150).

Table 1 Additives and their concentrations

Additive	Model chemical name	Concentration
Friction reducer	Poly(acrylamide/sodium acrylate) [70:30] (PAA)	0.03% (1 gpt)
Surfactant	Nonylphenol Ethoxylate (Tergitol NP-40)	0.05%
Biocide	Glutaraldehyde	250 ppm
Clay control agent	Tetramethyl ammonium chloride (TMAC)	2%
Corrosion Inhibitor	Propargyl alcohol	0.10%
Scale Inhibitor	Diethylenetriamine penta(methylene phosphonic acid) (DTPMP)	100 ppm
Iron control agent	Citric acid	250 ppm
Gelling agent	Guar	0.20%

2.1.2 Results and discussion

Figure 9 shows the decrease in thickness with time in DI water at different temperatures. From the result, degradation rate in mm/h of each condition was calculated. A semi-log plot of temperature and the degradation rate were shown in Figure 10. As temperature increases the degradation rate was increased exponentially. This is because the hydrolysis reaction of PGA-FD is accelerated by higher temperature (Takahashi et al., 2018). Another reason of this acceleration in high temperature conditions can be higher diffusion rate of water molecule in the surface of PGA-FD. In all the cases, the pH of the fluid decreased from neutral to around 2 during the degradation test since hydrolysis of PGA generates carboxylic acid such as glycolic acid (Göktürk et al., 2015). Results of degradation test in 10% KCl, 15% HCl, and 0.1 M NaOH were shown in Figure 11. Degradation of PGA-FD in high concentration of 15% HCl and 10% KCl was slower compared to that in DI water. Chu (1981) also reported the degradation of PGA was slower in

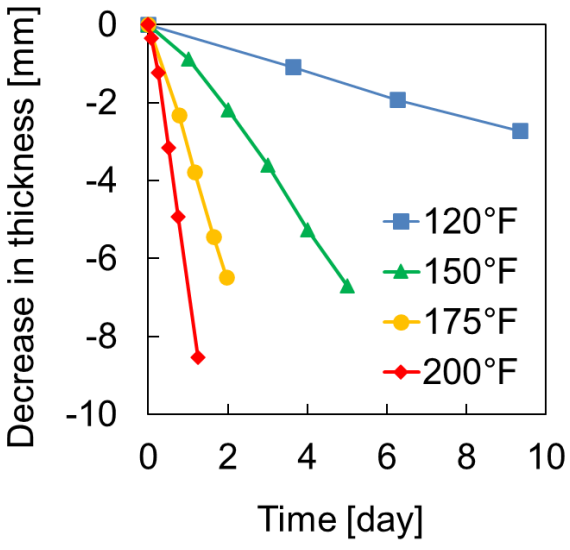

Figure 9 Results of the degradation test of PGA-FD in DI water at various temperatures

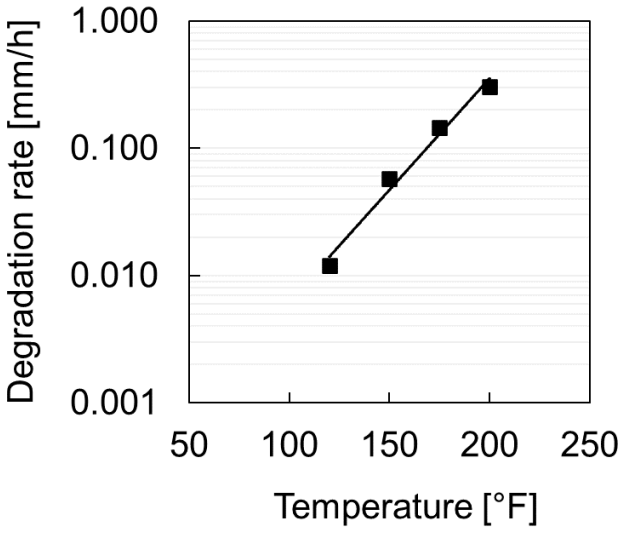

Figure 10 Relationship between temperature and the degradation rate of PGA-FD

lower pH condition than that in neutral pH condition. The effect was more significant for 15% HCl compared to 10% KCl. We hypothesize that oligomers with carboxylic group generated at PGA surface during degradation process could not be ionized nor dissolved into the solution in the presence of a large amount of ion species such as K^+ and H^+ so that they remained on the surface. Therefore, water molecules could not diffuse in the surface layer of PGA. As a result, the degradation of PGA-FD was retarded. This behavior was schematically shown in Figure 12. The reason of slower degradation of PGA-FD in 15% HCl compared to 10% KCl is presumed that an excess amount of proton had greater inhibitive effect on dissociation of oligomer and the degradation reaction than K^+. In contrast, 0.1 M NaOH accelerated degradation of PGA-FD. It is because hydrolysis reaction of polyester is promoted in basic condition (Chu, 1981; Woodard & Grunlan, 2018).

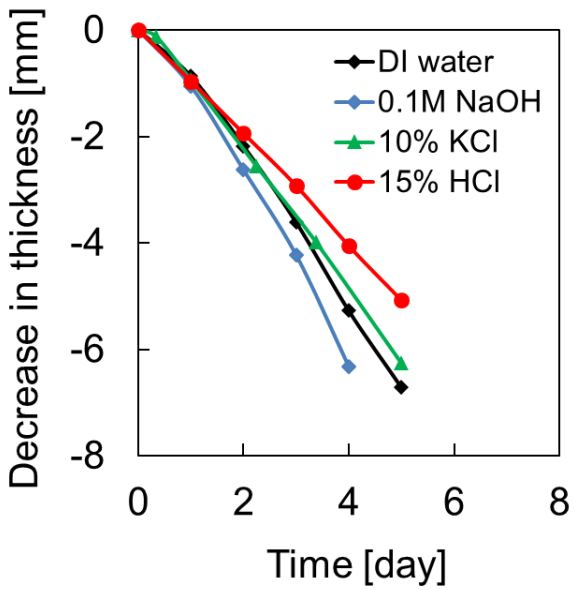

Figure 11 Results of the degradation test of PGA-FD with various solutions at 150°F

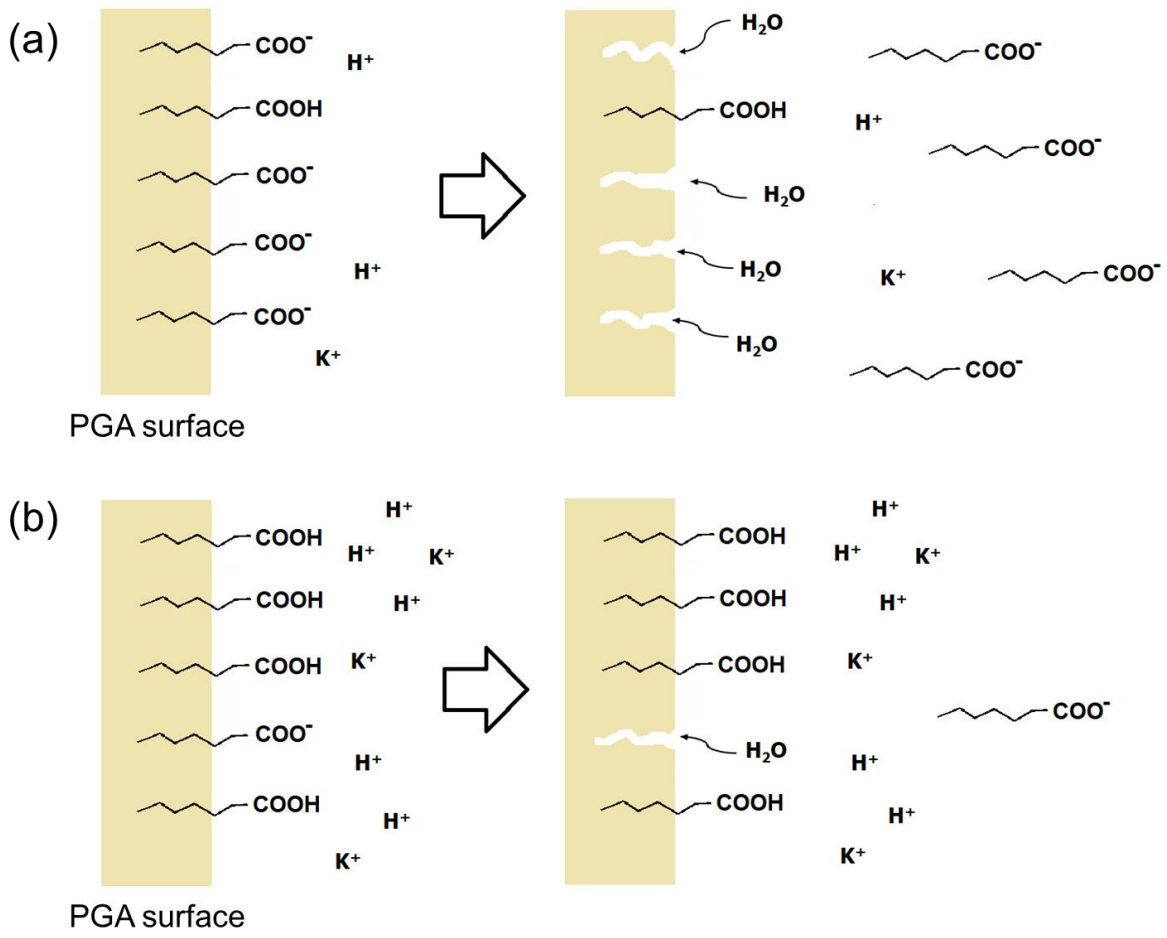

Figure 12 Degradation mechanism on PGA surface: (a) in DI water or a low ion concentration, (b) in a high ion concentration

Results of the degradation test in various salt solutions were shown in Figure 13. As one can see in the figure, there was no significant difference among them compared to the result in DI water. Degradation of PGA-FD in K_2SO_4 solution was slightly slower than others. This is because there was twice the amount of K^+ ion in the solution of K_2SO_4 compared to other salt solutions and it inhibited the degradation of PGA-FD.

Figure 14 shows the result of degradation test of PGA-FD with additives. Similar to the degradation test in various salt solutions, there was no remarkable difference in the degradation behavior between DI water and the solution with additives for 3 days. There was a slight difference

in the reduction in thickness between DI water and additive mixed solution after 4 days. This is presumably due to vaporization of water and concentration of the solution. Even though the viscosity of the solution with additives were much higher than DI water due to guar and poly(acrylamide/sodium acrylate) (PAA), the effect was relatively small in the test. This result indicates that additives and viscosity of fluid do not affect the degradation of PGA-FD significantly.

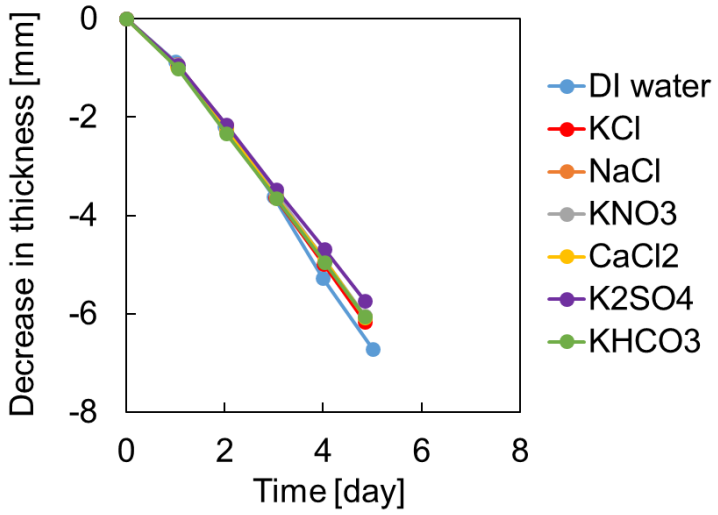

Figure 13 Results of the degradation test of PGA-FD with various salt solutions at 150°F

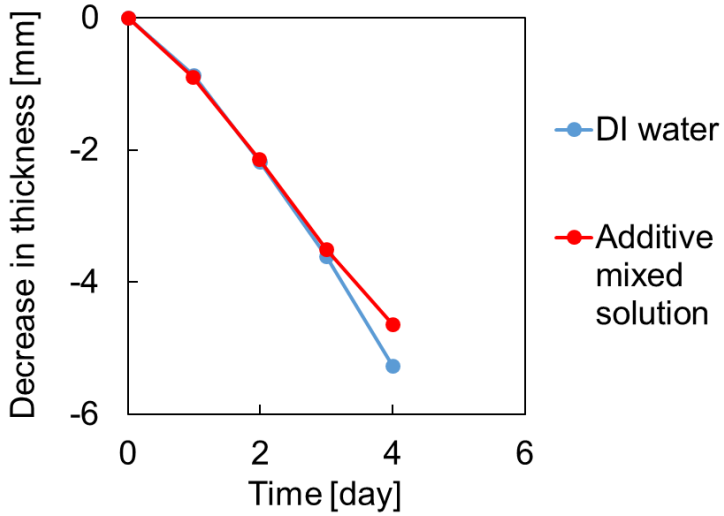

Figure 14 Results of the degradation test of PGA-FD with additive mixed solution at 150°F

2.2 Degradation test of fast degrading rubber

2.2.1 Material and methods

Rubber material used in this study was low temperature grade Kureha Degradable Rubber (R-FD) and provided by Kureha Corporation. For degradation test of R-FD, specimens cut from an actual seal element were used (Figure 15). The specimens have a volume that is one-twelfth of the seal element for 5.5-inch 23 lb/ft casing. The specimen was put in a beaker with 100 mL of solution and left in the thermostatic oven under specific temperatures without agitation. The condition was employed in the following all the tests. To investigate the effect of temperature on the degradation of R-FD, degradation tests in DI water at 125°F, 150°F, 170°F, and 200°F were conducted. Shore-A hardness of the samples was measured at a certain time interval with a durometer. The same degradation tests in 10% KCl solution, 15% HCl solution, and 0.1 M NaOH solution at 150°F were also performed at 150°F. A degradation test in a solution with the same additives and their concentration as shown in Table 1 was also conducted at 150°F. To study the effect of the type of salts on the degradation of R-FD, degradation tests in various types of salt solutions (K_2SO_4, KNO_3, $KHCO_3$, NaCl, KCl, and $CaCl_2$) were carried out in a solution with a concentration of 0.27 M at 150°F. For this test, specimens with the dimension of 2 cm × 2 cm × 2 cm were used. All the tests were duplicated.

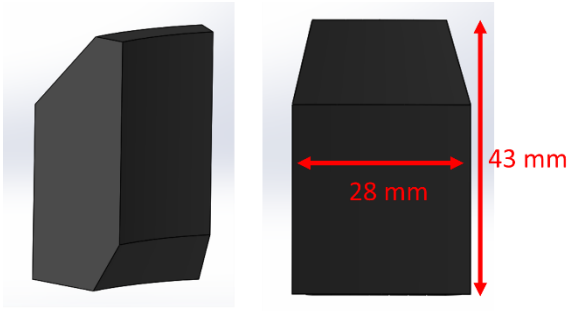

Figure 15 Test specimen of R-FD

2.2.2 Results and discussion

Figure 17 shows the result of degradation test of R-FD in different temperatures. From the result, degradation rates were calculated by dividing the change in Shore-A hardness by time. A semi-log plot of temperature and the degradation rates was shown in Figure 16. Shore-A hardness of R-FD became 0 after 1 day, 2 days, 8 days, and 12 days at 200°F, 175°F, 150°F, and 125°F, respectively. Similar to PGA-FD, the degradation of R-FD was accelerated exponentially with increase in temperature. Stevenson and Kusy (1995) studied a polyurethane under two different temperature conditions and reported higher temperature caused faster decrease in the molecular weight and mechanical strength of the material. Chaffin et al. (2014) also concluded that Arrhenius plot can be employed to demonstrate a relationship between temperature and change in the molar mass of their polyurethane samples. They found the molecular mass of their samples reduced with increase in temperature due to scissions of molecular chains. It is suggested that the similar scissions of molecular chain were occurred for R-FD in our study as well. Faster diffusion of water

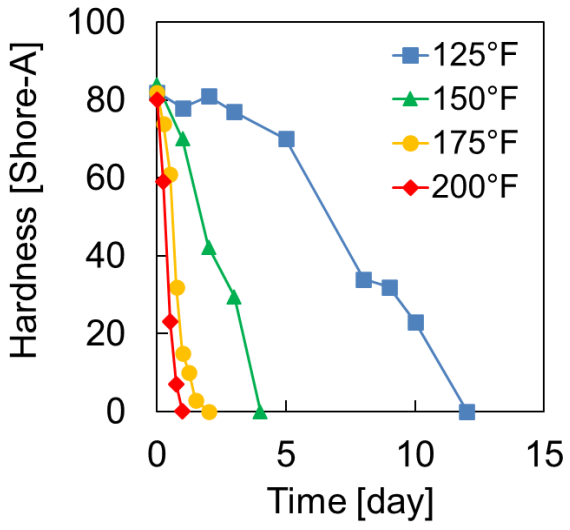

Figure 16 Results of the degradation test of R-FD in DI water at different temperatures

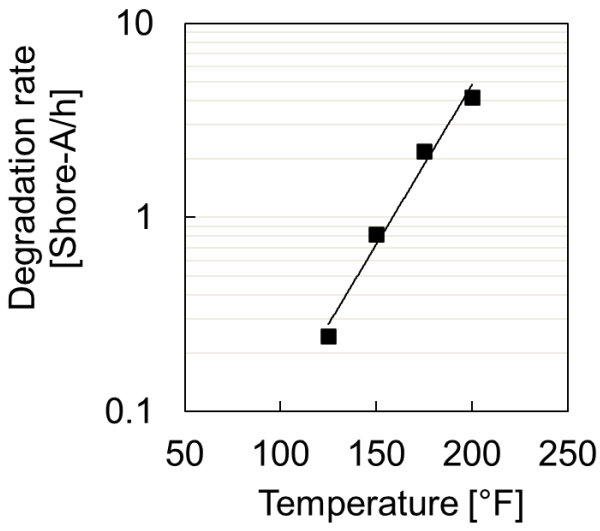

Figure 17 Relationship between temperature and the degradation rate of R-FD

molecule inside R-DF in higher temperature is also another reason of the accelerated degradation of R-FD in higher temperatures (Pretsch, et al., 2009).

Results of the degradation test in 10% KCl solution, 15% HCl solution, and 0.1 M NaOH solution were shown in Figure 18. For comparison, the result in DI water at the same temperature was also shown in the figure. There was no significant difference in the degradation behavior among 10% KCl solution, 0.1 M NaOH solution, and DI water. It is known that salts do not affect degradation of polyurethane and this result is consistent with it (Xie et al., 2019). In general, NaOH accelerates hydrolysis of ester groups and promotes the degradation (Chan-Chan et al., 2010; Clemitson, 2008). Unlike other researches, we did not find a significant difference between 0.1 M NaOH and DI water. The prime cause of the discrepancy is probably due to the relatively low concentration of NaOH. Another possible reason of the discrepancy is that Shore-A hardness is not so accurate to detect the small difference. In contrast, 15% HCl solution showed faster

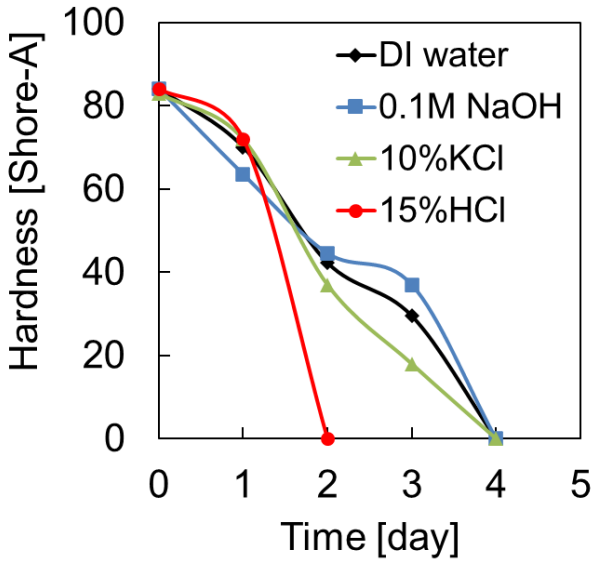

Figure 18 Results of the degradation test of R-FD in 10% KCl solution, 15% HCl solution, and 0.1M NaOH solution at 150°F

degradation and its Shore-A hardness became zero after 2 days. It is widely known that acids catalyze and accelerate hydrolysis of polyester linkage of polyurethanes (Xie et al., 2019). Therefore, an excess amount of proton in the 15% HCl solution promoted hydrolysis of the ester groups in R-FD. From the result we concluded that R-FD cannot be used in strong acid fluid similar to Mg-FD.

Results of the degradation test of R-FD in various salt solutions were shown in Figure 19. For comparison, the result in DI water at the same temperature was also shown in the figure. There was no significant difference between the result in DI water and those in the salt solutions. As suggested by the aforementioned results, degradation of R-FD was not affected by salt ions. Figure 20 shows the result of degradation test in the additive mixture solution. As one can see in the figure, the degradation of R-FD was not affected by the additives in the solution. These results revealed that the effects of salt, additives and viscosity of the fluid on the degradation of R-FD were very small and can be ignored.

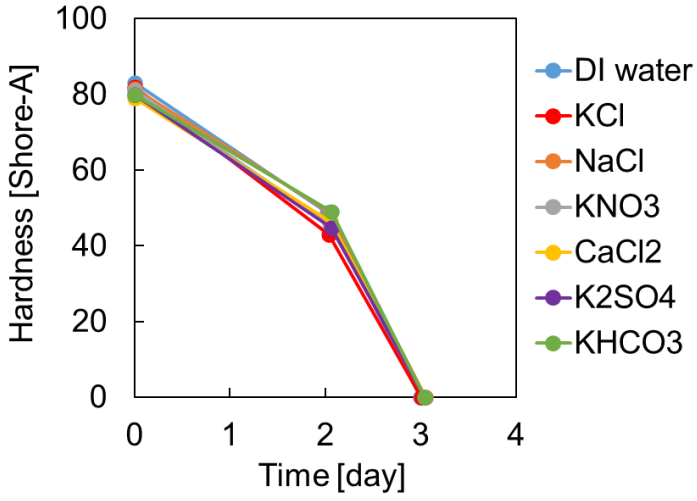

Figure 19 Results of the degradation test of R-FD in various salt solutions at 150°F

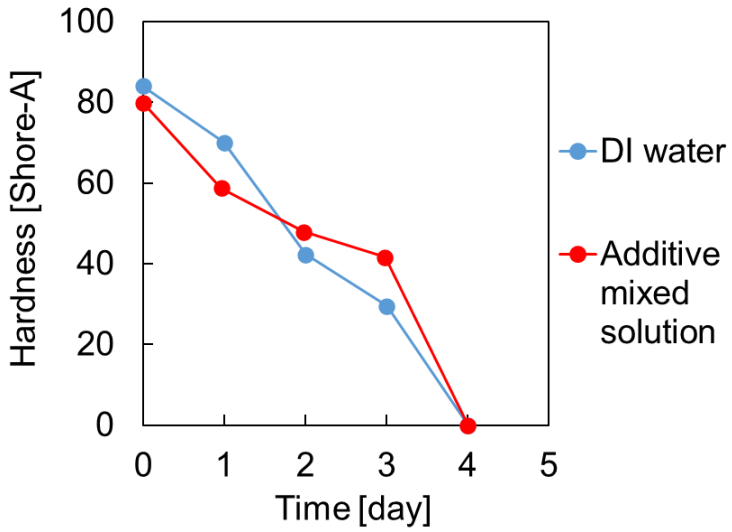

Figure 20 Results of the degradation test of R-FD with additive mixed solution at 150°F

2.3 Degradation test of fast degrading Mg alloy

2.3.1 Material and methods

A low temperature grade degradable Mg alloy (Mg-FD) was supplied by Kureha Corporation and used in this study. A cubic specimen of Mg-FD with the dimension of 1 cm × 1 cm × 1 cm was used in the following degradation tests. The specimen was soaked in a beaker filled with 50 mL of KCl solution (0.05%, 0.3%, 2%, 10%) and left the beaker in a water bath without agitation. The test was performed at various temperatures (120°F, 150°F, 175°F, 200°F). Thickness and weight of the samples were measured at a certain time interval. Degradation tests of Mg-FD in various concentrations of HCl solutions (0.1%, 1%, 3%, 5%, 10%, and 15%) at 150°F were conducted under the same experimental procedure as above.

To examine the effect of high pH, degradation test of Mg-FD in a 200 mL of 0.1 M and 0.01 M NaOH solution with 0.3% KCl was performed at 150°F in the thermostatic oven without agitation. The following degradation tests were also conducted with the same amount of solution (200 mL) and temperature (150°F) in the thermostatic oven without agitation. Degradation tests of Mg-FD in various types of salt solutions (K_2SO_4, KNO_3, $KHCO_3$, NaCl, and $CaCl_2$) were carried out in a solution with a concentration of 0.27 M. The concentration was employed to compare the degradation behavior of Mg-FD in 2% (0.27 M) KCl solution. To evaluate the effect of additives in slickwater on the degradation of Mg-FD, a degradation test was conducted in 0.3% KCl solution with eight additives. The additives and their concentrations for the test were the same as those in Table 1. To elucidate the effect of each additive on the degradation of Mg-FD, degradation tests of Mg-FD with each additive in 0.3% KCl solution were also carried out.

2.3.2 Results and discussion

Figure 21 shows the results of degradation test of Mg-FD with 0.3% KCl solution at various temperatures. The decrease in thickness was greater at higher temperature. A semi-log plot of temperature and the degradation rate in various concentrations of KCl solutions was shown in Figure 22. For all the KCl concentrations, the degradation rate increased with increase in temperature. During the degradation of Mg through the chemical reaction of Eq. 3, $Mg(OH)_2$ is generated and precipitated as its solubility is low. As chloride ion is extremely corrosive, it stimulates metal dissolution and causes pitting corrosion (Johnson & Liu, 2013; Fontana, 1986). Mg ion dissolved in solution reacts with chloride ion and produces $MgCl_2$, which is water soluble. In addition, chloride ion reacts with $Mg(OH)_2$ and converts it to $MgCl_2$ (Peng et al., 2014). Due to these combined factors, fast degradation of Mg-FD was achieved. Therefore, degradation rate increased with increase in KCl concentration. The pH of solution increased with time and reached about 10-11 after the tests. This was resulted from the reduction of water during degradation of

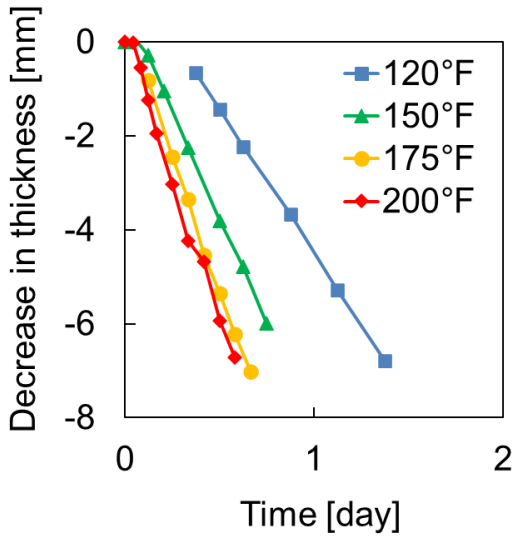

Figure 21 Results of the degradation test of Mg-FD with 0.3% KCl solution at various temperatures

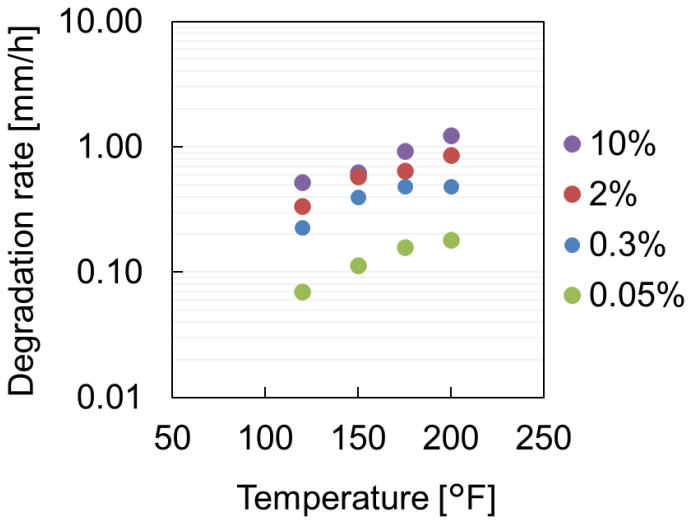

Figure 22 Relationship between temperatures and the degradation rates of Mg-FD in various concentrations of KCl solutions

Mg and generation of OH^- ion which is shown in Eq. 2. Ning et al. (2015) reported 10.43 was pH of the solution saturated with Mg^{2+} ion and it agrees with this result.

Figure 23 shows relationship between concentration of HCl and degradation rate at 150°F. The degradation rate increased with increase in HCl concentration. The degradation rates in HCl solutions were extremely high compared to those in KCl solutions. It is suggested that HCl dissolved protective layer of $Mg(OH)_2$ on Mg-FD surface immediately after the formation and promoted chloride ion to attack Mg-FD surface. An excess amount of proton was also presumed to promote the reaction of Eq. 2 on Mg-FD surface and corrosion of Mg-FD. As the degradation is too fast in HCl solutions with 1% or more of the concentration, Mg-FD should not be used in acidic fluids.

The pH of 0.1 M NaOH solution with 0.3% KCl and 0.01 M NaOH solution with 0.3% KCl during the test were about 12.3-12.4 and 11.3-12.0, respectively. Result of the degradation test in 0.1 M and 0.01 M NaOH solution with 0.3% KCl at 150°F was shown in Figure 24. For

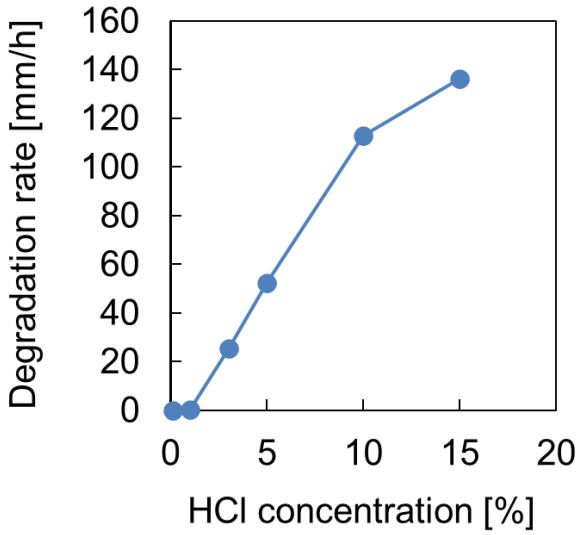

Figure 23 Relationship between HCl concentration and degradation rate at 150°F

comparison, the result of degradation test in 0.3% KCl solution without NaOH was also shown in the figure. The decrease in thickness of Mg-FD with NaOH was obtained from the following calculation based on the weight since the degraded sample was not a cubic shape due to severe pitting corrosion. It assumes that the sample is a cubic shape and the thickness of the sample decreases uniformly during the degradation.

$$Sample\ thickness\ [mm] = \left(\frac{wight\ [g]}{1.8\left[{}^{g}/_{cm^3}\right]} \times 1000\right)^{1/3} \quad (7)$$

$$Decrease\ in\ thickness\ [mm] = -(degraded\ Sample\ thickness\ [mm] - Original\ thickness\ [mm]) \quad (8)$$

Compared to the degradation of Mg-FD in 0.3% KCl solution without NaOH, that with NaOH was slower. The higher the concentration of NaOH, the slower the degradation of Mg-FD. $Mg(OH)_2$ is a typical corrosion product of Mg alloys and it easily precipitates in the presence of hydroxy ions

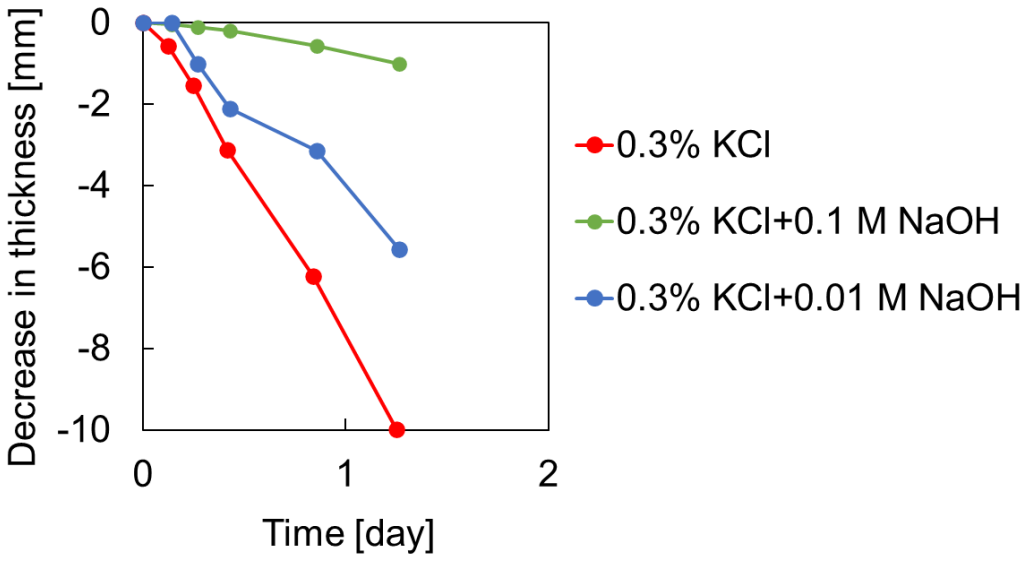

Figure 24 Result of the degradation test in 0.1 M and 0.01 M NaOH solution with 0.3% KCl at 150°F

and Mg^{2+}. Many researchers concluded $Mg(OH)_2$ works as a passivation film and prevents corrosion of Mg (Peng et al., 2014; Takahashi et al., 2018; Ning et al., 2015; González et al., 2013). It was suggested that $Mg(OH)_2$ layer formed on the surface of Mg-FD in the presence of a large amount of hydroxy ion worked as a passivation film and impeded the degradation reaction. This result indicates Mg-FD cannot be used in strong alkaline fluids.

Degradation test results with various salt solutions at 150°F were shown in Figure 25. The result with $CaCl_2$ solution was calculated by Eq.7 and Eq. 8 as the degraded sample was not cubic shape due to severe pitting corrosion (Figure 26), whereas the samples with other salt solutions showed a relatively uniform corrosion. The degradation profile of Mg-FD in NaCl solution was similar to that in KCl solution. In contrast, the degradation of Mg-FD in other salt solutions was slower than that in NaCl solution and KCl solution. For $KHCO_3$ solution, no degradation was observed during the test period. The order of the degradation rates was as follows: $KHCO_3 < K_2SO_4 < KNO_3 < CaCl_2 < KCl \leq NaCl$. Even though $CaCl_2$ solution contains twice amount of

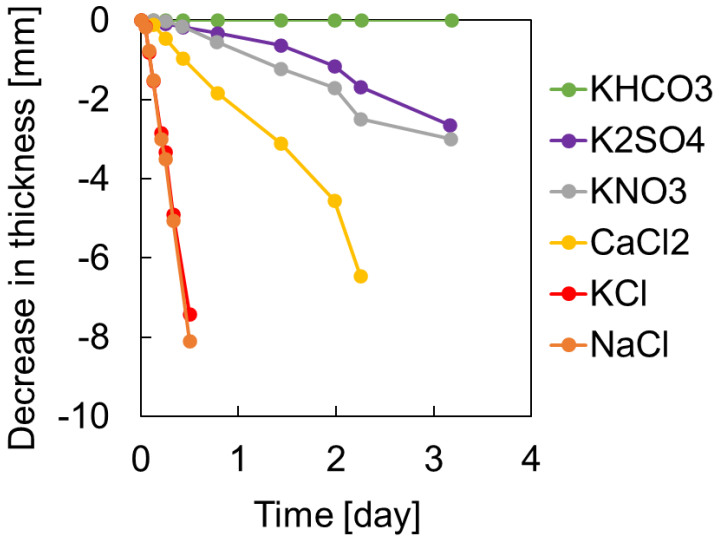

Figure 26 Results of the degradation tests of Mg-FD in various salt solutions at 150°F

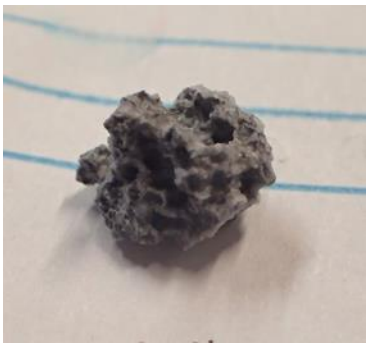

Figure 25 Mg-FD sample after soaking for 34 hours in $CaCl_2$ solution

chloride ion, its corrosion rate was slower than that of KCl or NaCl. This is because Ca cation is divalent and divalent cations inhibit dissolution of Mg^{2+} (Ning et al., 2015; Murphy et al., 2019). The corrosion rate of KNO_3 was greater than that of K_2SO_4 as the size of NO_3^- is smaller than SO_4^{2-} and it enabled the ion to penetrate passivation film on the surface of Mg-FD. In addition, corrosion byproducts were accumulated on the surface of Mg-FD which was soaked in K_2SO_4 solution (Figure 27), whereas other solutions did not show the accumulation of byproducts. This is also another cause of slower degradation of Mg-FD in K_2SO_4 solution since it inhibits diffusion of SO_4^{2-} ion to Mg-FD surface. Hihara and Kondepudi (1994) also reported greater degradation rate of Mg in the presence of NO_3^- compared to SO_4^{2-}. In addition, it was reported that $MgAl_2(SO_4)_4 \cdot 2H_2O$ particles are precipitated in the presence of SO_4^{2-} and retard degradation of Mg (Chen et al., 2005). Presumably, no degradation of Mg-FD in $KHCO_3$ solution was resulted from a precipitation of $MgCO_3$ or more stable giorgiosite ($Mg_5(CO_3)_4(OH)_2 \cdot 5H_2O$) on the surface (Xin et al., 2008).

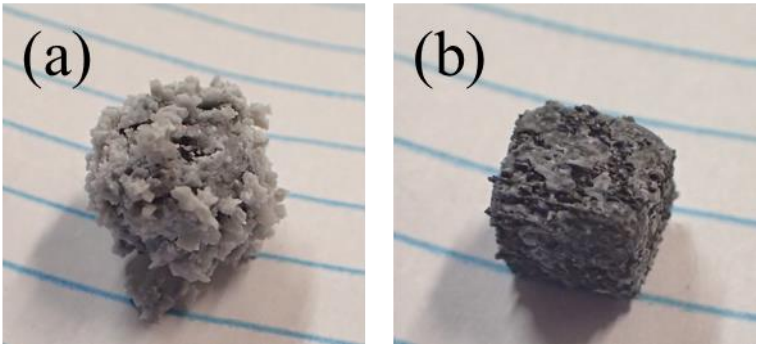

Figure 27 Mg-FD sample after soaking for 34 hours in K_2SO_4 solution: (a) before wash, (b) after wash

Figure 28 shows the result of the degradation test of Mg-FD in 0.3% KCl solution with eight additives at 150°F. For comparison, the result in 0.3% KCl solution (without the additives) was also included in the figure. The decrease in thickness was calculated by Eq. 7 and Eq. 8 as the degraded sample was not a cubic shape due to a partial pitting corrosion. The degradation of Mg-FD with additives was slower compared to that without the additives. Accumulations of byproducts on the surface of Mg-FD was observed in the presence of the additives (Figure 29). On the other hand, it was not observed in the absence of the additives.

Results of the degradation test of Mg-FD in 0.3% KCl with each additive were shown in Figure 30. Each additive affected differently on the degradation of Mg-FD. The order of the degradation rates was the following: PAA < Guar < Tergitol < Propargyl alcohol < Citric acid < DTPMP ≅ Glutaraldehyde ≅ no additives < TMAC. PAA and Guar showed significantly lower degradation rate. This is because they increased the viscosity of the solutions and inhibited

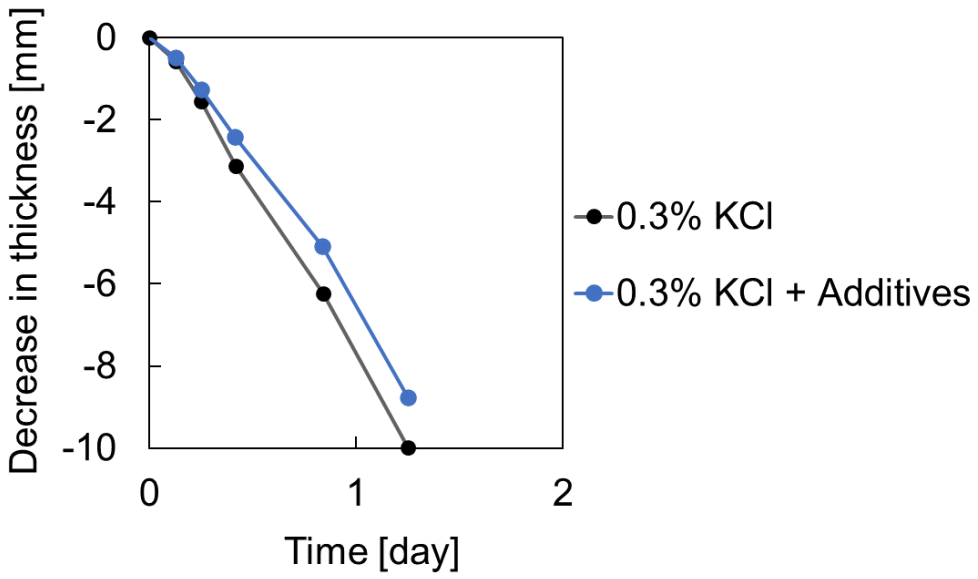

Figure 28 Result of the degradation test of Mg-FD in 0.3% KCl solution with and without additives at 150°F

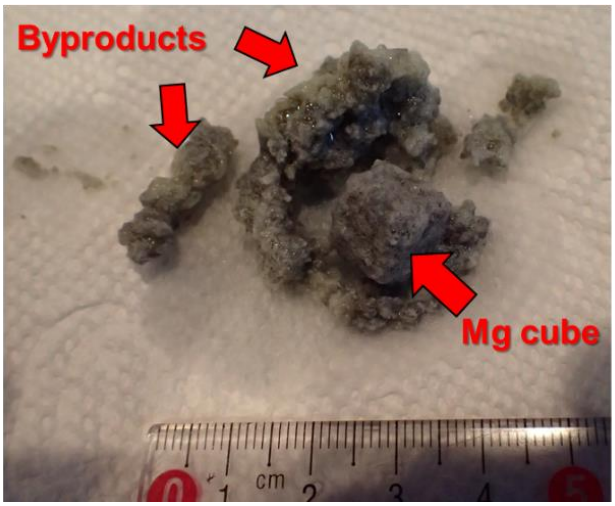

Figure 29 Mg-FD sample after 3 hours of soaking in 0.3% KCl solution with eight additives

the diffusion of degradation byproducts of Mg-FD from the surface to the solution. It caused accumulation of the byproducts on the surface of Mg-FD as shown in Figure 31 and resulted in inhibiting the diffusion of chloride ions to the surface. The accumulation of the byproducts in the

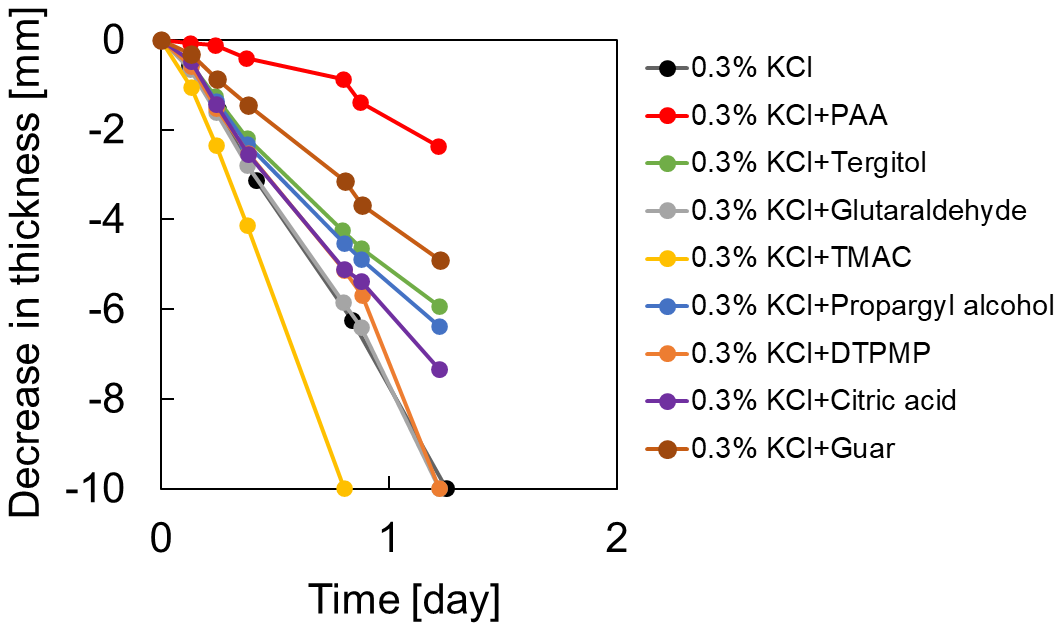

Figure 30 Results of the degradation tests of Mg-FD in 0.3% KCl solutions with each additive at 150°F

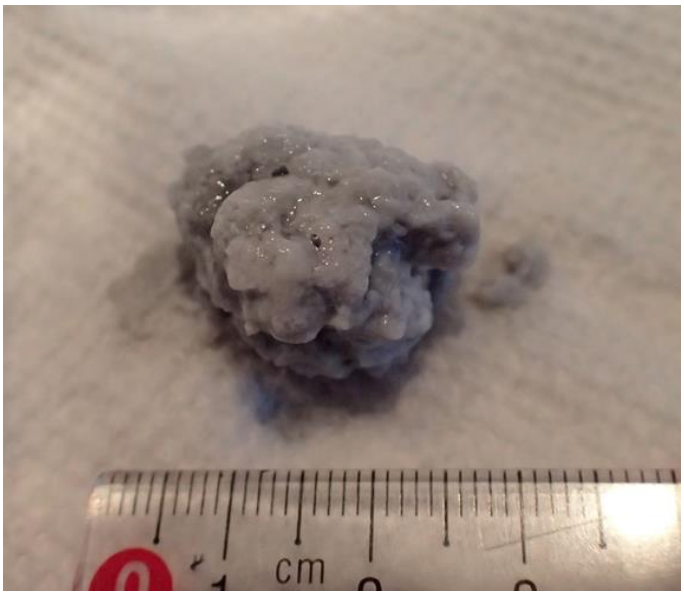

Figure 31 Mg-FD sample after 3 hours of soaking in 0.3% KCl + 0.5 gpt of PAA solution

solution with PAA was more severe compared to that with guar. As a result, the degradation of Mg-FD was delayed in the presence of these additives. The accumulated byproduct was easily removed by rinsing with water. Tergitol also retarded the degradation of Mg-FD. It promotes the generation of stable hydrogen bubbles during the chemical reaction of Eq. 3 due to its surface-active function and the bubbles would hinder the diffusion of chloride ions to the Mg surface. This is probably responsible for the slower degradation of Mg-FD in the presence of Tergitol. Propargyl alcohol is a common corrosion inhibitor that adsorbs on the metal surface and forms a physical barrier which is 20-200 Å in thickness (Finšgar & Jackson, 2014; Shank & McCartney, 2013). This is the reason for retarded corrosion of Mg-FD in the presence of propargyl alcohol. Citric acid also delayed the degradation of Mg-FD. This reason is not clear but we hypothesize that stable and insoluble chelates were formed on the surface of Mg-FD by citric acid and impeded the degradation of Mg-FD. Lehr and Saidman (2018) also proposed this effect by citric acid for an improved corrosion resistance of a Mg alloy. Another possible cause is that citric acid formed

chelates with the dopants of Mg-FD and removed them from the surface, and it resulted in less galvanic corrosion. In contrast, DTPMP and glutaraldehyde did not affect the degradation of Mg-FD. TMAC accelerated the degradation of Mg-FD as it contains and releases chloride ion into the solution. These results indicate that additives in the fluid are of great importance for the degradation of Mg-FD as they affect differently on it.

When we consider the time required to degrade the entire body of DFP composed of the three fast degrading materials, the control factor is most likely the degradation of PGA-FD as it requires the longest time to complete the degradation in most of the cases. Using the results obtained from the tests conducted in this section, we can estimate the degradation profile of all the materials in various conditions. However, the most reliable way to estimate the time required for the complete degradation of DFP composed of the three materials is to conduct degradation test using actual fluid obtained from the well or field where the DFP is being used.

3. LABORATORY TESTS OF FAST DEGRADING MATERIALS AND FRAC PLUG COMPONENTS

3.1 Tensile and compression tests of fast degrading materials

3.1.1 Materials and methods

Tensile test of PGA-FD was conducted with a universal testing machine (INSTRON, 5582) at 150°F according to ASTM D638. Type V specimens and 20 mm/min of the strain rate were employed. Tensile test of Mg-FD was performed at room temperature with Autograph 250 kN (Shimadzu) at the strain rate of 3 mm/min based on JIS Z2201. No.10 type test specimen was used for the tensile test of Mg-FD. Compression test of R-FD was carried out at the strain rate of 20 mm/min with INSTRON 5582 at 150°F according to JIS K 7018. Specimens with the dimension of ϕ5 and 3 mm thickness were used for the compression test.

3.1.2 Results and discussion

Stress-strain curves obtained from the tensile test of PGA-FD and Mg-FD are shown in Figure 32 and Figure 33, respectively. Figure 34 shows the stress-strain curve obtained from the compression test of R-FD. The maximum tensile strengths and strain of PGA-FD were 86.3 MPa and 197%, respectively. The maximum tensile strengths and strain of Mg-FD were 313.8 MPa and 16%, respectively. These values are similar to other degradable Mg alloy available in market (Luxfer MEL Technologies, 2020). Nominal stress of R-FD was small at low strain but increased drastically above 80% of the strain. This is the common behavior of elastomers.

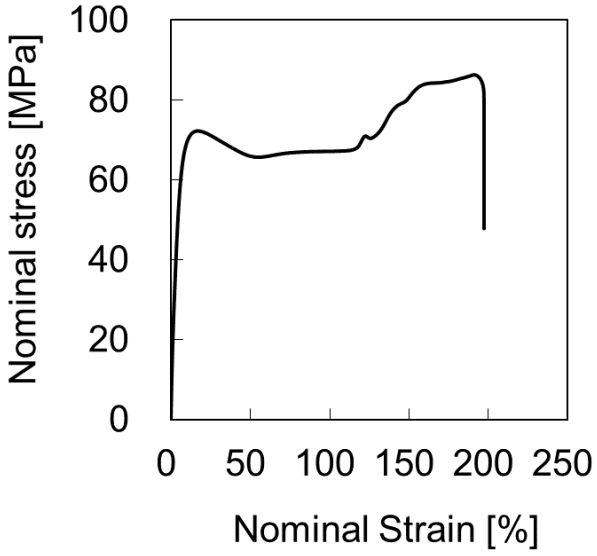

Figure 32 Stress-strain curve of PGA-FD

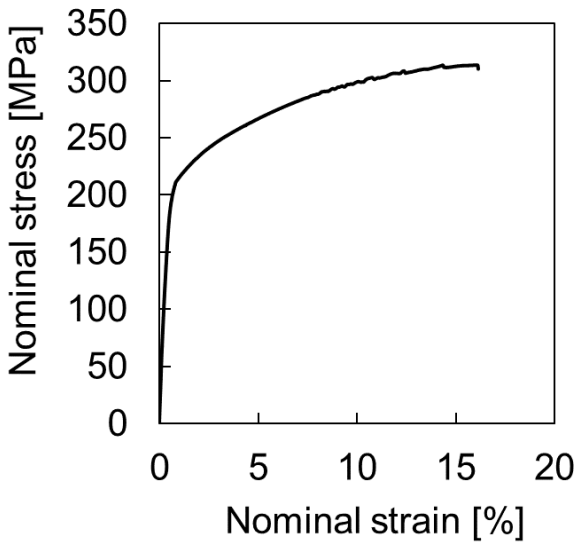

Figure 33 Stress-strain curve of Mg-FD

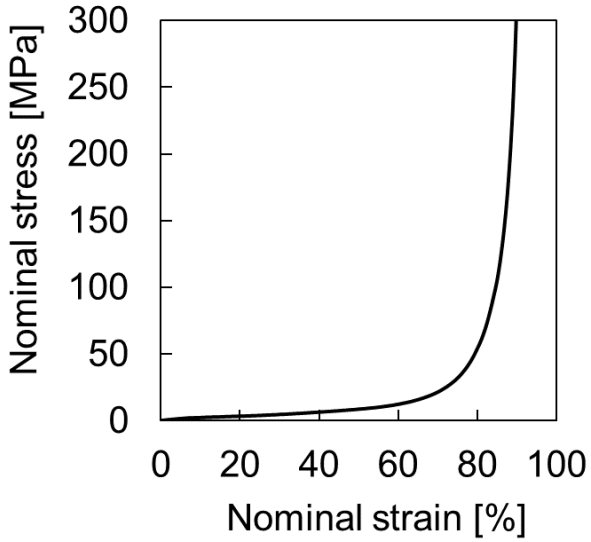

Figure 34 Stress-strain curve of R-FD

3.3 Slip loading test

3.2.1 Material and methods

A loading test of slip parts composed of Mg-FD with a universal testing machine (Tokyo Koki Testing Machine Co., Ltd., RUE type-200) was carried out at room temperature. Figure 35 shows a sketch of the test assembly. The slip has iron screws on the surface as shown in Figure 36. The iron screws anchor the slip in the casing. Load was increased at a rate of about 10 kN/sec. By applying axial load to a load cylinder on the top of the assembly in Figure 35 (a), the load was applied to the lower slip through the lower cone and its load tolerance can be evaluated. A 23 lb/ft P110 casing and parts for 23 lb/ft DFP were used for this test.

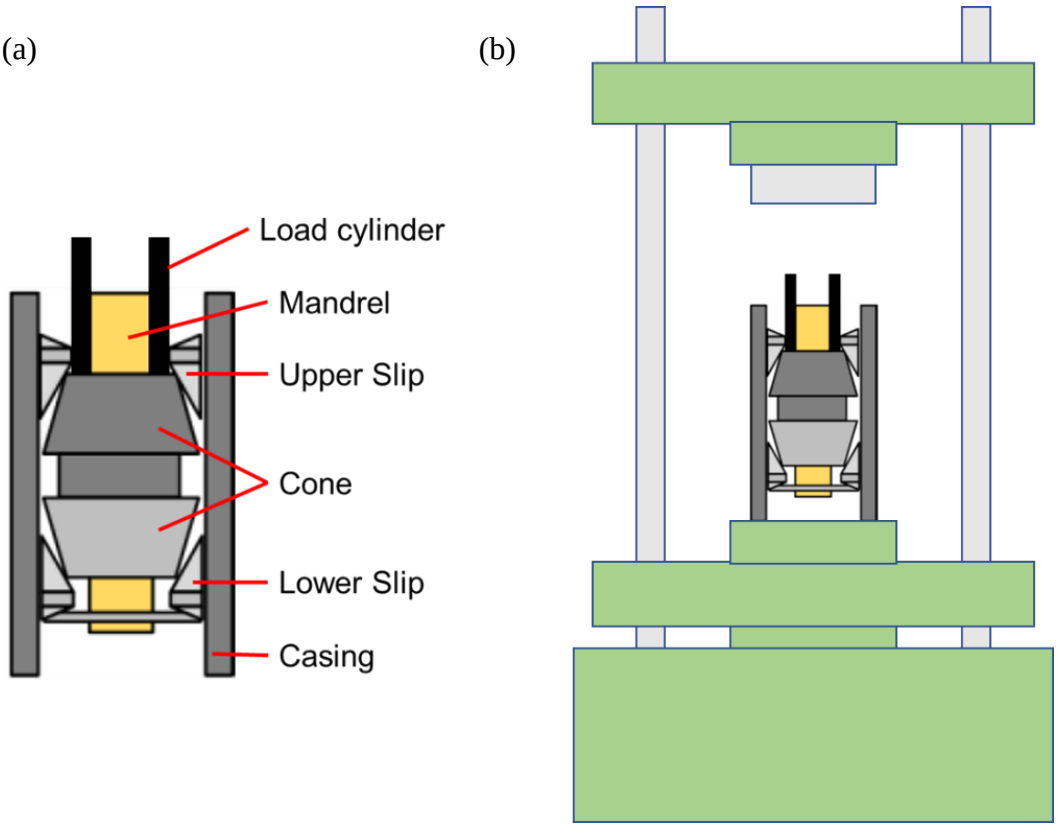

Figure 35 Sketch of the test assembly for the slip loading test: (a) slip assembly, (b) slip assembly on universal testing machine

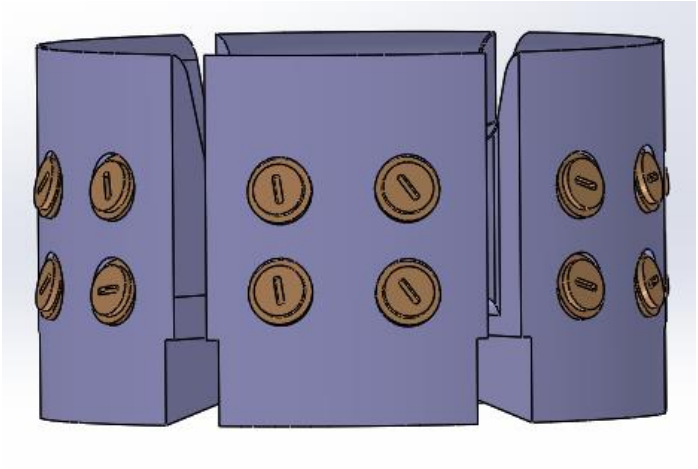

Figure 36 Slip part

3.2.2 Results and discussion

The maximum applied load in this study was the peak value before the load started to decline due to failure or large deformation of slips. As the universal testing machine does not have a function to collect or save data, the maximum applied load was read from a load meter of the machine. The maximum load applied at the failure was 767 kN equivalent to 10,063 psi based on cross-sectional area of the casing. Until reaching the maximum load, the lower slip successfully kept the assembly in the casing without releasing the anchoring function. Figure 37 shows the inside of the casing after the test. There were dents by anchored iron chips but there was no indication of spatial movement of iron chips. We concluded that this slip can hold more than 10,000 psi of pressure in a wellbore without slipping or moving downstream. Since the upper slip and sealing element also hold a certain amount of load in actual DFP, this load tolerance of the lower slip is sufficient for the application to DFP. A slight plastic deformation was observed around the thread hole of the slip after the test but it is not a problem as DFP is single use.

Figure 37 Inside of the casing after the test: red arrows indicate scratched area by iron chips

3.4 Seal element compression test

3.4.1 Material and methods

A compression test of seal element composed of R-FD was conducted with a universal testing machine (MTS Systems Corporation, MTS 22 KIP) at 150°F. Figure 38 shows test assembly and universal testing machine with an oven for the test. An acrylic casing with its ID of 118.6 and parts for 23# DPF were used. Displacement was applied at the rate of 1 mm/sec. In this study, a seal length was defined as the length of the seal element contacted to the internal casing wall along axial direction. The seal length of R-FD was measured by a ruler every 1 mm of displacement. To examine the effect of surface roughness and friction on applied force, the same seal test with iron casing was also performed. In addition, the seal test with iron casing in oil wet

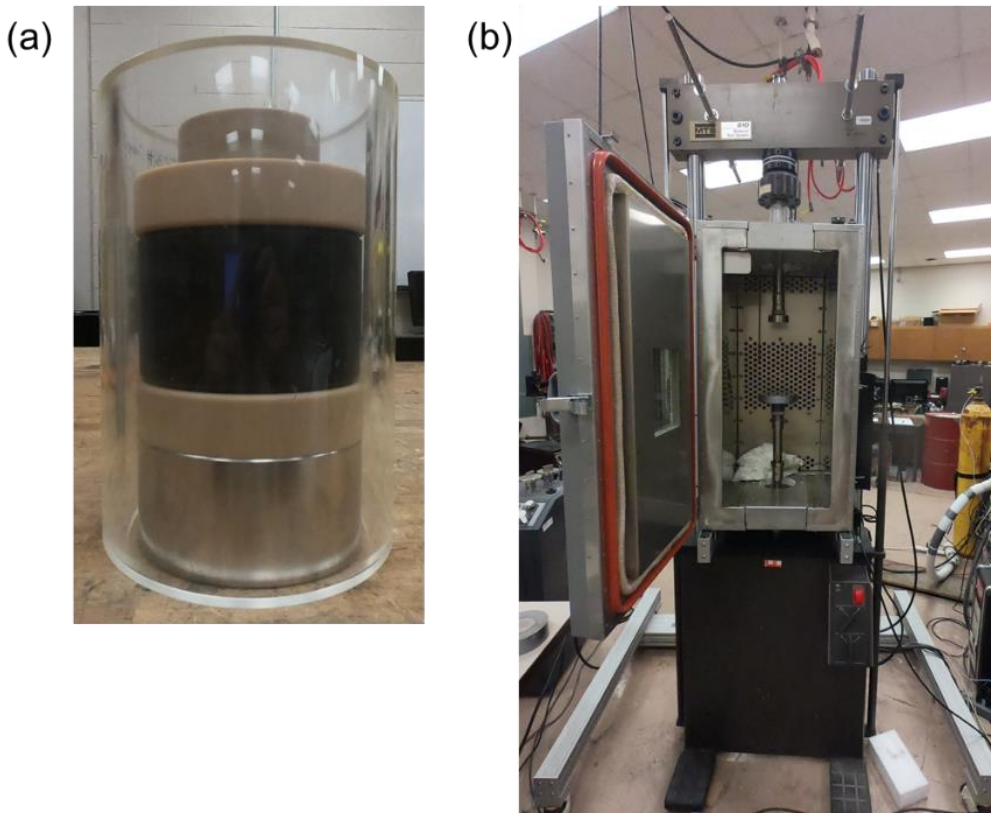

Figure 38 Test assembly (a) and universal testing machine (b)

condition was also conducted by applying oil to all the parts to study the influence of lubrication by fluid on the relationship between displacement and applied force.

3.4.2 Results and discussion

Figure 39 shows a relationship between the seal length and displacement obtained the compression test of seal element. Relationship between displacement and load obtained in this test was shown in Figure 40. The seal element started contacting with the acrylic casing from 11 mm of displacement. The seal length proportionally increased with increase in displacement. Until the seal element contacted the casing, the required load increased with displacement and then reached a plateau around 10 mm. There was almost no difference in applied load among three cases from 0 mm to 11 mm of displacement. This indicated that the friction between PGA-FD parts and seal element does not affect the required load for the displacement until the seal element starts contacting to the casing. At the onset of contact, the slope of load was sharply increased for all cases as shown in Figure 40. When the displacement was above 11 mm, applied load with iron casing at each displacement was higher than that with acrylic casing. Surface of the iron casing

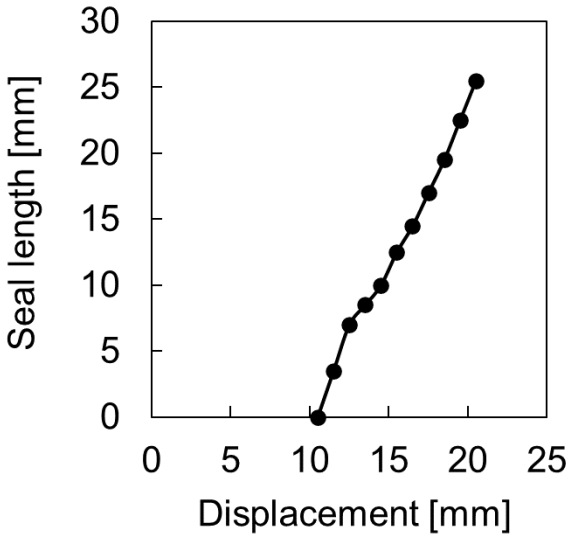

Figure 39 Relationship between displacement and the seal length at 150°F

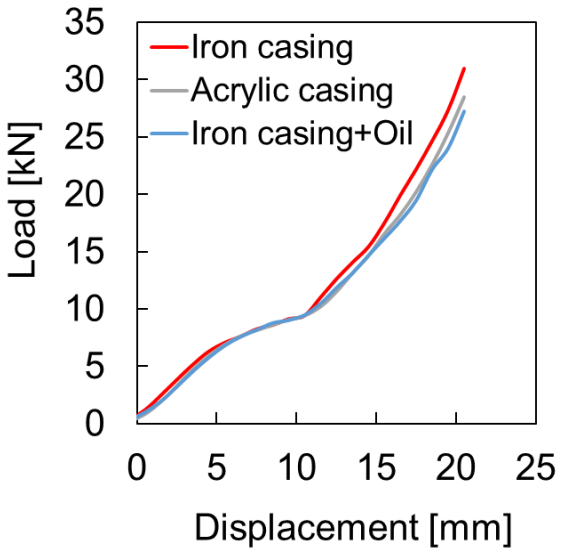

Figure 40 Relationship between displacement and load at 150°F

was relatively rough compared to the acrylic casing as it was made by machining. It is obvious that a higher friction due to the surface roughness of the iron casing caused this difference. Zhang and Zhang (2016) studied friction coefficients between a rubber and steel under three conditions which were dry, water wet, and oil wet. They concluded that the friction coefficient decreased in the following order: dry > water wet > oil wet. When oil is applied to inner surface of the iron casing and all other test components, the load required was smaller than dry condition. In actual wellbore condition, DFP is in fluid and wet. Therefore, it is expected that the relationship between the load and displacement in wellbore condition would lie between the curves of dry (red curve) and oil wet condition (blue curve) shown in Figure 40. At 20 mm of displacement, the seal length was 22.5 mm and applied force was 24.5 kN. In general, approximately 100-120 kN of force is applied by a setting tool at the set of frac plug in casings. This result indicates that the seal element composed of R-FD has a sufficient seal length even at a small applied force. The seal length is presumed to increase further by hydraulic pressure during hydraulic fracturing.

4. FINITE ELEMENT ANALYSIS OF FRAC PLUG COMPONENTS

4.1 Model description

Finite element analysis (FEA) was conducted to optimize the shape of DFP components using a commercial the finite element analysis software, ABAQUS/CAE 2018. Axisymmetric model was used in all the finite element analyses in this study. For elastic material data of PGA-FD at 150°F, 1.785 GPa of Young's modulus and 0.3 of Poisson's ratio were used. In the case of 200°F, 1.20 GPa of Young's modulus and 0.3 of Poisson's ratio were employed. For the material data in plastic region of PGA-FD, isotropic hardening rule was selected, and the effective strain and true stress data obtained from the tensile test were input as the nonlinear plasticity data. In the case of R-FD, the nominal stress-strain curve obtained from the compression test was directly input in ABAQUS as a hyperelastic material data. Marlow model was selected as the hyperelastic model of R-FD. Poisson's ratio of R-FD was set to 0.495. "Hard contact" was selected as the normal behavior for all the contact settings. It is a setting that does not allow any penetrations of two contact surfaces. For the tangential behavior, the penalty method was selected and the friction factor of all the materials except for self-contact of R-FD was set to 0.2. The friction factor of self-contact of R-FD was set to 1.0 because the friction factor between rubber materials are about 1 to 4 (Bowden & Tabor, 1964). The 8-node quadrilateral element was employed for all parts in all analyses except for models with seal element. The 4- node quadrilateral element was used for models with seal element to achieve convergence. For the model of R-FD, the hybrid formulation option was used. Optimization of mesh size was conducted prior to each analysis and shown in Appendix A. All settings mentioned above were used for all the following analyses.

Figure 41 depicts a finite element model used to investigate the effect of neck angle of the mandrel on its stress state at a large tension. The neck angle of the mandrel was varied from 20°

to 90°. The mesh size was set to 0.3 mm. In the case of 30°, the total number of elements of the mandrel and load ring were 36,643 and 6,115, respectively. Length, ball seat angle, outer diameter and inner diameter of the mandrel were 132 mm, 45°, 90 mm and 30 mm, respectively. Outer diameter and height of the load ring were 104.8 mm and 30 mm, respectively. Material data of PGA-FD at 150°F was used for this analysis. Encastre (fully built-in) was selected as its boundary

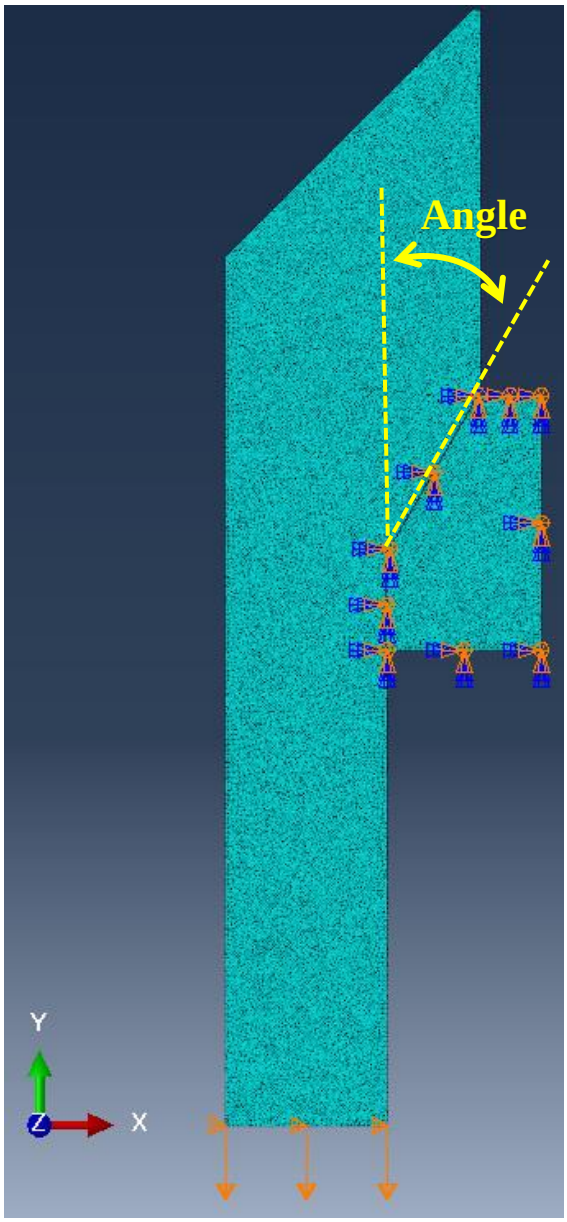

Figure 41 Finite element model of mandrel and load ring

condition of the entire load ring and a 10 mm of enforced displacement downward was set to the bottom of the mandrel to stretch it.

For optimization of the size of PGA-FD frac ball, several sizes of the ball (1.1”, 1.3”, 1.5”, and 1.75”) were analyzed with the finite element models. The finite element model of 1.3-inch ball was shown in Figure 42. Total length, ball seat angle, neck angle, inner diameter and outer diameter of the mandrel were 57 mm, 45°, 30°, 25 mm, and 70 mm, respectively. The mesh size was set to 0.25 mm. In the case of 1.75-inch ball, the total numbers of elements of the ball and the mandrel

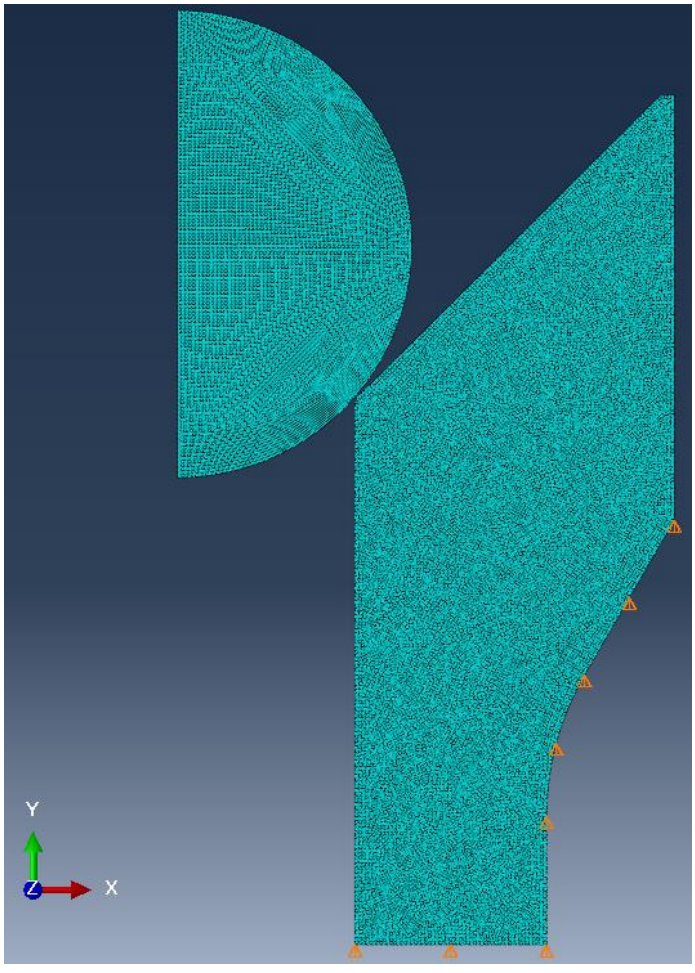

Figure 42 Finite element model of frac ball and mandrel

were 15,120 and 18,392, respectively. The bottom and the neck of the mandrel were fixed to vertical direction (y-axis direction) as shown in the figure. The reason of fixing the neck of the mandrel is that there is a load ring in actual DFP and it is precluded from moving vertically by a slip part. A 69 MPa (10,000 psi) was applied to outer side of the ball and the mandrel. Material data of PGA-FD at 200°F was used for this simulation.

The deformation behavior of the mandrel and the seal element under a high pressure was simulated with models varying the designs of the socket and the seal element. The mesh size of each part was set to 0.5 mm. Material data of PGA-FD and R-FD at 150°F were employed for the following analyses. To begin with, a validation of FEA result with the test result obtained in Section 3.4 was conducted with an original model (Figure 43). Length, outer diameter, and inner diameter of the mandrel were 112 mm, 68.3 mm, and 30 mm, respectively. Outer diameter, inner

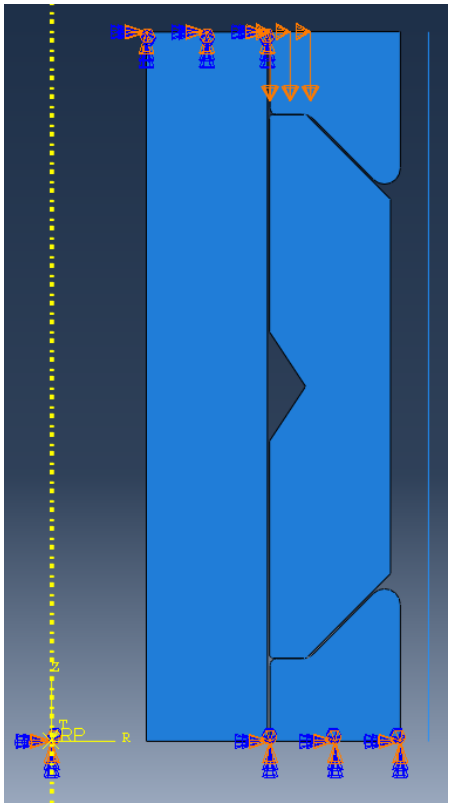

Figure 43 Original model

diameter, and length of the socket were 109.5 mm, 68.3 mm, and 24 mm, respectively. Length and inner diameter of the casing were 112 mm and 119 mm, respectively. Outer diameter, inner diameter, and length of the seal element were 107.3 mm, 69 mm, and 85.7 mm, respectively. All the parts for this FEA were modeled with the same size as the actual parts used in Section 3.4. The casing was modeled as a rigid body and the reference point was fixed. Bottom of the lower socket and top of the mandrel were also fully fixed. An enforced displacement downward was applied to the upper left of the upper socket. This partial enforced displacement to the top of the upper socket simulates the actual condition of Section 3.4 as the load was applied to the upper socket with the load cylinder in the test. The seal length was defined as a length of the seal element contacted to the casing along axial direction. The contact between the casing and the seal element was recognized based on the contact pressure. When the value was 0.1 MPa or more, it was regarded as “contacted” in this study.

For optimization of the socket and the seal element design, a protrusion was added to the socket and the effect of different protrusion length (15-55 mm), its angle (0°, 5°, 20°, 25°, 30°), and outer lip angle (30°, 45°, 60°) of the lower socket on the stress state of the mandrel under a high pressure were investigated. The terms and their locations in the socket were schematically shown in Figure 44. The reason of adding the protrusion structure to the original model of the lower socket is to prevent a large deformation of the seal element toward the gap between the lower socket and the mandrel and reduce tensile stress on the mandrel by the deformed seal element. Dimensions of the lower socket of the models were shown in Table 2. A model which has no protrusion on the socket is referred to as Base model 1 in this study. All other dimensions except for outer diameter of two sockets and dimensions of lower socket shown in Table 2 were the same as the original model. All the models except for the original model, Model 16, and Model

17 do not have a gap between the socket and the casing. Therefore, their outer diameter was 119 mm. Figure 45 illustrates Base model 1, Model 2, Model 14, and Model 16. All other models including their FEA results were shown in Appendix B. In reality, outer diameter of all the parts of DFP should be smaller than the inner diameter of casing to avoid being stuck in the casing during run-in operation. Therefore, there should be a certain gap between casing and the parts of actual DFP. However, the gap was removed in this FEA to prevent a large deformation of the seal

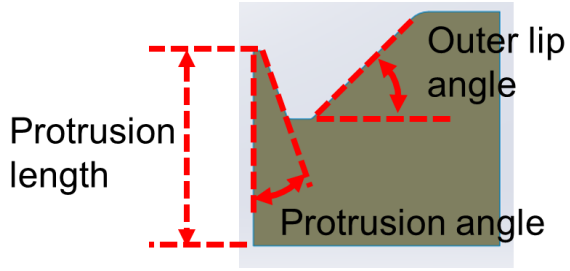

Figure 44 Terms and their locations in the lower socket

Table 2 Dimensions of the lower socket

Model	Protrusion length [mm]	Protrusion angle [°]	Outer lip angle [°]
Base model 1	0	-	45
Model 1	15	20	45
Model 2	20	20	45
Model 3	25	20	45
Model 4	15	25	45
Model 5	15	30	45
Model 6	20	20	30
Model 7	20	20	60
Model 8	40	5	45
Model 9	45	5	45
Model 10	50	5	45
Model 11	55	5	45
Model 12	40	0	45
Model 13	45	0	45
Model 14	50	0	45
Model 15	55	0	45
Model 16	20	20	60
Model 17	50	0	60

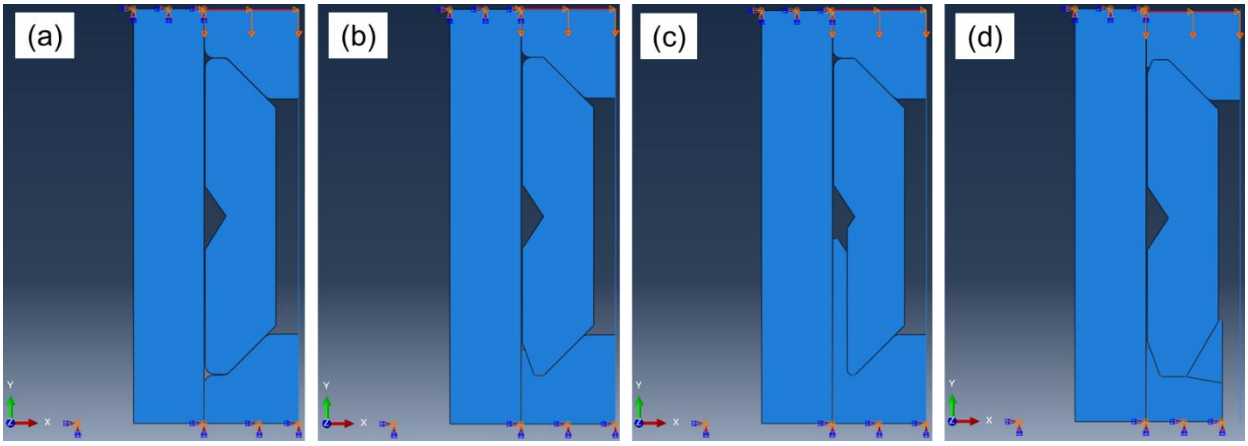

Figure 45 Finite element models of R-FD: (a) Base model 1, (b) Model 2, (c) Model 14, (d) Model 16

element between the lower socket and the casing under a high pressure and circumvent converge issues due to the large strain. To simulate more realistic model for actual DFP design, Model 16 and Model 17, which have a gap between the lower socket and the casing, were used. Their lower sockets are composed of two parts: an inner socket and an outer socket. The latter expands radially and fills the gap between the casing and the outer socket when a large stress is applied by the seal element. The height of outer socket was 18 mm and its outer lip angle was set to 60°. For Model 16, the upper socket was the same design as the lower socket of Model 1 and it enables them to achieve convergence of numerical calculation. An enforced displacement downward was set to the top of the upper socket for all the cases to apply pressure to the seal element. The equivalent pressure was calculated by dividing the reaction force on the top of the upper socket by the area. The casing was modeled as a rigid body in all the analyses. Bottom of the lower socket, top of the mandrel, and the entire body of the casing were fixed in horizontal and vertical directions. The seal length between the casing and the seal element at a 36 kN of the reaction force was measured to investigate the effect of socket and seal element shape on the sealing performance. This value was chosen as it is the reaction force when the displacement of the upper socket reached 20 mm

in FEA of Base model 1. 20 mm of displacement is the typical empirical displacement between the upper and lower sockets observed after setting of DFP in the casing.

In addition, FEA of seal elements with different notch angle, notch depth, and length were also conducted to examine the effect on the sealing performance. The terms and their locations in the seal element were schematically shown in Figure 46. In this analysis, the same lower socket as Model 1 was used for both the upper and lower socket to obtain better convergence. As for the analysis of notch angle, five models whose notch angles were 70°, 90°, 110°, 130°, and 150° were established. All other dimensions of each parts were the same as Base model 1. The model with 110° was referred to as Base model 2 in this study and was shown in Figure 47. Regarding the evaluation of notch depth, four models whose notch depth were -2.5 mm, -1.25 mm, +1.25 mm,

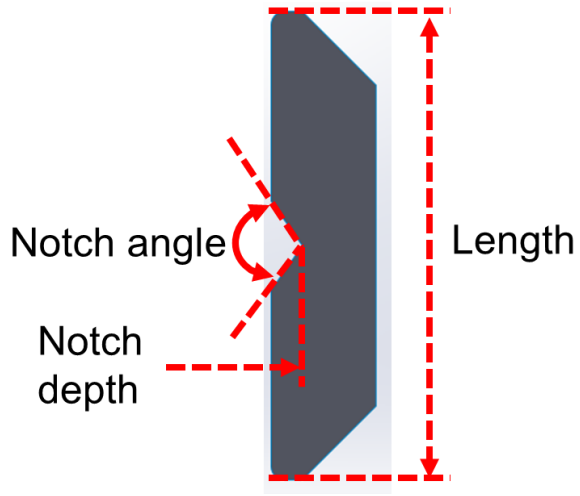

Figure 47 Terms and their locations for the seal element

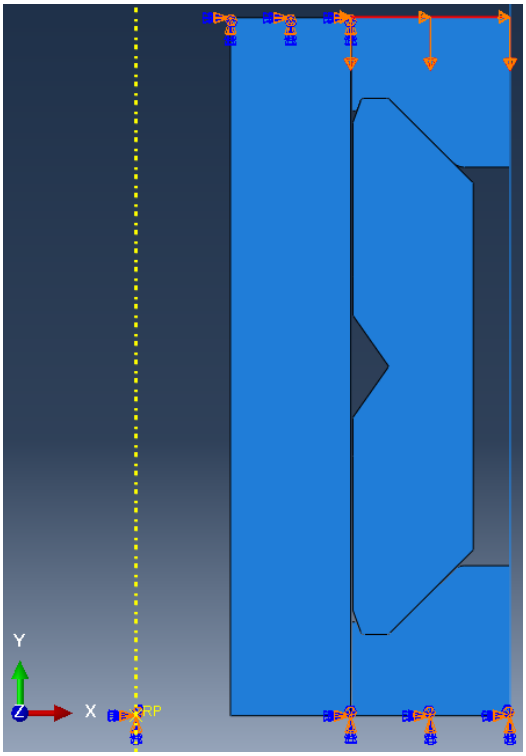

Figure 46 Finite element model of Base model 2

+2.5 mm compared to Base model 2 were employed. In regards to the analysis of the seal element length, four models whose length are -5, +5, +10, and +15 mm compared to Base model 2 were used. The casing was modeled as a rigid body in all analyses. Bottom of the lower socket, the top of the mandrel, and the entire body of the casing were fixed in horizontal and vertical directions. An enforced displacement downward was set to the top of the upper socket to apply pressure on the seal element.

To investigate the effect of mandrel thickness on the stress state under high pressure, FEA of two models with different mandrel thicknesses (+1.25 mm and +2.5 mm) was conducted. The 4-node quadrilateral element was used in this analysis. Except for the mandrel thickness, other designs and conditions were the same as Base model 2.

4.2 Results and discussion

In this study, von Mises yield criterion was used. Mises stress is defined as

$$\sigma_v = \sqrt{3J_2'} = \sqrt{\frac{1}{2}[(\sigma_1 - \sigma_2)^2 + (\sigma_2 - \sigma_3)^2 + (\sigma_3 - \sigma_1)^2]} \quad (7)$$

where J_2' is the second deviatoric stress invariant and σ_1, σ_2, and σ_3 are principal stresses for each axis. Mises stress converts a stress tensor in a multiaxial field to a scholar value. In case of plastics and metals, the effect of hydrostatic pressure on the plastic deformation can be generally negligible. Therefore, the yield function f is defined as

$$f = 3J_2' - Y^2 = \frac{3}{2}s_{ij}s_{ij} - Y^2 \quad (8)$$

where Y and s_{ij} are the yield strength of the material and the deviatoric stress, respectively. The equation defines the yield surface as a cylindrical surface as shown in Figure 48. When $f = 0$, initial yield of the material occurs. From Eq. 7 and Eq. 8 the following relationship is derived.

$$Y = \sqrt{\frac{1}{2}[(\sigma_1 - \sigma_2)^2 + (\sigma_2 - \sigma_3)^2 + (\sigma_3 - \sigma_1)^2]} \quad (9)$$

Eq. 9 means that yielding occurs when Mises stress is equal to the yield stress of the material.

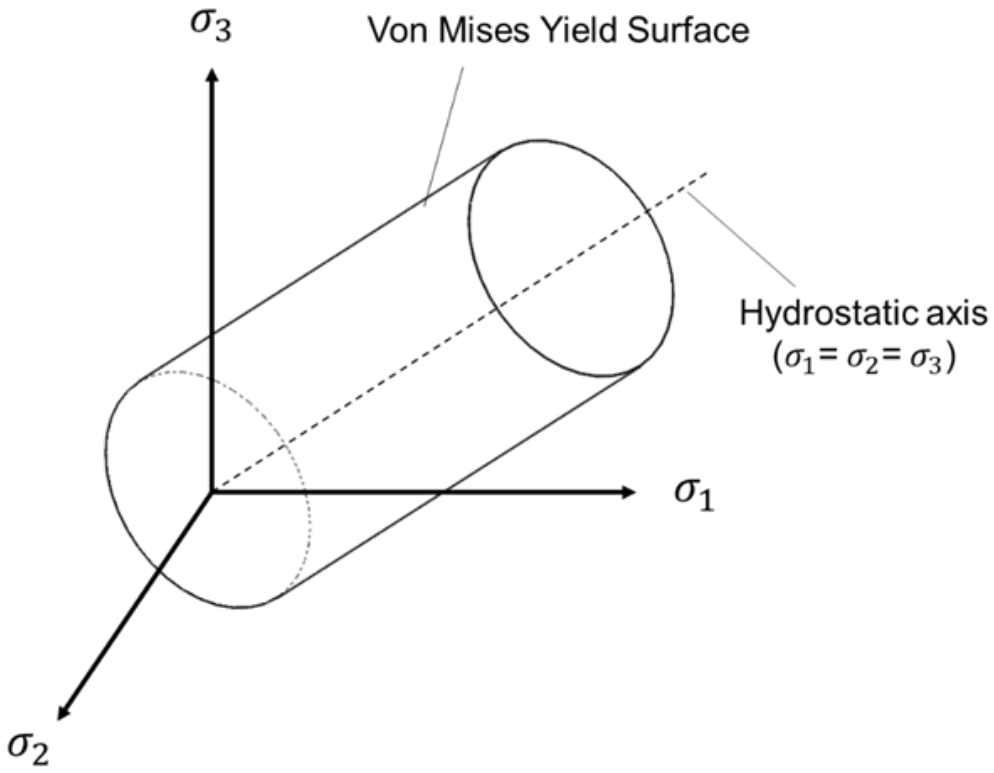

Figure 48 Von Mises yield surface

The maximum Mises stress on the mandrel for models with different neck angle at 10 mm of displacement of the mandrel bottom was shown in Figure 49. As the neck angle increased, the maximum Mises stress on the mandrel was increased, and for 60° and above, the value reached a plateau that is about 110 MPa. This indicated bending force occurred on the neck of the mandrel was greater for the designs with greater neck angle. Therefore, a mandrel with a lower neck angle has better tolerance to tensile stress. As there was no significant difference in Mises stress between 20° and 30° neck angles, the latter model was selected as the neck angle of mandrel for further analysis.

Figure 50 shows contour plots of Mises stress at 69 MPa obtained from the FEA of frac balls. The maximum Mises stress on the balls was observed at the contact surface between inner edge of the mandrel and lower side of the ball. For all the cases, plastic deformation of the ball occurred at 69 MPa and the ball started to go inside of the mandrel. The same behavior of frac balls after the pressure test were reported by several authors. Baihly et al. (2012) conducted pressure tests of

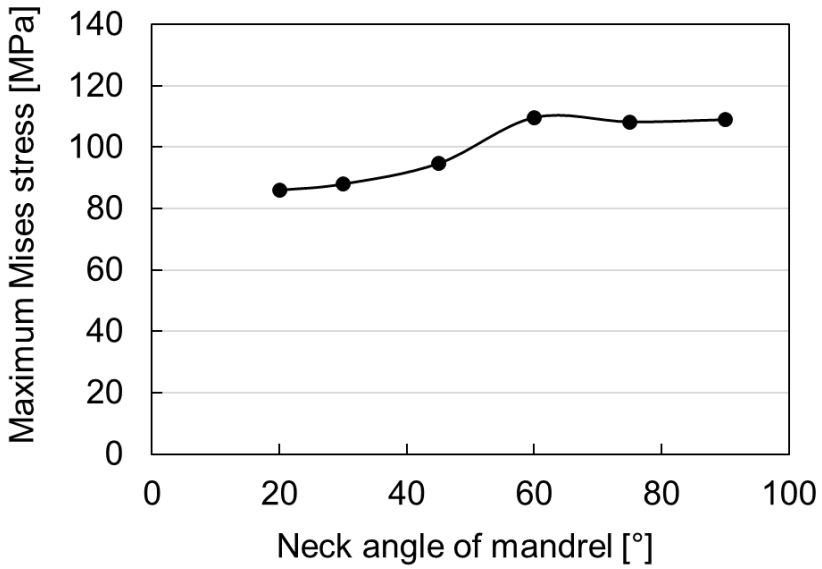

Figure 49 The maximum Mises stress on the mandrel with different neck

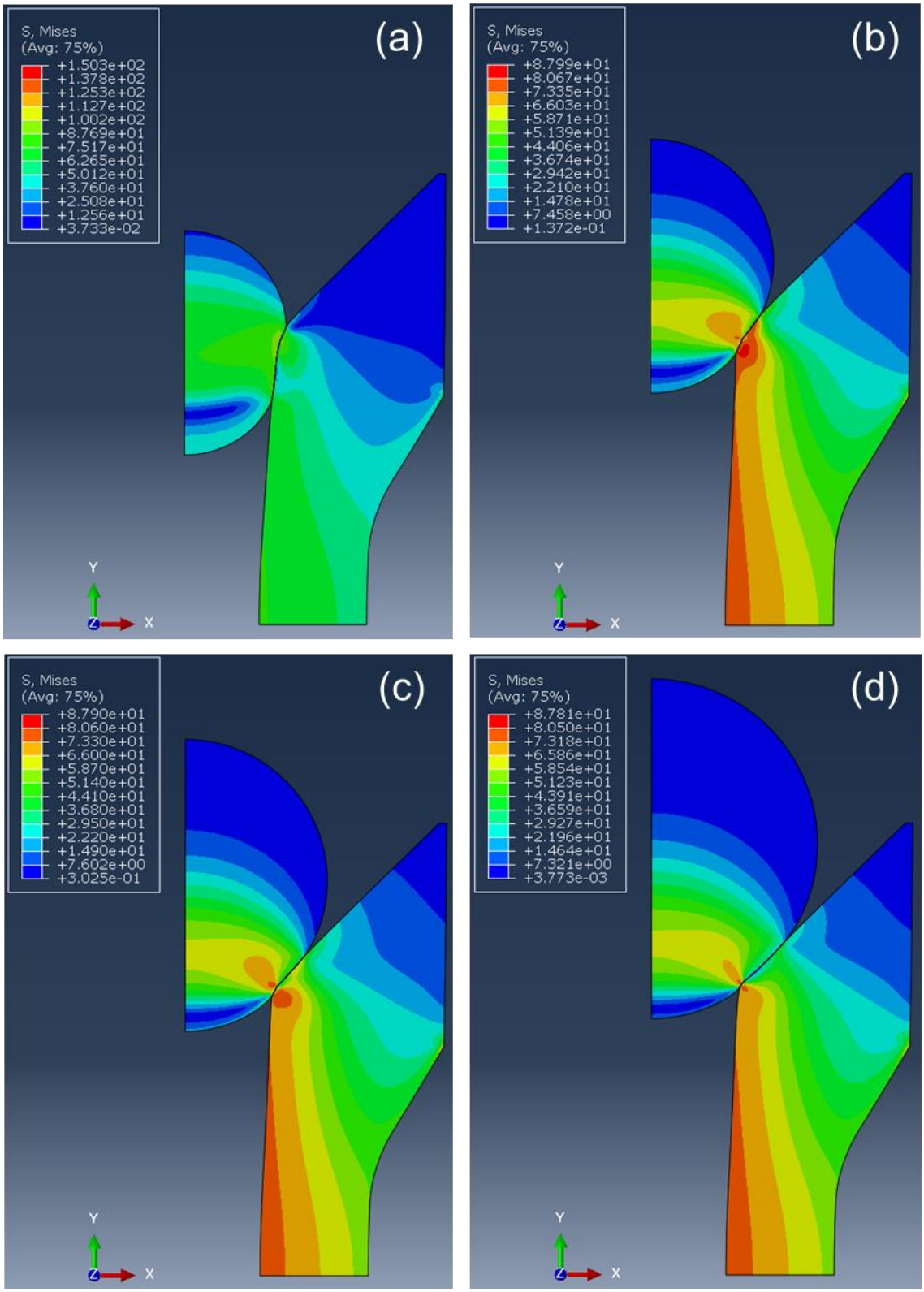

Figure 50 Mises stress at 69 MPa: (a) 1.1-inch ball, (b) 1.3-inch ball, (c) 1.5-inch ball, (d) 1.75-inch ball

frac balls composed of a composite material under 10,000 psi and observed large deformation of ball called “egging” (Figure 51). Zheng et al. (2016) reported a plastic deformation of a Mg ball after a pressure test under 60 MPa (Figure 52). They also reported a stress concentration at the contact between the ball and the edge of the ball seat (Figure 52 (c)).

In all models, the lower side of mandrel was also deformed inward by a high pressure applied on outer side of mandrel. For 1.1-inch ball, the maximum Mises stress was 150 MPa, whereas those of other size of the balls were about 88 MPa. The minimum true strains of 1.1-inch, 1.3-inch, 1.5-inch, and 1.75-inch ball in the minimum principle stress direction were -0.54, -0.18, -0.18, and -0.17, respectively. Deformation of 1.1-inch ball was more significant among them and 1.1-inch ball started penetrating into the mandrel as shown in Figure 50 (a). This is suggested to be the main reason of the large Mises stress and strain observed in 1.1-inch ball. Therefore, this size of ball has a risk to fail in the practical applications. Accordingly, frac ball made of PGA-FD with the diameter larger than 1.1-inch should be used for DFP. The FEA result of 1.3-inch ball was compared to a

Figure 51 Example of ball deformation or egging during laboratory testing of a composite ball (Reprinted from Baihly et al., 2012)

1.3-inch ball after 69 MPa of pressure test (Figure 53). The 1.3-inch ball after pressure test deformed at the contact to inner edge of mandrel and their deformations look quite similar.

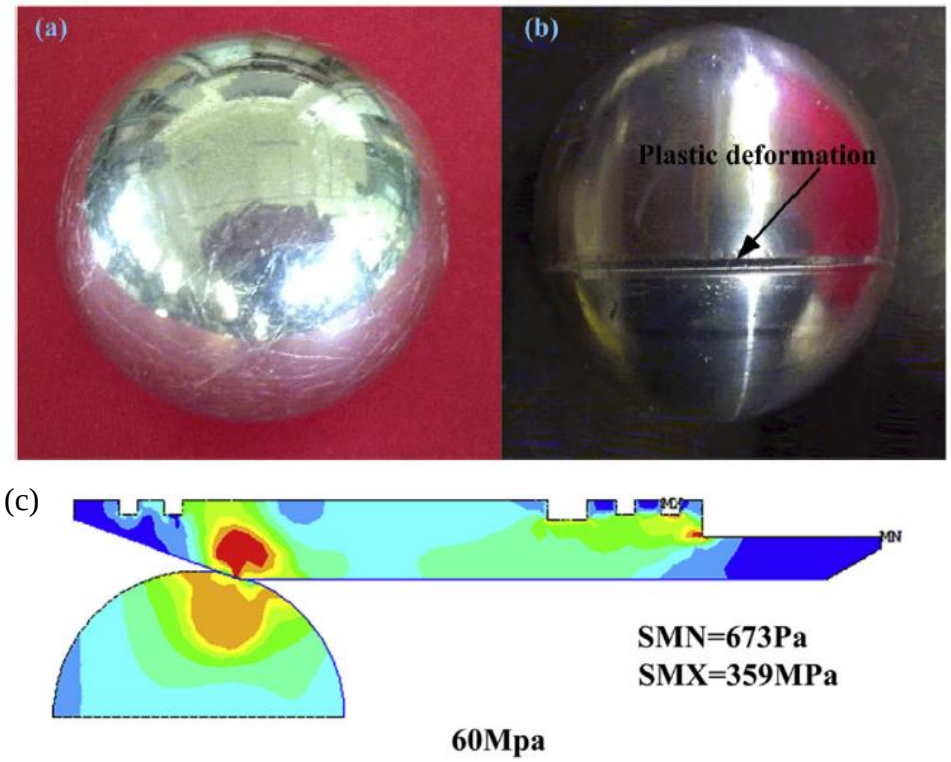

Figure 53 Comparison of frac ball and Mises stress: (a) before test, (b) after test, (c) Mises stress under 60 MPa (Adapted from Zheng et al., 2016)

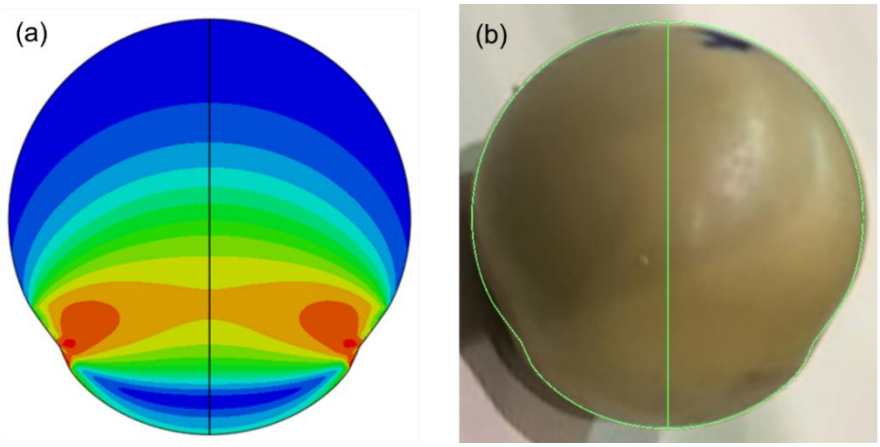

Figure 52 Comparison between FEA and the test result: (a) FEA, (b) ball after pressure test; The green line in the right figure shows the outline of deformed ball shape in FEA

Figure 54 shows FEA result of the original model at 20 mm of displacement. The seal element was compressed and contacted to the casing after 20 mm displacement as shown in Figure 54 (a). The seal length can be measured from the nodes with contact pressure (CPRESS), which is more than 0.1 MPa as shown in Figure 54 (b). The seal length was 23.8 mm. The maximum compression pressure on the right side of the seal element was observed in the middle and the value was 3.1 MPa. This is due to the presence of a notch in the middle of the seal element. Comparison between the test result from Section 3.4 and the FEA result of the original model was shown in Figure 55. The test data in Figure 55(a) is the result with the iron casing (dry condition) shown in Figure 40. The test data in Figure 55 (b) is the result with the acrylic casing shown in Figure 39. As one can see in Figure 55, the FEA results agreed well with the test result for both of the load and seal length. Under the displacement from 5 mm to 10 mm, the load required in the test was slightly lower than the FEA result. Voids in the seal element were presumably the cause of this difference.

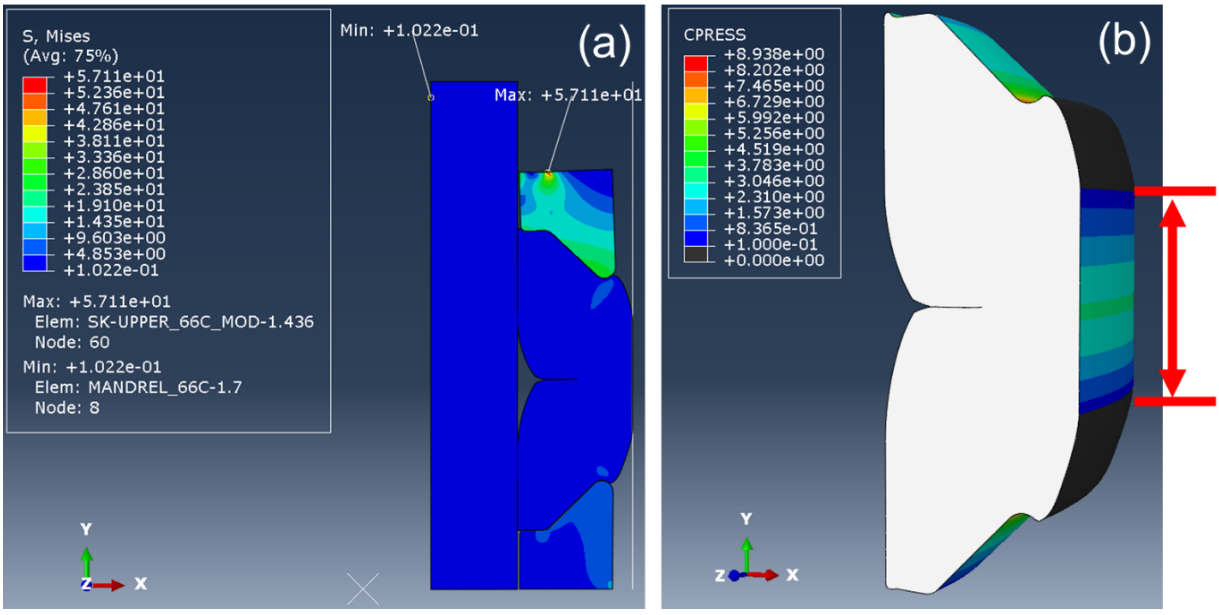

Figure 54 FEA result of the original model at 20 mm of displacement: (a) Mises stress of entire model, (b) contact pressure on the seal element; The red arrow indicates seal length.

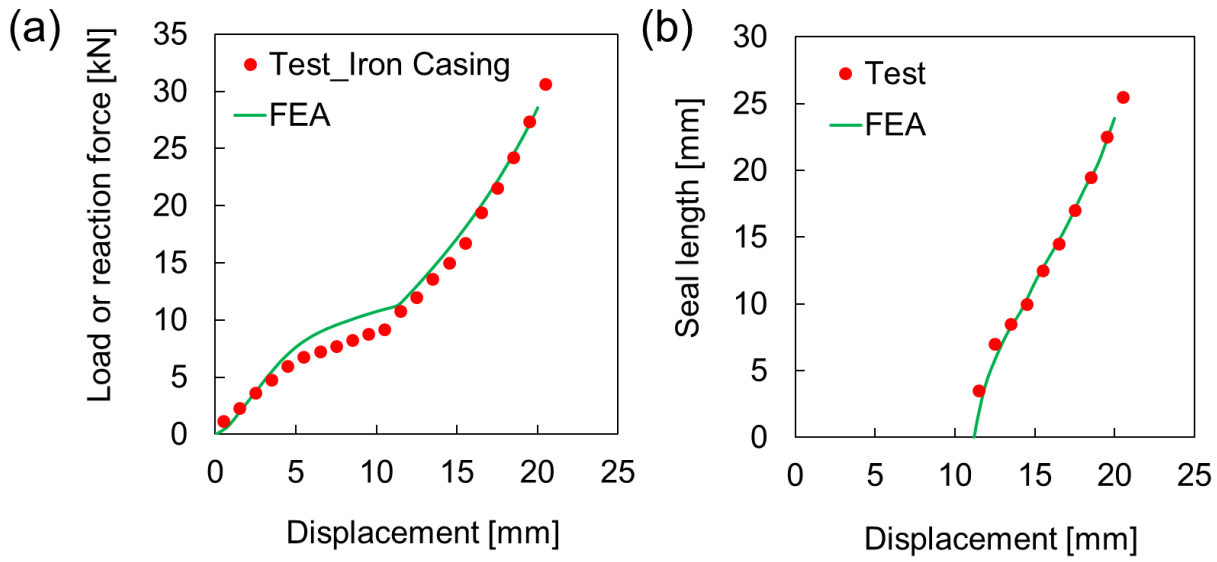

Figure 55 Comparison between the test result and FEA result: (a) load, (b) seal length

Figure 56 shows the stress state and principal plastic strains of Base model 1 at 60 MPa of equivalent pressure. Other FEA results of Base model 1 such as displacement, true strain, and magnitude of plastic strain were shown in Appendix-B. Compressed seal element pressed the mandrel inward and the mandrel was deformed significantly at 60 MPa of equivalent pressure. The maximum Mises stress was observed at the inside of the mandrel and the value was 76.5 MPa. Deformed seal element was protruded to the gap between the mandrel and sockets. The maximum in-plane principal plastic strain was observed at the inside of the mandrel as shown in Figure 56 (b). This tensile stress inside the mandrel was occurred due to the compression by deformed seal element. The minimum in-plane principal plastic strain was found at the upper right side of the mandrel where the protruded seal element contacted with the mandrel. This point of the mandrel has a risk of failure as there is not only the seal element but also high-pressure fluid in actual DFP. The minimum displacements of mandrel to U1 (x-axis) and U2 (y-axis) direction at 60 MPa of equivalent pressure were shown in Figure 57. The transparent meshed model shown in Figure 57

depicts the original shape of the mandrel. It was shown that the mandrel was deformed 2.017 mm inward and 3.952 mm downward. It is considered that the minimum displacement to U2 direction

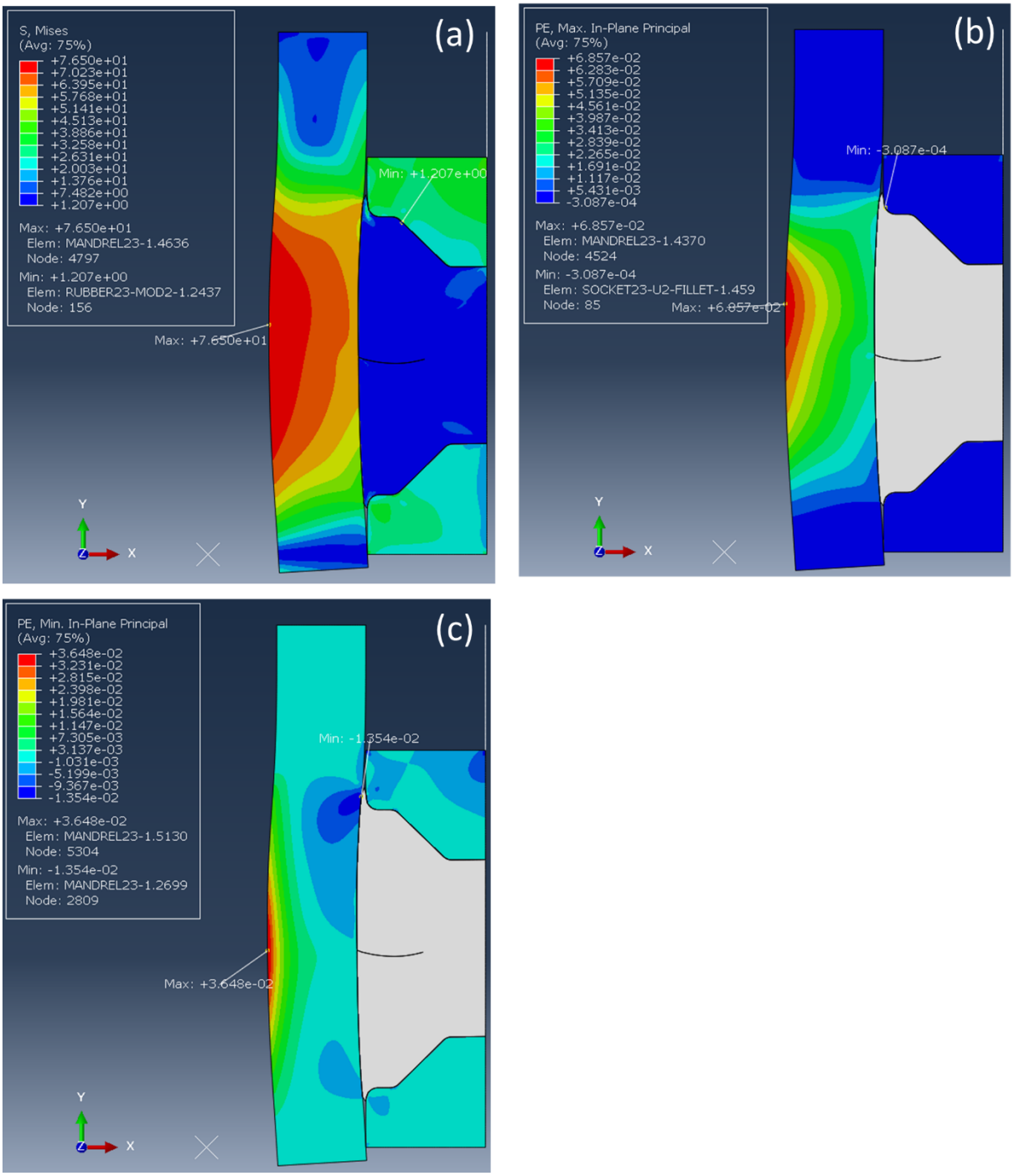

Figure 56 FEA result of Base model 1: (a) Mises stress, (b) the maximum in-plane principal plastic strain, (c) the minimum in-plane principal plastic strain

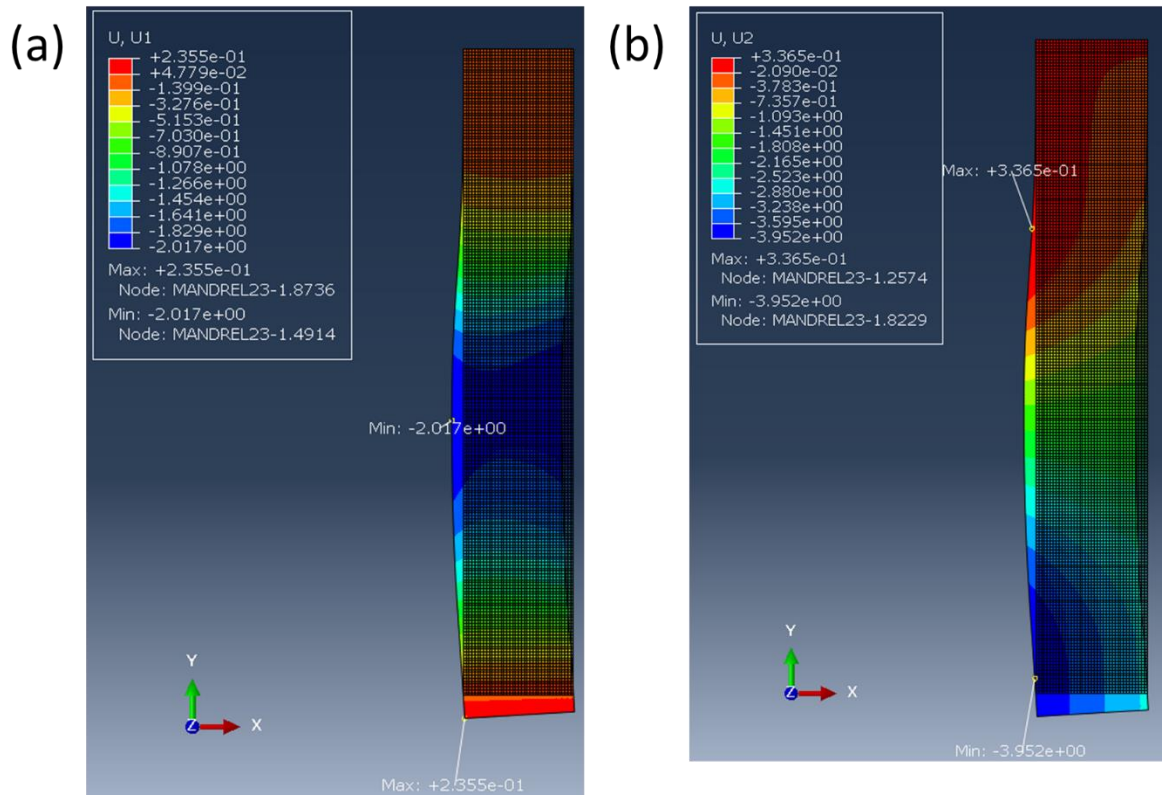

Figure 57 Displacement of the mandrel of Base model 1: (a) U1 (x-axis) direction (b) U2 (y-axis) direction

was caused by tensile stress due to the downward deformation of the seal element. In order to improve pressure tolerance of DFP, this deformation should be reduced.

Contour plots of Mises stress of Model 1, Model 2, and Model 3 at 60 MPa of equivalent pressure were shown in Figure 58. Similar to Base model 1, the mandrel of all the models was deformed inward due to a compression stress by the deformed seal element. However, unlike Base model 1, there was no invasion of the seal element to the gap between the mandrel and lower socket as the protrusion of the lower socket prevented it for these models. As the maximum Mises stresses of these models were observed at the base of protrusion of the lower socket, there is a risk of failure at the point. The maximum Mises stress, the maximum and the minimum logarithmic strain, and the minimum displacement to U1 (x-axis) and U2 (y-axis) directions for the mandrel

of the models were shown in Figure 59 where Base, 15, 20, and 25 in Figure 59 mean result of Base model 1, Model 1, Model 2, and Model 3, respectively. The maximum Mises stresses of Model 1, Model 2, and Model 3 were smaller than Base model 1 and the value decreased with

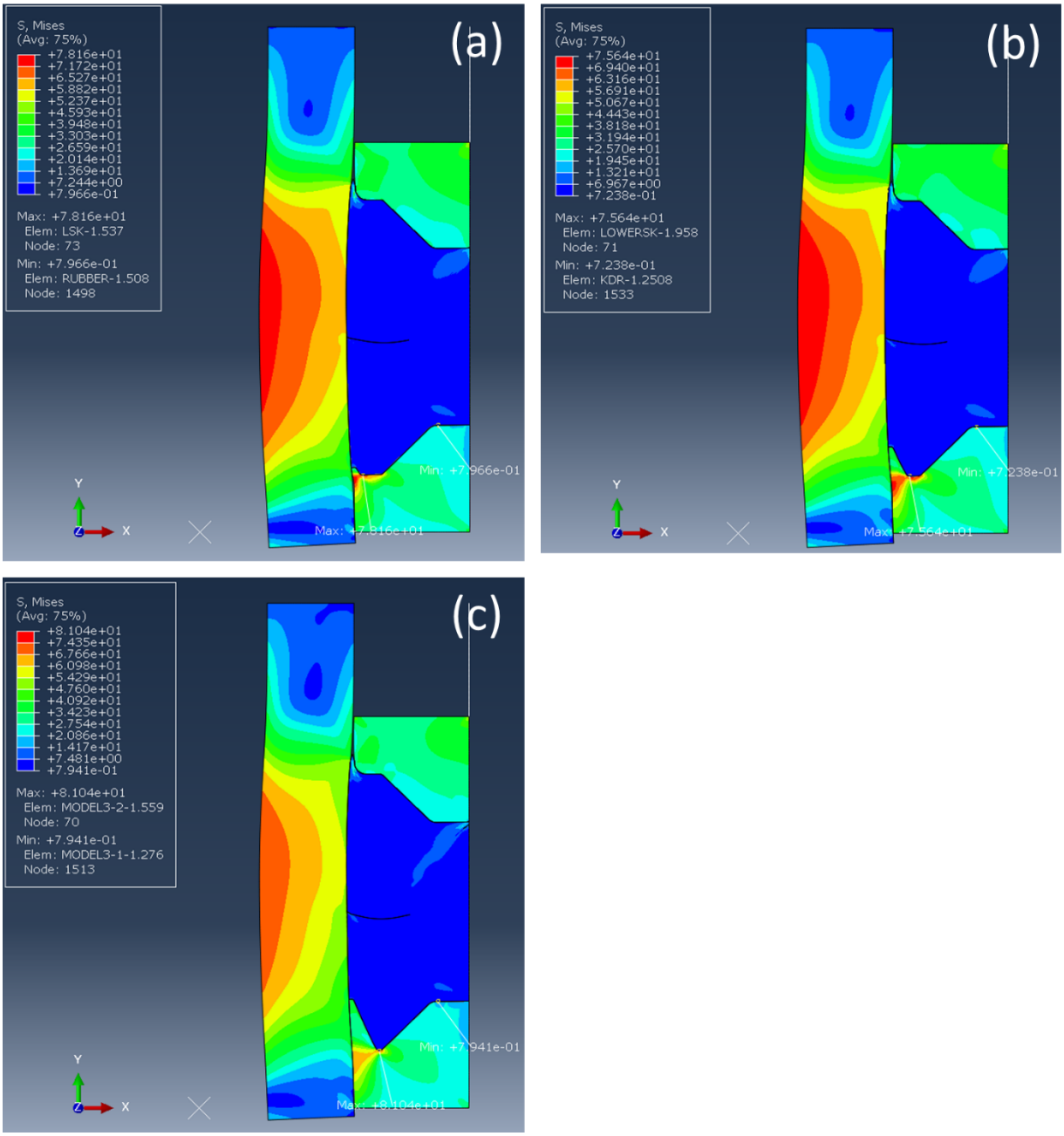

Figure 58 Mises stress at 60 MPa of equivalent pressure: (a) Model 1, (b) Model 2, (c) Model 3

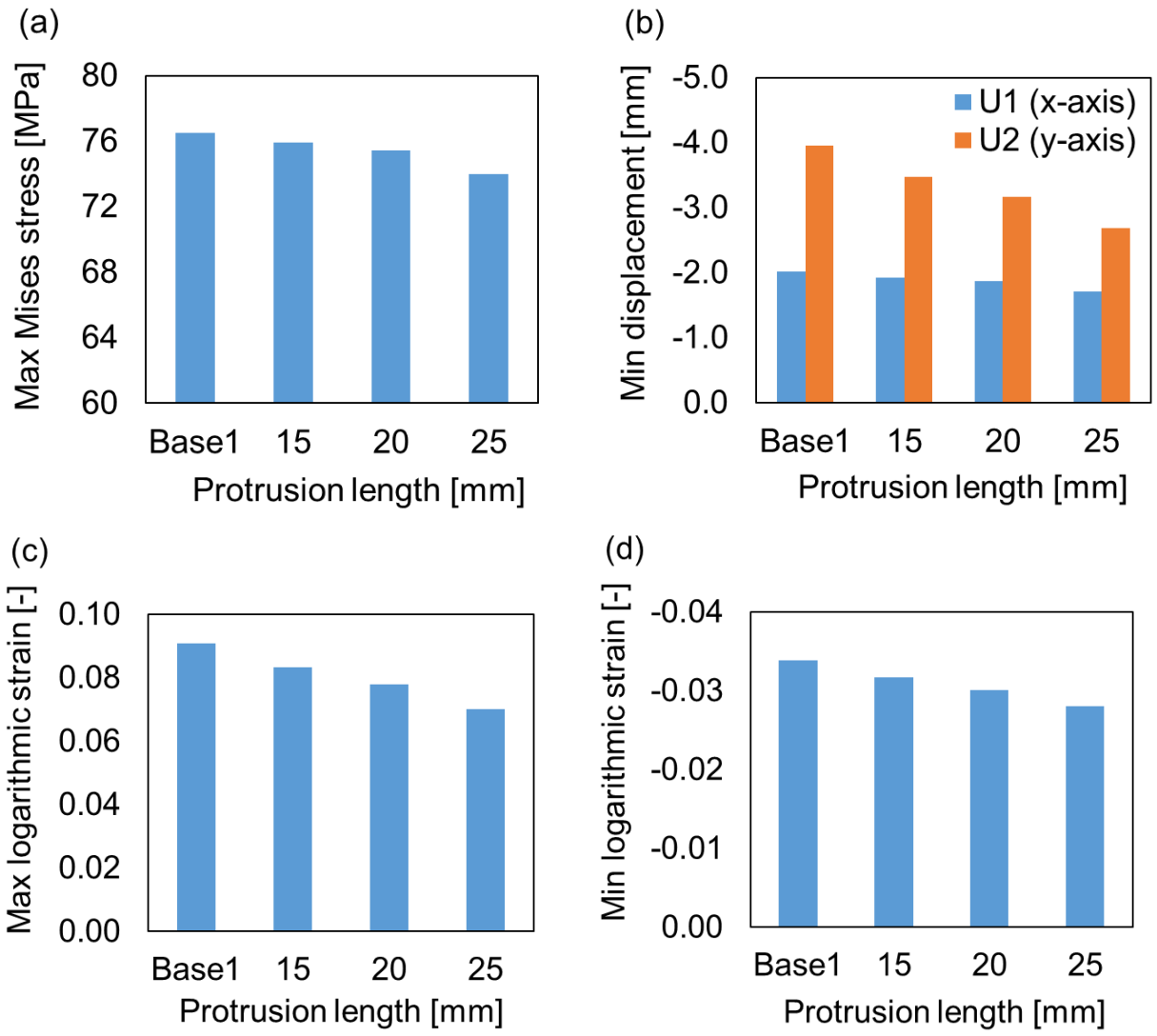

Figure 59 FEA results on the mandrel of models with different protrusion lengths: (a) the maximum Mises stress, (b) the minimum displacement, (c) the maximum logarithmic strain, (d) the minimum logarithmic strain

increase in the protrusion length. The magnitude of the minimum displacement of the mandrel to U2 direction decreased with increase in the protrusion length. The displacement of U1 direction showed similar tendency but the decrease was less than that of U2 direction. The maximum logarithmic strain on the left of the mandrel decreased with increase in the protrusion length. The magnitude of the minimum logarithmic strain at the point of contact between upper left of the seal

element and the mandrel was decreased with increase in the protrusion length. Presumably the protrusion of the lower socket prevented the seal element from deforming inward and downward and it resulted in the suppression of mandrel deformation. The effect was greater for longer protrusion. Adding a protrusion to the lower socket has more effect on suppressing the deformation of mandrel to axial direction than that to radial direction.

Contour plots of Mises stress of Model 4 and Model 5 at 60 MPa of equivalent pressure were shown in Figure 60. The mandrel was stretched axially and largely deformed inward at the same time at 60 MPa in the both models. Since the maximum Mises stresses of these models were observed at the base of protrusion of the lower socket, there is a risk of failure at this point for these models as well. Figure 61 shows the maximum Mises stress, the maximum and the minimum logarithmic strain, and the minimum displacement to U1 (x-axis) and U2 (y-axis) directions for the mandrel of the models. Base1, 20, 25, and 30 in Figure 61 mean the results of Base model 1,

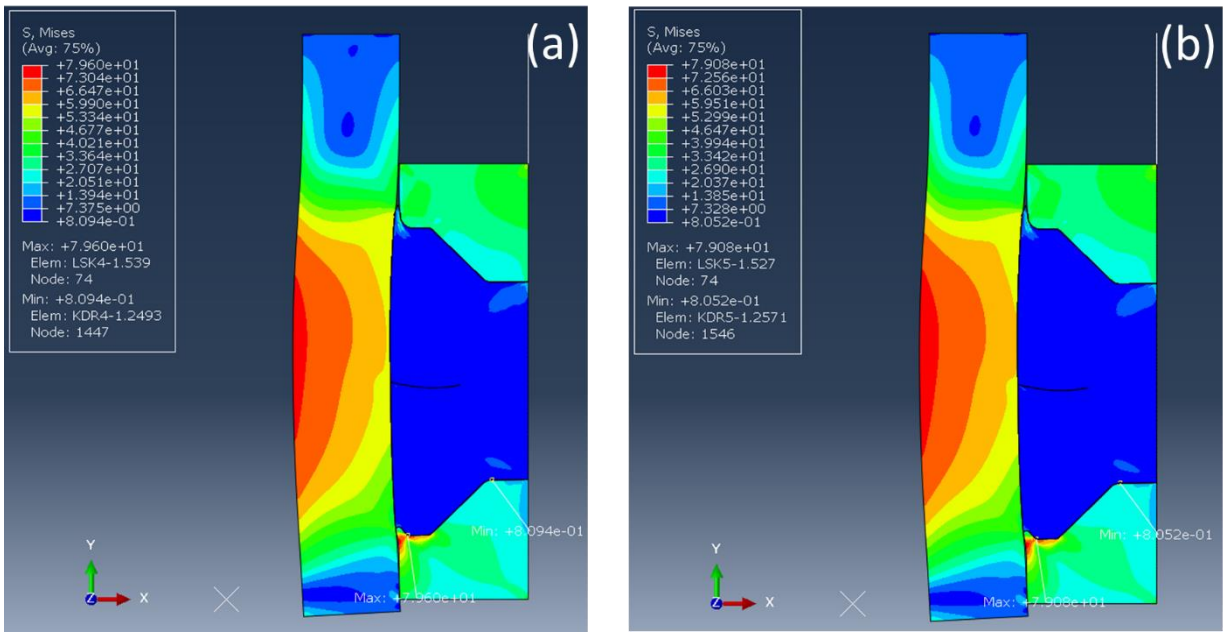

Figure 60 Mises stress at 60 MPa of equivalent pressure: (a) Model 4, (b) Model 5

Model 1, Model 4, and Model 5, respectively. There was no significant difference in the maximum Mises stresses of these models compared to Base model 1. Even though these models showed smaller magnitude of strain or displacement than Base model 1, there were no difference in the values among these models. We can conclude that the angle of protrusion does not affect stress state and deformation of the mandrel.

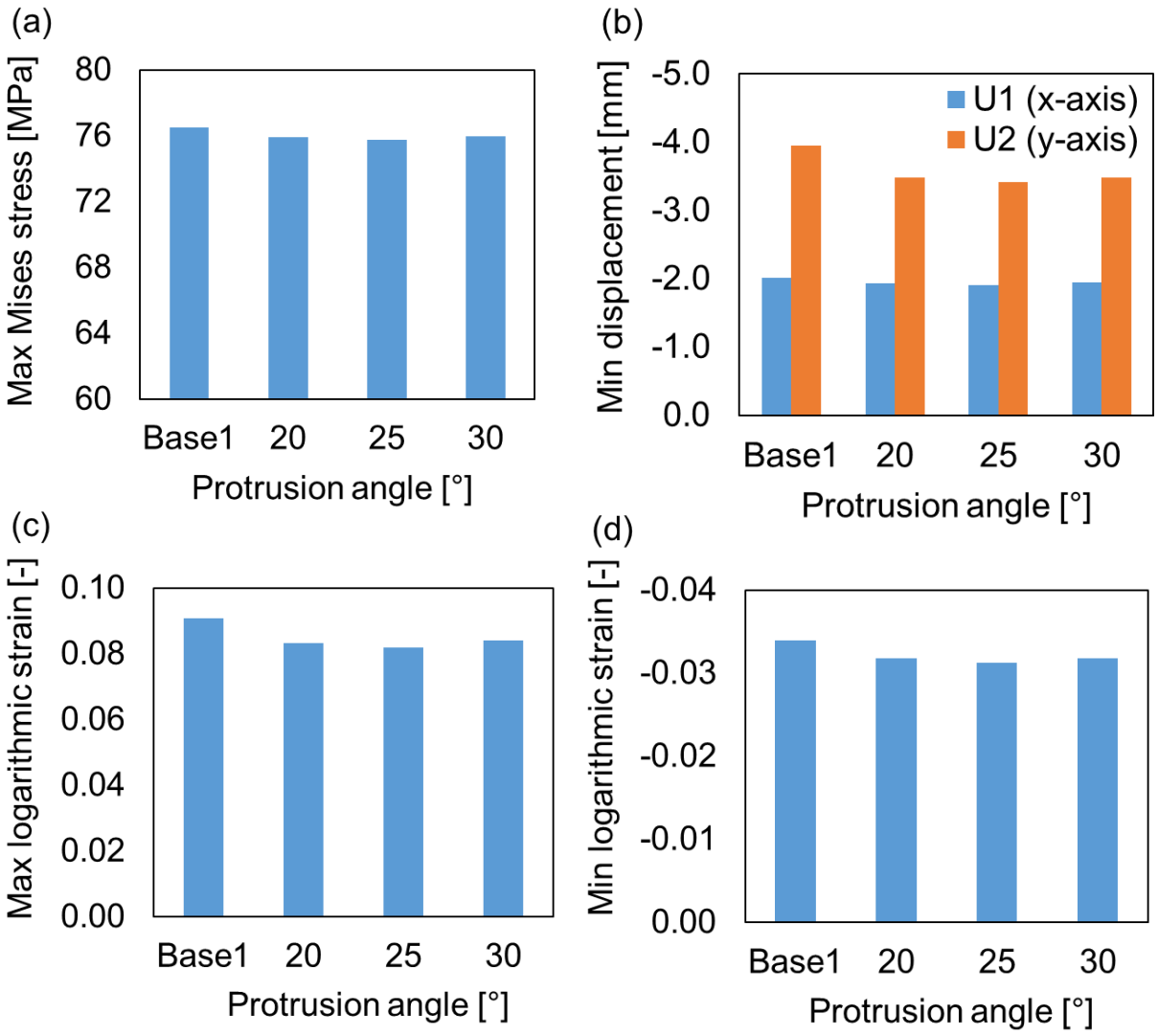

Figure 61 FEA results on the mandrel of models with different protrusion angles: (a) the maximum Mises stress, (b) the minimum displacement, (c) the maximum logarithmic strain, (d) the minimum logarithmic strain

Figure 62 shows Mises stress of Model 6 and Model 7 at 60 MPa of equivalent pressure. Similar to previous models, the mandrel was deformed inward due to compression by the seal element. Figure 63 shows the maximum Mises stress, the maximum and the minimum logarithmic strain, and the minimum displacement to U1 (x-axis) and U2 (y-axis) directions for the mandrel of Model 2, Model 6, and Model 7 where Base1, 30, 45, and 60 mean the results of Base model 1, Model 6, Model 2, and Model 7, respectively. As the outer lip angle increases, the maximum Mises stress is increased. The magnitude of the minimum displacement to U1 (x-axis) and U2 (y-axis) directions increased with increase in the outer lip angle. Similar tendency was observed for the maximum and the minimum logarithmic strain. When the lip angle is large, the seal element tends to deform to the mandrel side as the outer lip prevents the seal element from deforming to the casing side. In contrast, the seal element tends to deform to the casing side when the lip angle is

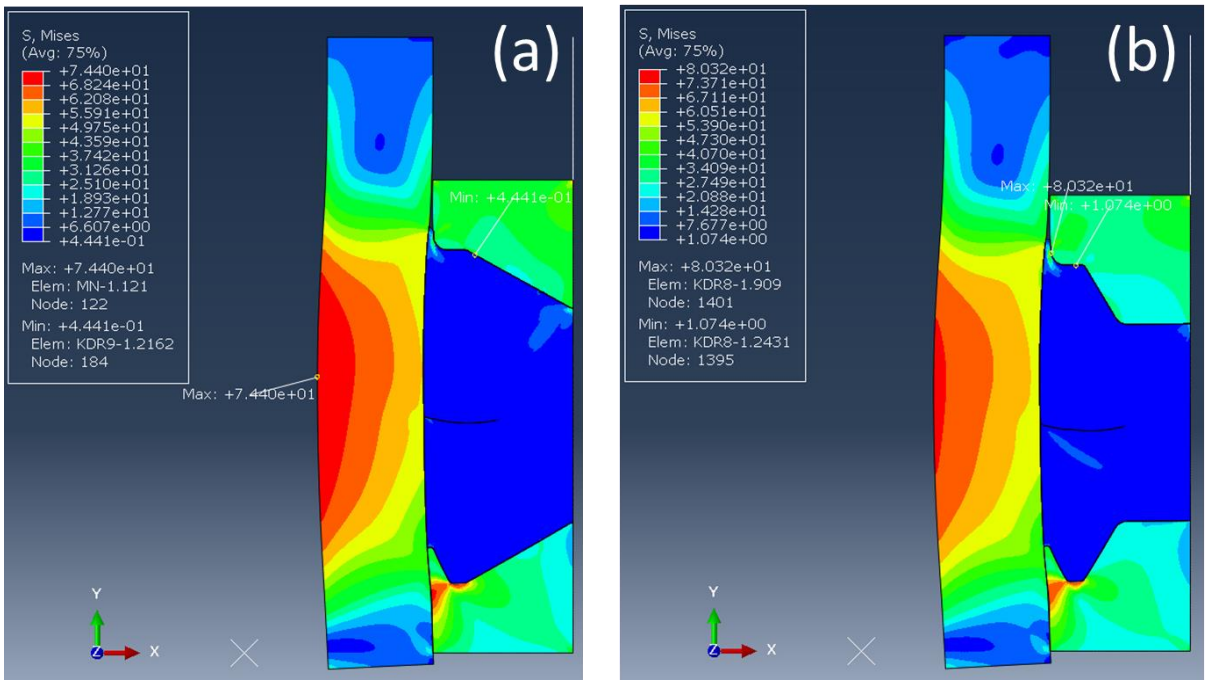

Figure 62 Mises stress at 60 MPa of equivalent pressure: (a) Model 6, (b) Model 7

small. Therefore, the stress and strain on the mandrel of Model 6 with the outer lip angle of 30° was smaller than other models.

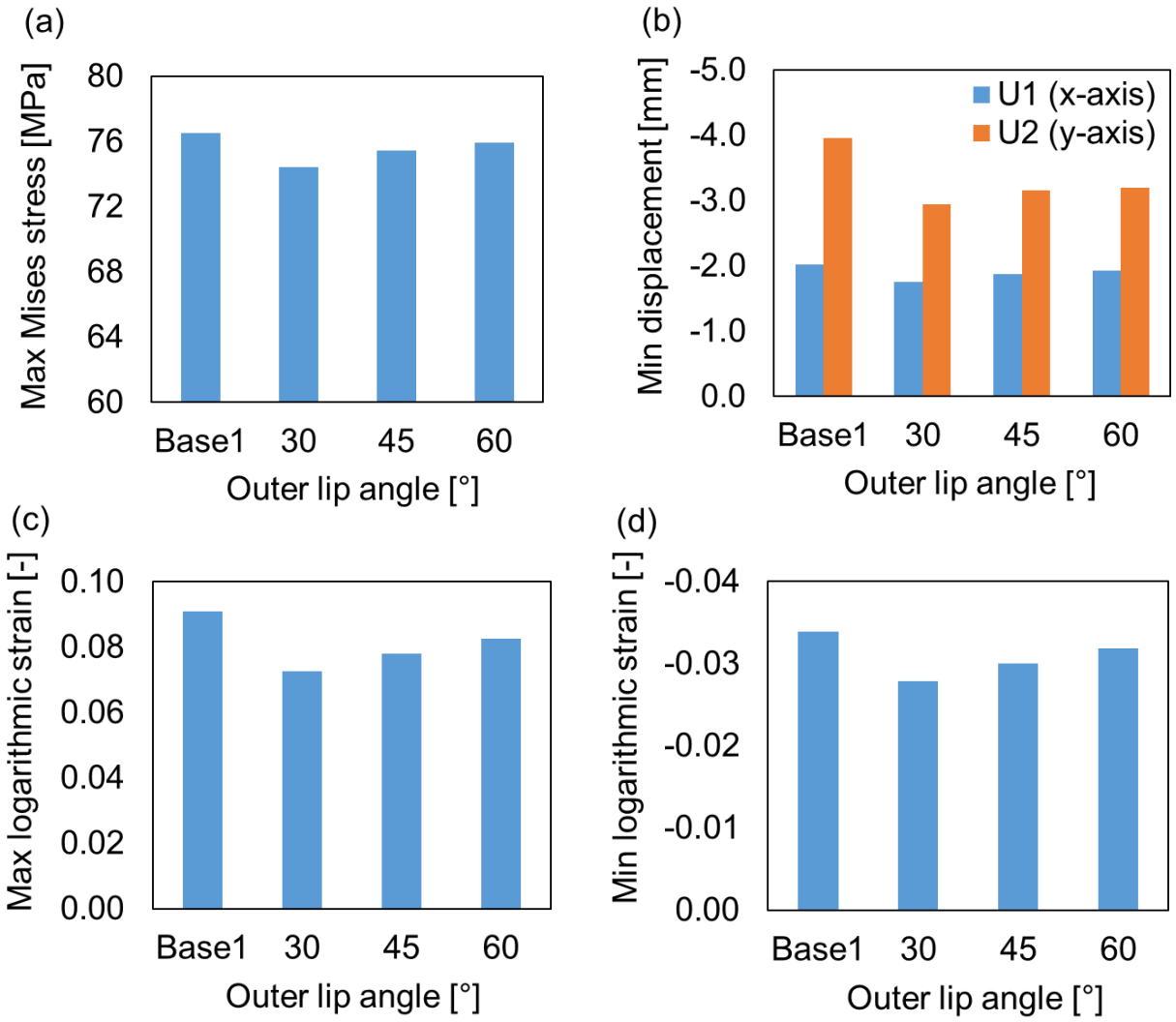

Figure 63 FEA results on the mandrel of models with different outer lip angles: (a) the maximum Mises stress, (b) the minimum displacement, (c) the maximum logarithmic strain, (d) the minimum logarithmic strain

Figure 64 shows a stress state and principal plastic strains of Model 14 at 60 MPa of equivalent pressure. As one can see in Figure 64, the protrusion of the lower socket covered lower left half of the seal element. As a result, the area where Mises stress is more than 70 MPa on the mandrel became smaller than Base Model 1. The minimum displacements of the mandrel of Model 14 to U1 (x-axis) and U2 (y-axis) directions at 60 MPa of equivalent pressure were shown in Figure 65. Compared to Base model 1 (Figure 57), the magnitude of the minimum displacements of Model 14 was much smaller. It would appear that the coverage of the mandrel by protrusion of the lower socket inhibited the seal element from deforming the mandrel.

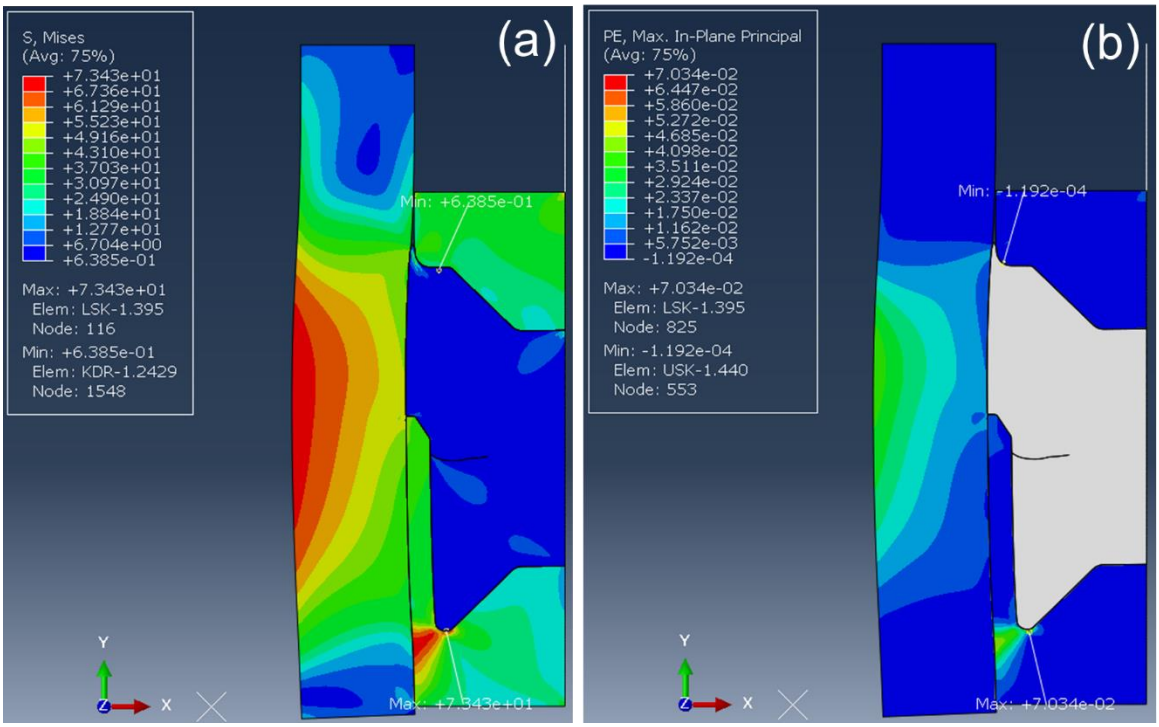

Figure 64 FEA result of Model 14: (a) Mises stress, (b) the maximum in-plane principal plastic strain, (c) the minimum in-plane principal plastic strain

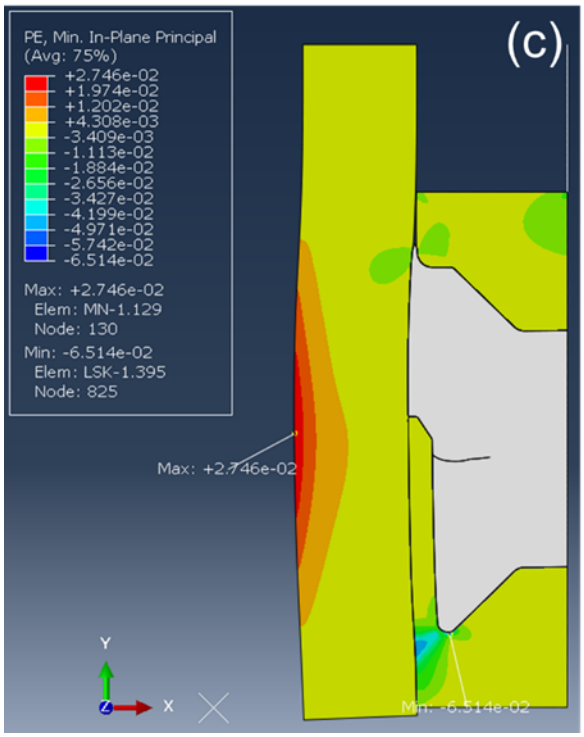

Figure 64 Continued

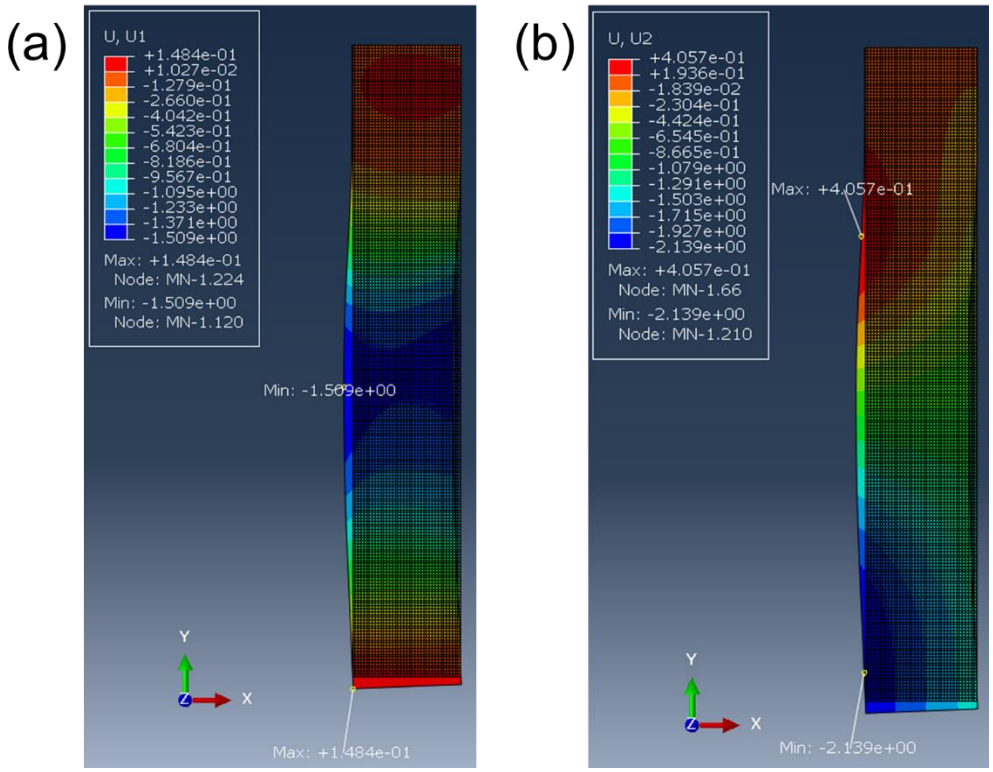

Figure 65 Displacement of the mandrel of Model 14: (a) U1 (x-axis) direction (b) U2 (y-axis) direction

Figure 66 shows the maximum Mises stress, the maximum and the minimum logarithmic strain, and the minimum displacement to U1 (x-axis) and U2 (y-axis) directions for the mandrel of Base model 1, Model 8, 9, 10, 11, 12, 13, 14, and 15. In the figure, legends of Model 8, 9, 10, and 11 were labeled as “5° inclination” and legends of Model 12, 13, 14, and 15 were labeled as “No inclination”. Hence, 40, 45, 50, and 55 of “5° inclination” in the figure mean the results of Model 8, Model 9, Model 10, and Model 11, respectively. Similarly, 40, 45, 50, and 55 of “No inclination” in the figure mean the results of Model 12, Model 13, Model 14, and Model 15, respectively. FEA results of model 10 was not shown in the figure as the calculation was not converged. Similar to Model 1 to 3, Mises stress and the magnitude of logarithmic strain and displacement of these models decreased as the protrusion length increased. However, there was no difference in the results between Model 14 (50 mm) and Model 15 (55 mm). For Model 14 and 15, coverage of the mandrel by the protrusion was more than half of the seal element length at 60 MPa of equivalent pressure. Therefore, the effect of lengthening a protrusion of the lower socket on preventing deformation of the mandrel was small for the protrusion length more than 50 mm. Model 14 was the best model among Model 1 to Model 15 as it had the lowest stress and strain.

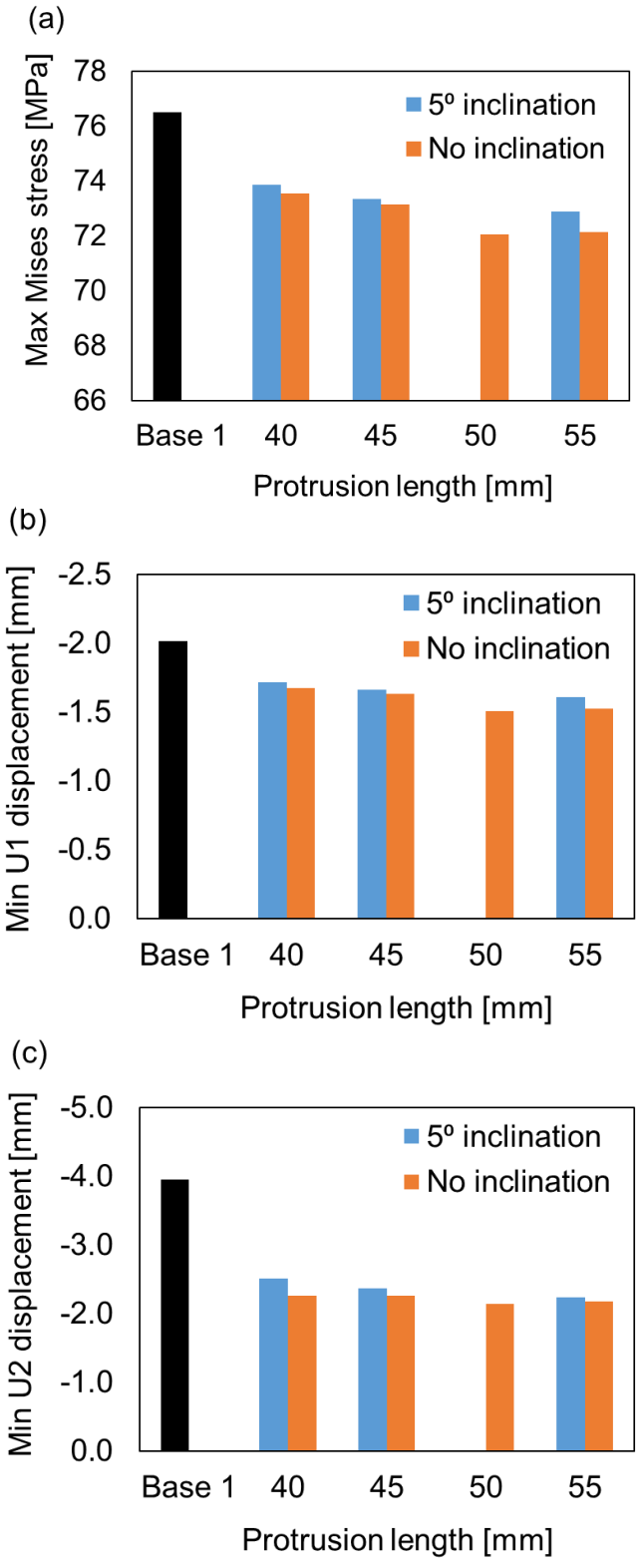

Figure 66 FEA results on the mandrel of models with different protrusion angles: (a) the maximum Mises stress, (b) the minimum U1 displacement, (c) the minimum U1 displacement, (d) the maximum logarithmic strain, (e) the minimum logarithmic strain

(d)

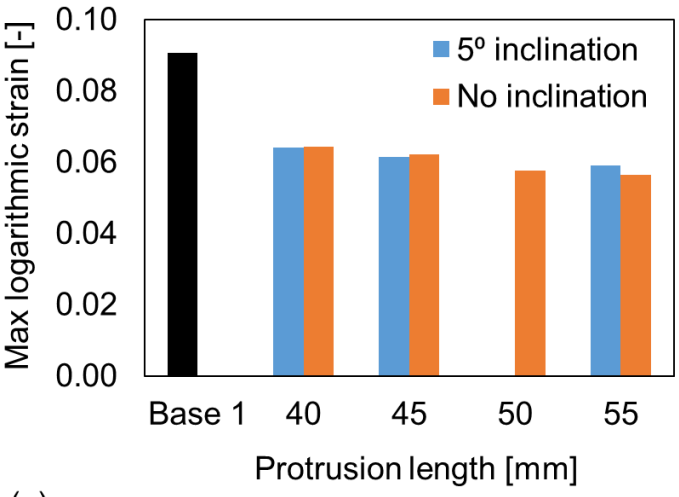

(e)

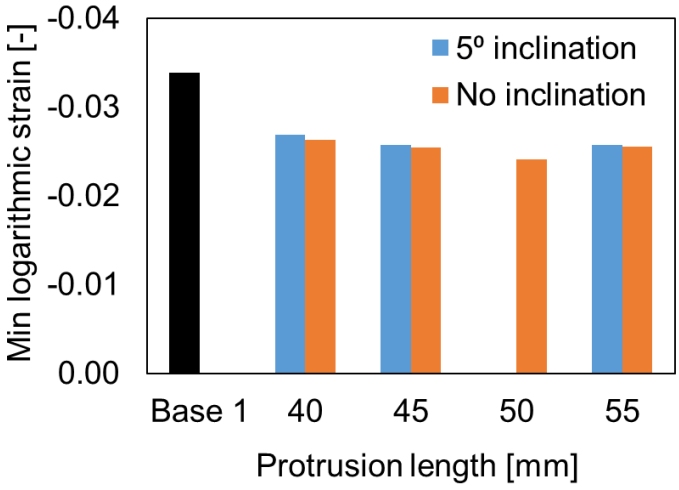

Figure 66 Continued

Figure 67 shows FEA results of Model 16 and Model 17. For both cases, the outer socket was expanded radially and contacted to the casing at 60 MPa of equivalent pressure as expected. This behavior of the outer socket prevented the seal element from penetrating into the gap between the casing and outer socket. As shown in the figure, the area above 70 MPa of Mises stress on the mandrel of Model 17 was smaller than that of Model 16. The reason is that the larger coverage of the mandrel by the protrusion of lower socket prevented deformation of the mandrel. Figure 68 shows the maximum Mises stress, the maximum and the minimum logarithmic strain, and the minimum displacement to U1 (x-axis) and U2 (y-axis) directions for the mandrel of Model 16 and 17. In addition to the result of Base model 1, those of Model 2 and 14 were also included in the figures for comparison. Model 2 is a counterpart of Model 16 as both of them have 20 mm of

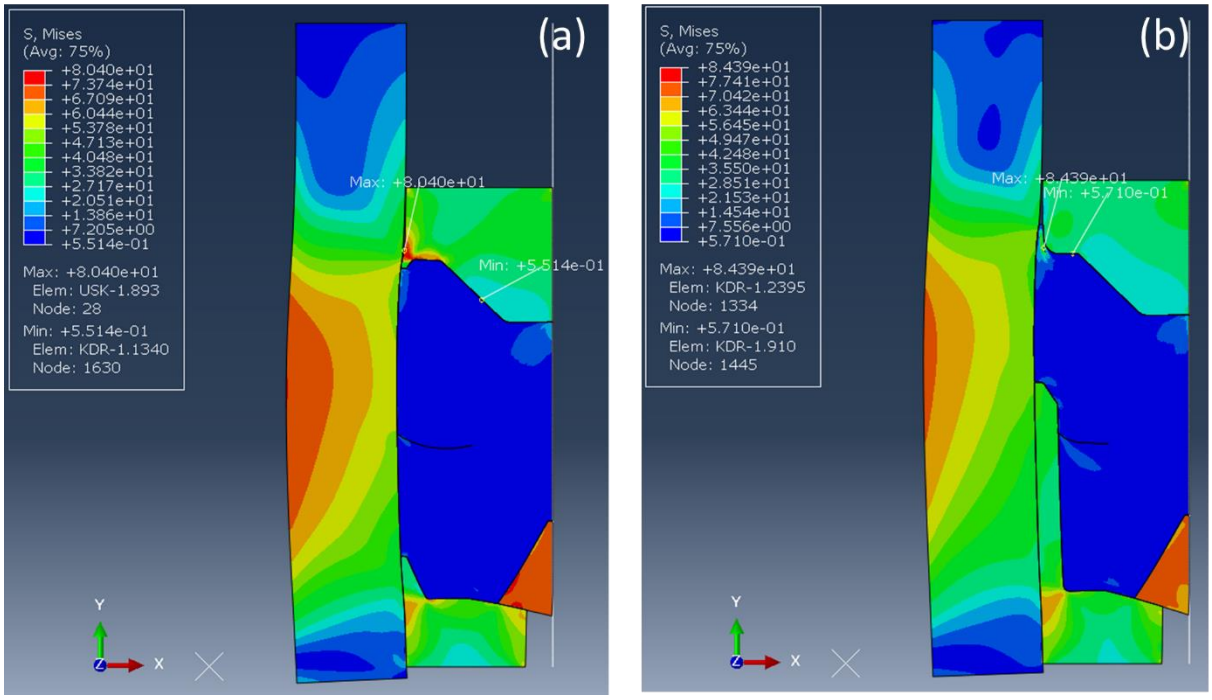

Figure 67 Mises stress at 60 MPa of equivalent pressure: (a) Model 16, (b) Model 17

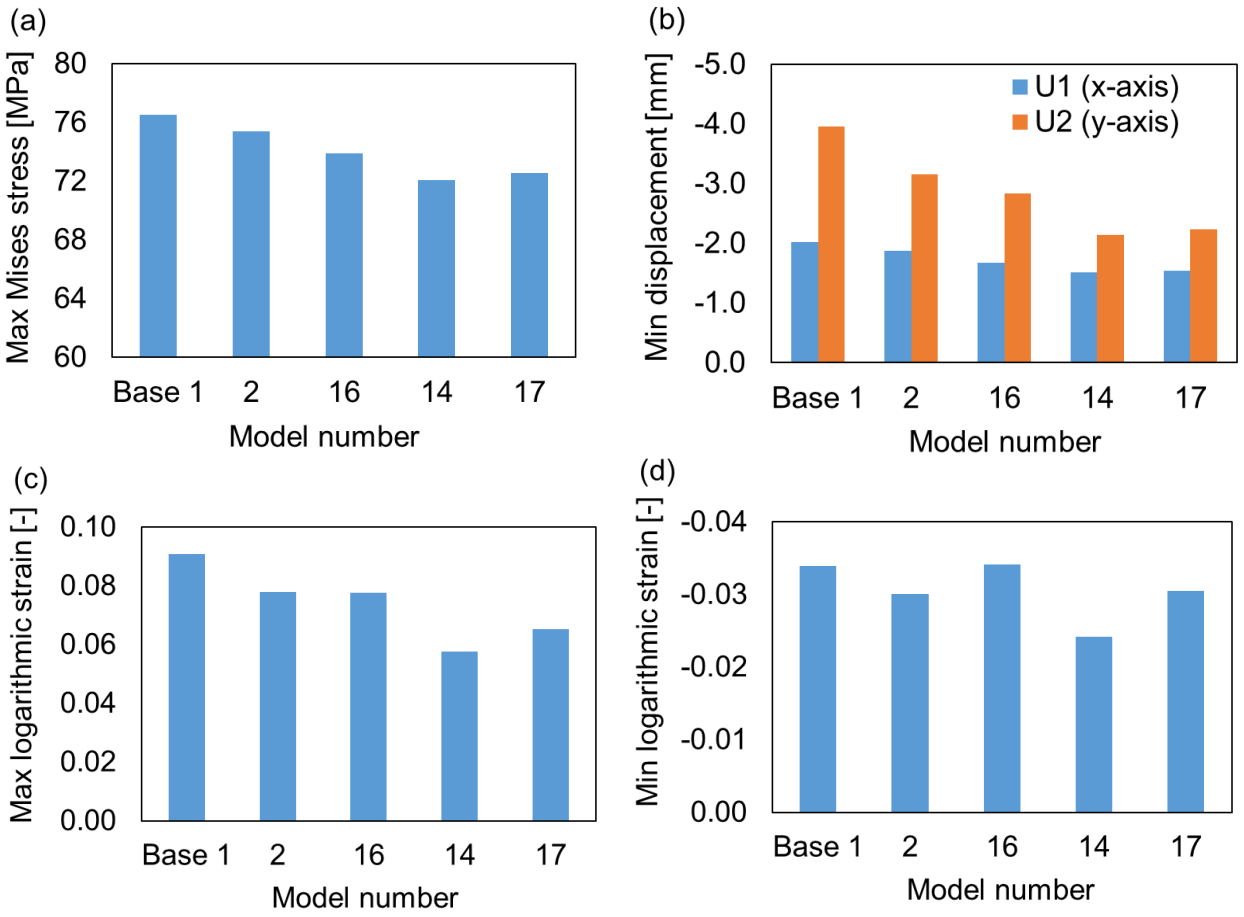

Figure 68 FEA results on the mandrel of Model 16 and Model 17 in comparison to previous models: (a) the maximum Mises stress, (b) the minimum displacement, (c) the maximum logarithmic strain, (d) the minimum logarithmic strain

protrusion, and Model 14 is a counterpart of Model 17 as both of them have 50 mm of protrusion. Base 1, 2, 16, 14, and 17 in the figure mean the results of Base model 1, Model 2, Model 16, Model 14, and Model 17, respectively. Mises stress and the magnitude of the minimum displacement of Model 16 were smaller than Model 2. This reason is that the seal element was able to deformed more to the casing side due to radial expansion of the outer socket. In addition, a protrusion on the upper socket prevented deformation of the mandrel. The magnitude of the minimum logarithmic strain on Model 16 was greater than that of Model 2 since the deformed protrusion of the upper socket pressed the mandrel. Mises stress and the magnitude of the minimum displacement of

Model 17 were similar to Model 14. It was inferred that the protrusion of the models was long so that it masked the stress reduction effect due to radial expansion of the outer socket. In contrast, the magnitude of the maximum and the minimum logarithmic strain on the mandrel of Model 17 were greater than that of Model 14. For Model 14, the displacement of the upper socket at 60 MPa of equivalent pressure was 24.9 mm and that of Model 17 was 27.8 mm. It indicates that as the displacement of the latter model was greater, the magnitude of the maximum and the minimum strain of the latter was greater as well.

Figure 69 shows contour plots of Mises stress on the lower socket of Model 2, Model 14, Model 16, and Model 17. The maximum Mises stress on the lower socket of Model 2 was observed at the base of protrusion and the value was 75.6 MPa, whereas that of Model 16 was 72.6 MPa. The reason of smaller Mises stress of Model 16 compared to Model 2 suggests that radial expansion of the outer socket made more space for the seal element to deform and reduced compressive stress to the protrusion. The same tendency was observed for the lower sockets of Model 14 and Model 17. The maximum Mises stress on the lower socket of Model 14 was 73.4 MPa and that of Model 17 was 69.7 MPa. These results indicated that the outer socket design reduces the risk of failure around the base of protrusion.

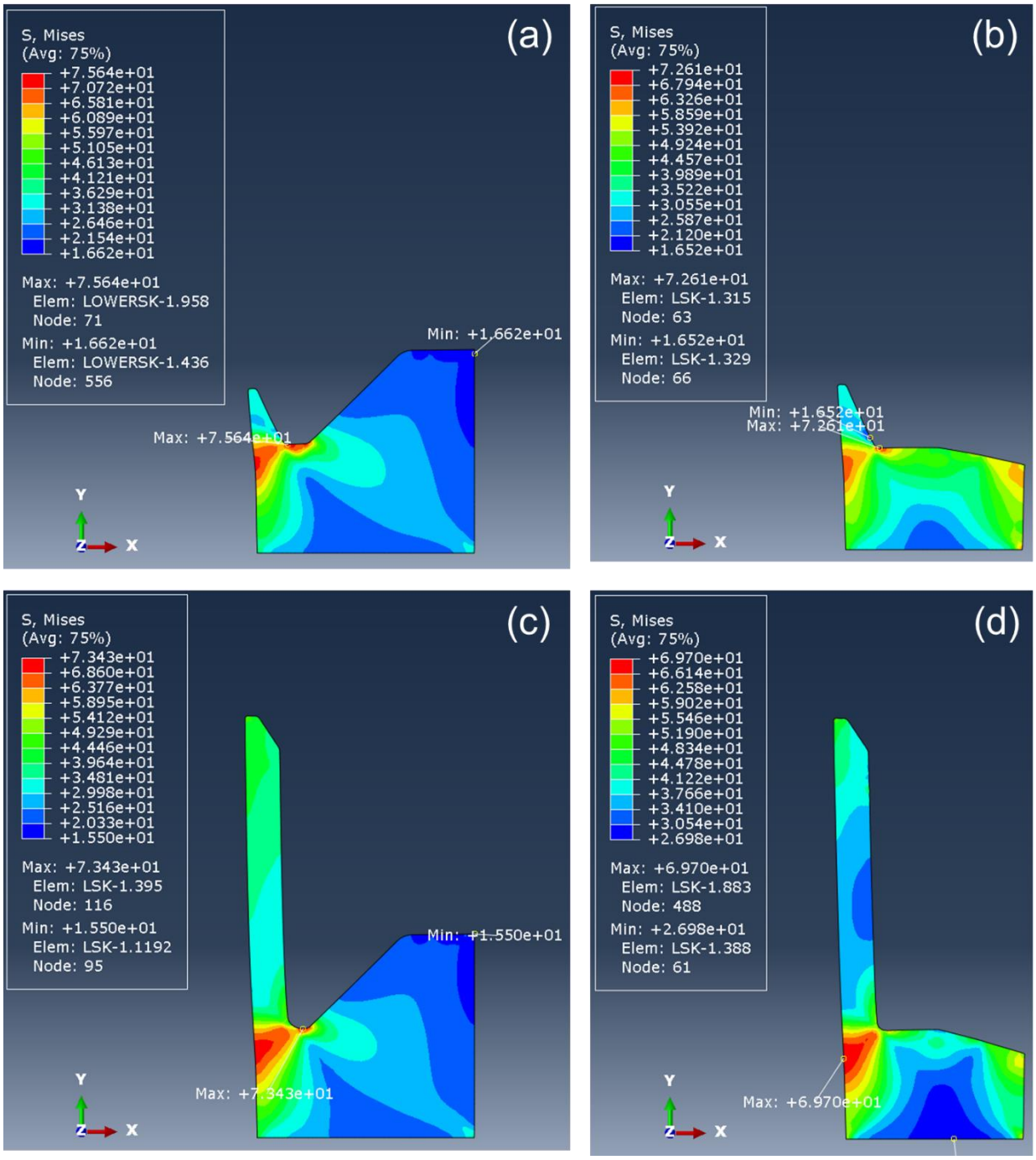

Figure 69 Mises stress on the lower socket at 60 MPa of equivalent pressure: (a) Model 2, (b) Model 16, (c) Model 14, (d) Model 17

Figure 70 shows the seal lengths and the maximum contact pressure between the casing and seal element of all the models at 36 kN of the reaction force on the upper socket. All the models had similar or greater seal length compared to Base model 1. The reason of the greater seal length was that the protrusion of the lower socket made the seal element deform more to the casing side. The maximum contact pressure of all the models except for Model 7 showed similar value and it ranged from 3.2 to 3.5 MPa. These results indicated the effect of adding protrusion to the lower socket on the sealing performance of the seal element in the casing is insignificant. The maximum contact pressure on Model 7 was higher than other models and it was 4.4 MPa. For Model 7, the displacement of the upper socket at 36 kN of the reaction force was -23 mm. Whereas those of other models were about -19 to -20 mm. The outer lip angle of Model 7 is 60° which made the seal element deform more to the mandrel side. Therefore, more compressed seal element contacted

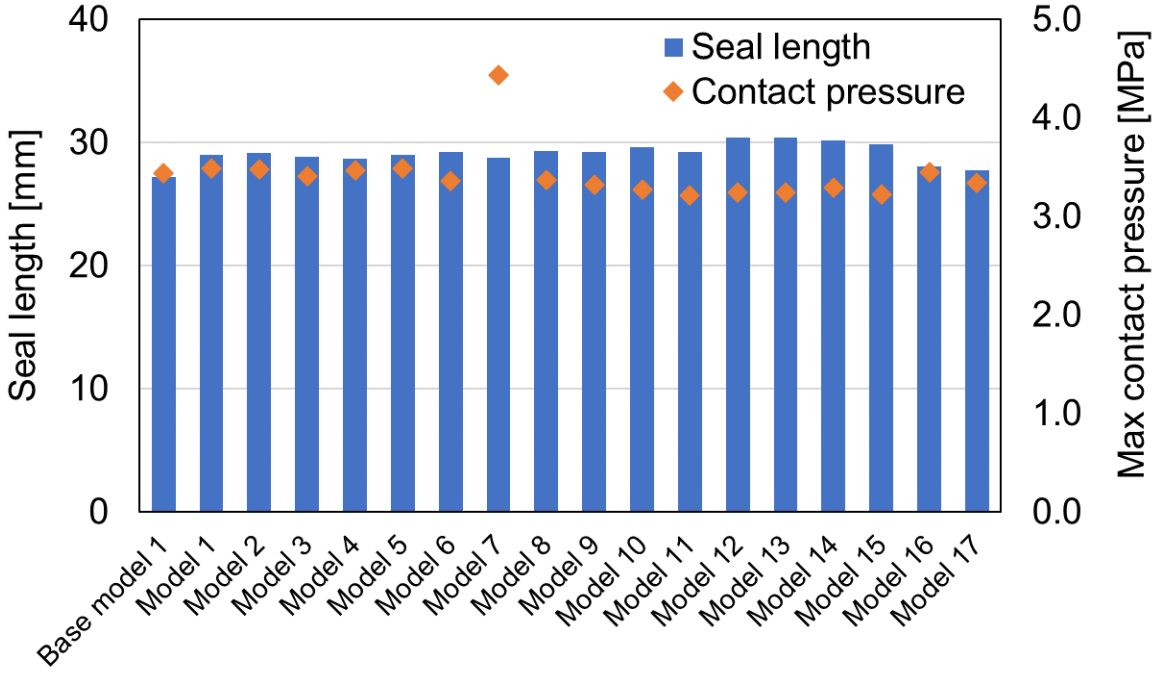

Figure 70 Seal length and the maximum contact pressure between the casing and seal element at 36 kN of the reaction force

with the casing once they started contacting. This greater displacement of the upper socket of Model 7 due to the high outer lip angle caused greater compression of the seal element and resulted in the large contact pressure.

Figure 71 shows the seal lengths and the maximum contact pressures between the casing and seal element at 36 kN of the reaction force on the upper socket for models with different notch angle (70°, 90°, 110°, 130°, and 150°). The result of Base model 2 was labelled as Base 2 in the figure. As one can see in the figure, the seal length decreased as the notch angle increased but the effect was insignificant. The reason of the slight decrease in the seal length indicated that there was more space for the seal elements with higher notch angle to deform to the mandrel side before it contacts to the casing. In contrast, the maximum contact pressure increased with increase in the notch angle and the effect was significant. It changed from 2.6 to 4.4 MPa. It indicates that the

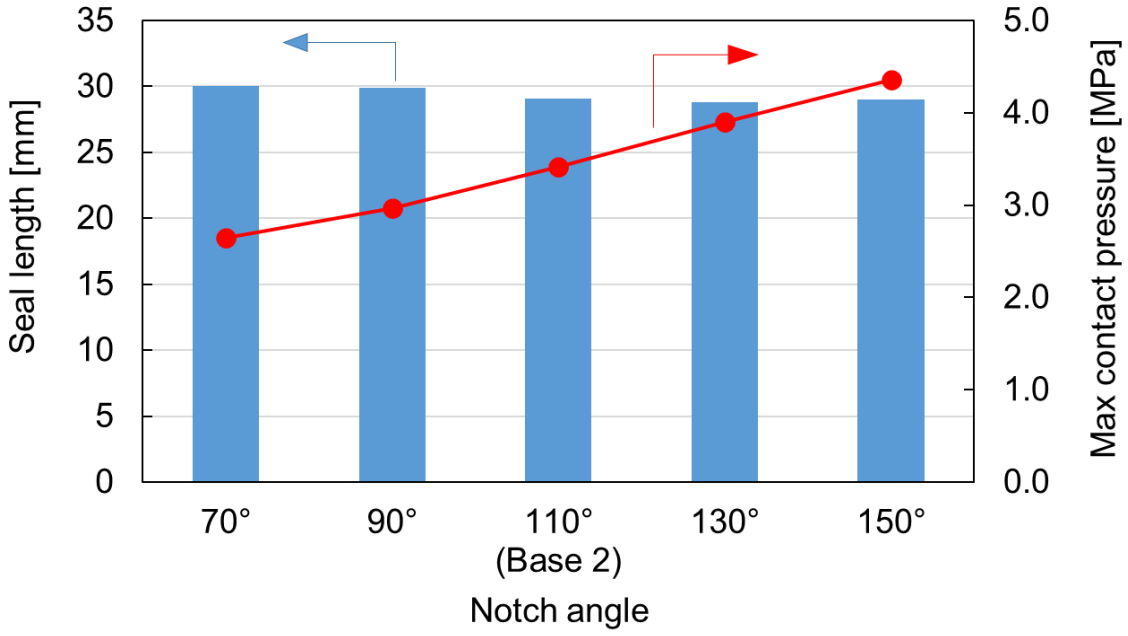

Figure 71 Seal lengths and the maximum contact pressures between the casing and seal element at 36 kN of the reaction force on the upper socket: Models with different notch angle

higher notch angle, the easier for the seal element to deform radially toward the casing side and it started contacting with the casing at an early stage. There was no significant difference in the stress and strain states on the mandrel at 60 MPa of equivalent pressure among the models.

Figure 72 shows seal lengths and the maximum contact pressures between the casing and seal element at 36 kN of the reaction force on the upper socket for models with different notch depth (-2.5 mm, -1.25 mm, Base model 2, +1.25 mm, and +2.5 mm). The result of Base model 2 was labelled as Base 2 in the figure. The seal length slightly decreased with increase in the notch depth. Since the volume of the seal element was smaller for the models with greater notch depth, the seal length obtained at the same applied force became smaller. On the other hand, the contact pressure

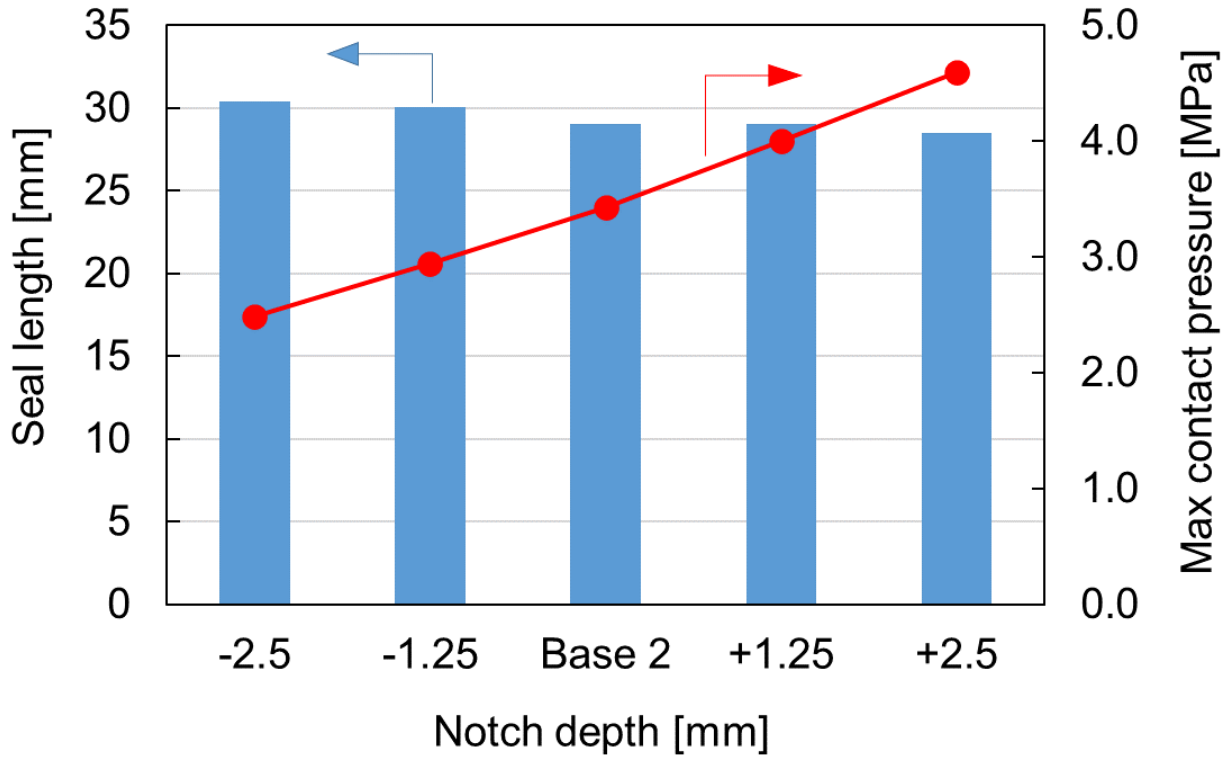

Figure 72 Seal lengths and the maximum contact pressures between the casing and seal element at 36 kN of the reaction force on the upper socket: Models with different notch depth

increased with increase in the notch depth. This reason was presumed that it was easy to deform radially to the casing side for models with greater notch depth. No significant difference in the stress and strain state on the mandrel were observed at 60 MPa of equivalent pressure among the models.

The seal lengths and the maximum contact pressures between the casing and seal element at 36 kN of the reaction force on the upper socket for models with different seal element length (-5 mm, Base model 2, +5 mm, +10 mm, and +15 mm) were shown in Figure 73. The result of Base model 2 was labelled as Base 2 in the figure. The seal length increased with the seal element length. However, even if the seal length became +15 mm, the seal length increased by only 5.8 mm from

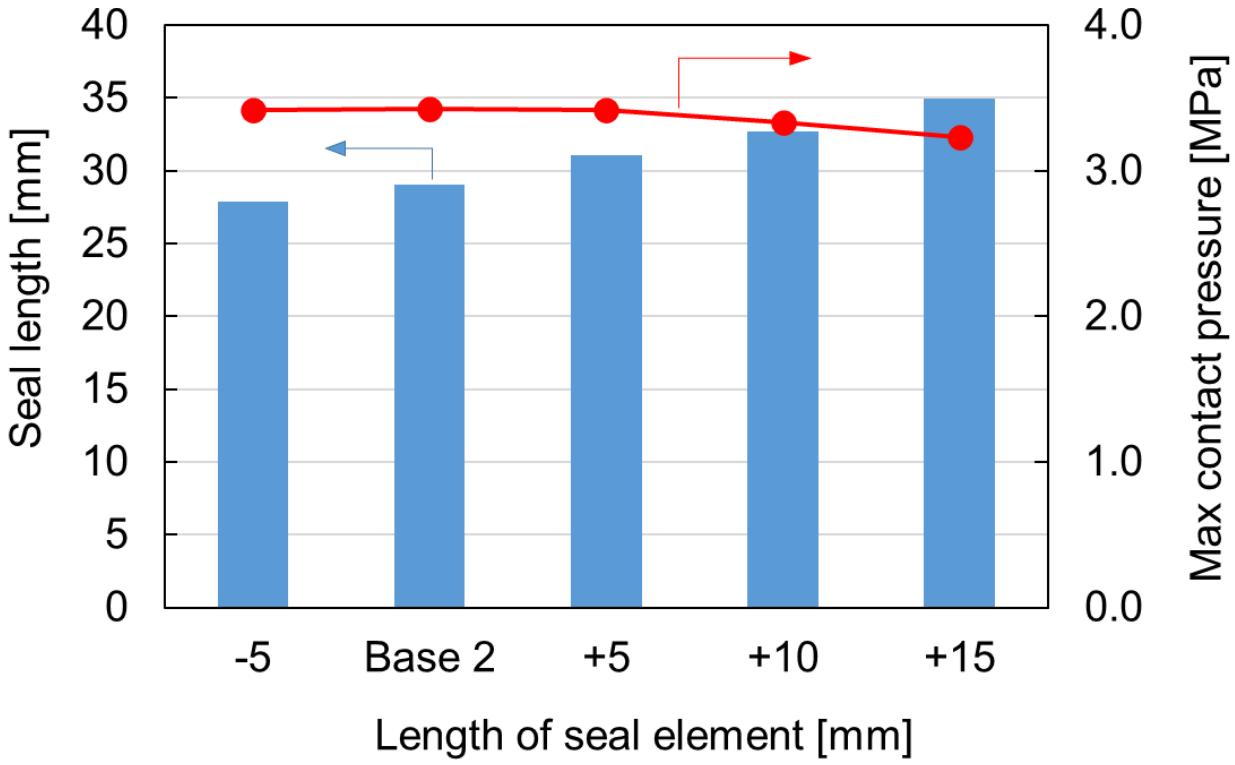

Figure 73 Seal lengths and the maximum contact pressures between the casing and seal element at 36 kN of the reaction force on the upper socket: Models with different seal element length

Base Model 2. It means the seal length was increased only about 0.4 mm by lengthening seal element by 1 mm. Even though the contact pressure decreased with increase in the length of seal element due to less compression of longer seal element, the change in the value was not significant.

Figure 74 shows Mises stress of models with different mandrel thickness obtained from FEA. The both models showed less deformation of the mandrel compared to Base model 2. Figure 75 shows the maximum Mises stress, the maximum and the minimum logarithmic strain, and the minimum displacement to U1 (x-axis) and U2 (y-axis) directions for the mandrel of models with different mandrel thickness. The result of Base model 2 was labelled as Base 2 in Figure 75. Mises stress, the magnitude of the minimum displacement and the maximum strain decreased as the thickness increased. The thicker the mandrel was, the stronger it was. In contrast, there was no difference in the magnitude of the minimum logarithmic strain among them as the shape of the right side of the mandrel was not affected by the change in the thickness.

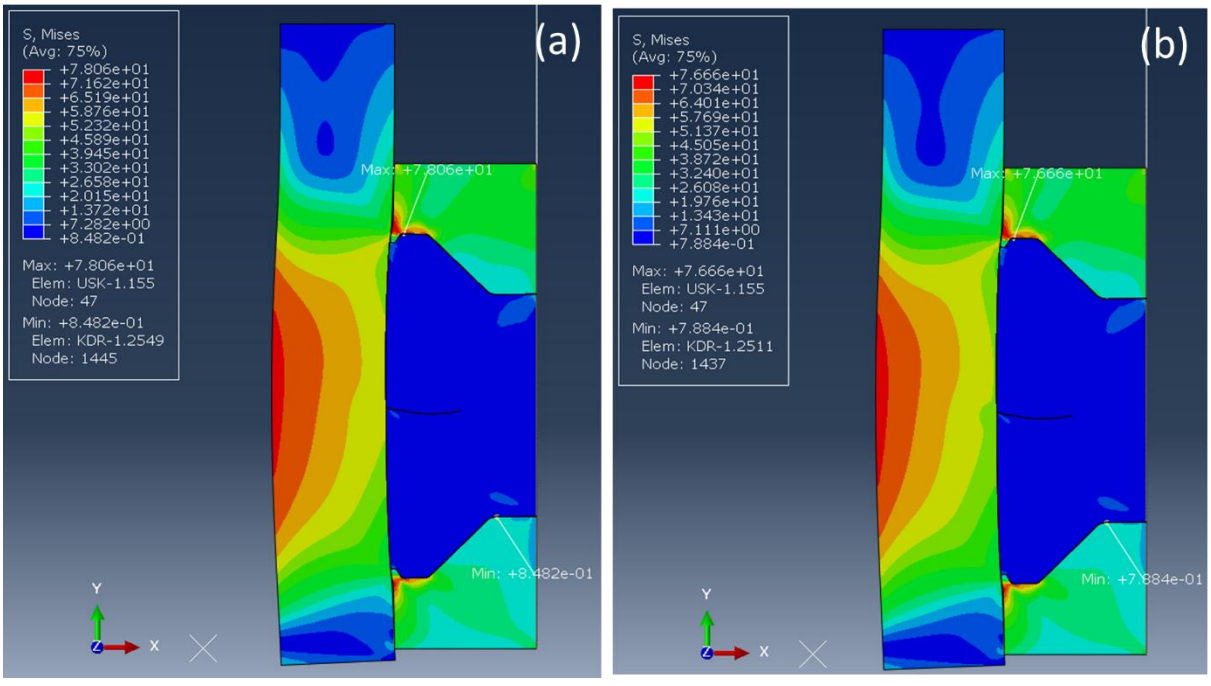

Figure 74 Mises stress at 60 MPa of equivalent pressure: (a) thickness +1.25 model, (b) thickness +2.5 model

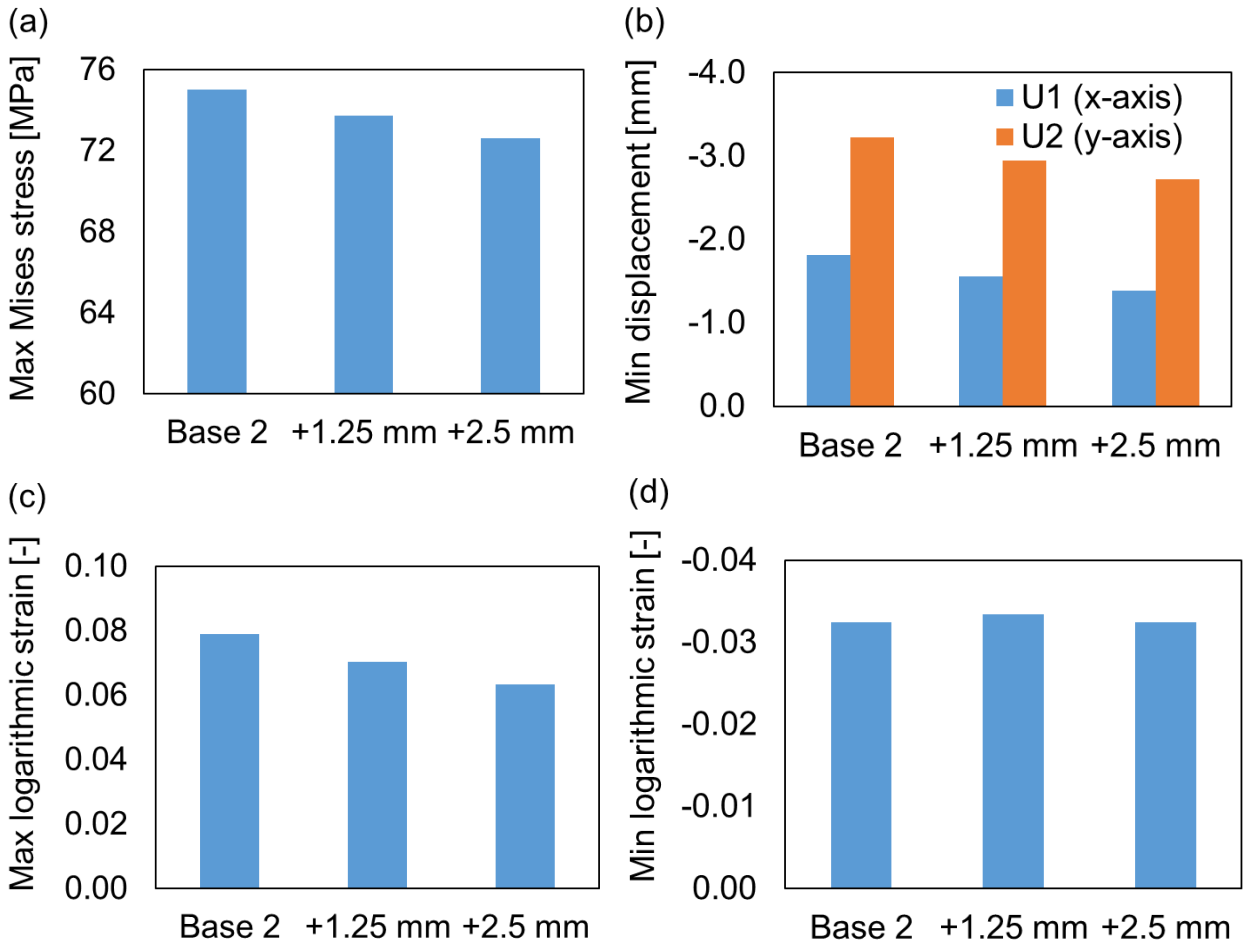

Figure 75 FEA results on the mandrel of models with different mandrel thicknesses: (a) the maximum Mises stress, (b) the minimum displacement, (c) the maximum logarithmic strain, (d) the minimum logarithmic strain

Summary of the designs studied and their effects on the stress, strain, and sealing performance was shown in Table 3. Changing the design of each part affected differently to the stress, strain, seal length, and contact pressure. Among all the designs studied, adding 50 mm of protrusion without inclination was the most effective design. From this knowledge, we could design parts of DFP with better performance.

Table 3 Summary of the designs and their effects

Factor		Effect
Socket	Protrusion length	The longer the length, the less stress and strain
	Protrusion angle	Almost no influence
	Outer lip angle	The smaller the angle, the less stress and strain
Seal element	Notch angle	The larger the angle, the greater contact pressure
	Notch depth	The deeper the depth, the greater contact pressure
	Length	The longer the length, the longer the seal length
Mandrel	Thickness	The thicker the mandrel, the less stress and strain
	Neck angle	The smaller the angle, the less stress and strain

5. PRESSURE TEST AND DEGRADATION TEST OF DEGRADABLE FRAC PLUG

5.1 Pressure test of DFP

5.1.1 Material and methods

A large pressure vessel with temperature capability was used to apply high hydraulic pressures to DFP in casing. Figure 76 depicts the test facility and DFP fixed in the casing. Tap water was filled in the vessel and the temperature was controlled from 150°F to 200°F. A DFP for 5.5" 2.3 lb/ft casing was assembled with parts composed of the fast degrading materials and it was soaked in the fluid for 30 mins to heat it up. After 30 mins, the DFP was taken out from the vessel and actuated by a setting tool to fix in a 23 lb/ft casing with thread. In this study, 5.5" 23 lb/ft P110 casing with the length of 900 mm was used. A lid with thread was put on the casing and the screw was tightened to isolate the space above seal element of the DFP. The sealed casing with DFP was soaked in the large vessel and pressure was applied by a pump. The DFP was hold under 8,000 psi for 30 mins followed by applying 10,000 psi for 60 mins at 150°F. Once 10,000 psi of pressures were successfully applied for 60 mins at 150°F, the pressure in the casing was decreased to arbitrary lower pressure and the fluid temperature of the vessel was increased to 200°F. Then, 8,000 psi was applied to the DFP for 30 mins followed by applying 10,000 psi until the DFP fails. Pressure was maintained within ±300 psi to the target pressure during the

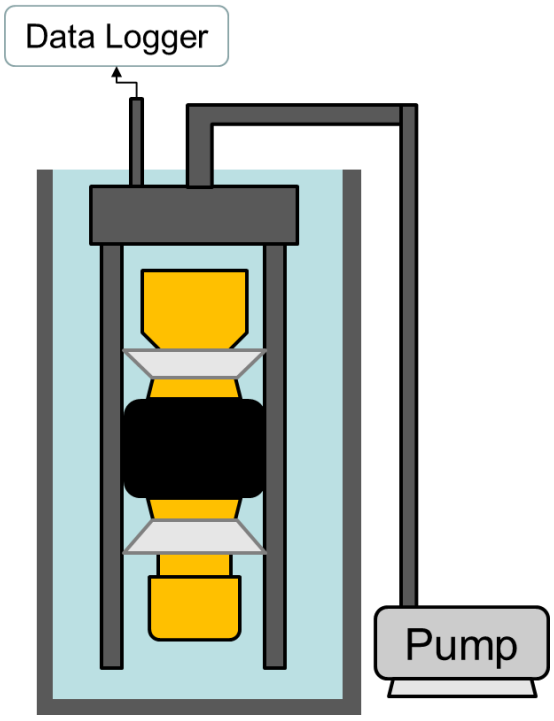

Figure 76 Sketch of the test facility for pressure test of DFP

test. Pressure was increased to the target pressure once the pressure decreases more than 300 psi from the target pressure. Pressure profile during the test was measured and recorded by a logger connected to the lid of the casing. For this study, DFP with no-protrusion lower socket and DFP with 20 mm protrusion lower socket were tested. The former is similar design as the original model in Section 4 and the latter is similar design as Model 16 except that its outer lip angle is 45° in this study.

5.1.2 Results and Discussion

The result of the pressure test for DFP with no-protrusion socket was shown in Figure 77. Small drops of pressure were observed during the test as one can see in the figure. It would seem that deformation of parts of DFP or slight slide of slip downward in the casing due to high pressure caused the small pressure fluctuations. The DFP was able to hold 8,000 psi for 30 mins and 10,000

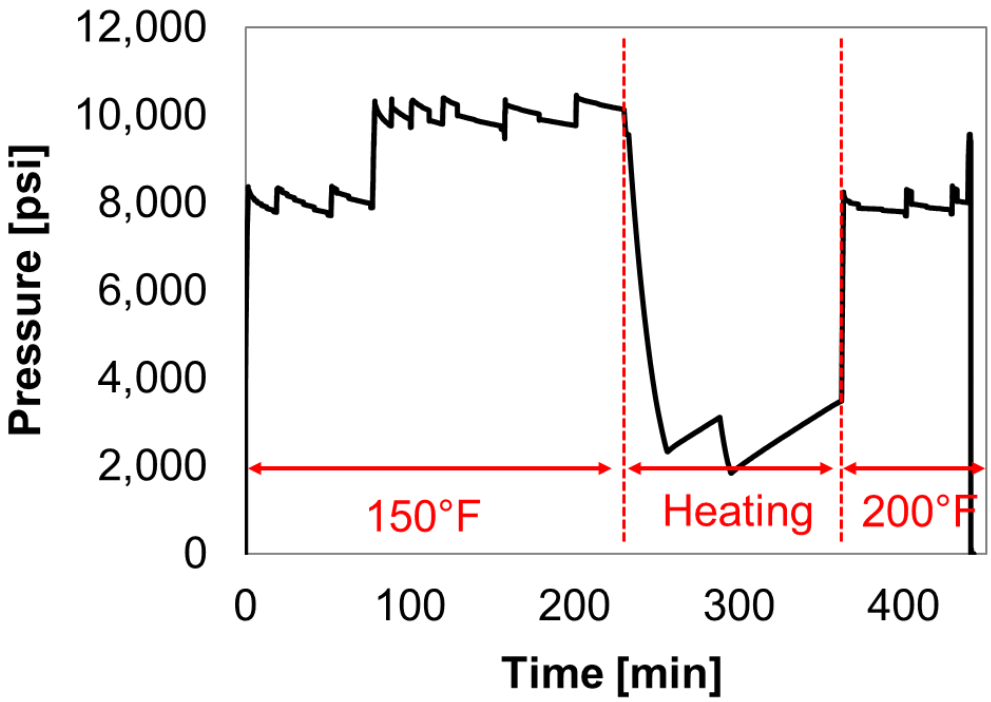

Figure 77 Result of the pressure test for DFP with no-protrusion socket

psi for 60 mins at 150°F. At 200°F, the DFP successfully held 8,000 psi for 30 mins. However, it failed around 9,000 psi due to breakage of the mandrel during increasing vessel pressure to 10,000 psi. The DFP was broken at the part of the seal element (Figure 78), and this result agrees with FEA result. Figure 79 shows the result of the pressure test for DFP with 20 mm protrusion lower socket. The DFP held 10,000 psi for 60 mins at 150°F. At 200°F, it held 8,000 psi for 30 mins and 10,000 psi for 60 mins. Compared to the result of the DFP with no-protrusion socket, the DFP with 20 mm protrusion showed better performance at higher pressure and temperature in the pressure test. This result agrees with FEA result discussed in the previous section.

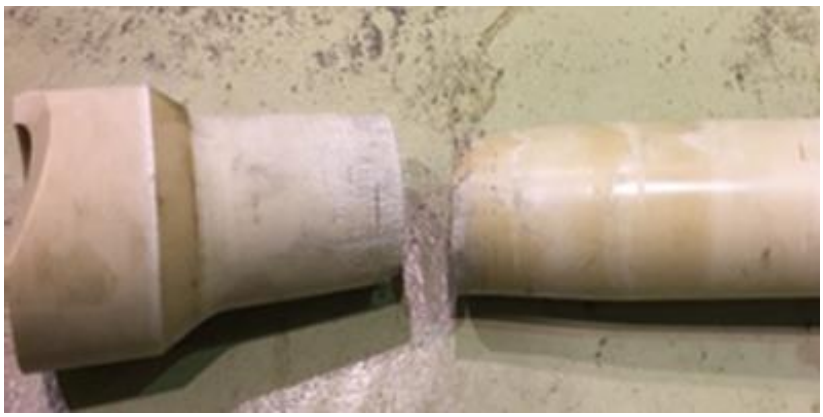

Figure 78 The Mandrel of the DFP with no protrusion lower socket after failure

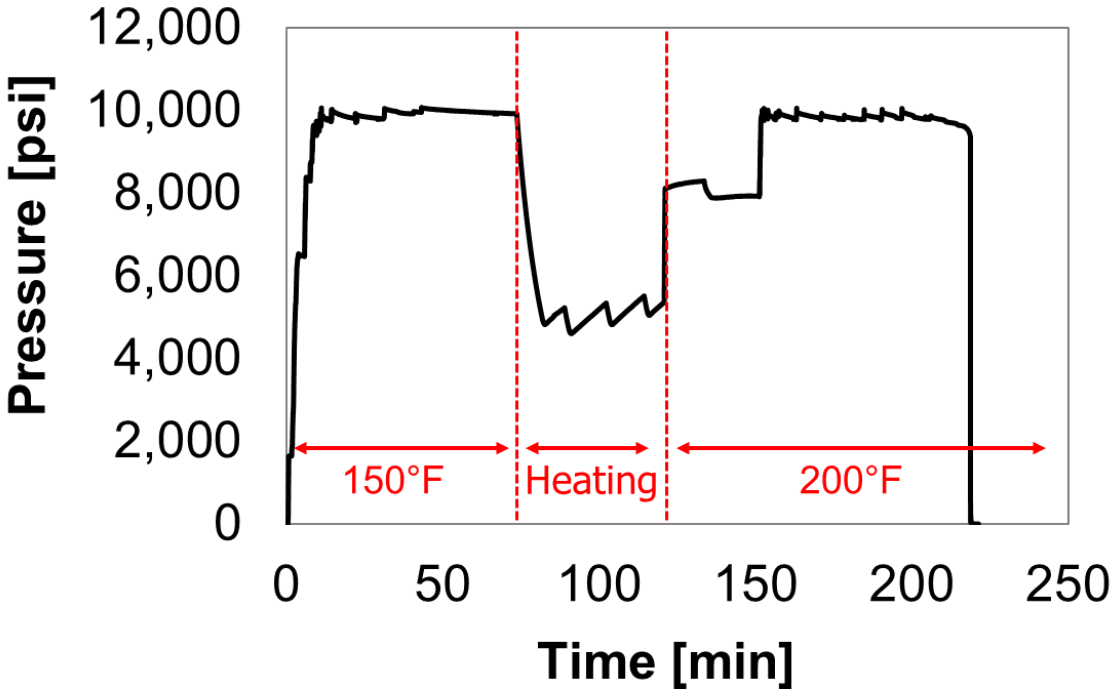

Figure 79 Result of the pressure test for DFP with 20 mm protrusion socket

5.2 Degradation test of DFP

5.2.1 Material and methods

Degradation test of 4.5” 13.5# DFP in a large vessel was performed at 150°F. The DFP was soaked in 400 L of 0.3% KCl solution. This amount of fluid simulates actual amount of fluid to DFP in multistage fracturing. Degradation behavior and change in the size of each parts were observed at certain time intervals. The pH of the fluid was also measured.

5.2.2 Results and Discussion

Figure 80 shows the result of the degradation test of the DFP. Mg-FD degraded completely and R-FD degraded into small pieces after 6 days. After 16 days, all parts including PGA-FD

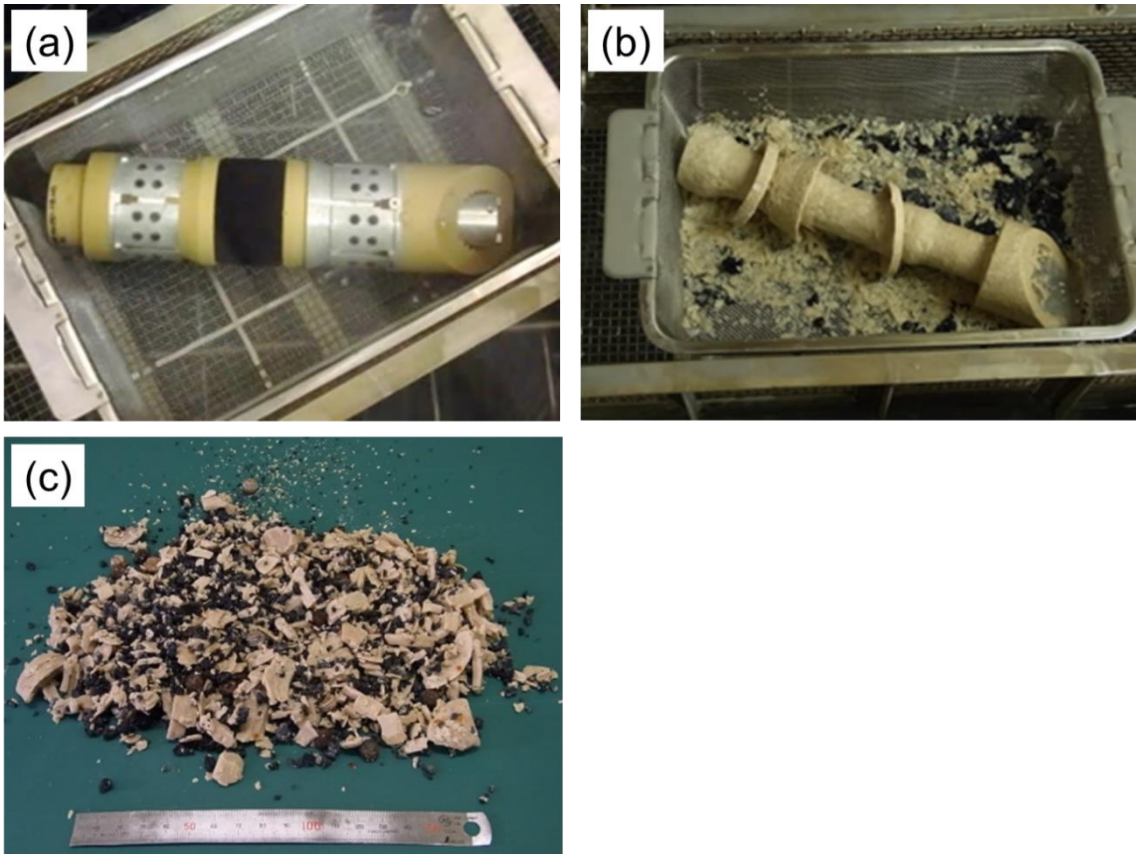

Figure 80 Result of the degradation test of DFP in 150°F: (a) before test, (b) after 6 days, (c) after 16 days

degraded into small pieces. Figure 81 shows a comparison of decrease in the thickness for Mg-FD and PGA-FD between a prediction based on the degradation test data of small specimens and the actual test data obtained from this DFP degradation test. The prediction data was calculated by the degradation rates obtained in Section 2. The values in Figure 81 are those from one side of the surface. For both Mg-FD and PGA-FD, the test results and calculated prediction data agreed well. Regarding R-FD, it was no possible to measure its Shore-A hardness during the test since the shape made it difficult to measure it by durometer. The pH of the fluid was relatively stable and was about 7 to 8 during the test (Figure 82).

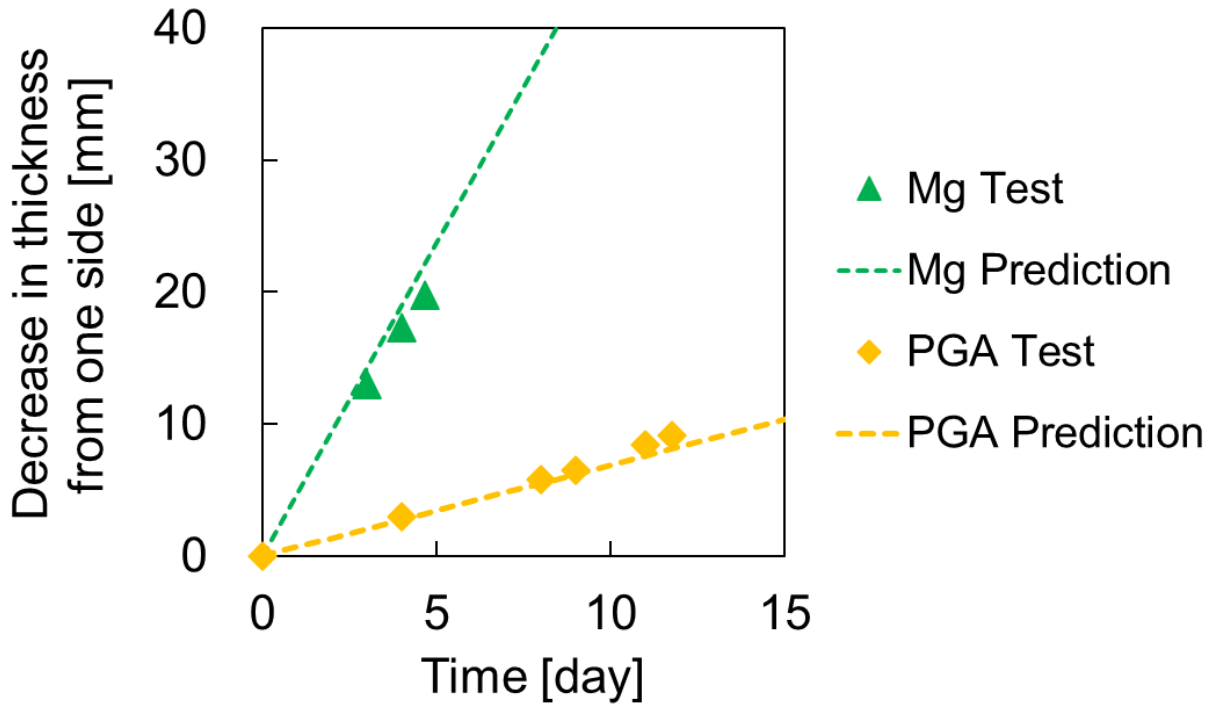

Figure 81 Comparison of the decrease in thickness from one side between a prediction and the test result from DFP degradation test

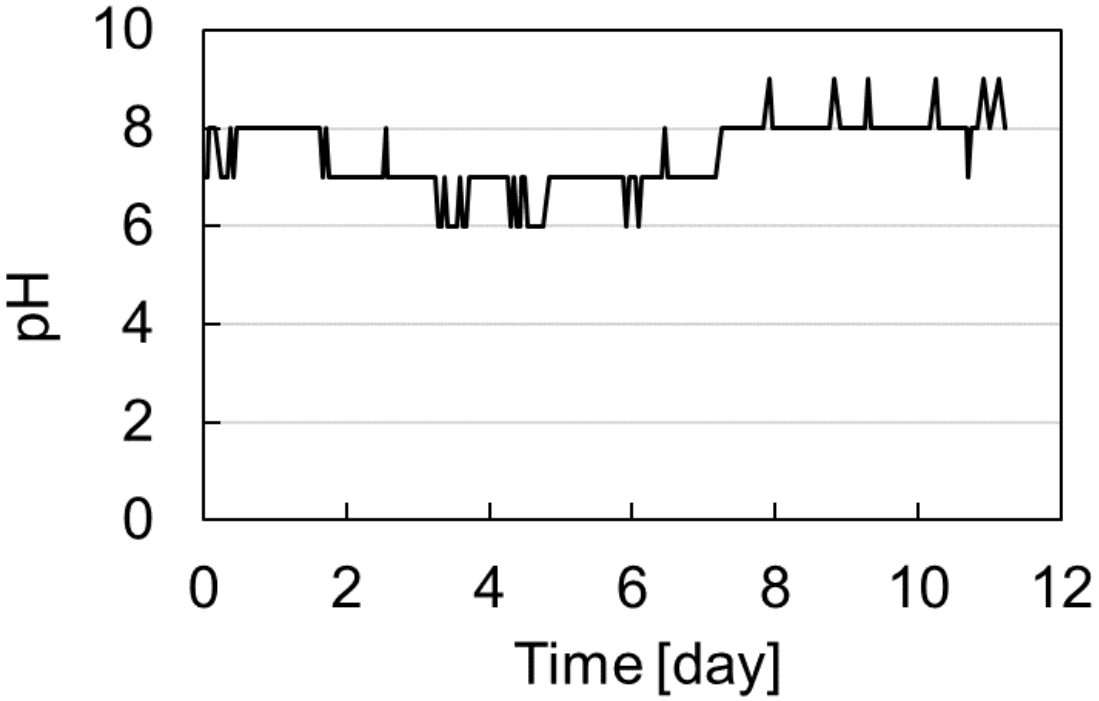

Figure 82 The pH of fluid during the degradation test of DFP

6. CONCLUSIONS

In this dissertation, we studied applicability of the three fast degrading material for DFP through various evaluations. The following summary and conclusions can be drawn from each section in the dissertation.

1. Degradation tests of fast degrading materials: Degradation rates of all the three materials increased with temperature in DI water. The type of solution affected differently on their degradation profile. Hydrochloric acid accelerated degradation of R-FD and Mg-FD. In contrast, it retarded the degradation of PGA-FD. NaOH did not affect the degradation of R-FD remarkably. On the other hand, it significantly inhibited the degradation of Mg-FD. Degradation of PGA-FD was promoted in the presence of NaOH. From the results obtained, we concluded that these fast degrading materials have preferable degradability for DFP application except for in a strong acid or alkaline fluid.

   The type of salts (KCl, NaCl, $CaCl_2$, KNO_3, K_2SO_4, $KHCO_3$) in the solution of the degradation test affected differently to the degradation profile of each fast degrading materials. The degradation of PGA-FD and R-FD was not affected by the salts tested significantly. On the other hand, the degradation rate of Mg-FD was greater in the order of $KHCO_3 < K_2SO_4 < KNO_3 < CaCl_2 < KCl \leq NaCl$ under the same concentration. For PGA-FD and R-FD, the effect of additives in the solution on their degradation was almost negligible, whereas the degradation of Mg-FD was affected by additives and the impact was different for each. DTPMP and glutaraldehyde had little effect on the degradation. TMAC accelerated the degradation, while guar, PAA, citric acid, Tergitol, and propargyl alcohol retarded the degradation. However, the reduction in the degradation rate of Mg-FD by these additives does not affect the complete degradation of DFP as a whole since the degradation of Mg-FD is much faster than PGA-FD

and the degradation of PGA-FD is the control factor of the complete degradation of the developed DFP.

2. Laboratory mechanical test: Mechanical tests of the fast degrading materials were performed with the universal testing machine. Each material showed high mechanical strength with is similar to conventional frac plug materials. The loading test with the slip composed of Mg-FD indicated the slip was able to withstand 10,000 psi. The seal element made from R-FD showed good seal performance in the compression test.
3. Finite element analysis of frac plug components: Optimizations of designs of the mandrel, socket, and seal element were conducted with ABAQUS. For the neck angle of the mandrel, the model with smaller neck angle showed less Mises stress on the neck. From the FEA with various sizes of balls, we determined that the allowable minimum size of a frac ball composed of PGA-FD was 1.3 inches for 4.5" DFP. The results of FEA showed that adding the protrusion to the lower socket decreased stress and strain on the mandrel under high pressure. It was found that the longer the protrusion, the lower the stress and strain. Adding 50 mm protrusion was the best design to improve pressure tolerance of the DFP. Length of the seal element, notch angle, and notch depth affected its seal length and contact pressure.
4. Pressure test and degradation test of DFP: Pressure tests of DFP composed of the three fast degrading materials with the large pressure vessel was carried out. The DFP using the lower socket with the protrusion successfully withstood 10,000 psi in 200°F. This result satisfies the market standard of frac plugs, which is 10,000 psi pressure rating. In the degradation test at 150°F, the DFP disintegrated into small pieces after 16 days. The degradation behavior was consistent with the results from degradation test with small specimens.

From the results discussed above, we concluded that the three fast degrading materials have sufficient mechanical strength and degradability to use them for DFP application and DFP composed of the materials have enough performance as a frac plug.

REFERENCES

Baihly, J., Aviles, I., Johnson, J. & Melenyzer, G., 2012. Sleeve Activation Sleeve Activation in Open-holeFracturing Systems: A Ball Selection Study. Paper presented at the 2012 SPE Canadian Unconventional Resources Conference, Calgary, Alberta, Canada, SPE 162657. DOI: https://doi.org/10.2118/162657-MS

Barati, R. & Liang, J., 2014. A Review of Fracturing Fluid Systems Used For Hydraulic Fracturing of Oil and Gas Wells. *Journal of Applied Polymer Science*, 131(16). DOI: 10.1002/app.40735

Bowden, F. P. & Tabor, D., 1964. *The Friction and Lubrication of Solids. Part II*, Oxford at the Clarendon Press, London.

Chaffin, K. A., Chen, X., McNamara, L., Bates, F. S. & Hillmyer, M. A., 2014. Polyether Urethane Hydrolytic Stability after Exposure to Deoxygenated Water. *Macromolecules*, 47(15), p. 5220−5226. DOI: https://doi.org/10.1021/ma500904d

Chan-Chan, L. H., Solis-Correa, R., Vargas-Coronado, R. F., Cervantes-Uc, J. M., Cauich-Rodriguez, J. V. et al., 2010. Degradation studies on segmented polyurethanes prepared with HMDI, PCLand different chain extenders. *Acta Biomaterialia*, 6(6), p. 2035–2044. DOI:10.1016/j.actbio.2009.12.010

Chen, J., Wang, J., Han, E., Dong, J. & Ke, W., 2005. Corrosion behavior of AZ91D magnesium alloy in sodium sulfate solution. *Materials and Corrosion*, 57(10), pp. 789-793. DOI: 10.1002/maco.200503959

Chu, C. C., 1981. The in-vitro degradation of poly(glycolic acid) sutures - effect of pH. *Journal of Biomedical Materials Research*, 15(6), pp. 795-804. DOI: https://doi.org/10.1002/jbm.820150604

Clemitson, I., 2008. *CASTABLE POLYURETHANE ELASTOMERS*, [Online] CRC Press, Available at: https://epdf.pub/castable-polyurethane-elastomers.html. [Accessed 5 May 2020].

Duan, P., Sadana, A., Xu, Y., Deng, G. & Pratt, B., 2018. Degradable Packing Element for Low-Temperature Fracturing Applications. Paper presented at the Offshore Technology Conference, Houston, Texas, OTC-28979-MS. DOI: https://doi.org/10.4043/28979-MS

Finšgar, M. & Jackson, J., 2014. Application of corrosion inhibitors for steels in acidic media for the oil and gas industry: A review. *Corrosion Science*, Volume 86, p. 17–41. DOI: http://dx.doi.org/10.1016/j.corsci.2014.04.044

Fontana, M. G., 1986. *Corrosion Engineering*. 3 ed., McGraw-Hill Book Company, Singapore

Fripp, M. & Walton, Z., 2016. Degradable Metal for Use in a Fully Dissolvable Frac Plug. Paper presented at the Offshore Technology Conference, Houston, Texas, OTC-27187-MS. DOI: https://doi.org/10.4043/27187-MS

Fripp, M. & Walton, Z., 2017. Fully Dissolvable Frac Plug Using Dissolvable Elastomeric Elements. Paper presented at the SPE Middle East Oil & Gas Show and Conference, Manama, Kingdom of Bahrain, SPE-183752-MS. DOI: https://doi.org/10.2118/183752-MS

Fripp, M., Walton, Z. & Norman, T., 2017. Fully Dissolvable Fracturing Plug for Low-Temperature Wellbores. Paper presented at the SPE Annual Technical Conference and Exhibition, San Antonio, Texas, SPE-187335-MS. DOI: https://doi.org/10.2118/187335-MS

Garza, R., Sadana, A., Khatiwada, S. & Duan, P., 2017. Novel Degradable Polymeric Composite Balls for Hydraulic Fracturing. Paper presented at the Offshore Technology Conference, Houston, Texas, OTC-27905-MS. DOI: https://doi.org/10.4043/27905-MS

Göktürk, E., Pemba, A. G. & Miller, S. A., 2015. Polyglycolic acid from the direct polymerization of renewable C1 feedstocks. *Polymer Chemistry*, 6(21), p. 3918–3925. DOI: https://doi.org/10.1039/C5PY00230C

González, S., Pellicer, E., Suriñach, S., Baró, M. D. & Sort, J., 2013. Biodegradation and Mechanical Integrity of Magnesium and Magnesium Alloys Suitable for Implants. *Biodegradation - Engineering and Technology*, Rolando Chamy and Francisca Rosenkranz, IntechOpen. DOI: 10.5772/55584. Available at: https://www.intechopen.com/books/biodegradation-engineering-and-technology/biodegradation-and-mechanical-integrity-of-magnesium-and-magnesium-alloys-suitable-for-implants [Accessed 5 May 2020]

Hihara, L. H. & Kondepudi, P. K., 1994. Galvanic corrosion between SiC monofilament and magnesium in NaCl, $NaSO_4$ and $NaNO_3$ solutions for application to metal-matrix composites. *Corrosion Science*, 36(9), pp. 1585-1595. DOI: https://doi.org/10.1016/0010-938X(94)90055-8

Hou, Y., Galland, P., Vanlue, D., Johnson, M., Davies, E. et al., 2014. Performance tests of Boss Hog Frac Plugs under Temperature and Pressure. Paper presented at the Society for the Advancement of Materials and Process Engineering, Orlando, Florida.

Jin, N., Xiao, S. & Zhang, S., 2019. Dissolvable Plug Solution for Offshore Squeeze Cementing Overcoming Downhole Restriction in North Sea. Paper presented at the SPE Subsea Well Intervention Symposium, Galveston, Texas, SPE-197077-MS. DOI: https://doi.org/10.2118/197077-MS

Jin, N. & Zeng, Q., 2017. Dissolvable Tools in Multistage Stimulation. Paper presented at the SPE/IATMI Asia Pacific Oil & Gas Conference and Exhibition, Jakarta, Indonesia, SPE-186184-MS. DOI: https://doi.org/10.2118/186184-MS

Johnson, I. & Liu, H., 2013. A Study on Factors Affecting the Degradation of Magnesium and a Magnesium-Yttrium Alloy for Biomedical Applications. *PLoS ONE*, 8(6), p. e65603. DOI: 10.1371/journal.pone.0065603

Balanaga karthik, B., P.Selvakumar & C.Thangavelu, 2014. Inhibition of Carbon Steel Corrosion by DTPMP-SPT-Zn+2 System. *International Journal of Scientific and Research Publications,*

4(2). Available at: http://www.ijsrp.org/research-paper-0214.php?rp=P262310 [Accessed 8 May 2020]

Keerthivasan, V. K. & Koløy, T. R., 2019. Dissolvable Technology Enhances Operational Efficiency of Offshore Completion Operations on the NCS. Paper presented at the SPE Norway One Day Seminar, Bergen, Norway, SPE-195634-MS. DOI: https://doi.org/10.2118/195634-MS

Khatiwada, S., Duan, P., Garza, R. & Sadana, A. K., 2017. Degradable Thermoset Polymer Composite for Intervention-Less Downhole Tools. Paper presented at the Offshore Technology Conference, Houston, Texas, OTC-27894-MS. DOI: https://doi.org/10.4043/27894-MS

Kim, J. Y., Jing, Z. & Morita, N., 2019. Proppant Transport Studies Using Three Types of Fracture Slot Equipment, Paper presented at the 53rd U.S. Rock Mechanics/Geomechanics Symposium, New York City, New York, ARMA-2019-0273.

Koteeswaran, S., Habibpour, M., Puckette, J., Pashin, J. C. & Clark, P. E., 2018. Characterization of shale–fluid interaction through a series of immersion tests and rheological studies. *Journal of Petroleum Exploration and Production Technology*, Volume 8, p. 1273–1286. DOI: https://doi.org/10.1007/s13202-018-0444-5

Krasowska, K., Heimowska, A. & Rutkowska, M., 2015. Environmental Degradability of Polyurethanes, Thermoplastic Elastomers - Synthesis and Applications, Chapal Kumar Das, IntechOpen. DOI: 10.5772/60925. Available at: https://www.intechopen.com/books/thermoplastic-elastomers-synthesis-and-applications/environmental-degradability-of-polyurethanes [Accessed 5 May 2020]

Kumar, D., Xu, Z. & Chaemchaeng, P., 2018. Applicatino of Degradable Alloys in Gas Lift Valve. Paper presented at the SPE Middle East Artificial Lift Conference and Exhibition, Manama, Bahrain, SPE-192456-MS. DOI: https://doi.org/10.2118/192456-MS

Lehr, I. & Saidman, S., 2018. Corrosion protection of AZ91D magnesium alloy by a cerium-molybdenum coating -The effect of citric acid as an additive. *Journal of Magnesium and Alloys*, 6(4), pp. 356-365. DOI: https://doi.org/10.1016/j.jma.2018.10.002

Li, M., Chen, L., Wei, R., Liao, C. & Fu, T., 2018. The Application of Fully Dissolvable Frac Plug Technique in Weiyuan Gasfield. Paper presented at the SPE Kingdom of Saudi Arabia Annual Technical Symposium and Exhibition, Dammam, Saudi Arabia, SPE-192422-MS. DOI: https://doi.org/10.2118/192422-MS

Liu, M., Uggowitzer, P. J., Schmutz, P. & Atrens, A., 2008. Calculated Phase Diagrams, Iron Tolerance Limits, and Corrosion of Mg-Al Alloys. *Journal of the Minerals, Metals, and Materials Society*, 60(12), pp. 39-44. DOI: 10.1007/s11837-008-0164-2

Luxfer MEL Technologies, 2020. SoluMag® Magnesium Alloy Data sheet. [Online] Available at: https://www.luxfermeltechnologies.com/wp-content/uploads/2019/02/114071-Luxfer-SoluMag-Magnesium-Alloy-DS-SM-1001-0219-ST14.pdf [Accessed 20 March 2020].

Mainier, F., Pegoraro, P. I. F. S. & Santoro, M. V., 2018. Propargyl alcohol as a corrosion inhibitor for AISI 304L stainless steel in hydrochloric acid. *International Journal of Advanced Engineering Research and Science*, 5(10), pp. 168-172. DOI: 10.22161/ijaers.5.10.22

Murphy, M., Turski, M., Warfield, W. & Lyon, P., 2019. The Effect of Changes in Hydraulic Fracking Fluid Chemistries on the Dissolution Rate of Dissolvable Magnesium Frack Plug Components. Paper presented at the SPE Annual Technical Conference and Exhibition, Calgary, Alberta, Canada, SPE-195987-MS. DOI: https://doi.org/10.2118/195987-MS

Nichols, M. & Eis, A., 2017. Self-Removing Fracturing Plugs: A Study of Initial Adoption in the Williston Basin. Paper presented at the SPE Oklahoma City Oil and Gas Symposium, Oklahoma City, Oklahoma, SPE-185107-MS. DOI: https://doi.org/10.2118/185107-MS

Ning, C. et al., 2015. Influence of Surrounding Cations on the Surface Degradation of Magnesium Alloy Implants under a Compressive Pressure. *Langmuir*, 31(50), pp. 13561-13570. DOI: https://doi.org/10.1021/acs.langmuir.5b03699

Okura, M., Saijo, H., Yoshida, K. & Sato, H., 2012. Downhole tool member for hydrocarbon resource recovery. Patent No. US20180298714.

Okura, M., Takahashi, S., Kobayashi, T., Saijo, H. & Takahashi, T., 2015. Improvement of Impact Strength of Polyglycolic Acid for Self-DegradableTools for Low-Temperature Wells. Paper presented at the SPE Middle East Unconventional Resources Conference and Exhibition, Muscat, Oman, SPE-172969-MS. DOI: https://doi.org/10.2118/172969-MS

Peng, Q., Guo, J., Fu, H., Cai, X., Wang, Y. et al., 2014. Degradation behavior of Mg-based biomaterials containing different long-period stacking ordered phases. *Scientific reports*, Volume 4, 3620. DOI: https://doi.org/10.1038/srep03620

Pretsch, T., Jakob, I. & Muller, W., 2009. Hydrolytic degradation and functional stability of a segmented shape memory poly(ester urethane). *Polymer Degradation and Stability*, 94(1), pp. 61-73. DOI: https://doi.org/10.1016/j.polymdegradstab.2008.10.012

Shank, R. A. & McCartney, T. R., 2013. Comparative Study of Commercially Available Propargyl Alcohol-Free Corrosion Inhibitors for Hydrochloric Acid Systems. Paper presented at the NACE INTERNATIONAL CORROSION 2013 CONFERENCE & EXPO, Orlando, Florida

Stevenson, J. S. & Kusy, R. P., 1995. Structural degradation of polyurethane-based elastomeric modules. *Journal of Materials Science: Materials in Medicine*, Volume 6, pp. 377-384. DOI: https://doi.org/10.1007/BF00120277

Sun, Y., 2014. Impact of slickwater fracturing fluid compositions on the petrophysical properties of shale and tightsand: Doctoral Dissertations, Missouri University. Avaliable at: https://scholarsmine.mst.edu/doctoral_dissertations/2359/ [Accessed 8 May 2020]

Swor, L. & Sonnefeld, A., 2006. Self-Removing Frangible Bridge and Fracture Plugs. Paper presented at the SPE Annual Technical Conference and Exhibition, San Antonio, Texas, SPE-102994-MS. DOI: https://doi.org/10.2118/102994-MS

Szycher, M., 2012. Szycher's Handbook of Polyurethanes, 2nd edition, CRC Press LLC, pp. 711-738. Available at: https://ebookcentral.proquest.com/lib/tamucs/detail.action?docID=988755 [Accessed 8 May 2020]

Takahashi, S., Shitsukawa, A. & Okura, M., 2018. Degradation Study on Materials for Dissolvable Frac Plugs. Paper presented at the SPE/AAPG/SEG Unconventional Resources Technology Conference, Houston, Texas, URTEC-2901283-MS. DOI: https://doi.org/10.15530/URTEC-2018-2901283

Takahashi, T., Takahashi, S. & Okura, M., 2016. Development of Degradable Seal Elements for Fully Degradable Frac Plugs. Paper presented at the Offshore Technology Conference Asia, Kuala Lumpur, Malaysia, OTC-26596-MS. DOI: https://doi.org/10.4043/26596-MS

Tu, H., Aviles, I. & Dardis, M., 2019. Degradable Materials for Multi-Stage Stimulation. Paper presented at the Offshore Technology Conference, Houston, Texas, OTC-29282-MS. DOI: https://doi.org/10.4043/29282-MS

U.S. Environmental Protection Agency, 2015. Analysis of Hydraulic Fracturing Fluid Data from the FracFocus Chemical Disclosure Registry 1.0, Washington, D.C., Available at: https://www.epa.gov/hfstudy/analysis-hydraulic-fracturing-fluid-data-fracfocus-chemical-disclosure-registry-1-pdf [Accessed 8 May 2020]

Willberg, D. & Dismuke, K., 2009. Self-destructing filter cake. Patent No. US7482311B2.

Woodard, L. N. & Grunlan, M. A., 2018. Hydrolytic Degradation and Erosion of Polyester Biomaterials. *ACS Macro Letters* , 7(8), pp. 976-982. DOI: https://doi.org/10.1021/acsmacrolett.8b00424

Xie, F., Zhang, T., Bryant, P., Kurusingal, V., Colwell, J. et al., 2019. Degradation and stabilization of polyurethane elastomers. *Progress in Polymer Science*, Volume 90, pp. 211-268. DOI: 10.1016/j.progpolymsci.2018.12.003

Xin, Y., Huo, K., Tao, H., Tang, G. & Chu, P. K., 2008. Influence of aggressive ions on the degradation behavior of biomedical magnesium alloy in physiological environment. *Acta Biomaterialia*, 4(6), pp. 2008-2015. DOI: https://doi.org/10.1016/j.actbio.2008.05.014

Xu, Z., Agrawal, G. & Salinas, B. J., 2011. Smart Nanostructured Materials Deliver High Reliability Completion Tools for Gas Shale Fracturing. Paper presented at the SPE Annual Technical Conference and Exhibition, Denver, Colorado, SPE-146586-MS. DOI: https://doi.org/10.2118/146586-MS

Xu, Z. & Zhang, Z., 2019. The Art of Disintegration – Ten Years in Review of Disintegrable Metals and Downhole Tools. Paper presented at the Offshore Technology Conference, Houston, Texas, OTC-29624-MS. DOI: https://doi.org/10.4043/29624-MS

Yoshimura, K., Matsui, H. & Morita, N., 2014. Development of Polyglycolic and PolylacticAcid Fluid-lossControl Materials for Fracturing Fluids. Paper presented at the SPE International

Symposium and Exhibition on Formation Damage Control, Lafayette, Louisiana, SPE-168179-MS. DOI: https://doi.org/10.2118/168179-MS

Zhang, H. & Zhang, J., 2016. Static and Dynamic Sealing Performance Analysis of Rubber D-Ring Based on FEM. *Journal of Failure Analysis and Prevention*, Volume 16, pp. 165-172. DOI: https://doi.org/10.1007/s11668-016-0066-5

Zhang, Z., Xu, Z. & Salinas, B. J., 2013. In-situ Disintegrating Completion Tools by Means of Controlled Microgalvanic Cells. Paper presented at the SPE Annual Technical Conference and Exhibition, New Orleans, Louisiana, SPE-166237-MS. DOI: https://doi.org/10.2118/166237-MS

Zheng, C., Liu, Y., Wang, H., Qin, J., Chen, C. et al, 2016. Finite element analysis and experimental study on the deformation characteristics of an aluminum alloy fracturing ball. *Journal of Natural Gas Science and Engineering*, Volume 35, Part A, pp. 203-210. DOI: https://doi.org/10.1016/j.jngse.2016.08.037

APPENDIX A

OPTIMIZATION OF MESH SIZE FOR FINITE ELEMENT ANALYSIS

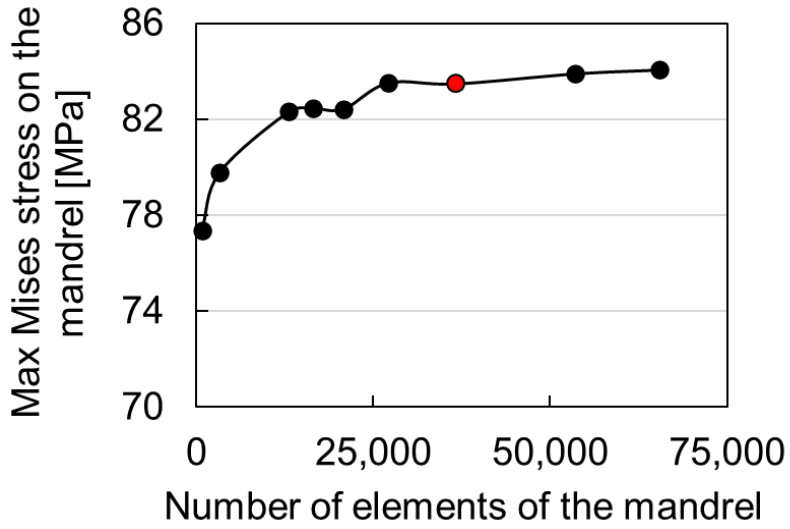

Figure A-1. Optimization of mesh size for FEA of the mandrel neck angle. The maximum Mises stress on the mandrel at 10 mm of displacement for the bottom of mandrel. The red dot indicates the selected mesh size.

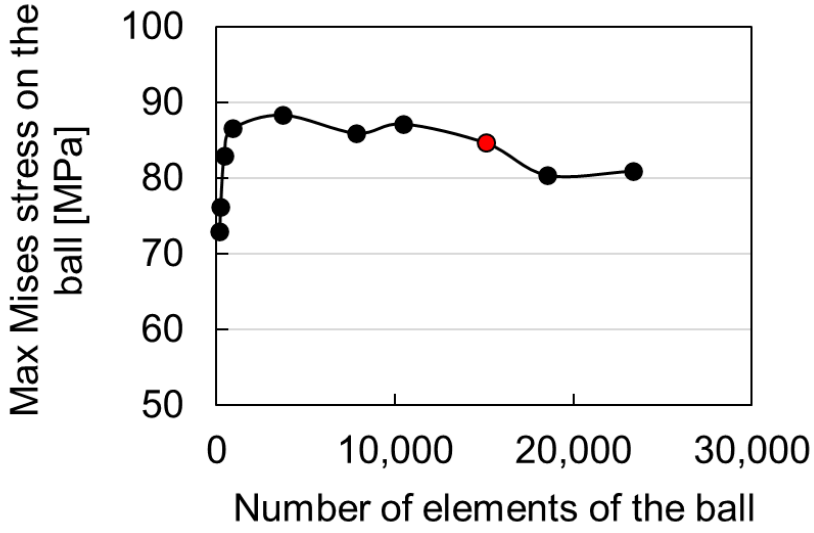

Figure A-2. Optimization of mesh size for FEA of 1.75-inch ball and mandrel. The maximum Mises stress on the ball under 69 MPa. The red dot indicates the selected mesh size.

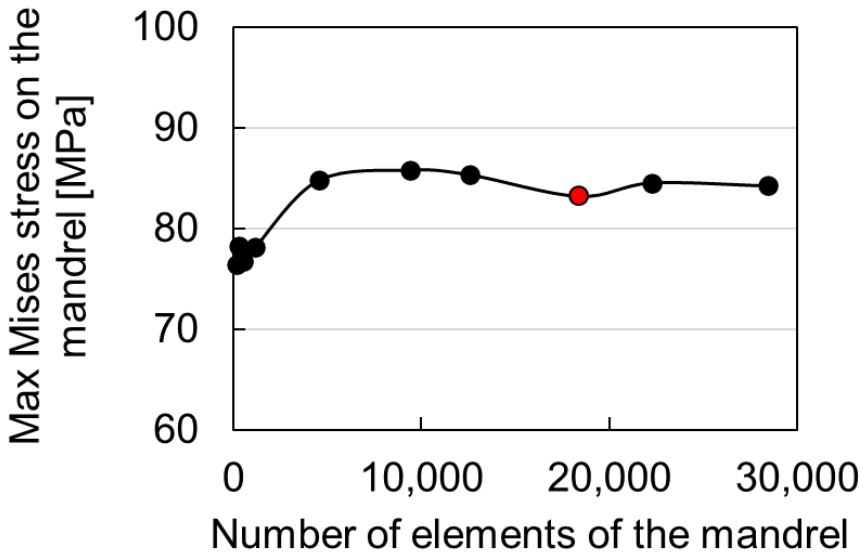

Figure A-3. Optimization of mesh size for FEA of 1.75-inch ball and mandrel. The maximum Mises stress on the mandrel under 69 MPa. The red dot indicates the selected mesh size.

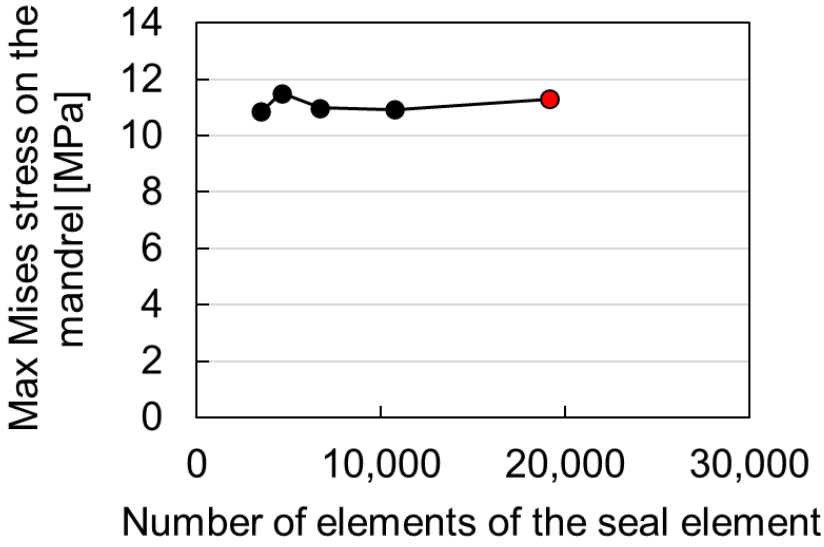

Figure A-4. Optimization of mesh size for FEA of the seal element. The maximum Mises stress on the mandrel at 25 mm of displacement of the upper socket. The red dot indicates selected mesh size.

APPENDIX B

RESULTS OF FINITE ELEMENT ANALYSIS

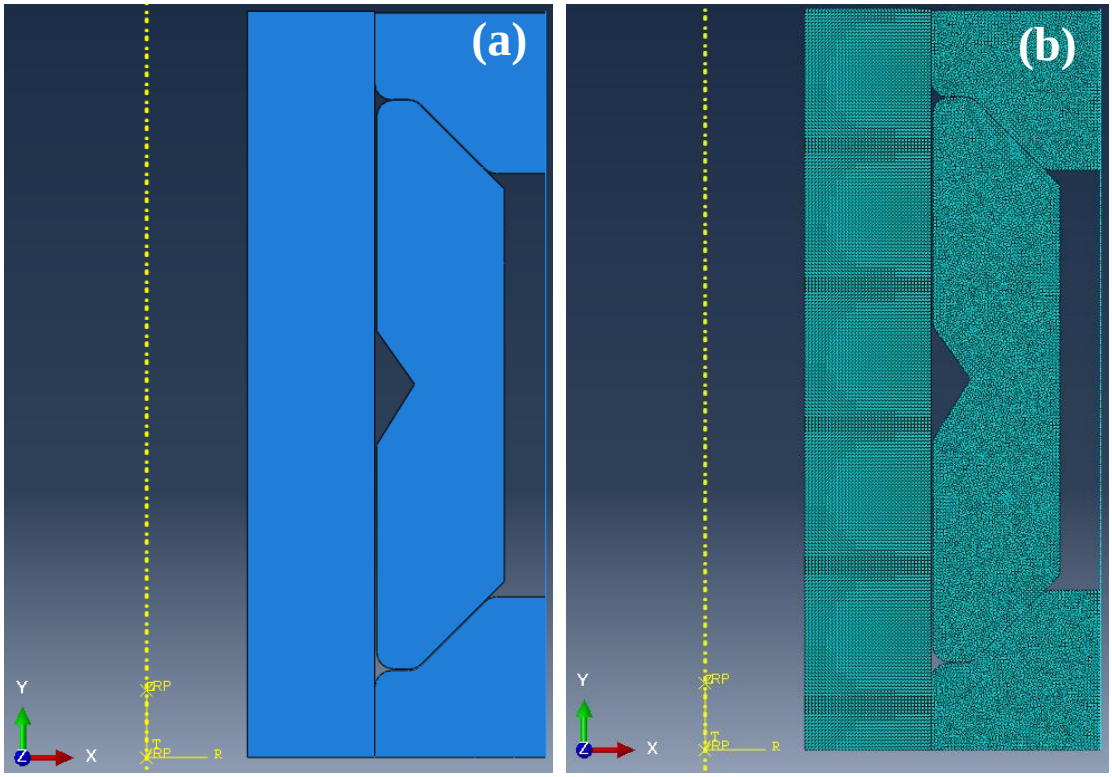

Figure B-1. FEA model and the results of control 1 at 60 MPa of the equivalent pressure: (a) Model, (b) FEA model, (c) Mises stress of the entire model, (d) Mises stress of the mandrel

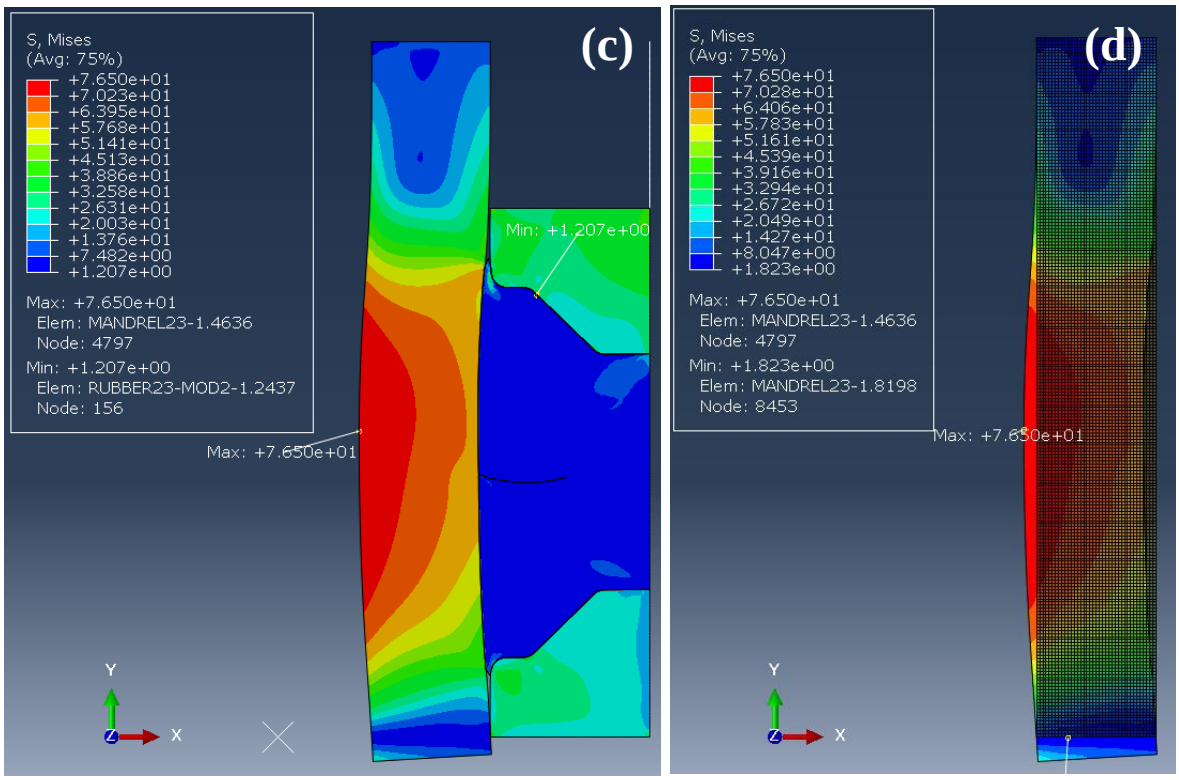

Figure B-1. Continued

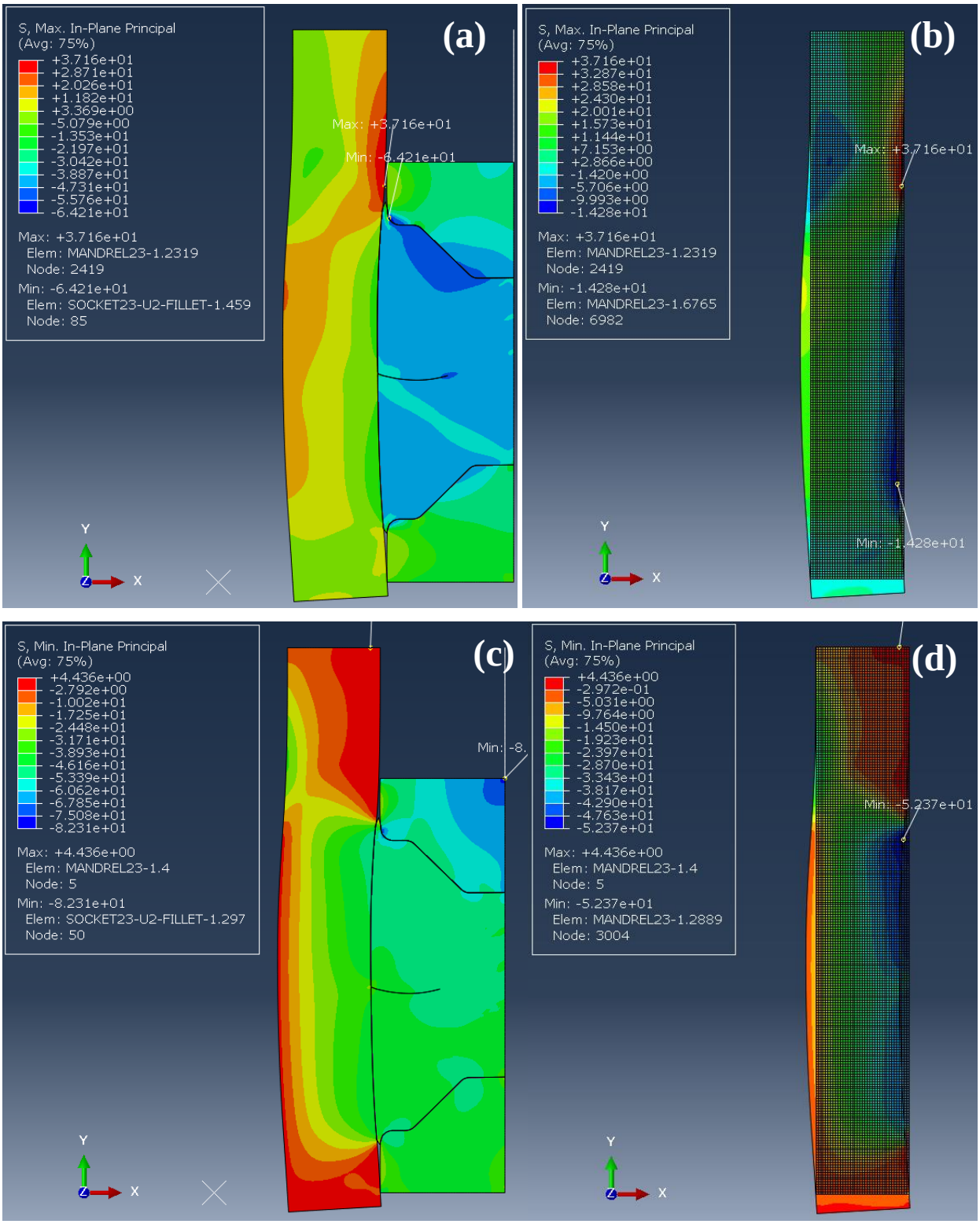

Figure B-2. FEA results of control 1 at 60 MPa of the equivalent pressure: (a)the maximum in-plane principal stress of the entire model, (b) the maximum in-plane principal stress of the mandrel, (c) the minimum in-plane principal stress of the entire model, (d) the minimum in-plane principal stress of the mandrel

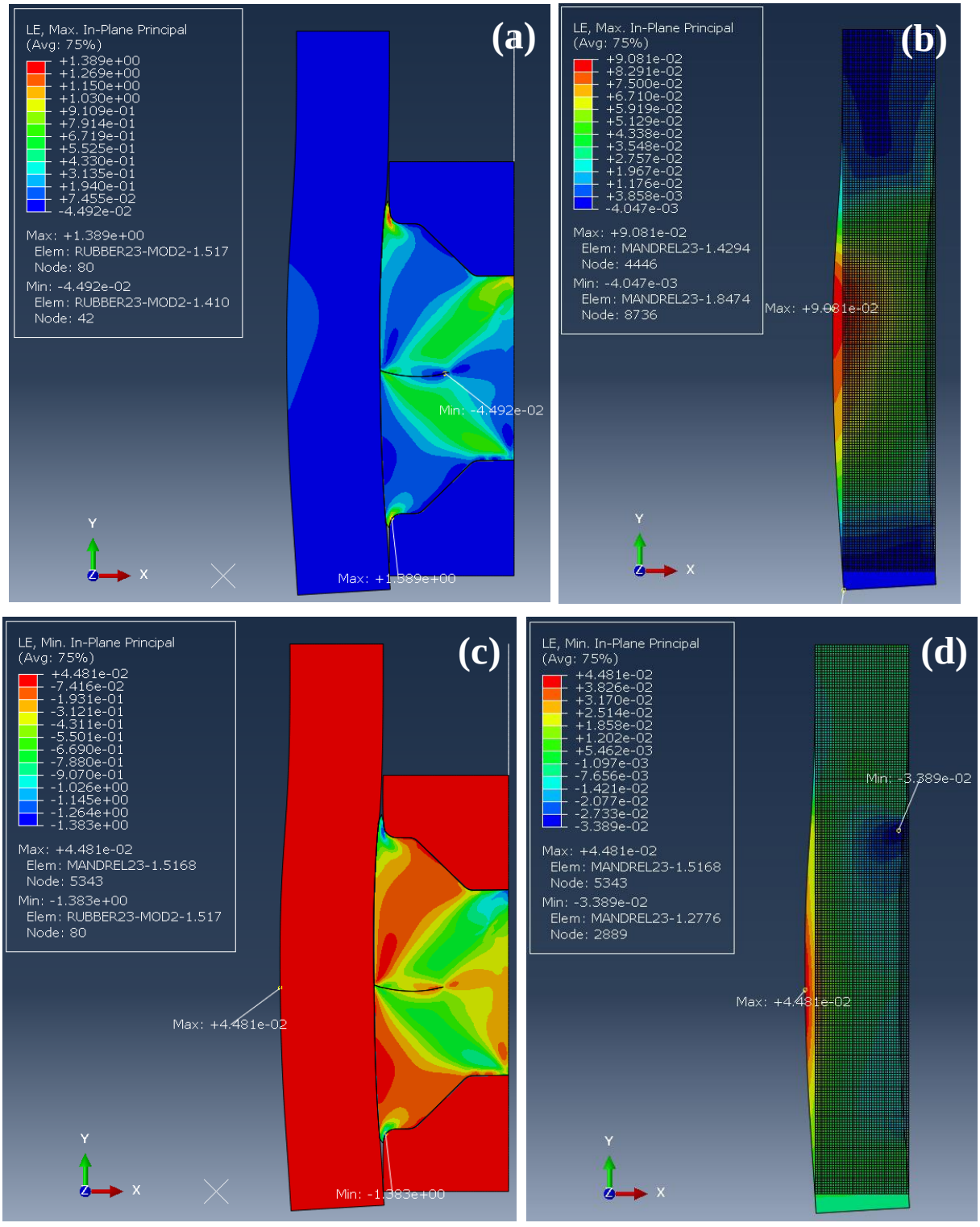

Figure B-3. FEA results of control 1 at 60 MPa of the equivalent pressure: (a) the maximum in-plane principal logarithmic strain of the entire model, (b) the maximum in-plane principal logarithmic strain of the mandrel, (c) the minimum in-plane principal logarithmic strain of the entire model, (d) the minimum in-plane principal logarithmic strain of the mandrel

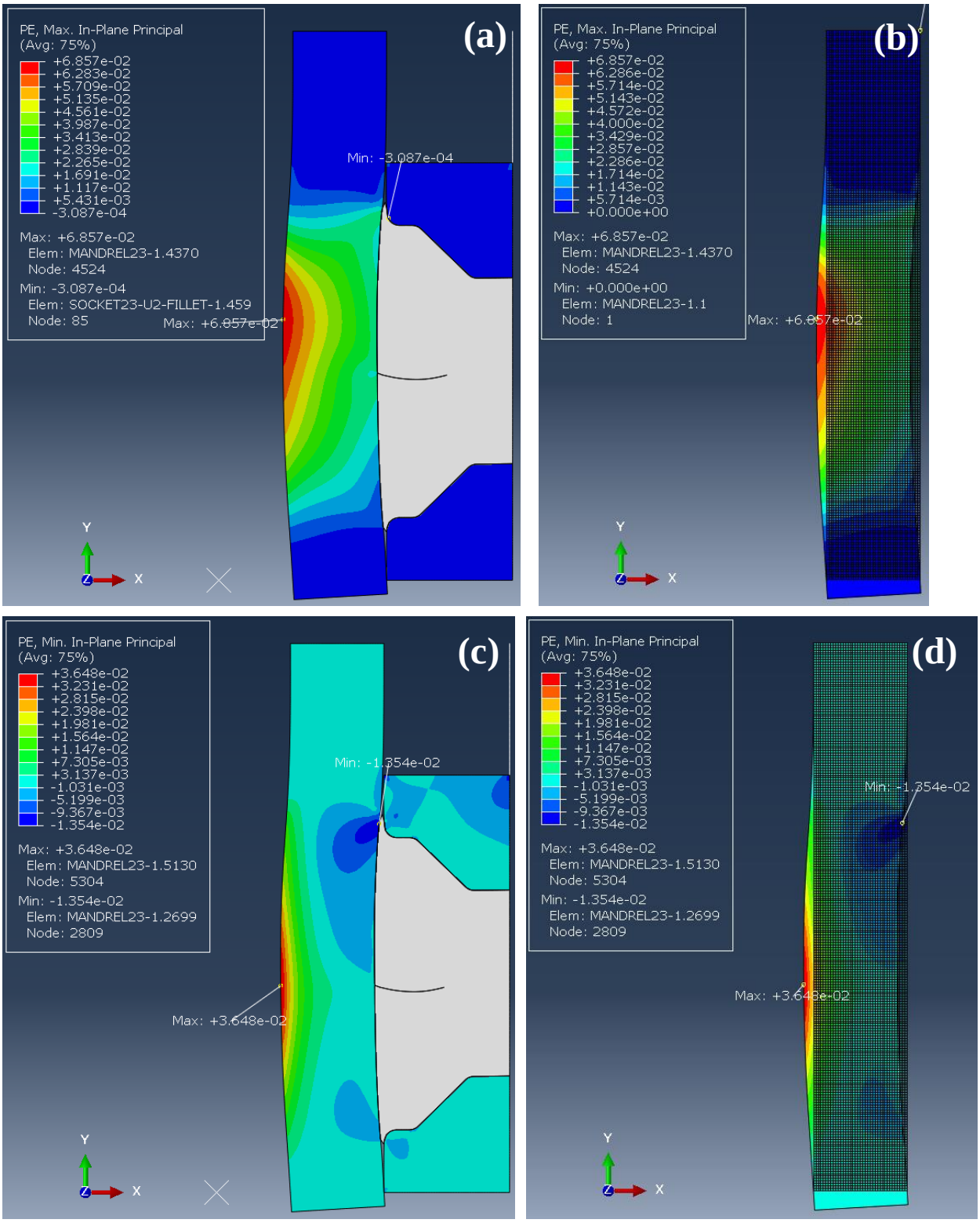

Figure B-4. FEA results of control 1 at 60 MPa of the equivalent pressure: (a) the maximum in-plane principal plastic strain of the entire model, (b) the maximum in-plane principal plastic strain of the mandrel, (c)the minimum in-plane principal plastic strain of the entire model, (d)the minimum in-plane principal plastic strain of the mandrel

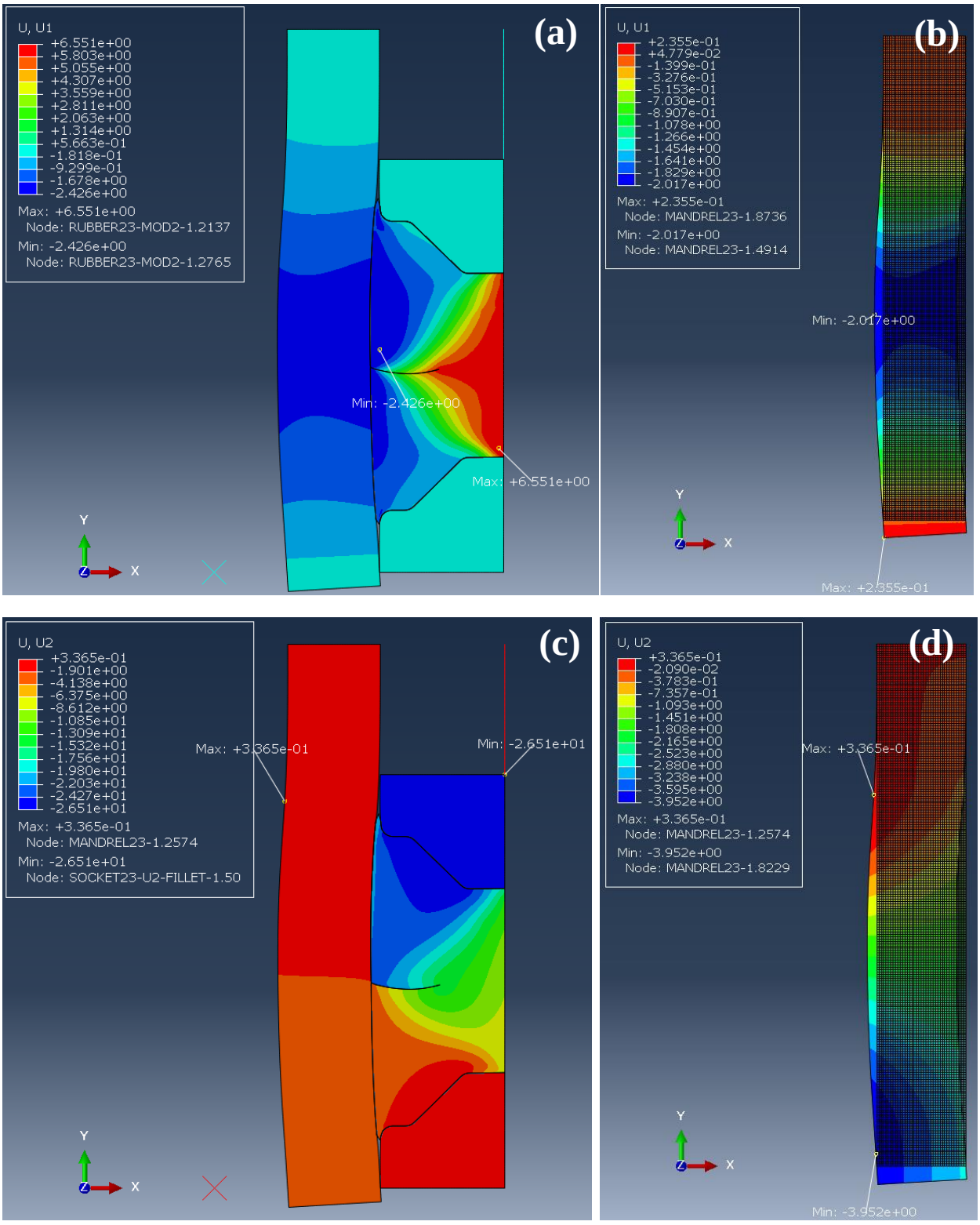

Figure B-5. FEA results of control 1 at 60 MPa of the equivalent pressure: (a) displacement to U1(x-axis) direction of the entire model, (b) displacement to U1(x-axis) direction of the mandrel, (c) displacement to U2(y-axis) direction of the entire model, (d) displacement to U2(y-axis) direction of the mandrel

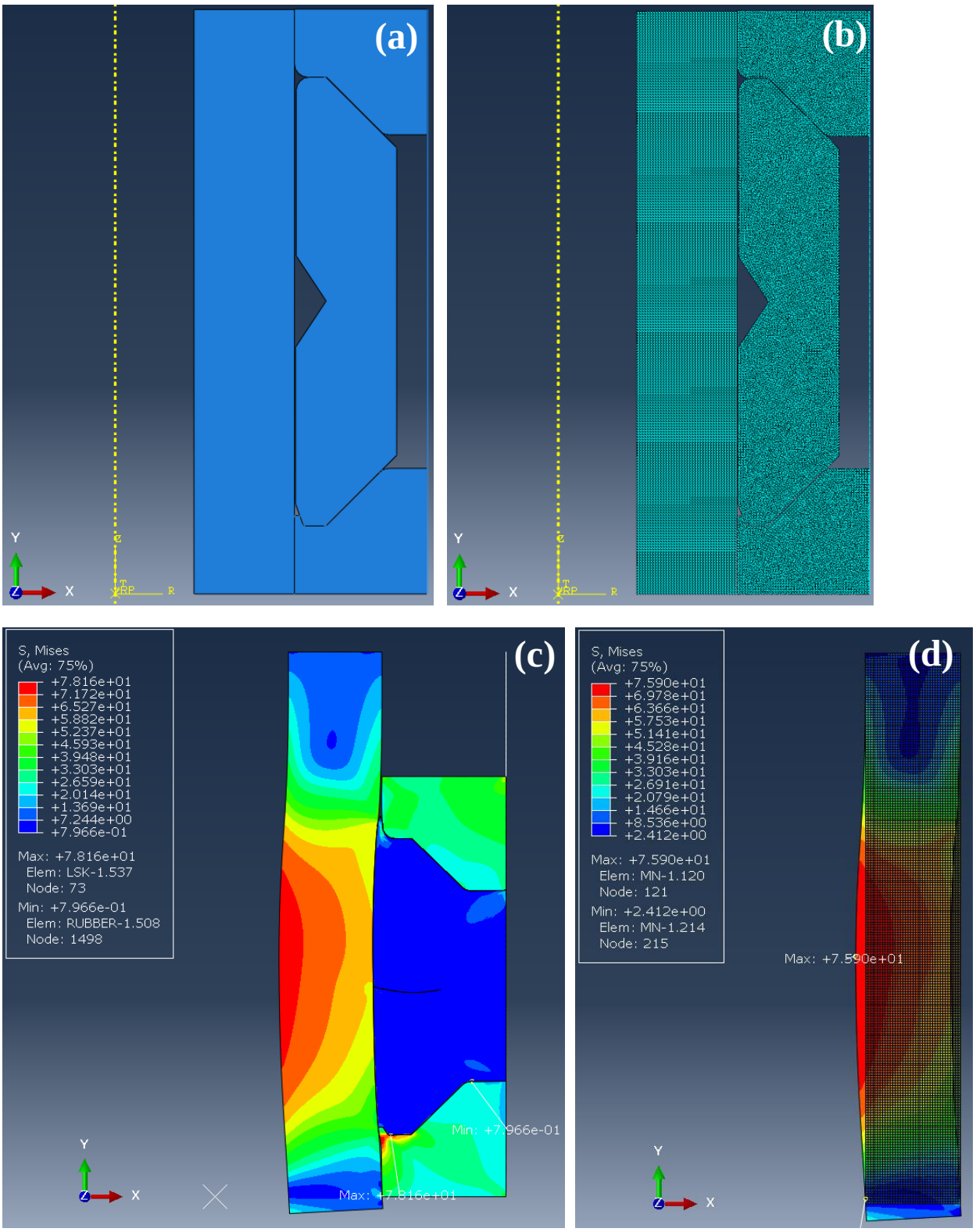

Figure B-6. FEA model and results of model 1 at 60 MPa of the equivalent pressure: (a) Model, (b) FEA model, (c) Mises stress of the entire model, (d) Mises stress of the mandrel

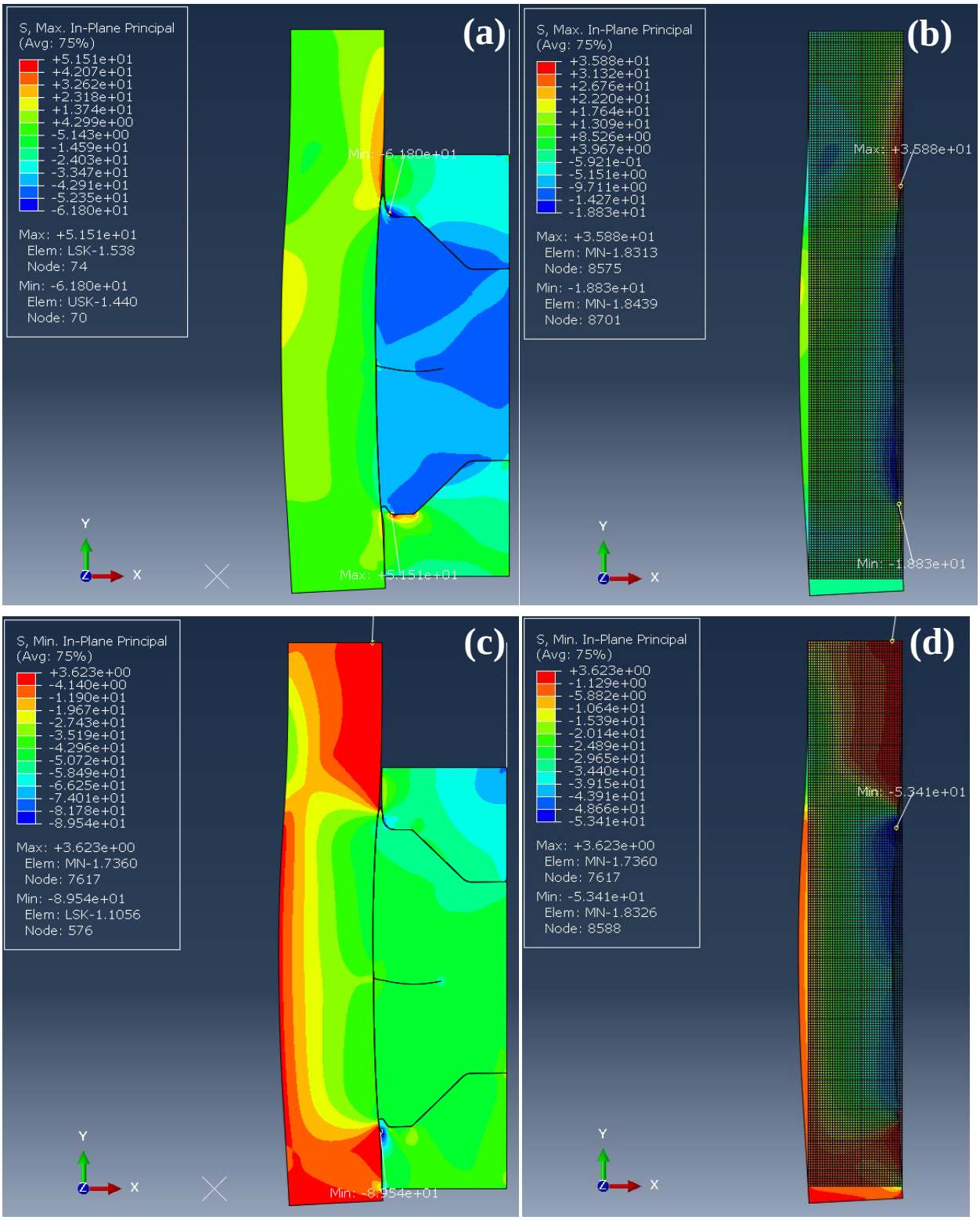

Figure B-7. FEA results of model 1 at 60 MPa of the equivalent pressure: (a) the maximum in-plane principal stress of the entire model, (b) the maximum in-plane principal stress of the mandrel, (c) the minimum in-plane principal stress of the entire model, (d) the minimum in-plane principal stress of the mandrel

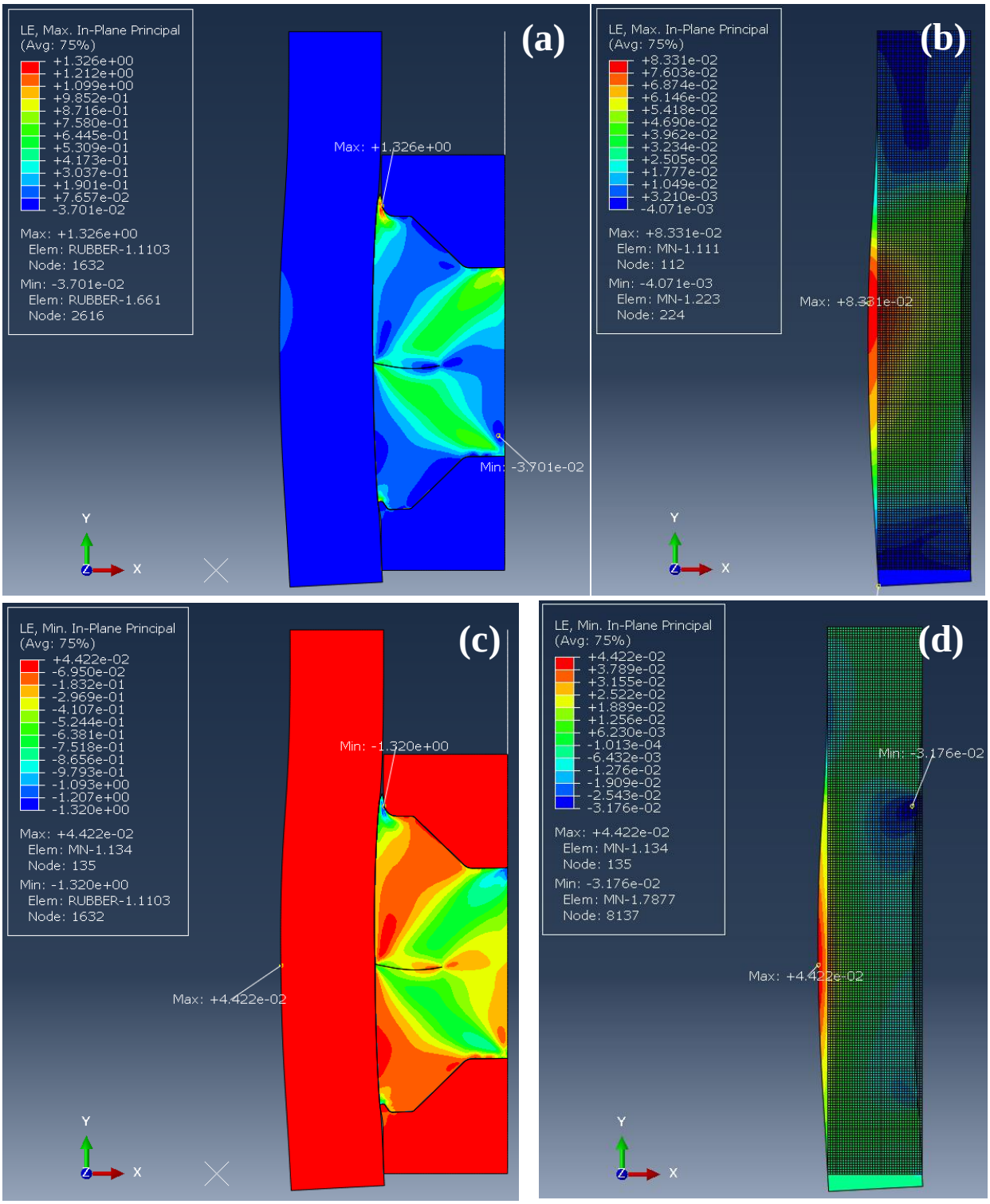

Figure B-8. FEA results of model 1 at 60 MPa of the equivalent pressure: (a) the maximum in-plane principal logarithmic strain of the entire model, (b) the maximum in-plane principal logarithmic strain of the mandrel, (c) the minimum in-plane principal logarithmic strain of the entire model, (d) the minimum in-plane principal logarithmic strain of the mandrel

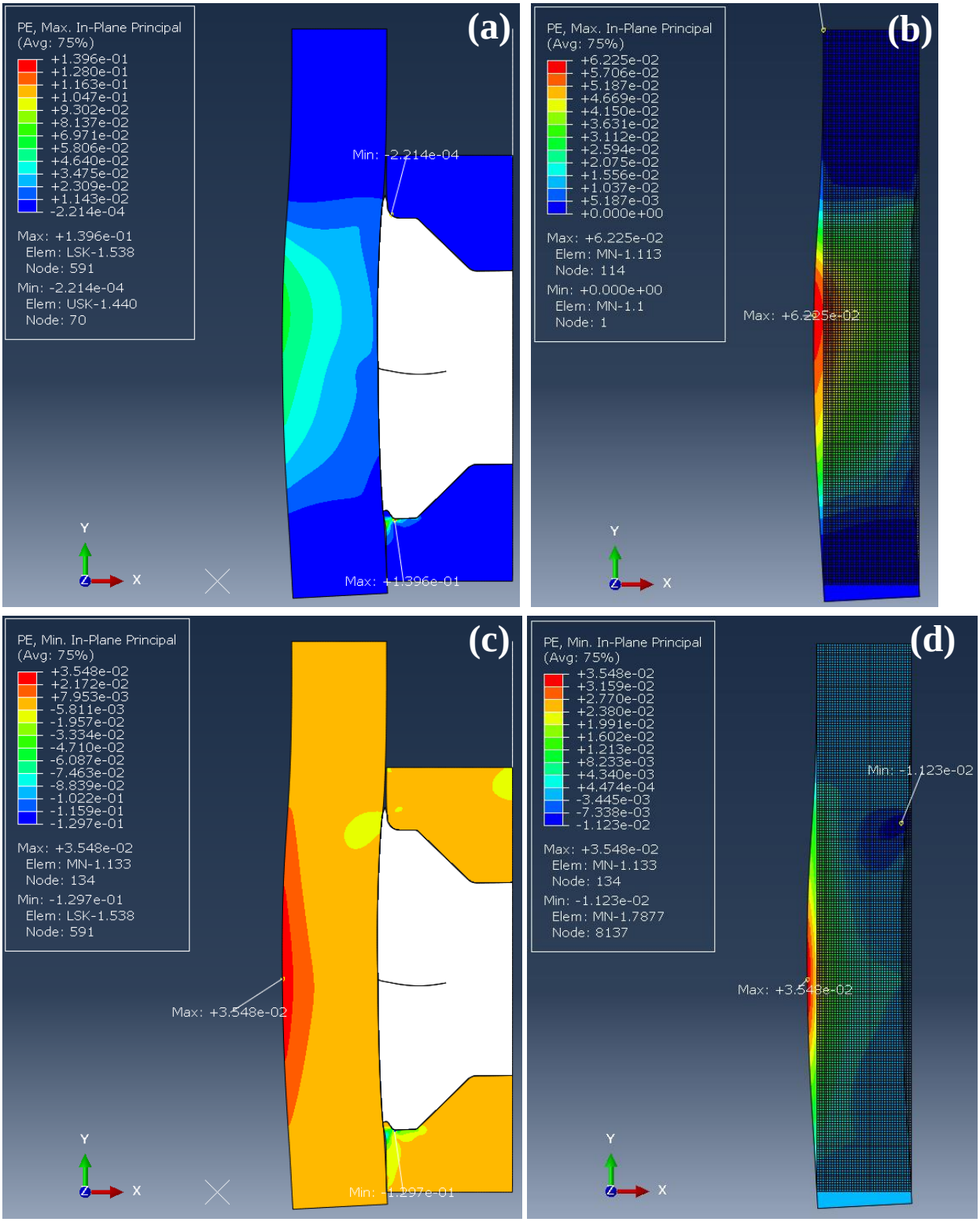

Figure B-9. FEA results of model 1 at 60 MPa of the equivalent pressure: (a) the maximum in-plane principal plastic strain of the entire model, (b) the maximum in-plane principal plastic strain of the mandrel, (c) the minimum in-plane principal plastic strain of the entire model, (d) the minimum in-plane principal plastic strain of the mandrel

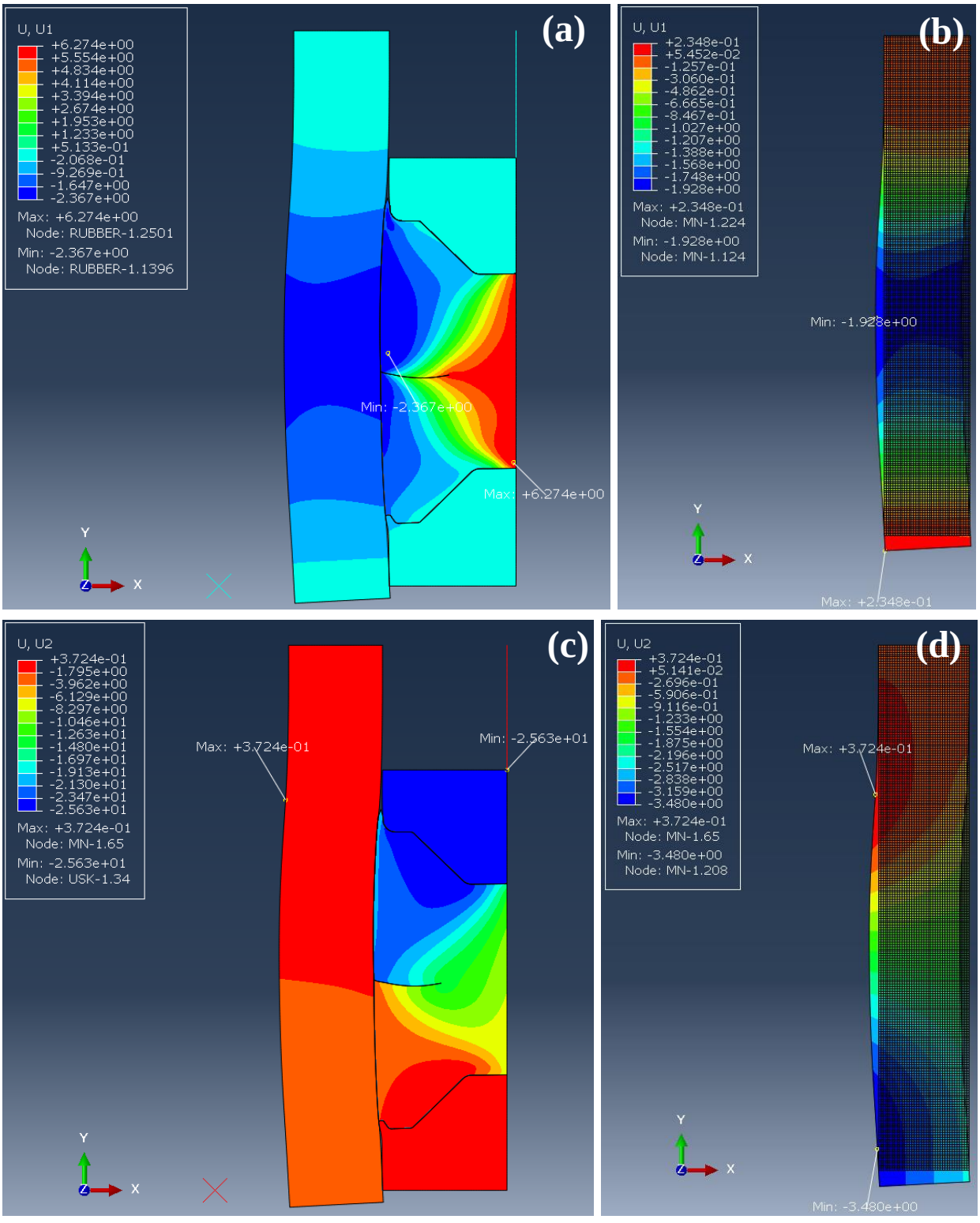

Figure B-10. FEA results of model 1 at 60 MPa of the equivalent pressure: (a) displacement to U1(x-axis) direction of the entire model, (b) displacement to U1(x-axis) direction of the mandrel, (c) displacement to U2(y-axis) direction of the entire model, (d) displacement to U2(y-axis) direction of the mandrel

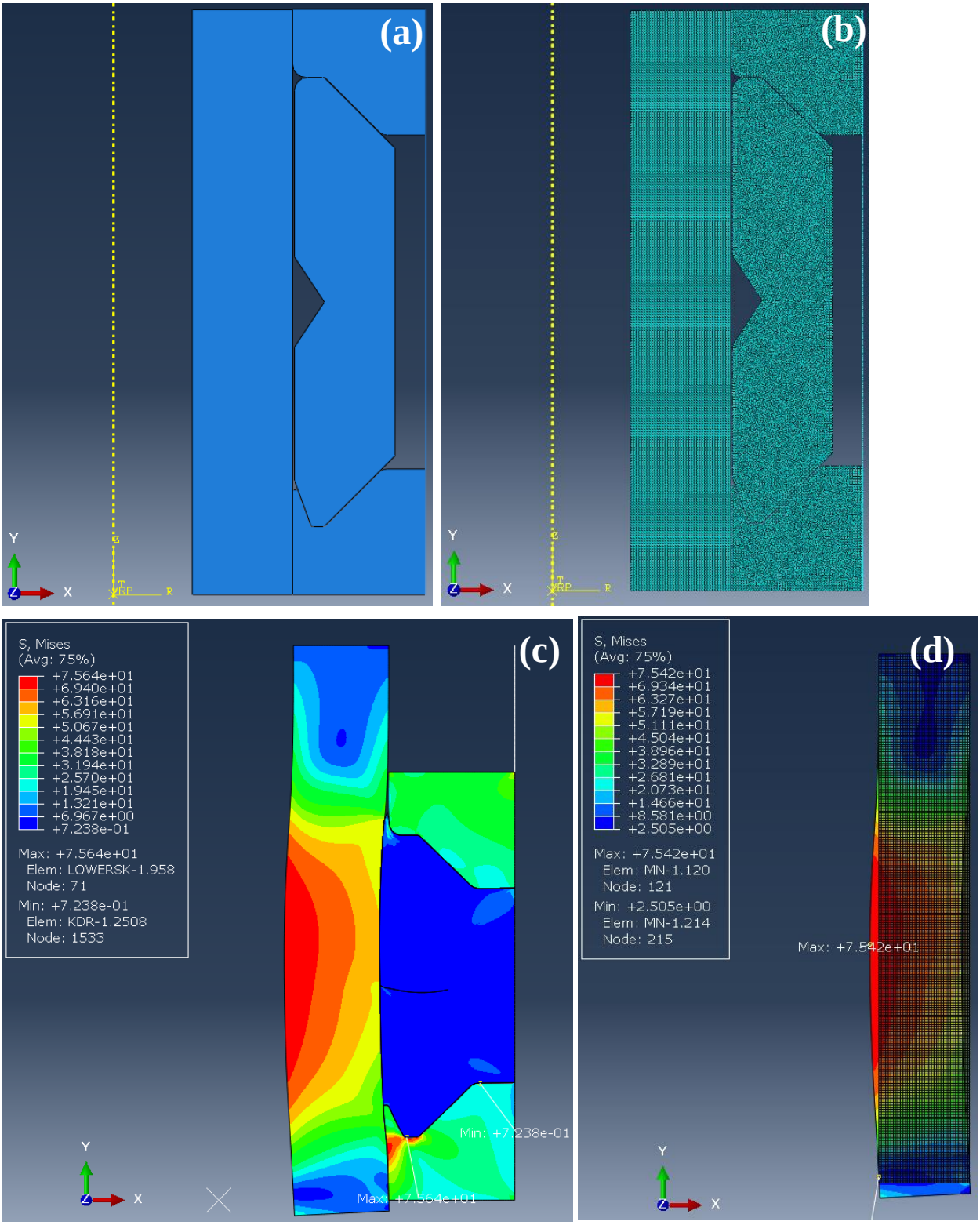

Figure B-11. FEA model and results of model 2 at 60 MPa of the equivalent pressure: (a) Model, (b) FEA model, (c) Mises stress of the entire model, (d) Mises stress of the mandrel

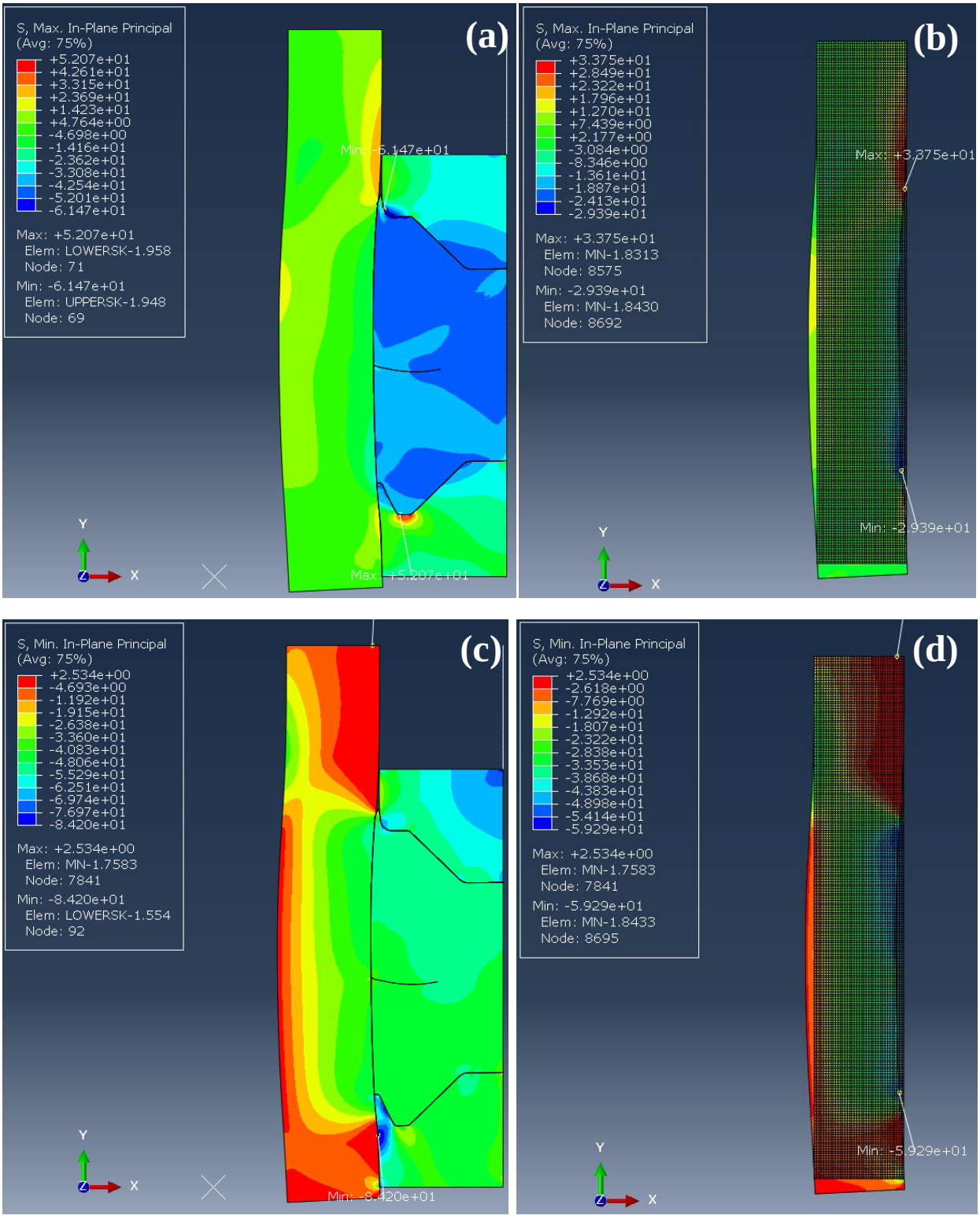

Figure B-12. FEA results of model 2 at 60 MPa of the equivalent pressure: (a) the maximum in-plane principal stress of the entire model, (b) the maximum in-plane principal stress of the mandrel, (c) the minimum in-plane principal stress of the entire model, (d) the minimum in-plane principal stress of the mandrel

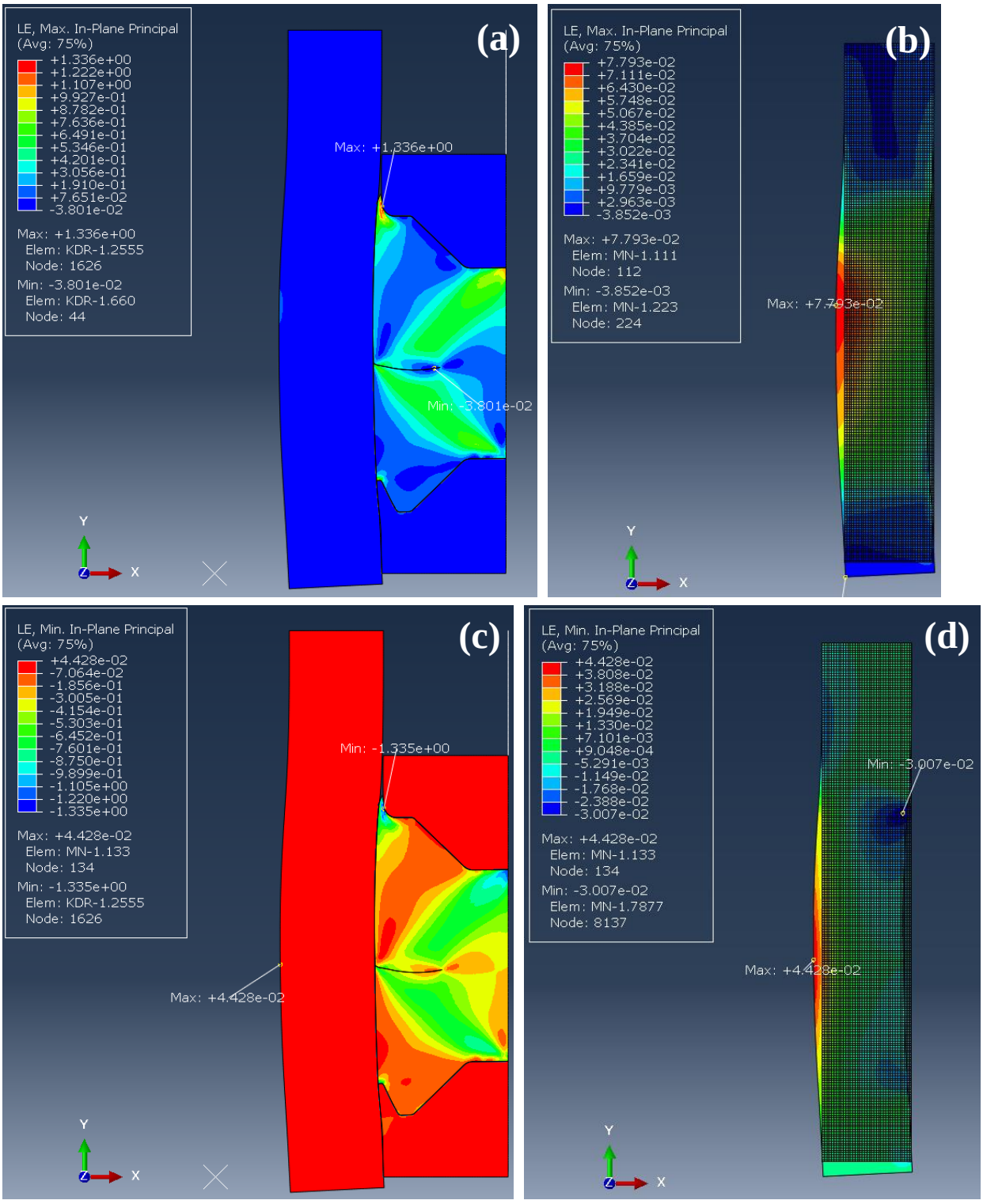

Figure B-13. FEA results of model 2 at 60 MPa of the equivalent pressure: (a) the maximum in-plane principal logarithmic strain of the entire model, (b) the maximum in-plane principal logarithmic strain of the mandrel, (c) the minimum in-plane principal logarithmic strain of the entire model, (d) the minimum in-plane principal logarithmic strain of the mandrel

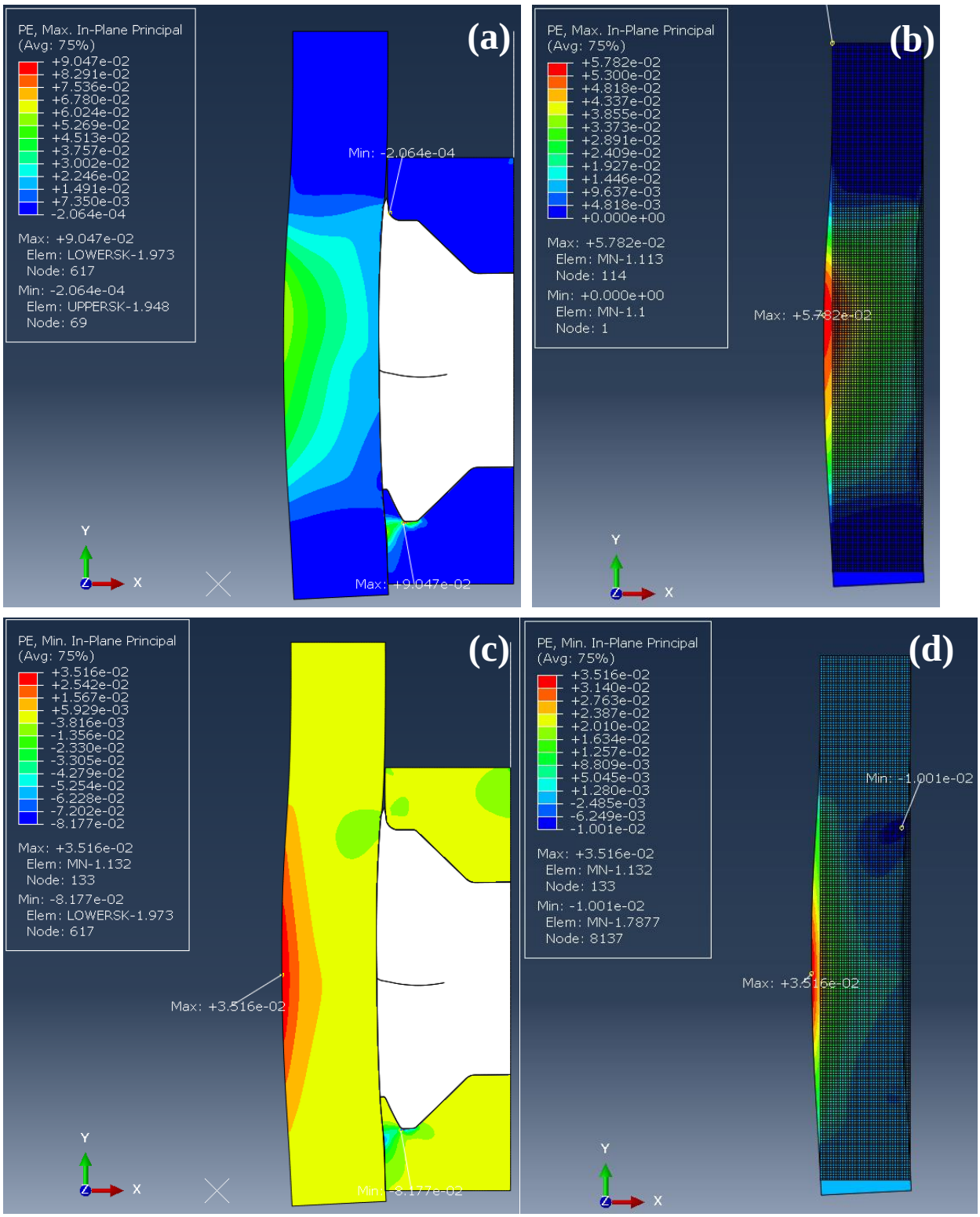

Figure B-14. FEA results of model 2 at 60 MPa of the equivalent pressure: (a) the maximum in-plane principal plastic strain of the entire model, (b) the maximum in-plane principal plastic strain of the mandrel, (c) the minimum in-plane principal plastic strain of the entire model, (d) the minimum in-plane principal plastic strain of the mandrel

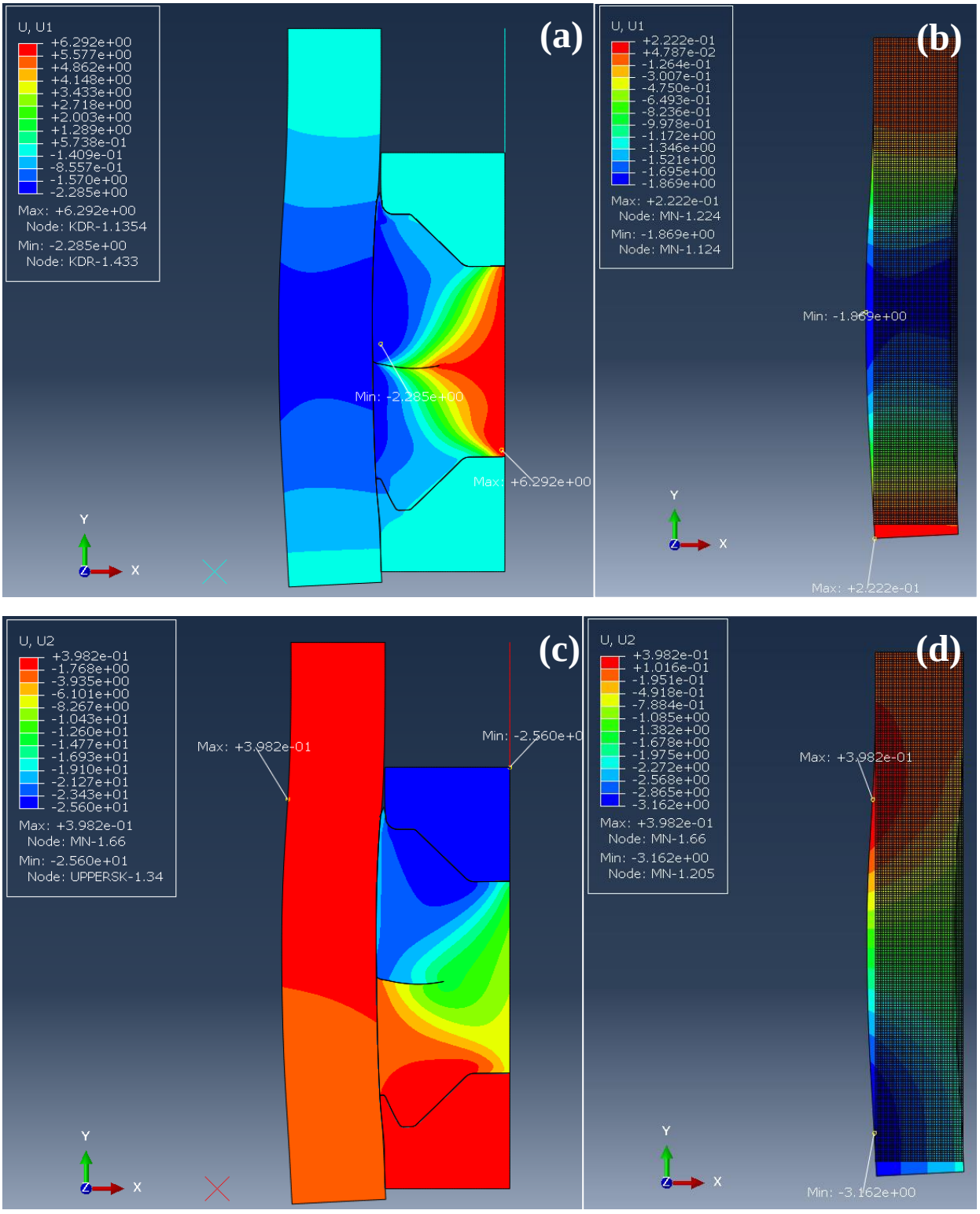

Figure B-15. FEA results of model 2 at 60 MPa of the equivalent pressure: (a) displacement to U1(x-axis) direction of the entire model, (b) displacement to U1(x-axis) direction of the mandrel, (c) displacement to U2(y-axis) direction of the entire model, (d) displacement to U2(y-axis) direction of the mandrel

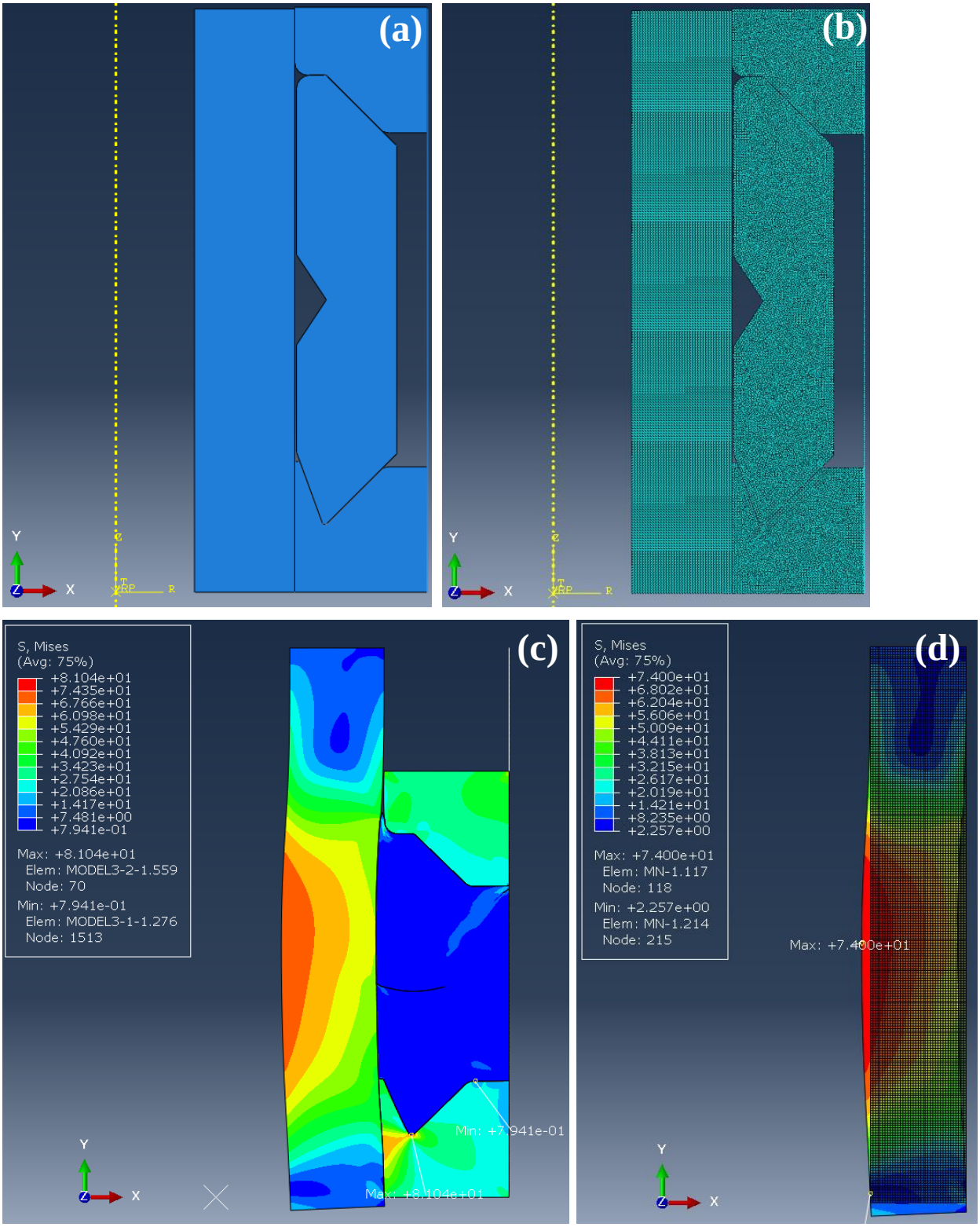

Figure B-16. FEA model and results of model 3 at 60 MPa of the equivalent pressure: (a) Model, (b) FEA model, (c) Mises stress of the entire model, (d) Mises stress of the mandrel

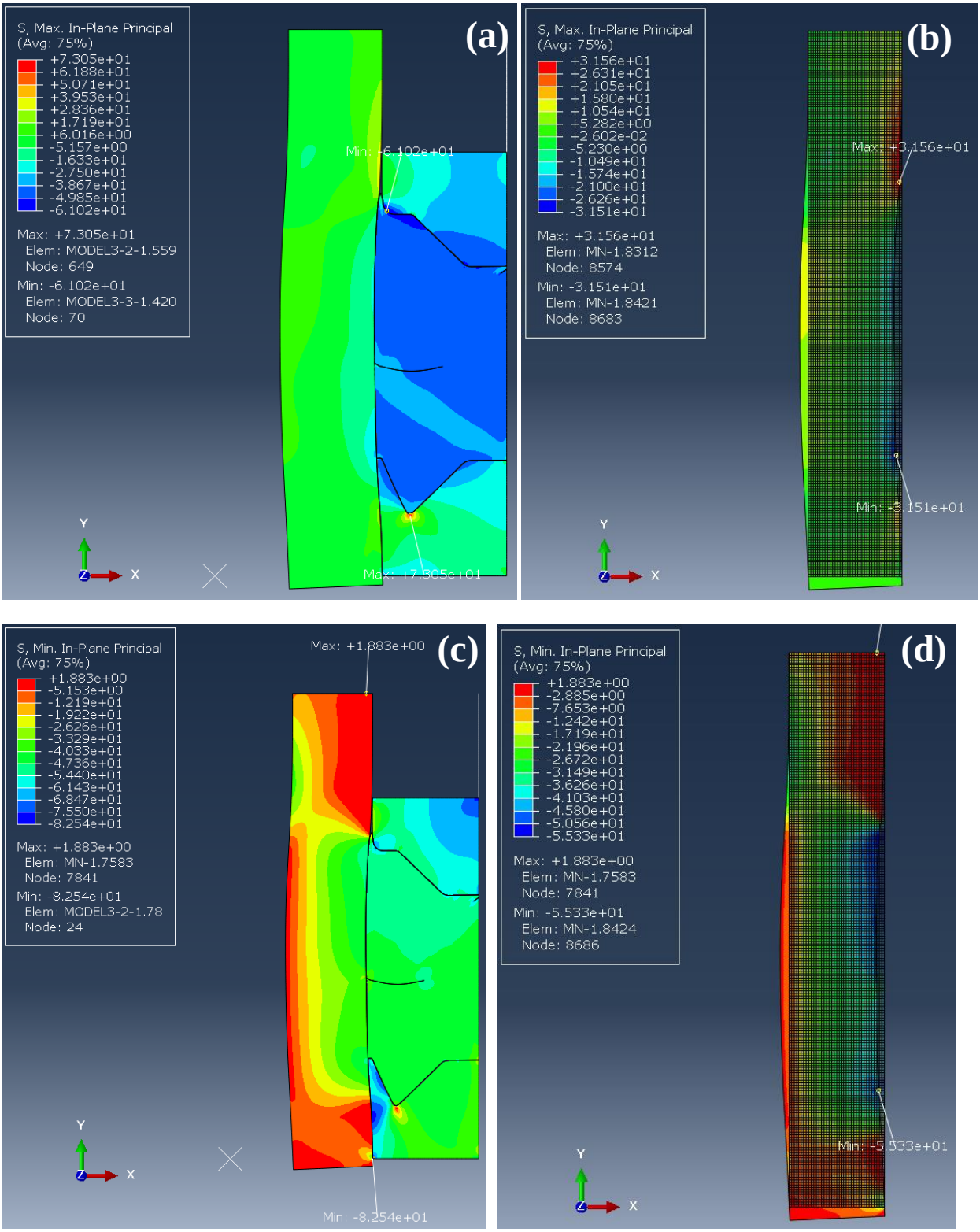

Figure B-17. FEA results of model 3 at 60 MPa of the equivalent pressure: (a) the maximum in-plane principal stress of the entire model, (b) the maximum in-plane principal stress of the mandrel, (c) the minimum in-plane principal stress of the entire model, (d) the minimum in-plane principal stress of the mandrel

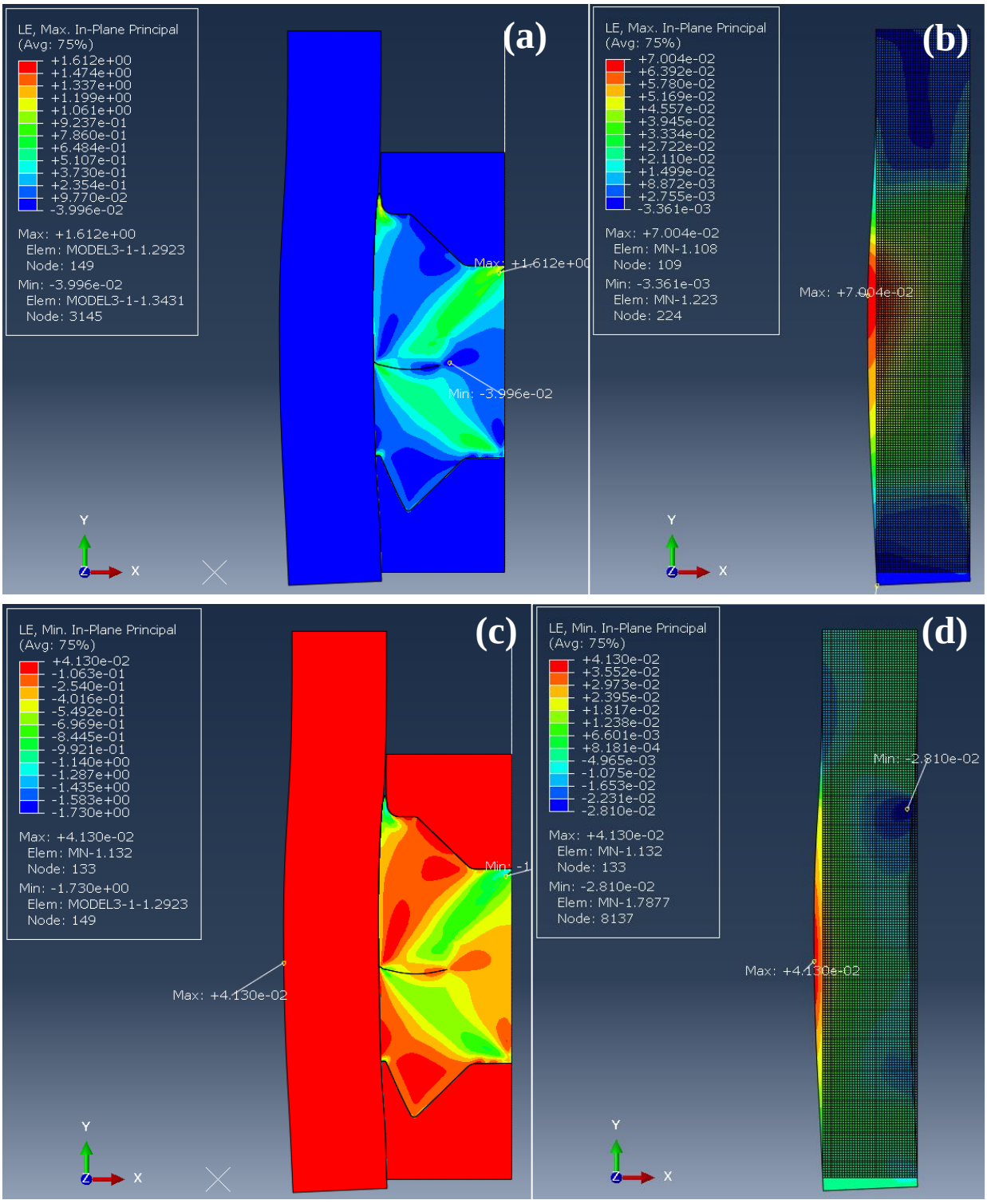

Figure B-18. FEA results of model 3 at 60 MPa of the equivalent pressure: (a) the maximum in-plane principal logarithmic strain of the entire model, (b) the maximum in-plane principal logarithmic strain of the mandrel, (c) the minimum in-plane principal logarithmic strain of the entire model, (d) the minimum in-plane principal logarithmic strain of the mandrel

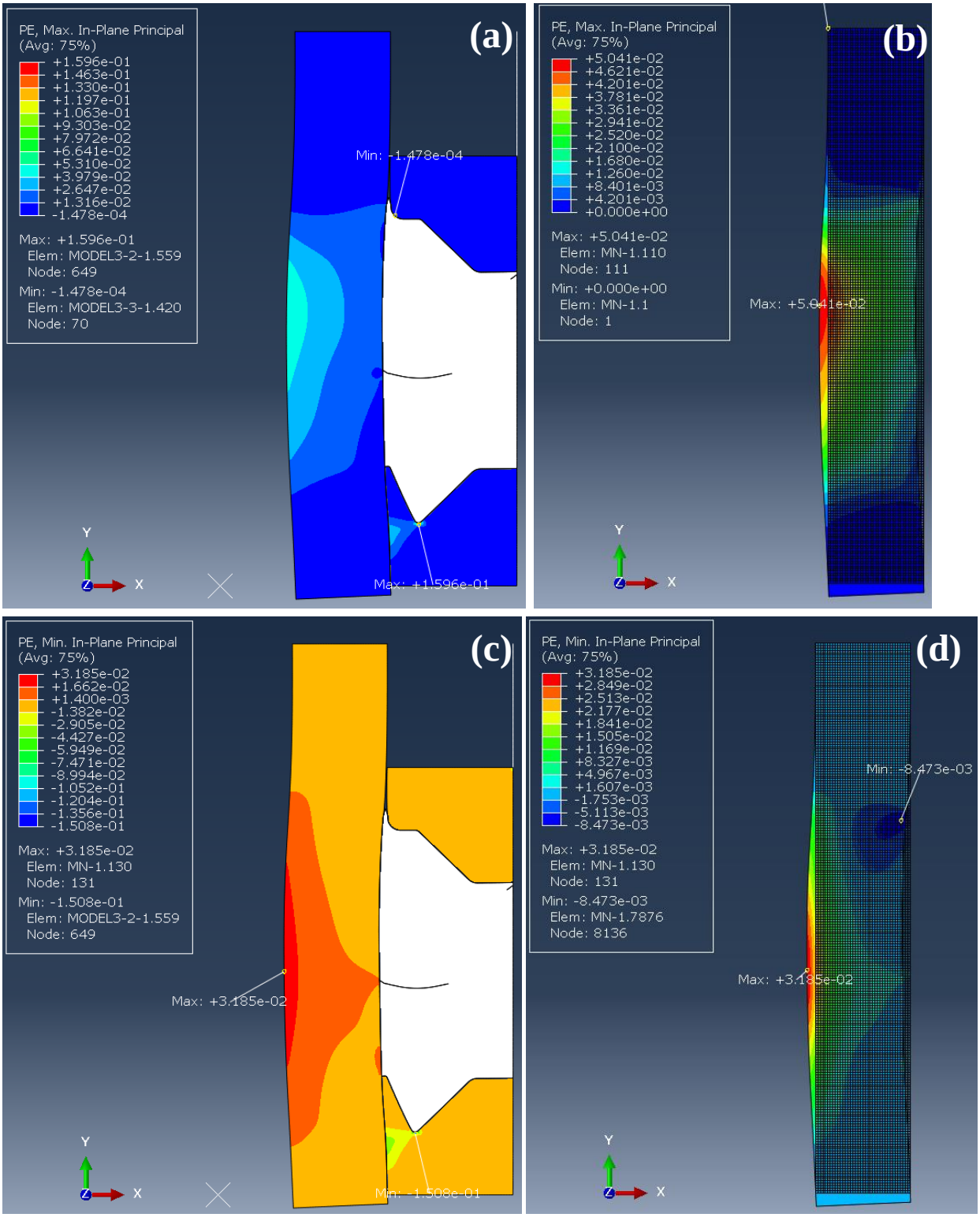

Figure B-19. FEA results of model 3 at 60 MPa of the equivalent pressure: (a) the maximum in-plane principal plastic strain of the entire model, (b) the maximum in-plane principal plastic strain of the mandrel, (c) the minimum in-plane principal plastic strain of the entire model, (d) the minimum in-plane principal plastic strain of the mandrel

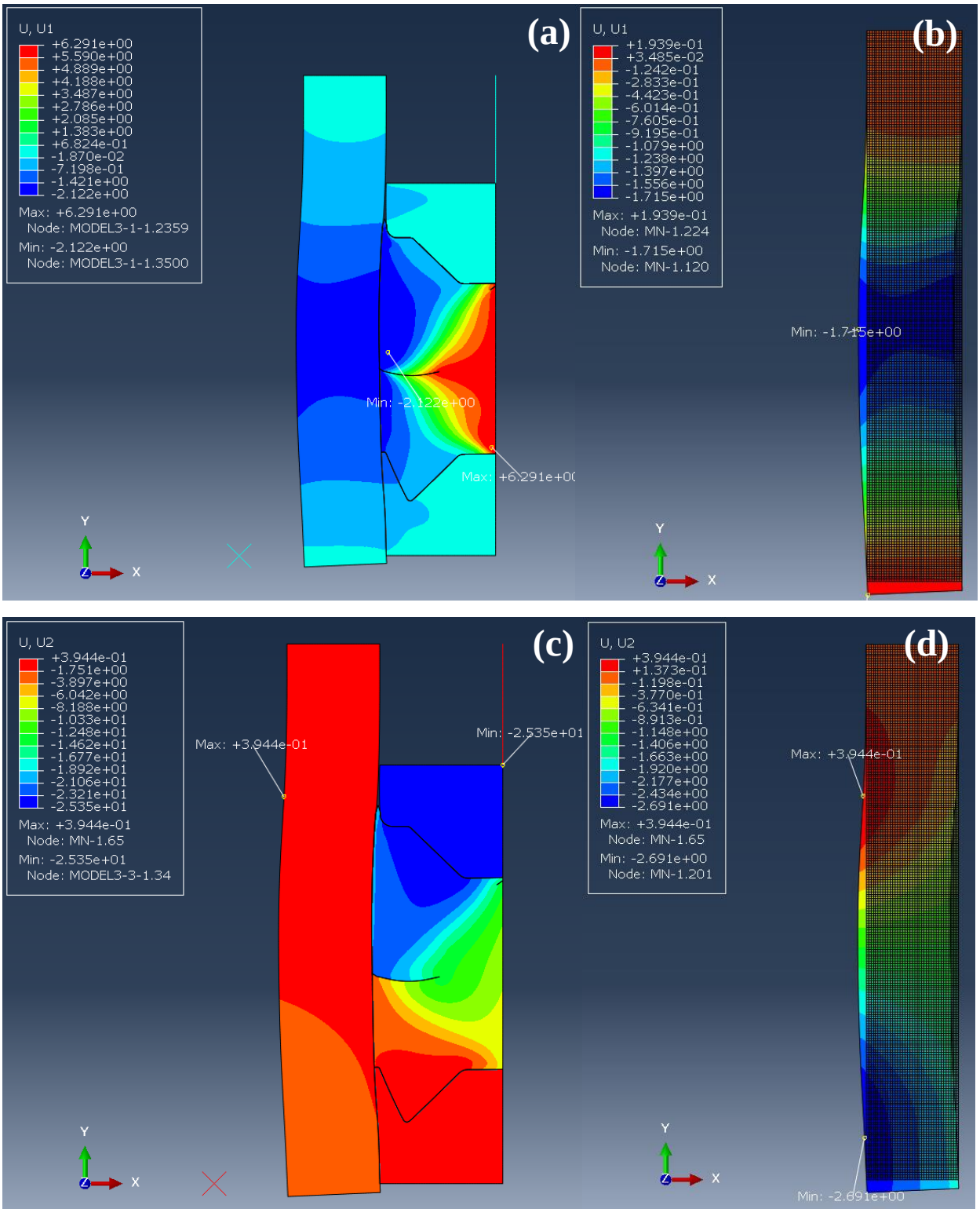

Figure B-20. FEA results of model 3 at 60 MPa of the equivalent pressure: (a) displacement to U1(x-axis) direction of the entire model, (b) displacement to U1(x-axis) direction of the mandrel, (c) displacement to U2(y-axis) direction of the entire model, (d) displacement to U2(y-axis) direction of the mandrel

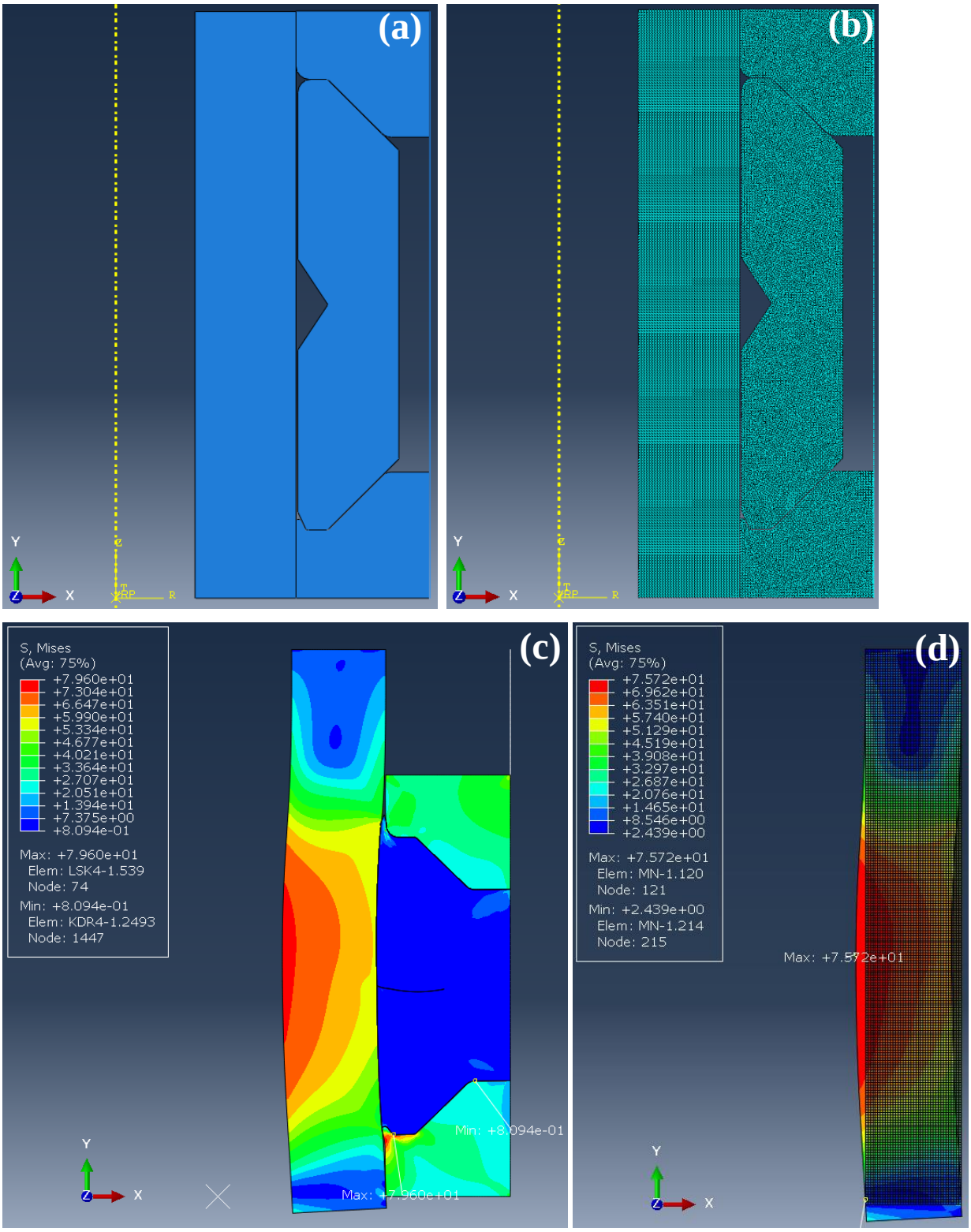

Figure B-21. FEA model and results of model 4 at 60 MPa of the equivalent pressure: (a) Model, (b) FEA model, (c) Mises stress of the entire model, (d) Mises stress of the mandrel

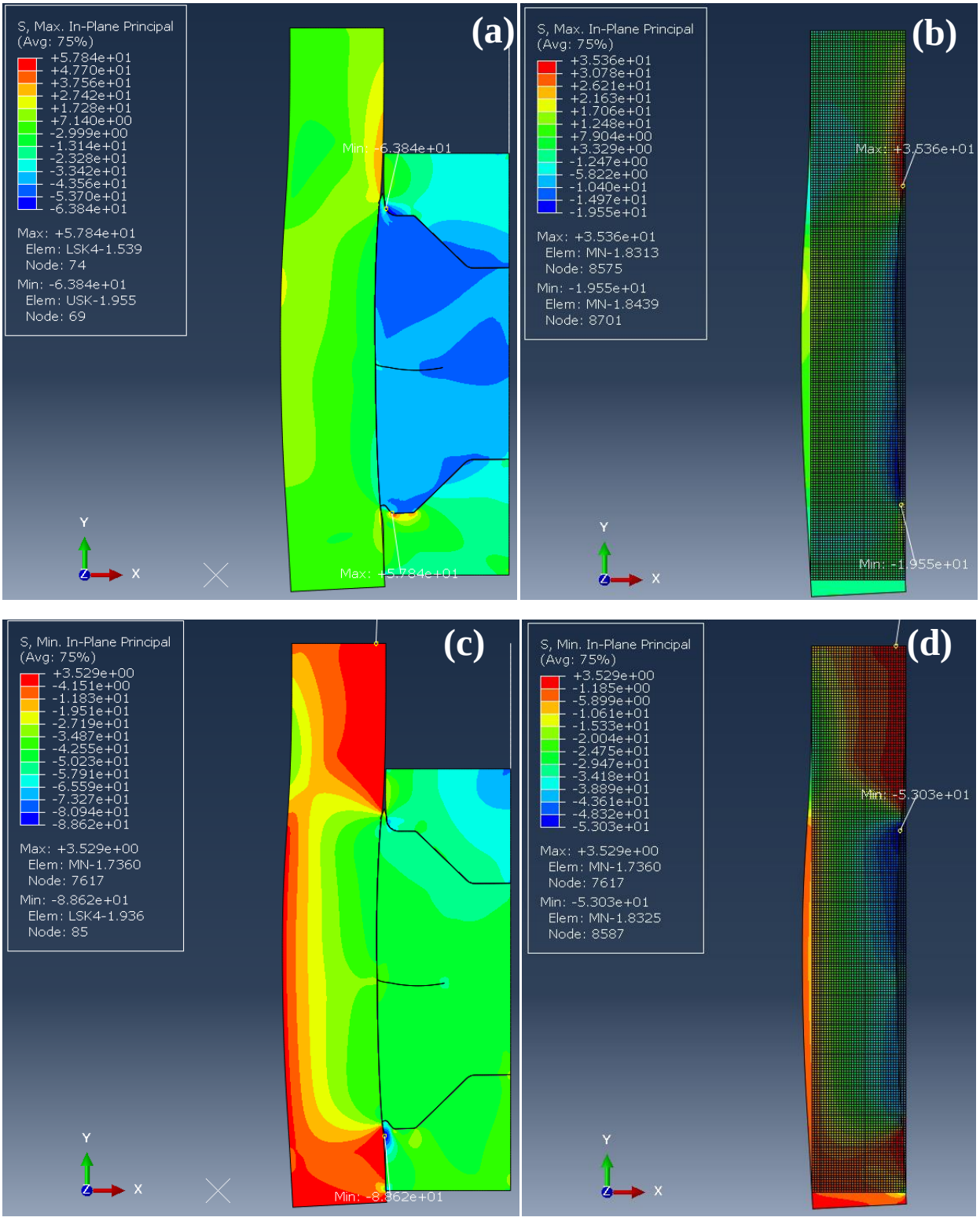

Figure B-22. FEA results of model 4 at 60 MPa of the equivalent pressure: (a) the maximum in-plane principal stress of the entire model, (b) the maximum in-plane principal stress of the mandrel, (c) the minimum in-plane principal stress of the entire model, (d) the minimum in-plane principal stress of the mandrel

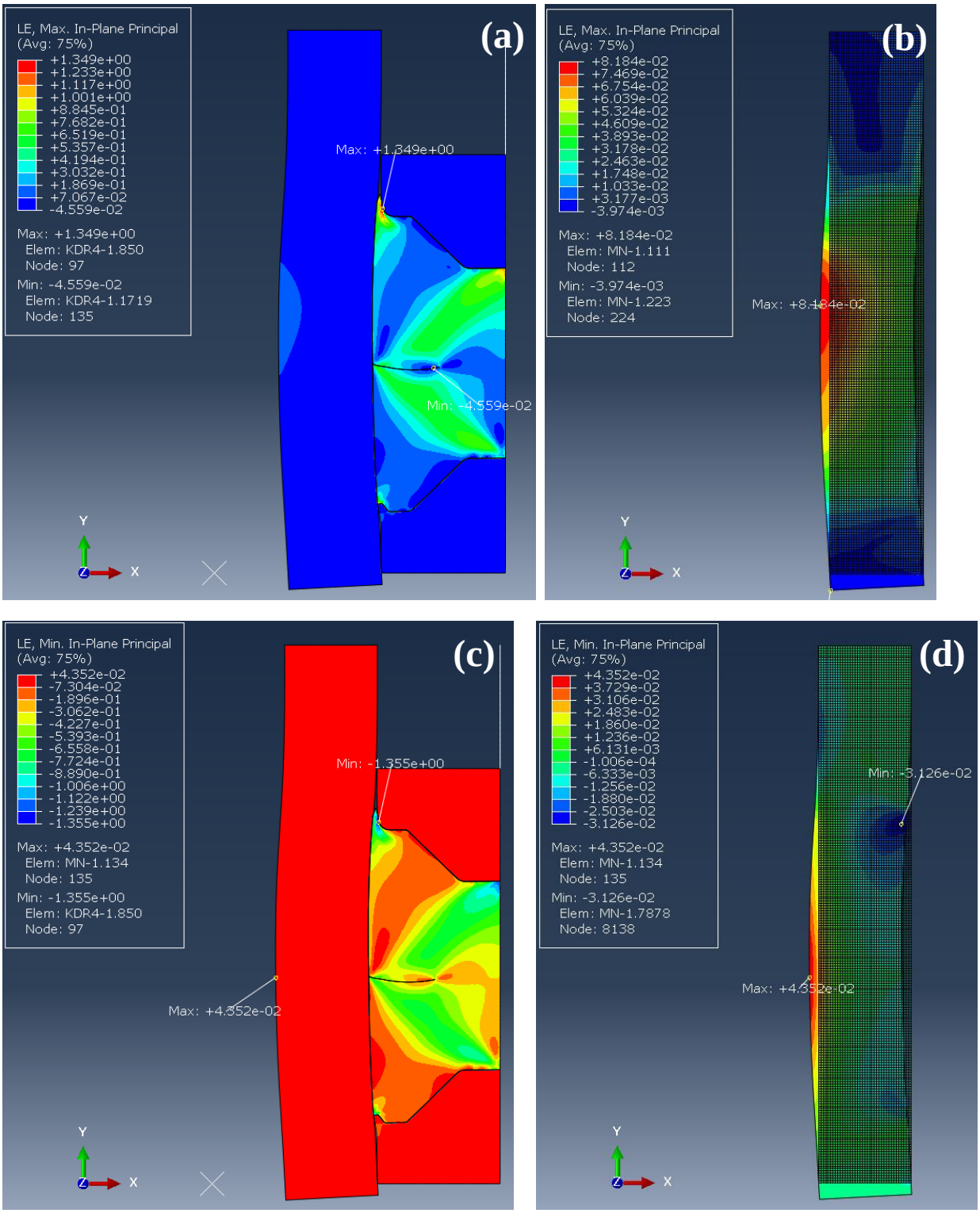

Figure B-23. FEA results of model 4 at 60 MPa of the equivalent pressure: (a) the maximum in-plane principal logarithmic strain of the entire model, (b) the maximum in-plane principal logarithmic strain of the mandrel, (c) the minimum in-plane principal logarithmic strain of the entire model, (d) the minimum in-plane principal logarithmic strain of the mandrel

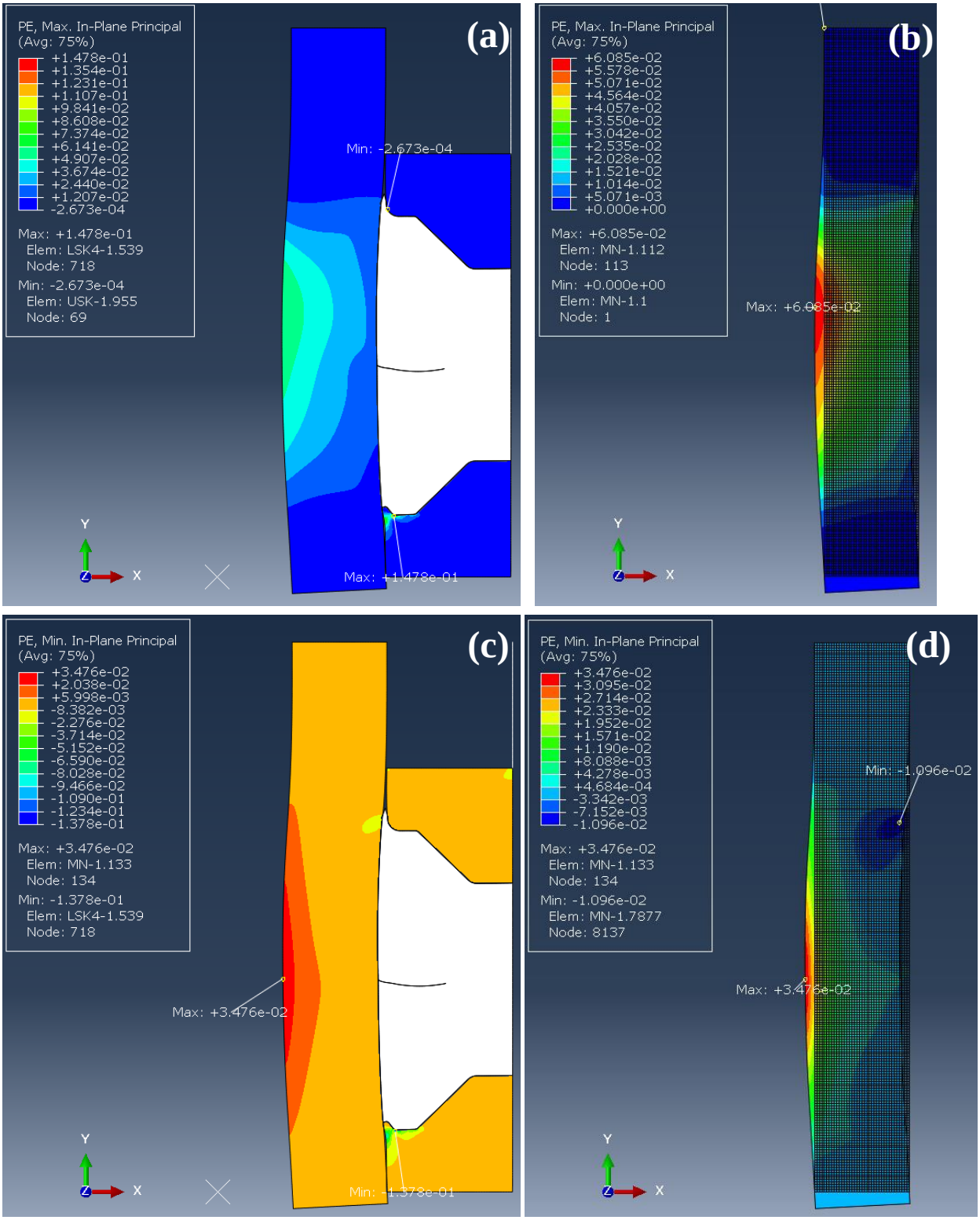

Figure B-24. FEA results of model 4 at 60 MPa of the equivalent pressure: (a) the maximum in-plane principal plastic strain of the entire model, (b) the maximum in-plane principal plastic strain of the mandrel, (c) the minimum in-plane principal plastic strain of the entire model, (d) the minimum in-plane principal plastic strain of the mandrel

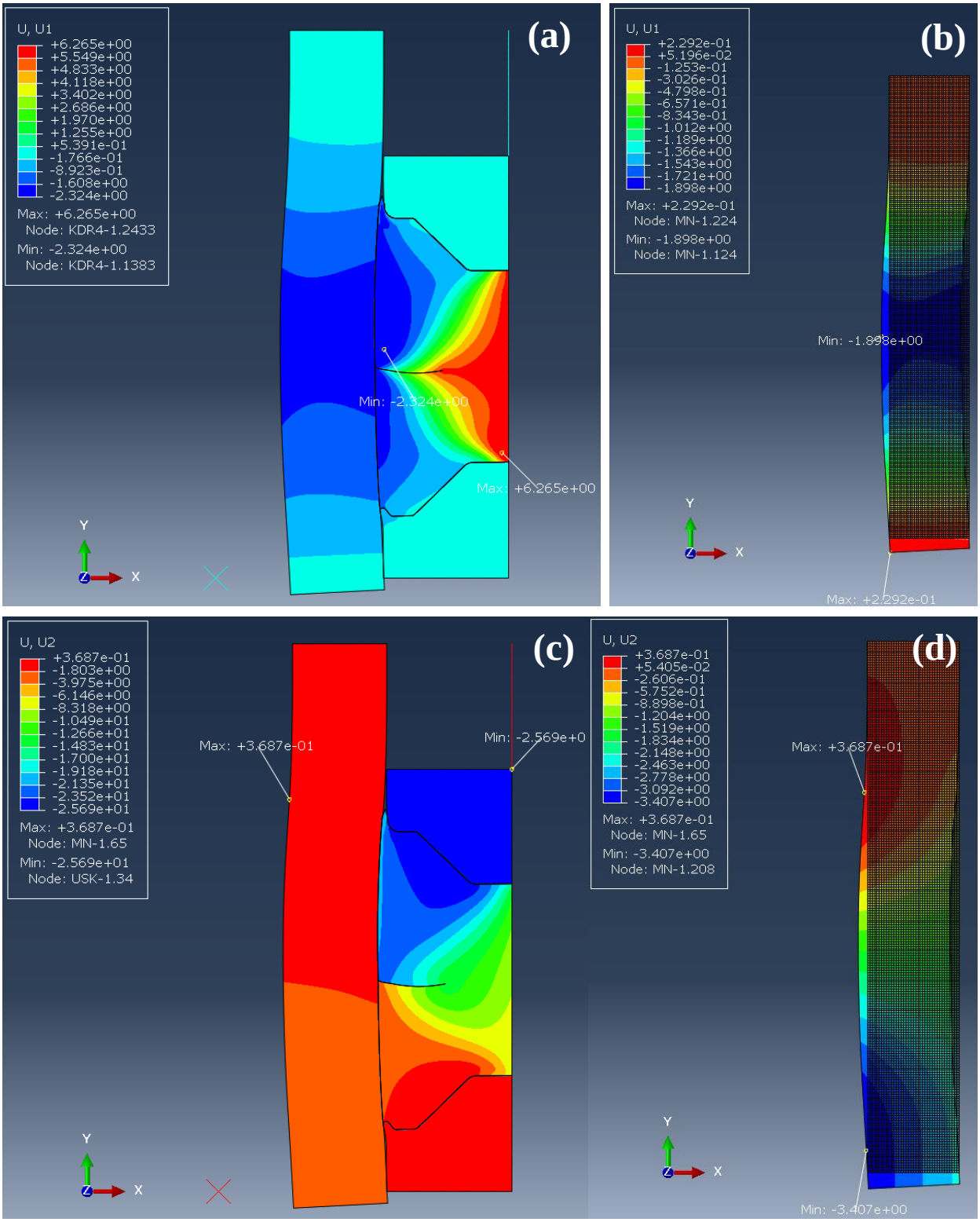

Figure B-25. FEA results of model 4 at 60 MPa of the equivalent pressure: (a) displacement to U1(x-axis) direction of the entire model, (b) displacement to U1(x-axis) direction of the mandrel, (c) displacement to U2(y-axis) direction of the entire model, (d) displacement to U2(y-axis) direction of the mandrel

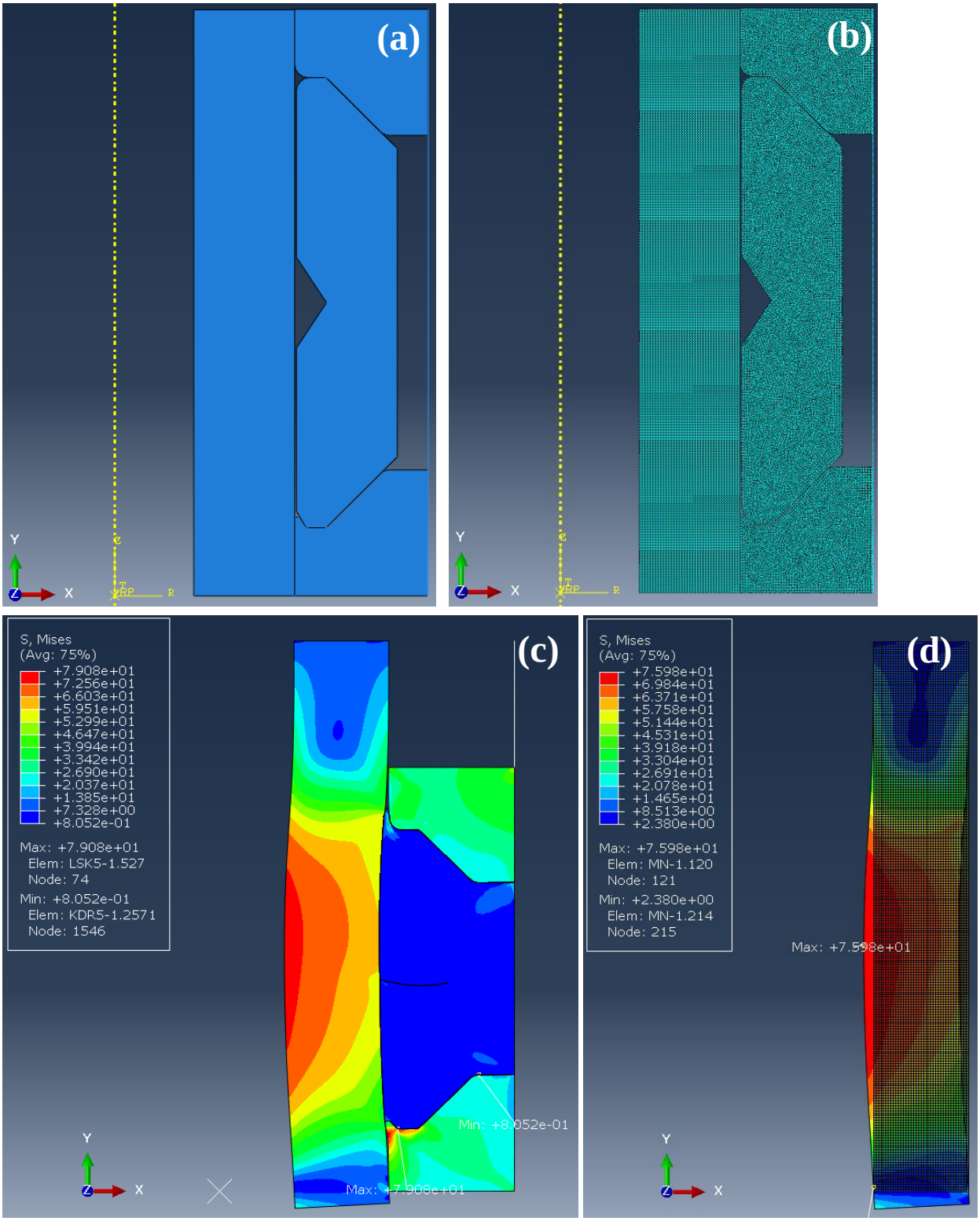

Figure B-26. FEA model and results of model 5 at 60 MPa of the equivalent pressure: (a) Model, (b) FEA model, (c) Mises stress of the entire model, (d) Mises stress of the mandrel

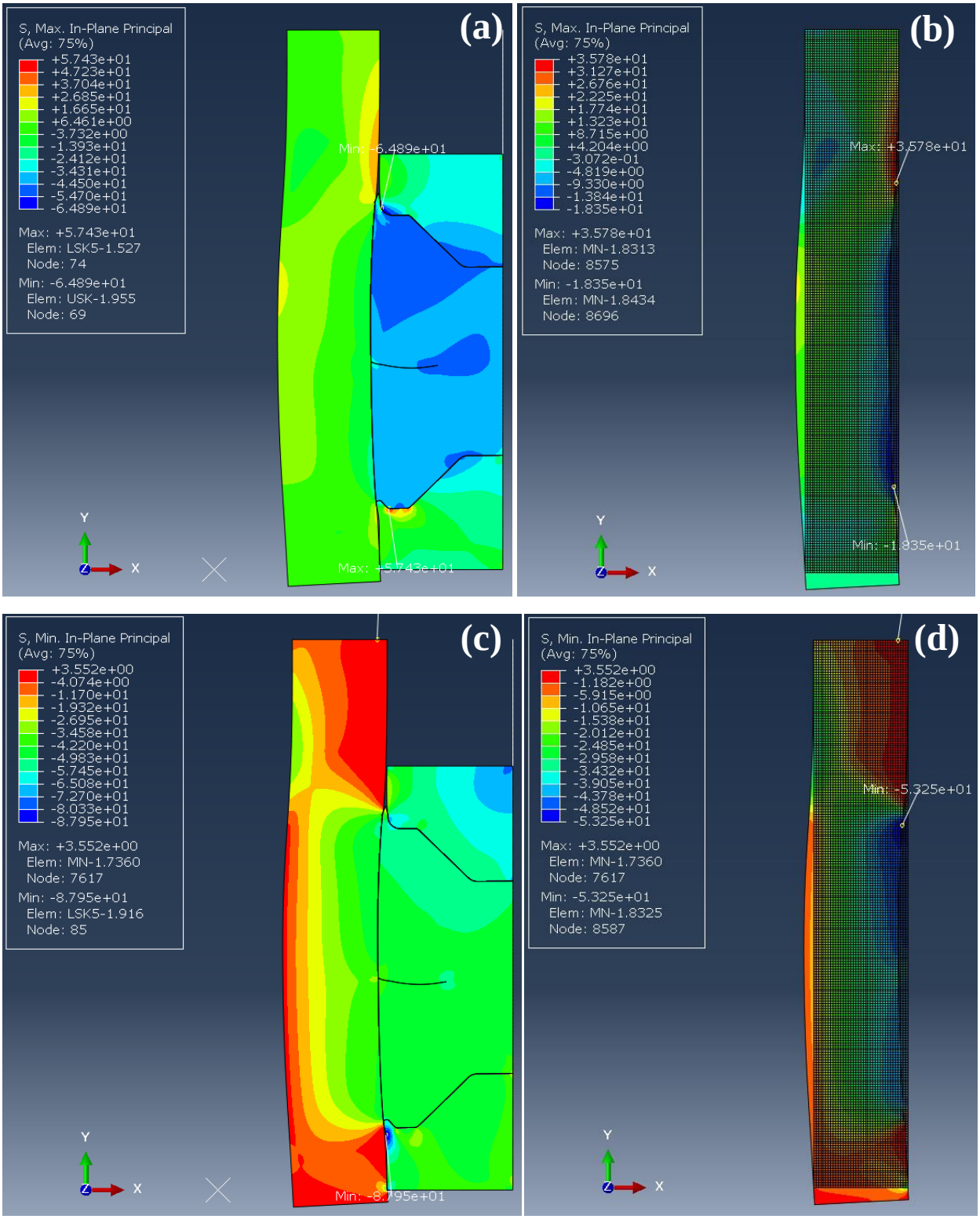

Figure B-27. FEA results of model 5 at 60 MPa of the equivalent pressure: (a) the maximum in-plane principal stress of the entire model, (b) the maximum in-plane principal stress of the mandrel, (c) the minimum in-plane principal stress of the entire model, (d) the minimum in-plane principal stress of the mandrel

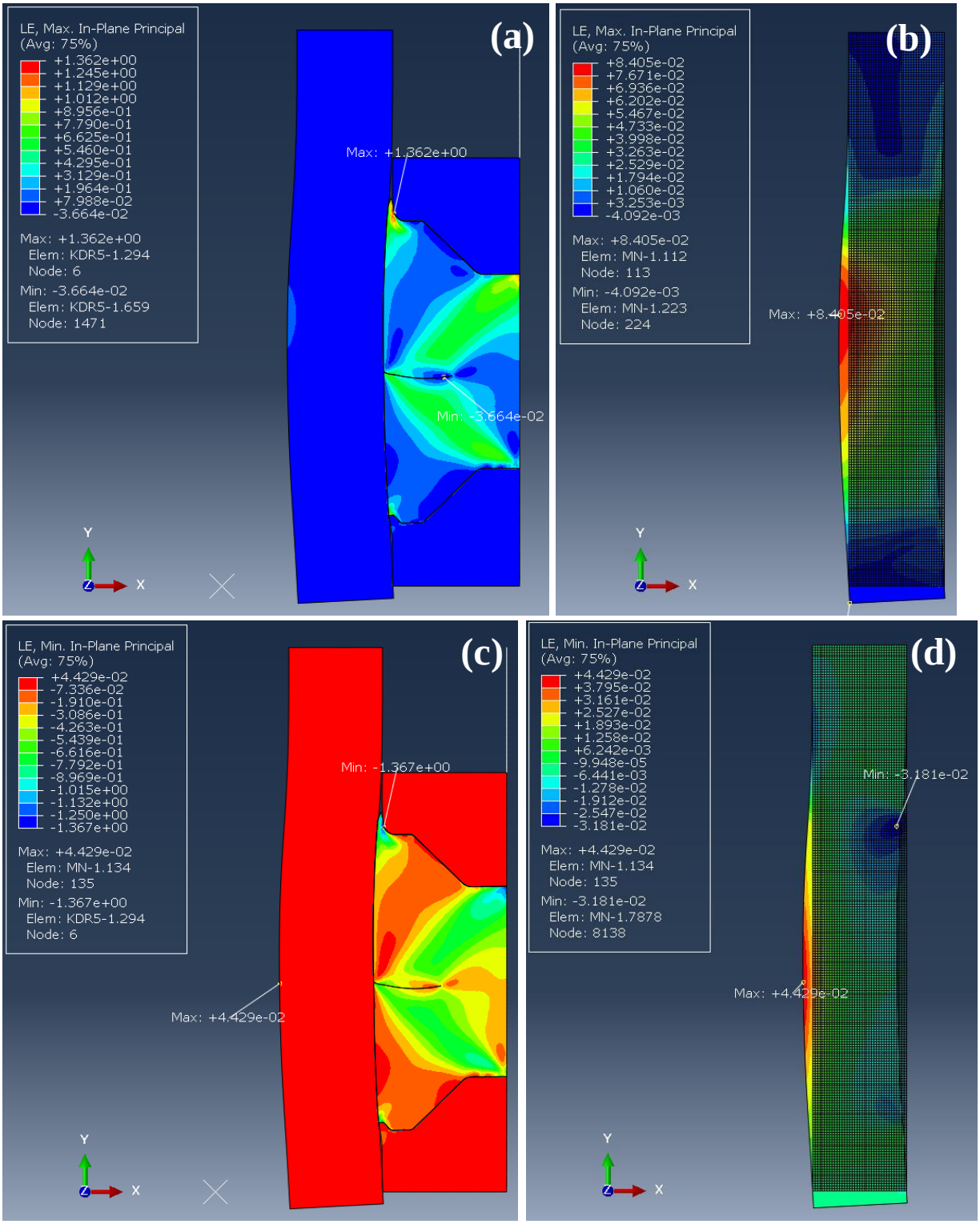

Figure B-28. FEA results of model 5 at 60 MPa of the equivalent pressure: (a) the maximum in-plane principal logarithmic strain of the entire model, (b) the maximum in-plane principal logarithmic strain of the mandrel, (c) the minimum in-plane principal logarithmic strain of the entire model, (d) the minimum in-plane principal logarithmic strain of the mandrel

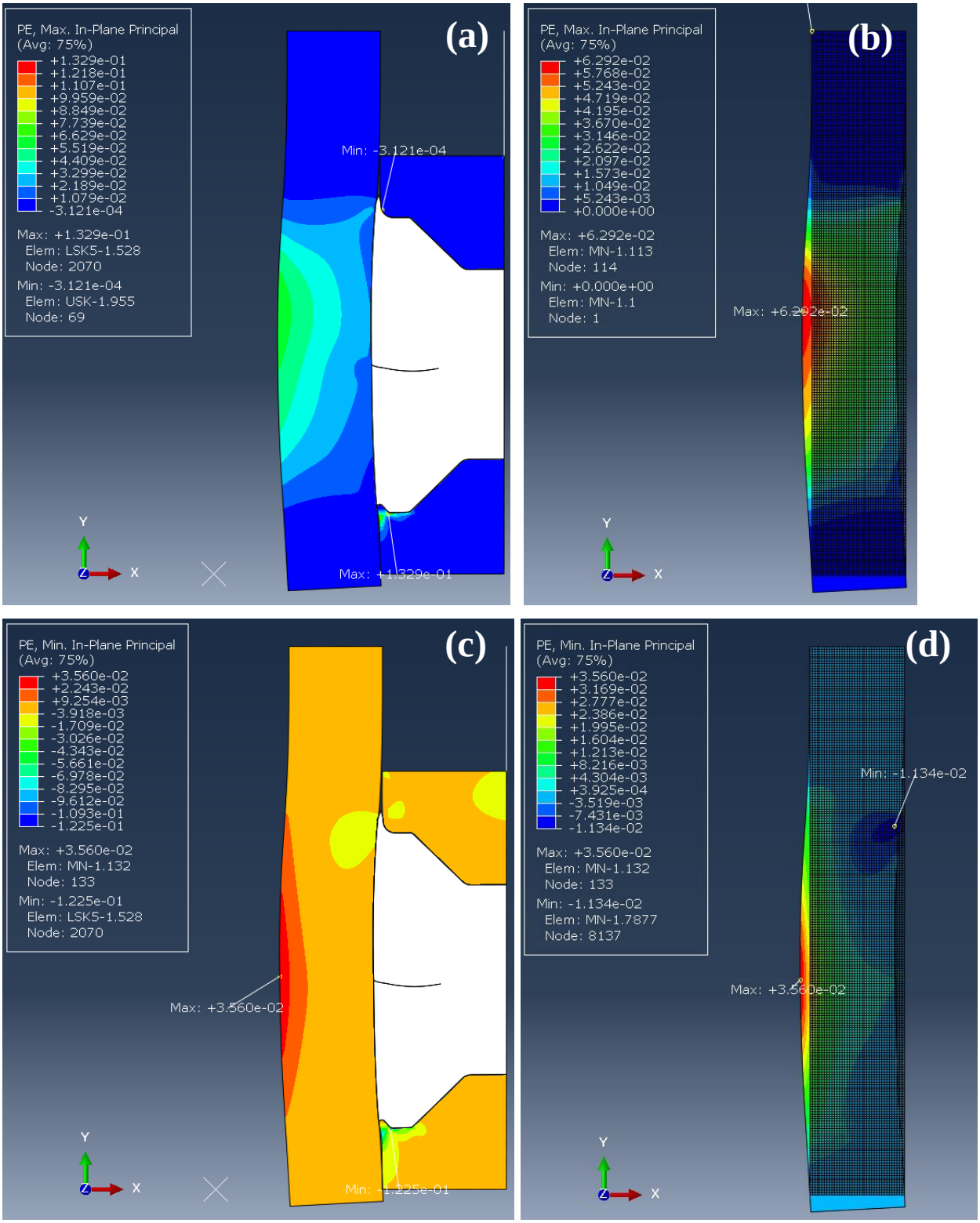

Figure B-29. FEA results of model 5 at 60 MPa of the equivalent pressure: (a) the maximum in-plane principal plastic strain of the entire model, (b) the maximum in-plane principal plastic strain of the mandrel, (c) the minimum in-plane principal plastic strain of the entire model, (d) the minimum in-plane principal plastic strain of the mandrel

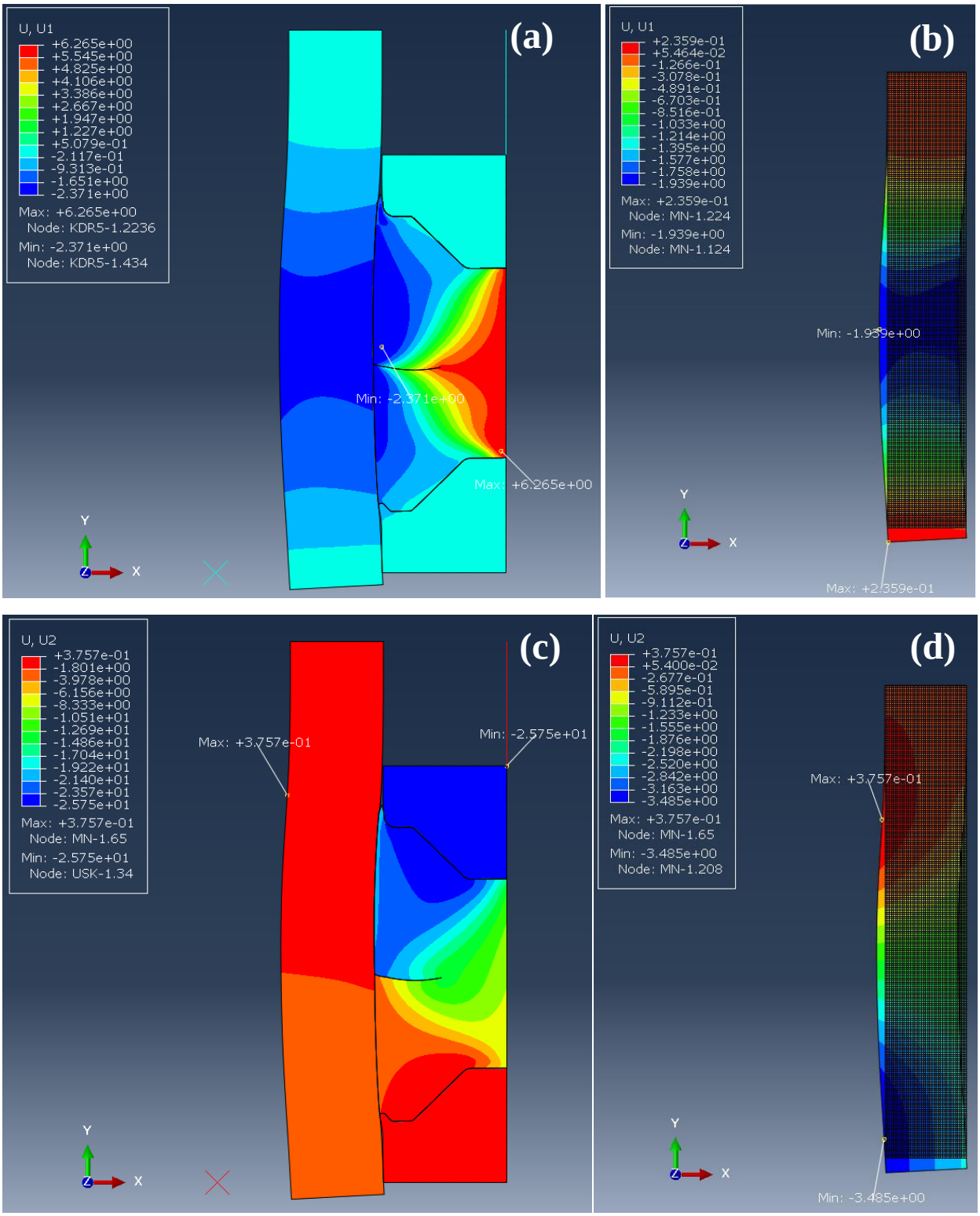

Figure B-30. FEA results of model 5 at 60 MPa of the equivalent pressure: (a) displacement to U1(x-axis) direction of the entire model, (b) displacement to U1(x-axis) direction of the mandrel, (c) displacement to U2(y-axis) direction of the entire model, (d) displacement to U2(y-axis) direction of the mandrel

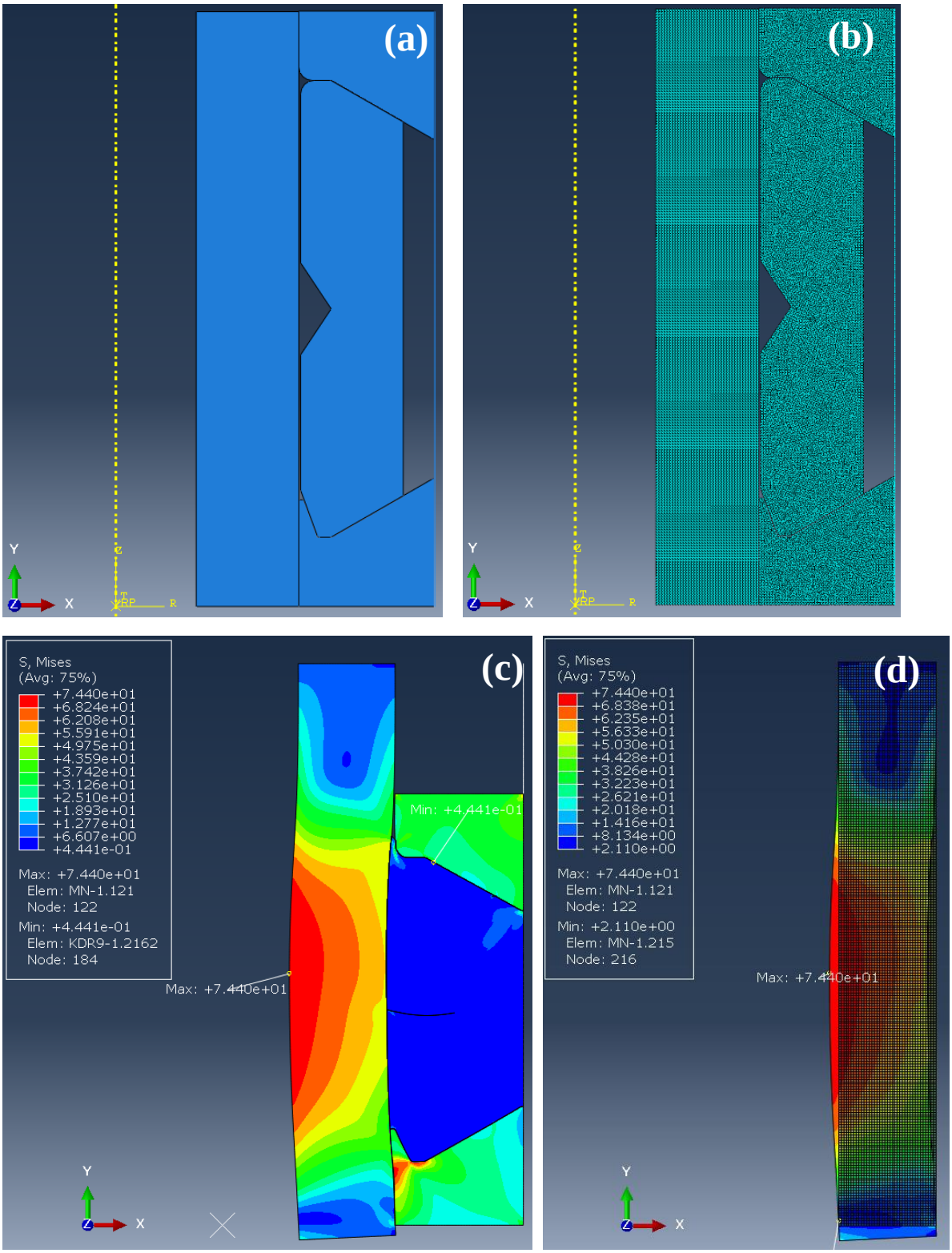

Figure B-31. FEA model and results of model 6 at 60 MPa of the equivalent pressure: (a) Model, (b) FEA model, (c) Mises stress of the entire model, (d) Mises stress of the mandrel

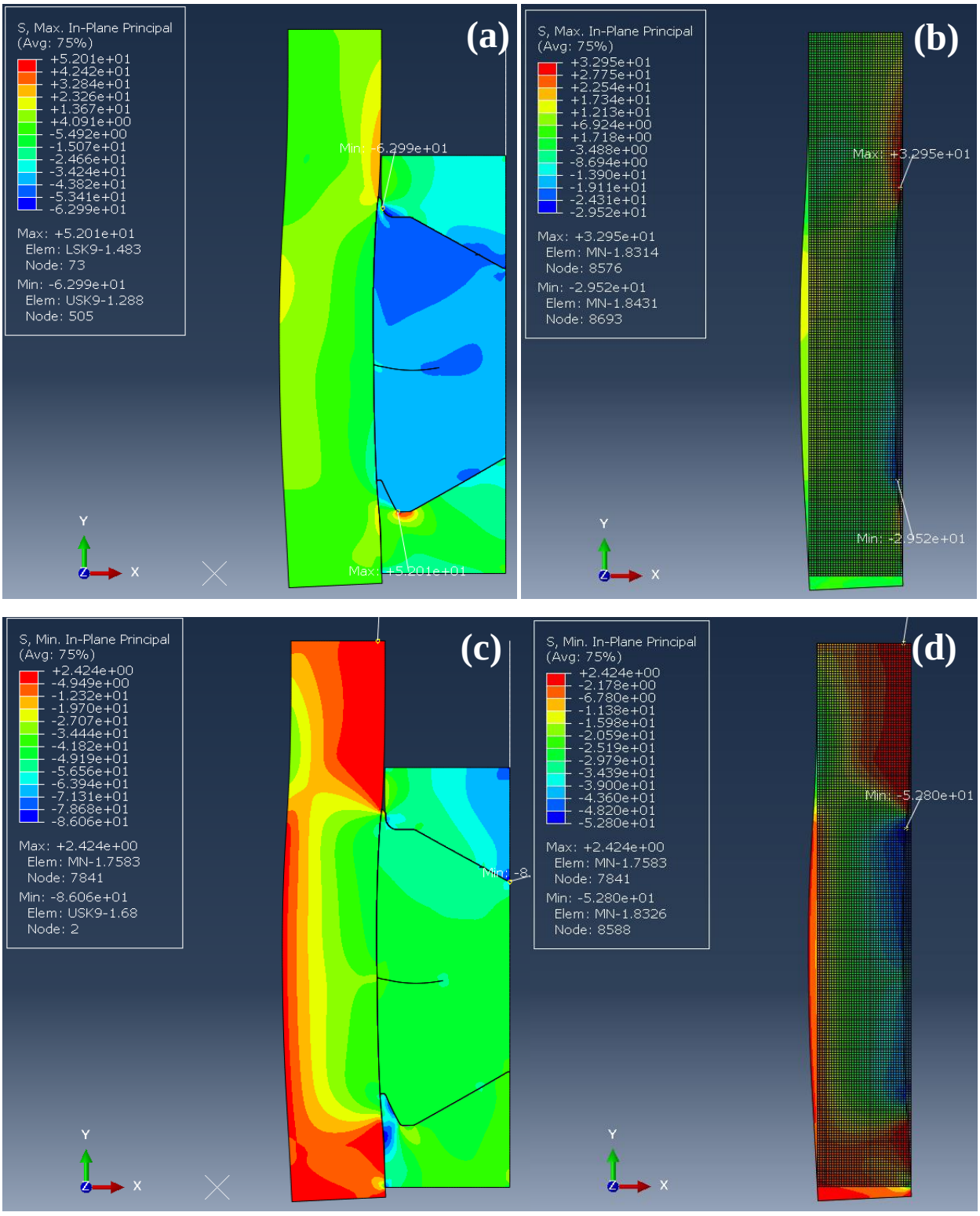

Figure B-32. FEA results of model 6 at 60 MPa of the equivalent pressure: (a) the maximum in-plane principal stress of the entire model, (b) the maximum in-plane principal stress of the mandrel, (c) the minimum in-plane principal stress of the entire model, (d) the minimum in-plane principal stress of the mandrel

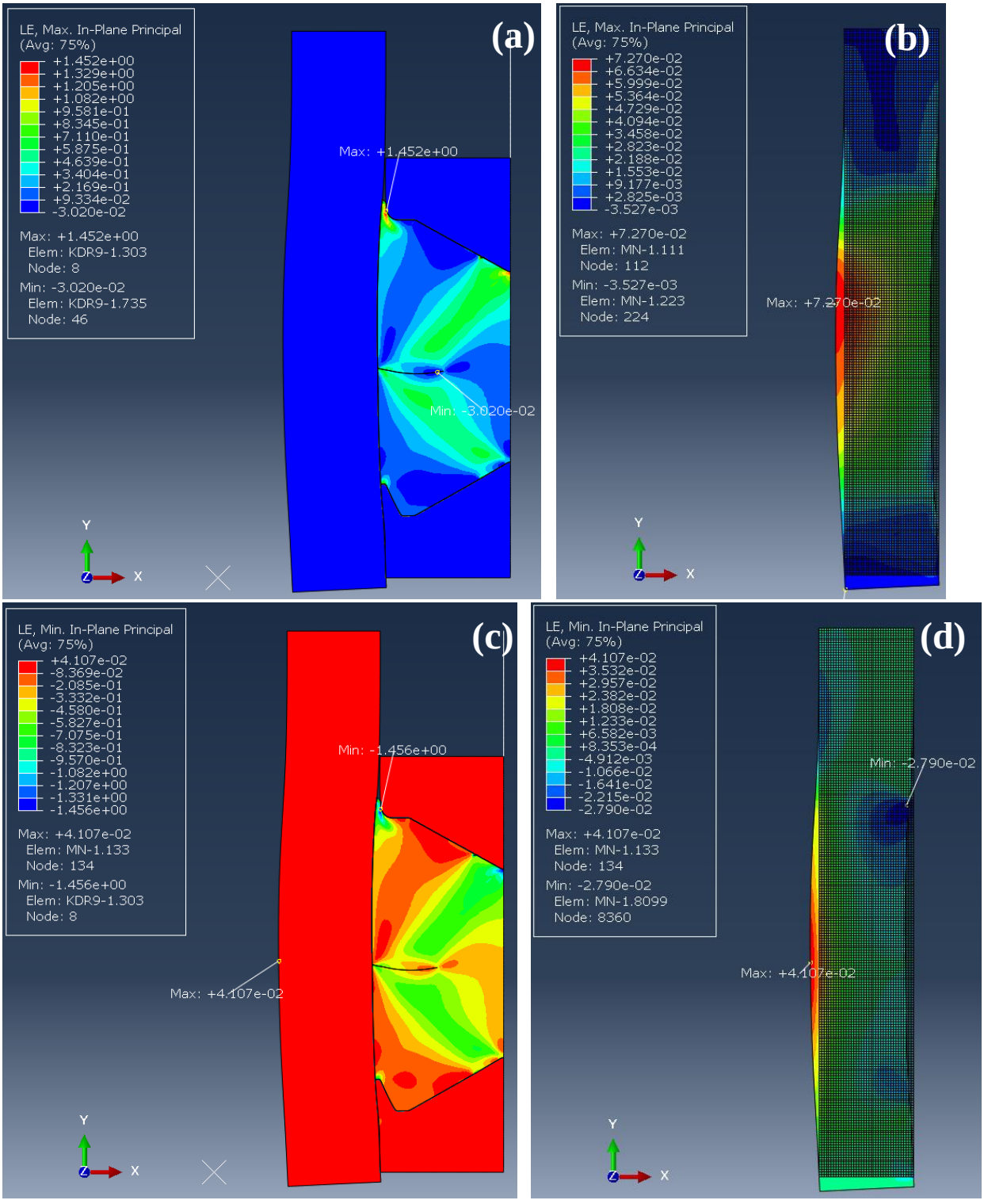

Figure B-33. FEA results of model 6 at 60 MPa of the equivalent pressure: (a) the maximum in-plane principal logarithmic strain of the entire model, (b)maximum in-plane principal logarithmic strain of the mandrel, (c) the minimum in-plane principal logarithmic strain of the entire model, (d) the minimum in-plane principal logarithmic strain of the mandrel

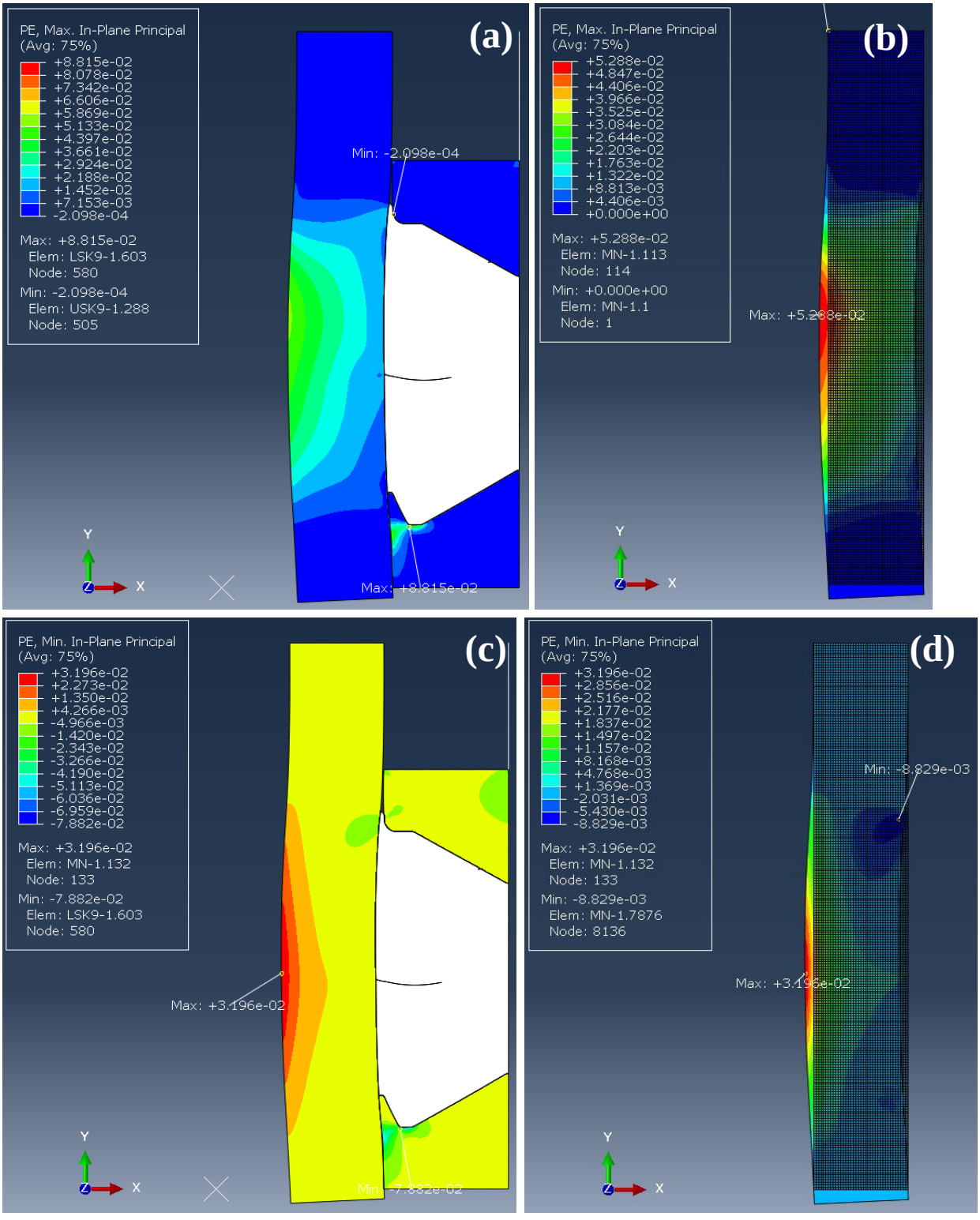

Figure B-34. FEA results of model 6 at 60 MPa of the equivalent pressure: (a) the maximum in-plane principal plastic strain of the entire model, (b) the maximum in-plane principal plastic strain of the mandrel, (c) the minimum in-plane principal plastic strain of the entire model, (d) the minimum in-plane principal plastic strain of the mandrel

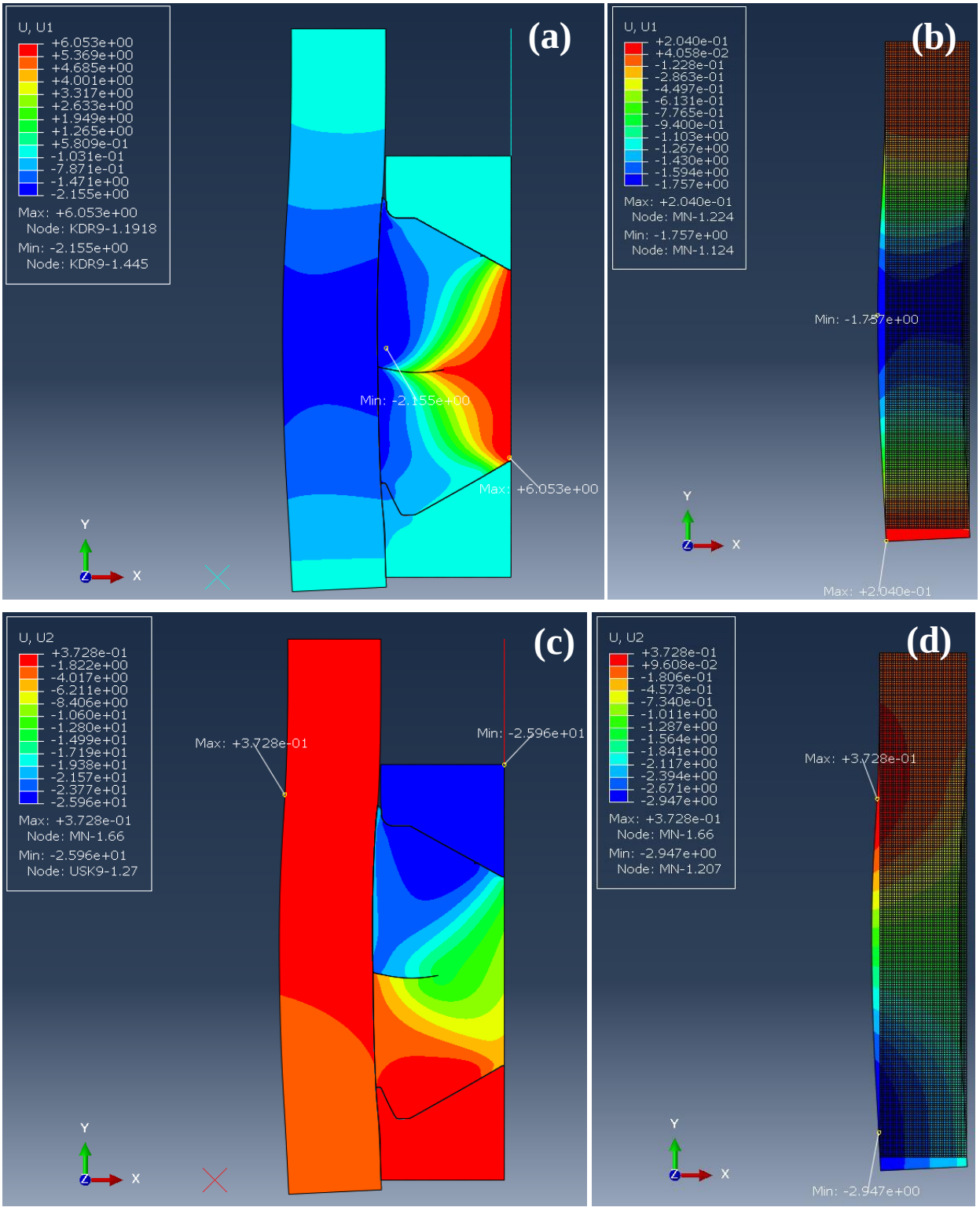

Figure B-35. FEA results of model 6 at 60 MPa of the equivalent pressure: (a) displacement to U1(x-axis) direction of the entire model, (b) displacement to U1(x-axis) direction of the mandrel, (c) displacement to U2(y-axis) direction of the entire model, (d) displacement to U2(y-axis) direction of the mandrel

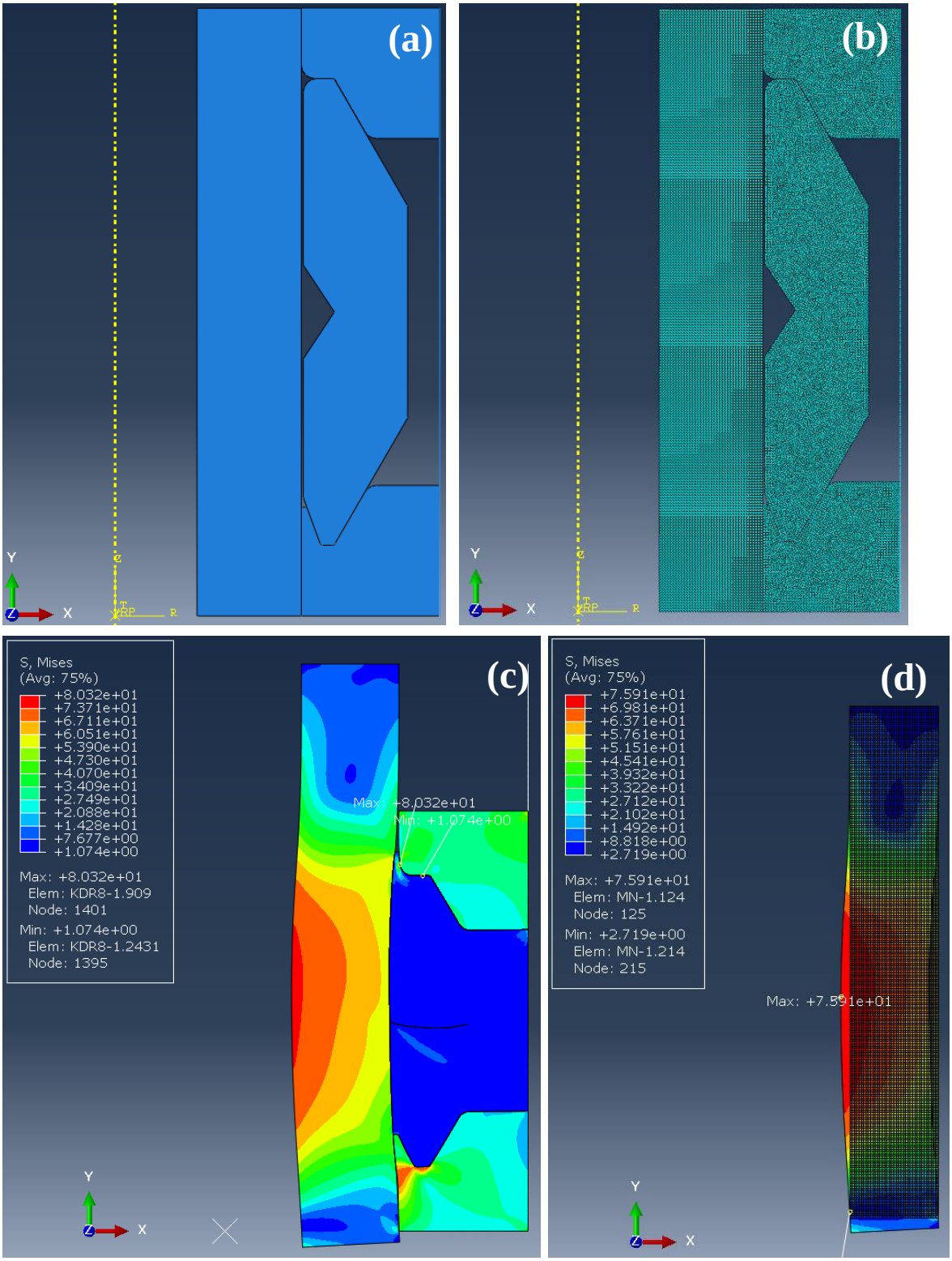

Figure B-36. FEA model and results of model 7 at 60 MPa of the equivalent pressure: (a) Model, (b) FEA model, (c) Mises stress of the entire model, (d) Mises stress of the mandrel

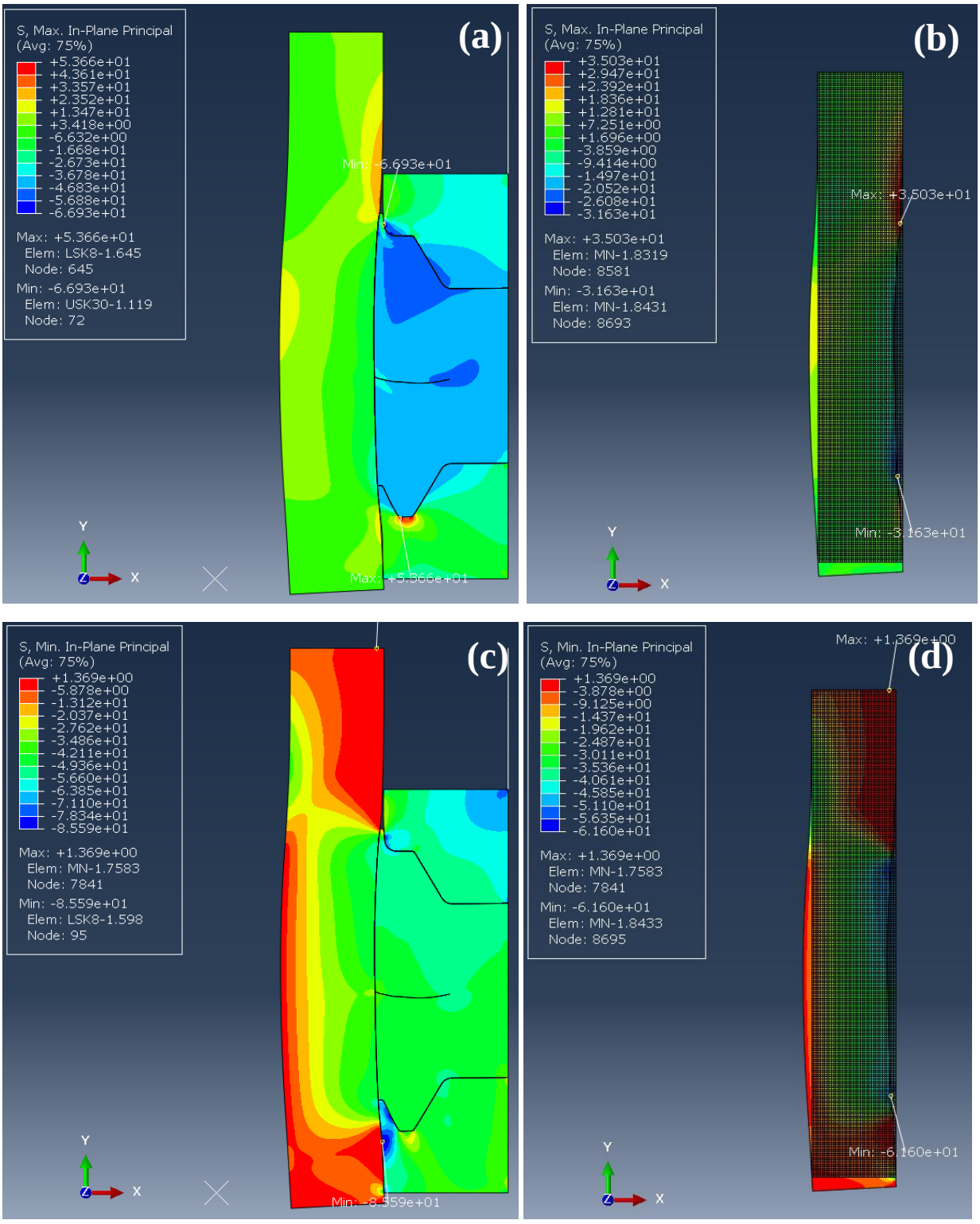

Figure B-37. FEA results of model 7 at 60 MPa of the equivalent pressure: (a) the maximum in-plane principal stress of the entire model, (b) the maximum in-plane principal stress of the mandrel, (c) the minimum in-plane principal stress of the entire model, (d) the minimum in-plane principal stress of the mandrel

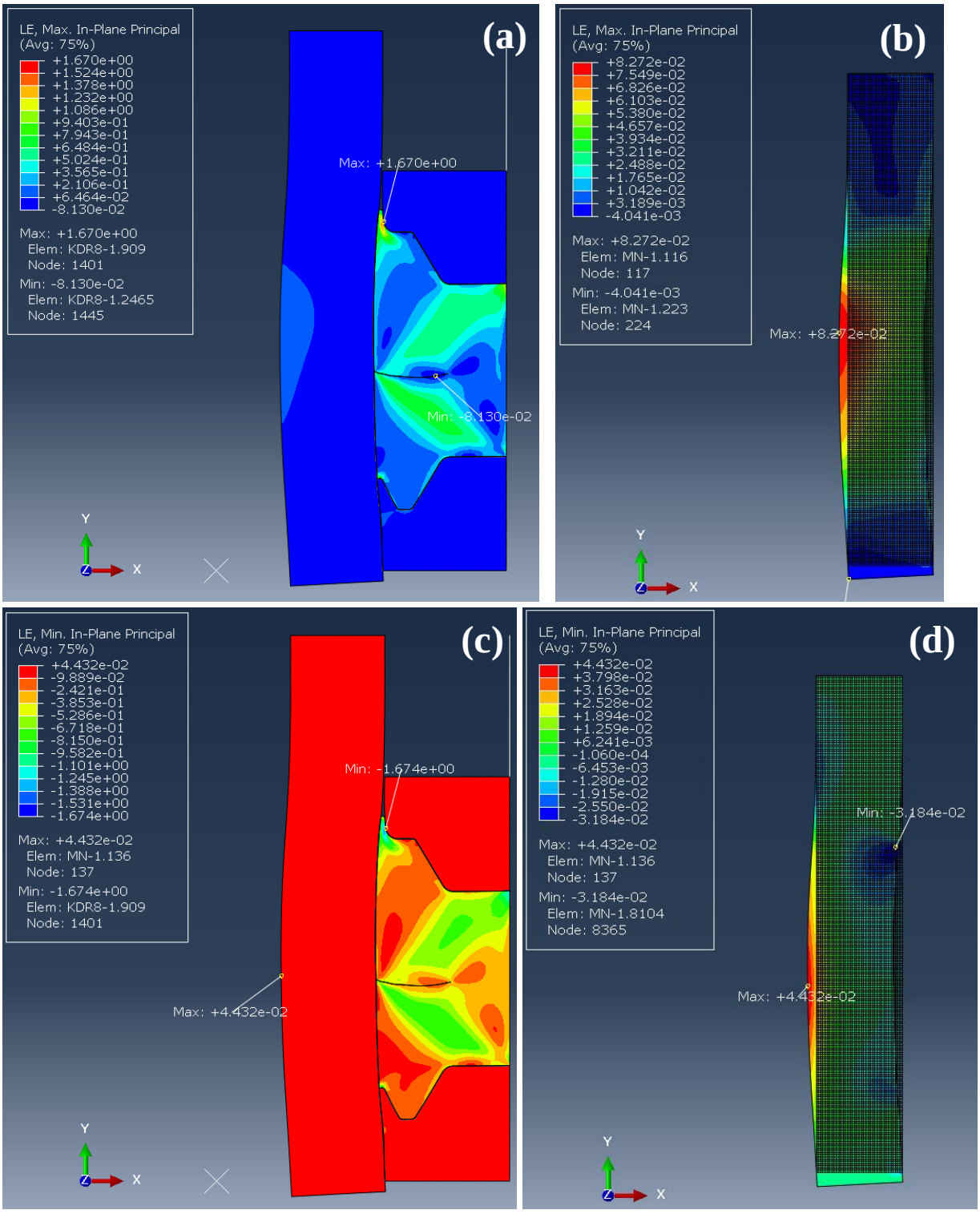

Figure B-38. FEA results of model 7 at 60 MPa of the equivalent pressure: (a) the maximum in-plane principal logarithmic strain of the entire model, (b) the maximum in-plane principal logarithmic strain of the mandrel, (c) the minimum in-plane principal logarithmic strain of the entire model, (d) the minimum in-plane principal logarithmic strain of the mandrel

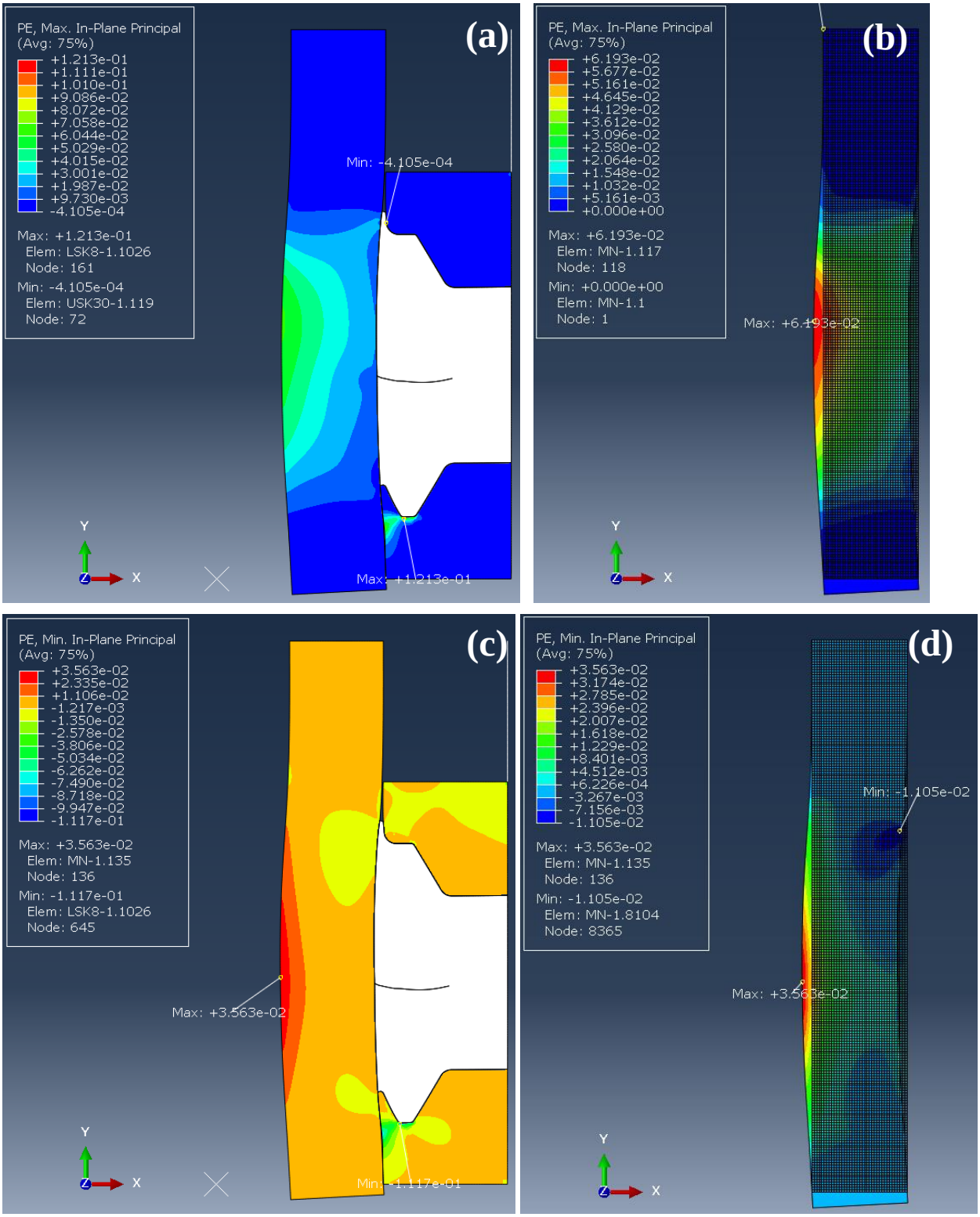

Figure B-39. FEA results of model 7 at 60 MPa of the equivalent pressure: (a) the maximum in-plane principal plastic strain of the entire model, (b) the maximum in-plane principal plastic strain of the mandrel, (c) the minimum in-plane principal plastic strain of the entire model, (d) the minimum in-plane principal plastic strain of the mandrel

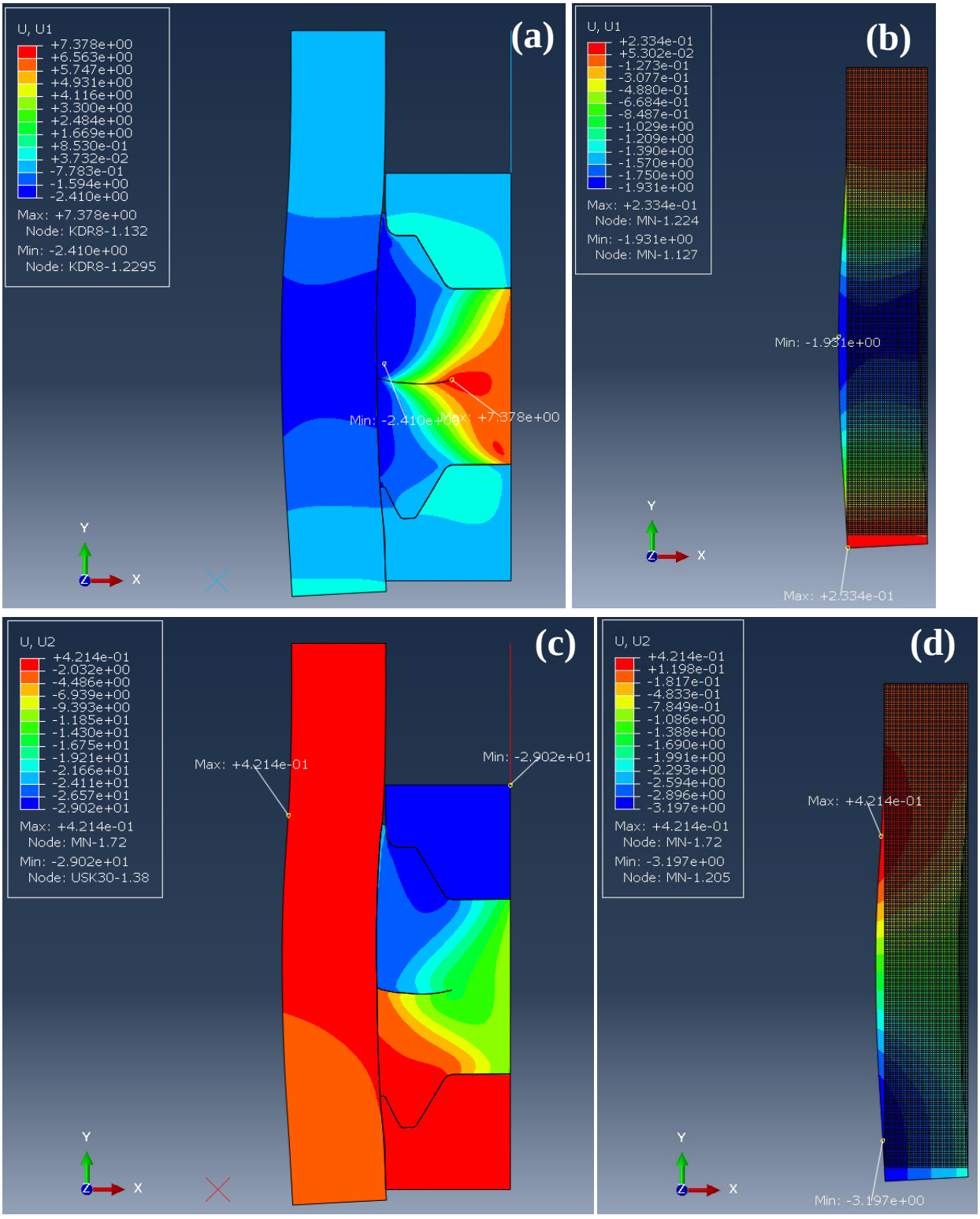

Figure B-40. FEA results of model 7 at 60 MPa of the equivalent pressure: (a) displacement to U1(x-axis) direction of the entire model, (b) displacement to U1(x-axis) direction of the mandrel, (c) displacement to U2(y-axis) direction of the entire model, (d) displacement to U2(y-axis) direction of the mandrel

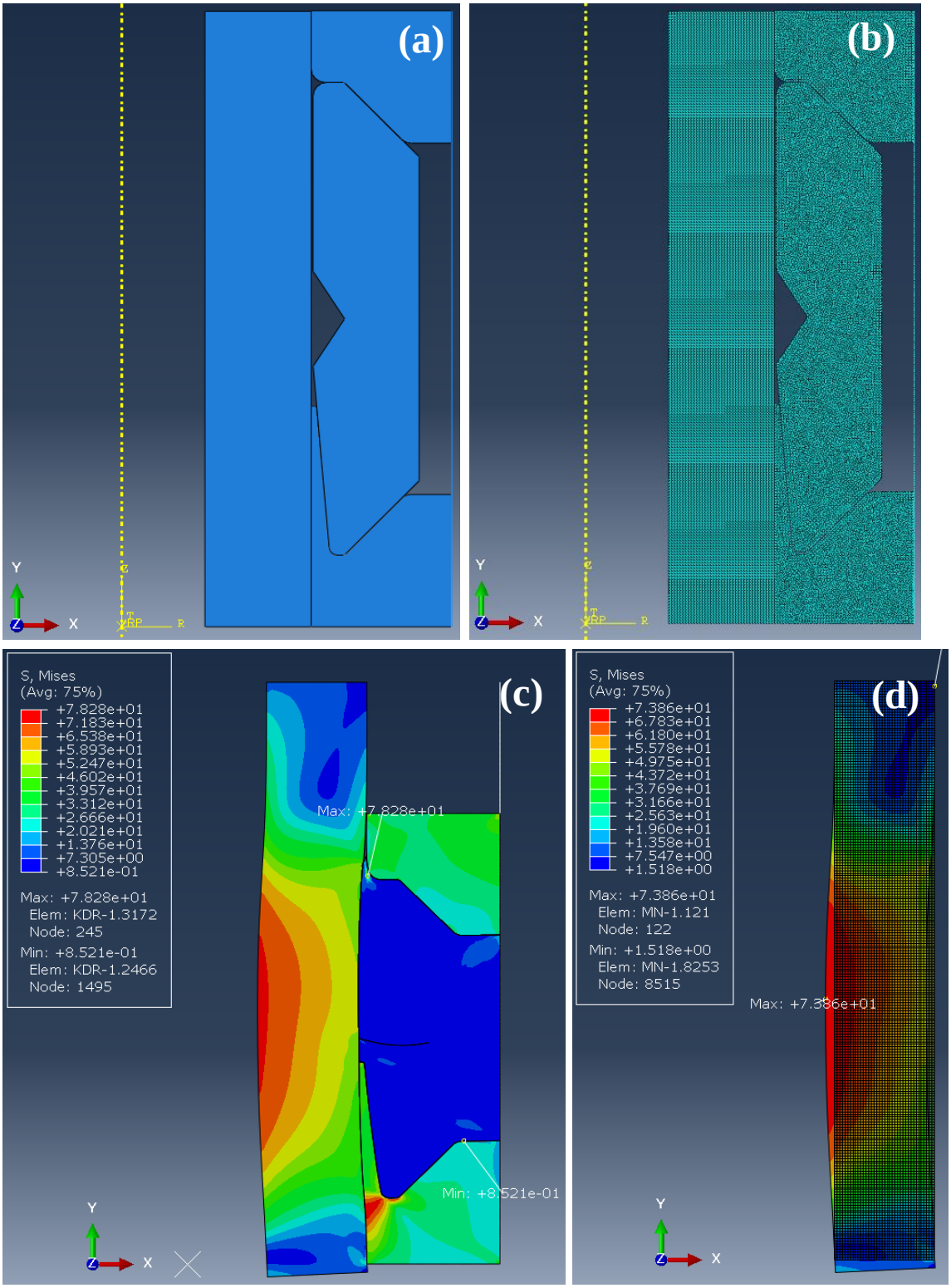

Figure B-41. FEA model and results of model 8 at 60 MPa of the equivalent pressure: (a) Model, (b) FEA model, (c) Mises stress of the entire model, (d) Mises stress of the mandrel

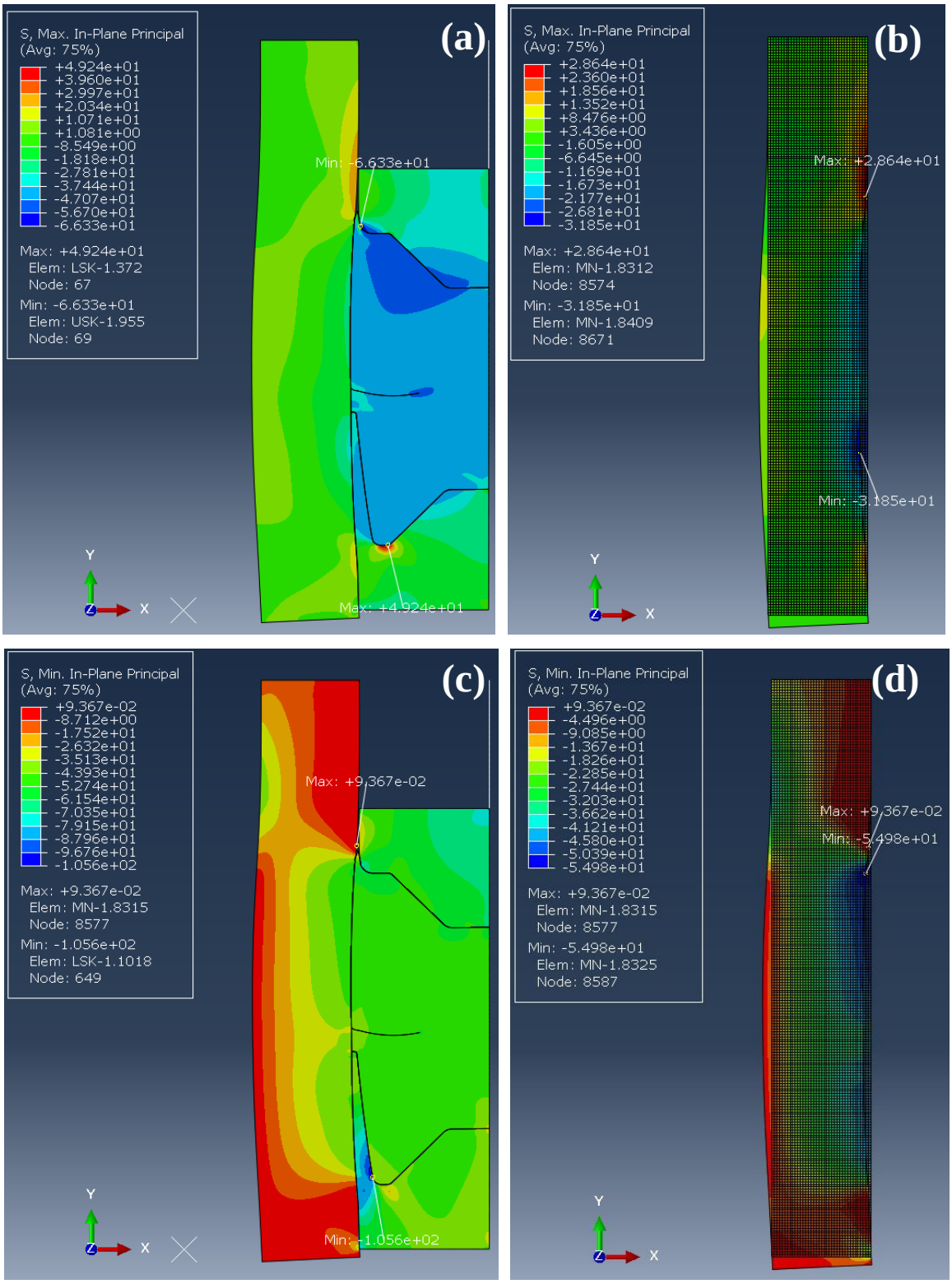

Figure B-42. FEA results of model 8 at 60 MPa of the equivalent pressure: (a) the maximum in-plane principal stress of the entire model, (b) the maximum in-plane principal stress of the mandrel, (c) the minimum in-plane principal stress of the entire model, (d) the minimum in-plane principal stress of the mandrel

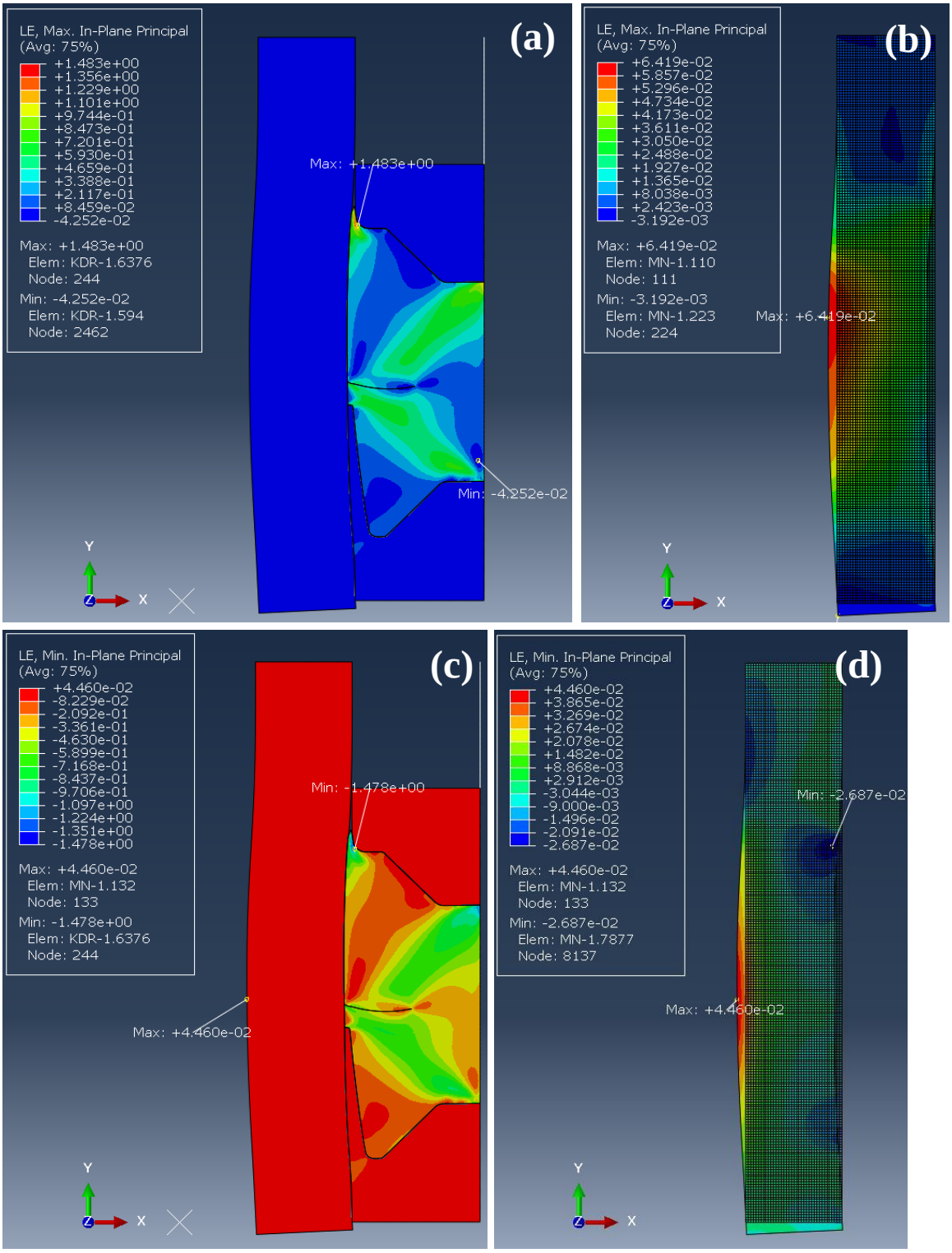

Figure B-43. FEA results of model 8 at 60 MPa of the equivalent pressure: (a) the maximum in-plane principal logarithmic strain of the entire model, (b) the maximum in-plane principal logarithmic strain of the mandrel, (c) the minimum in-plane principal logarithmic strain of the entire model, (d) the minimum in-plane principal logarithmic strain of the mandrel

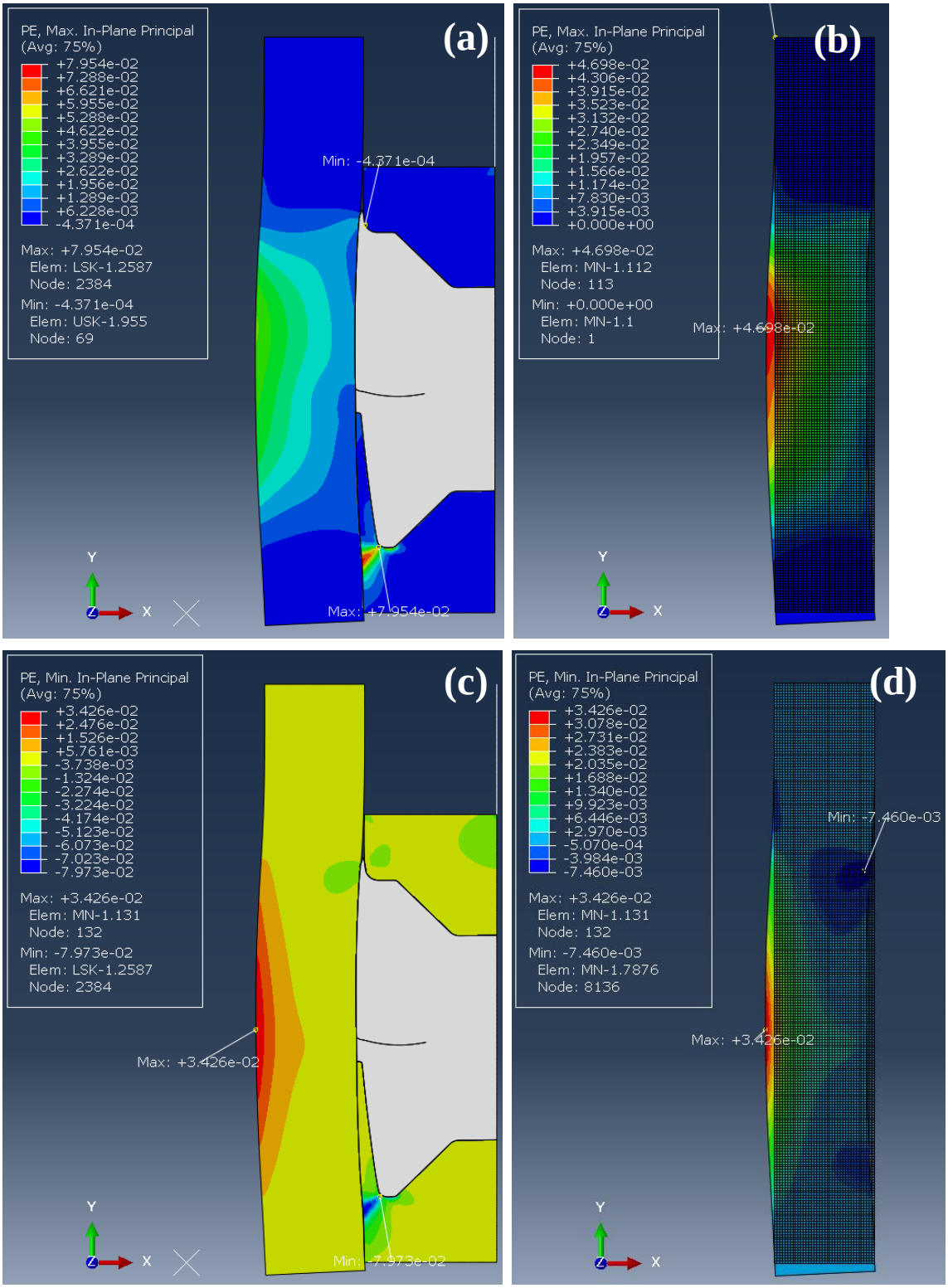

Figure B-44. FEA results of model 8 at 60 MPa of the equivalent pressure: (a) the maximum in-plane principal plastic strain of the entire model, (b) the maximum in-plane principal plastic strain of the mandrel, (c) the minimum in-plane principal plastic strain of the entire model, (d) the minimum in-plane principal plastic strain of the mandrel

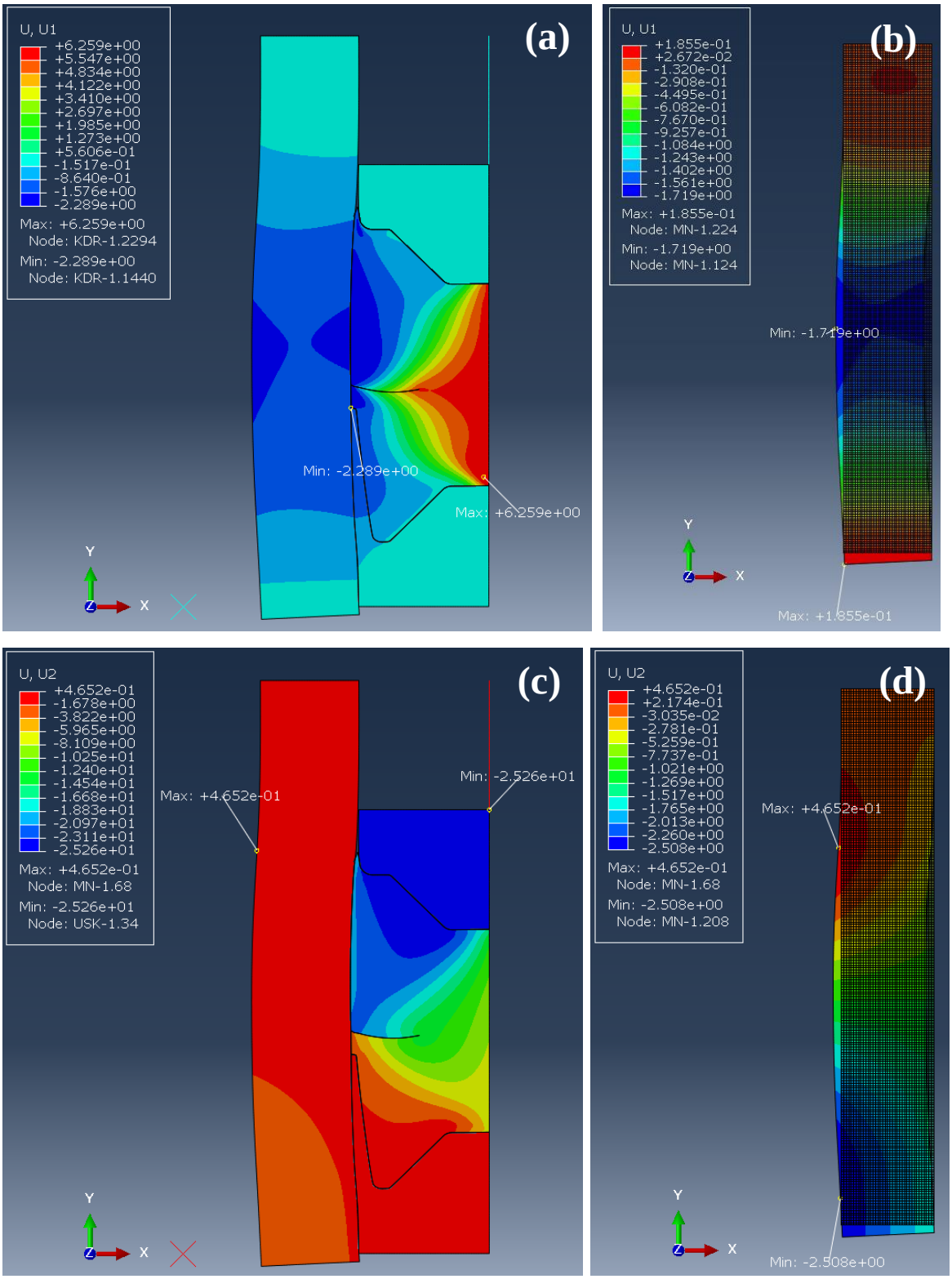

Figure B-45. FEA results of model 8 at 60 MPa of the equivalent pressure: (a) displacement to U1(x-axis) direction of the entire model, (b) displacement to U1(x-axis) direction of the mandrel, (c) displacement to U2(y-axis) direction of the entire model, (d) displacement to U2(y-axis) direction of the mandrel

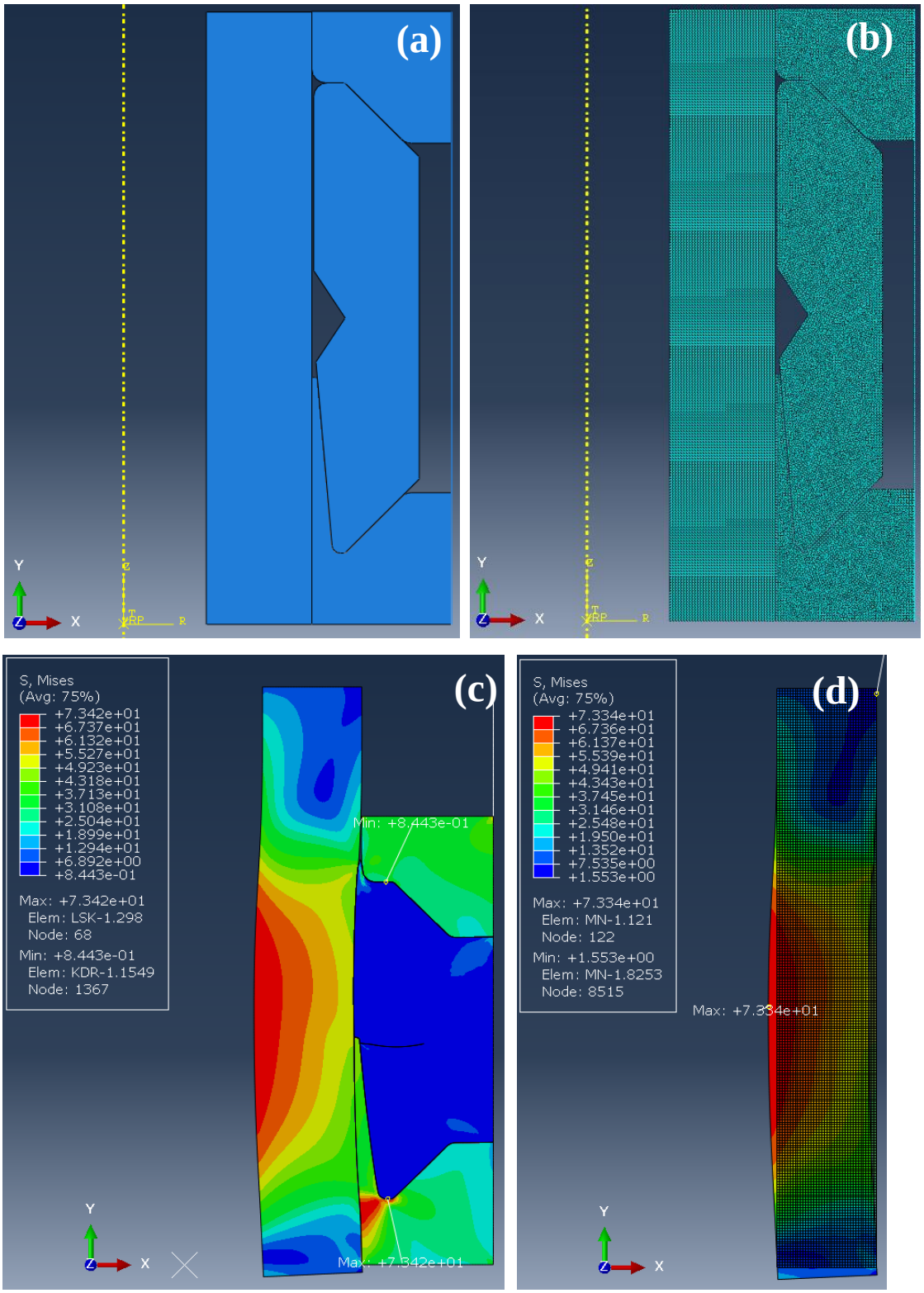

Figure B-46. FEA model and results of model 9 at 60 MPa of the equivalent pressure: (a) Model, (b) FEA model, (c) Mises stress of the entire model, (d) Mises stress of the mandrel

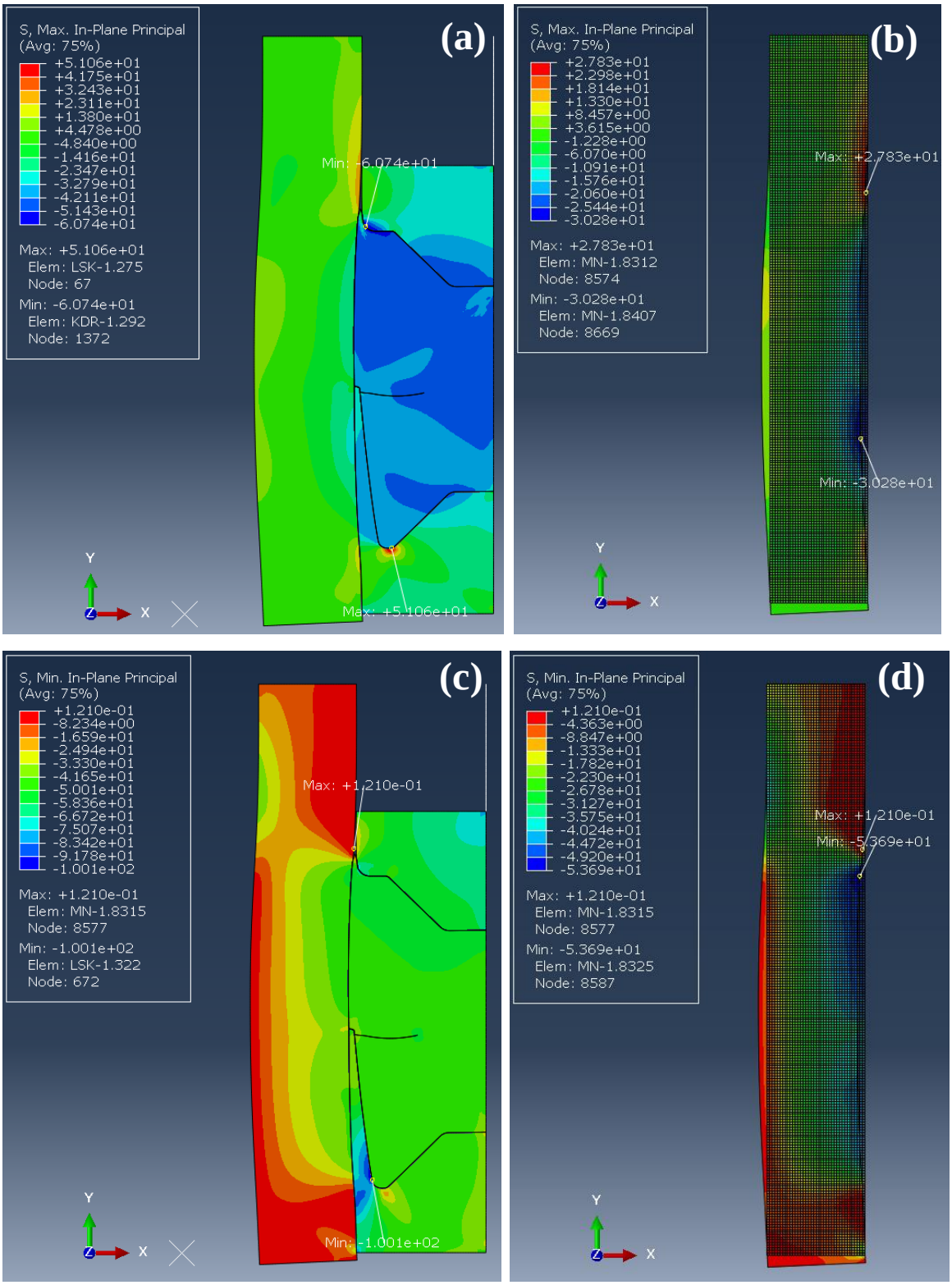

Figure B-47. FEA results of model 9 at 60 MPa of the equivalent pressure: (a) the maximum in-plane principal stress of the entire model, (b) the maximum in-plane principal stress of the mandrel, (c) the minimum in-plane principal stress of the entire model, (d) the minimum in-plane principal stress of the mandrel

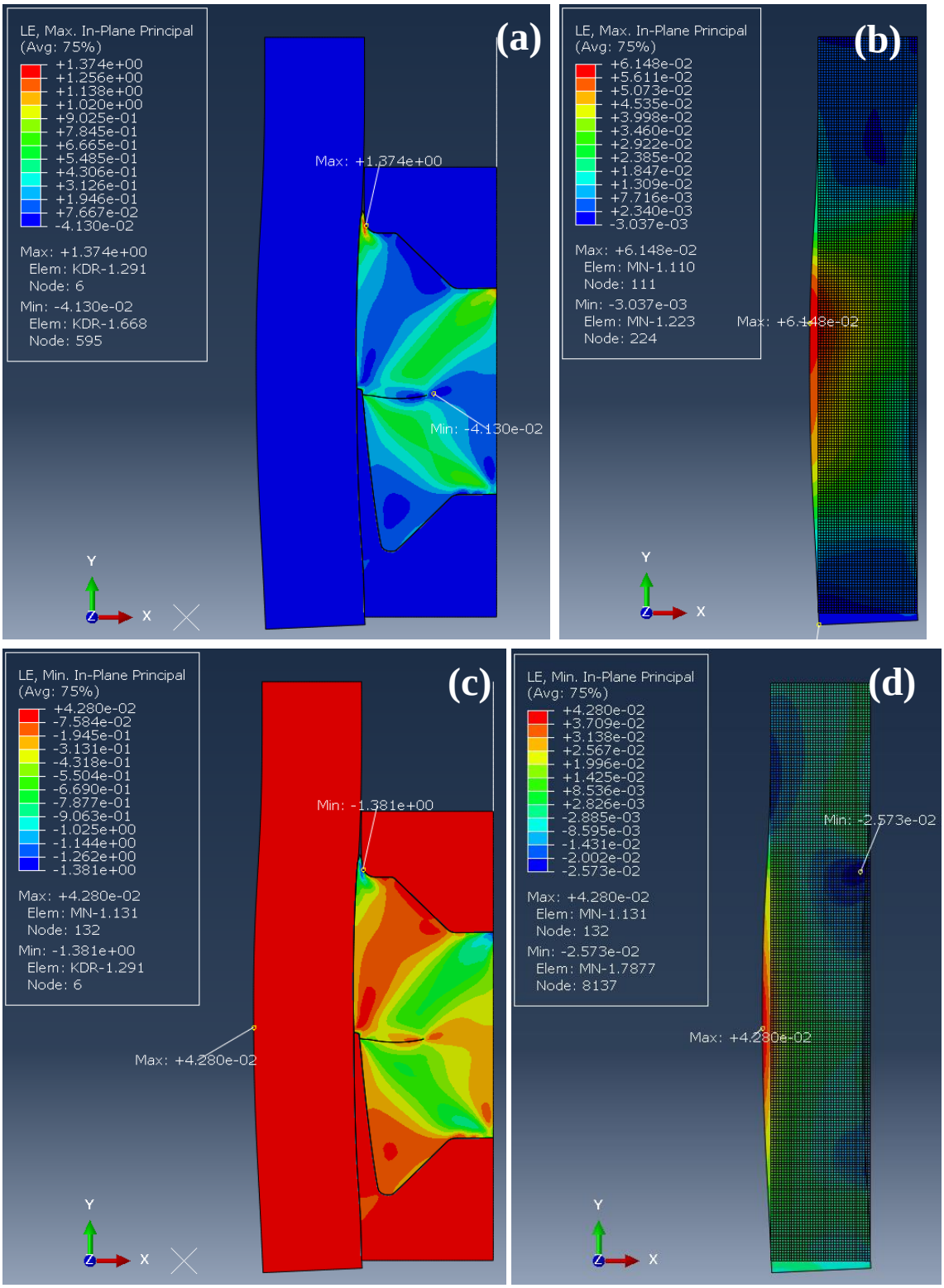

Figure B-48. FEA results of model 9 at 60 MPa of the equivalent pressure: (a) the maximum in-plane principal logarithmic strain of the entire model, (b) the maximum in-plane principal logarithmic strain of the mandrel, (c) the minimum in-plane principal logarithmic strain of the entire model, (d) the minimum in-plane principal logarithmic strain of the mandrel

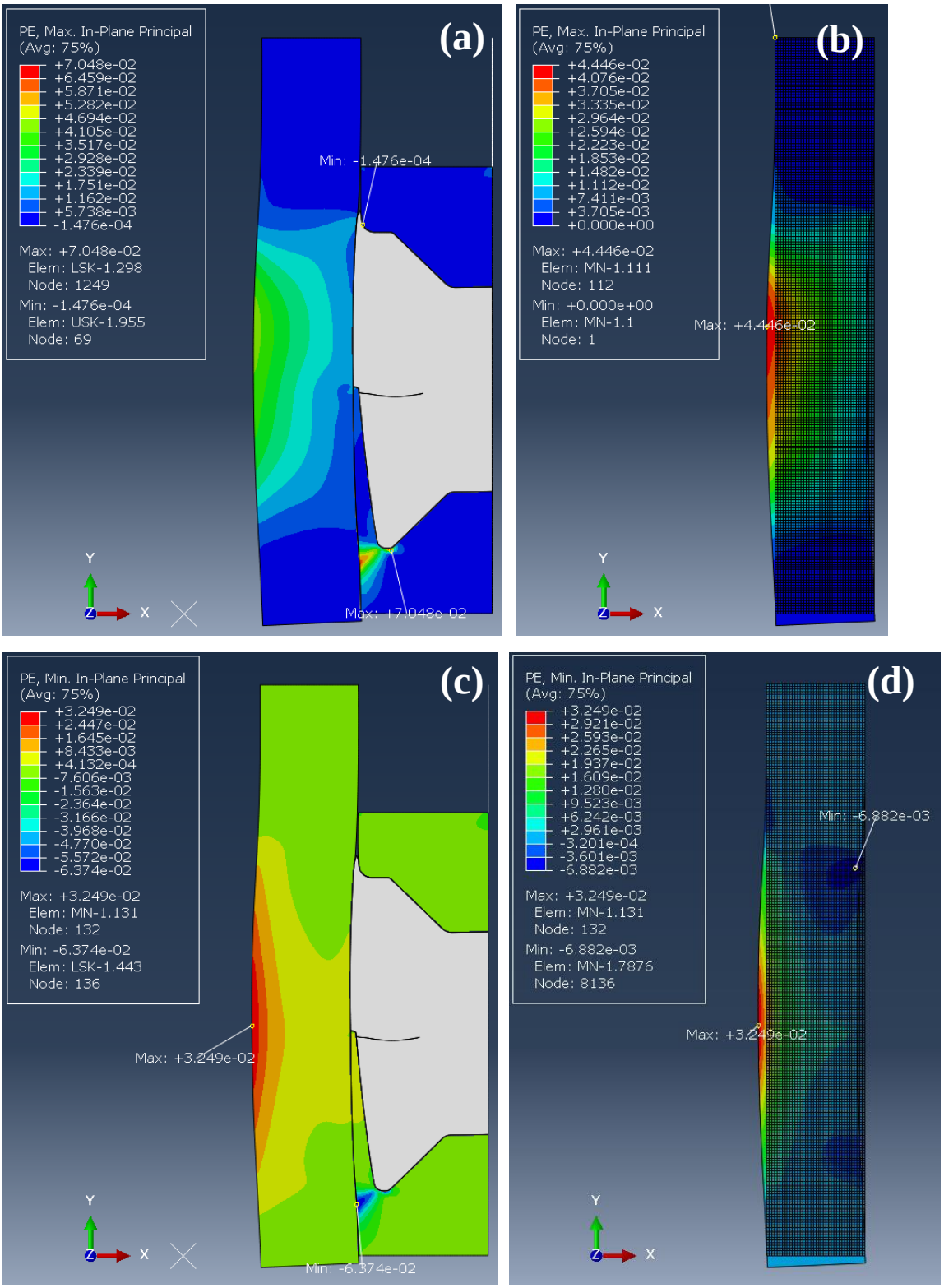

Figure B-49. FEA results of model 9 at 60 MPa of the equivalent pressure: (a) the maximum in-plane principal plastic strain of the entire model, (b) the maximum in-plane principal plastic strain of the mandrel, (c) the minimum in-plane principal plastic strain of the entire model, (d) the minimum in-plane principal plastic strain of the mandrel

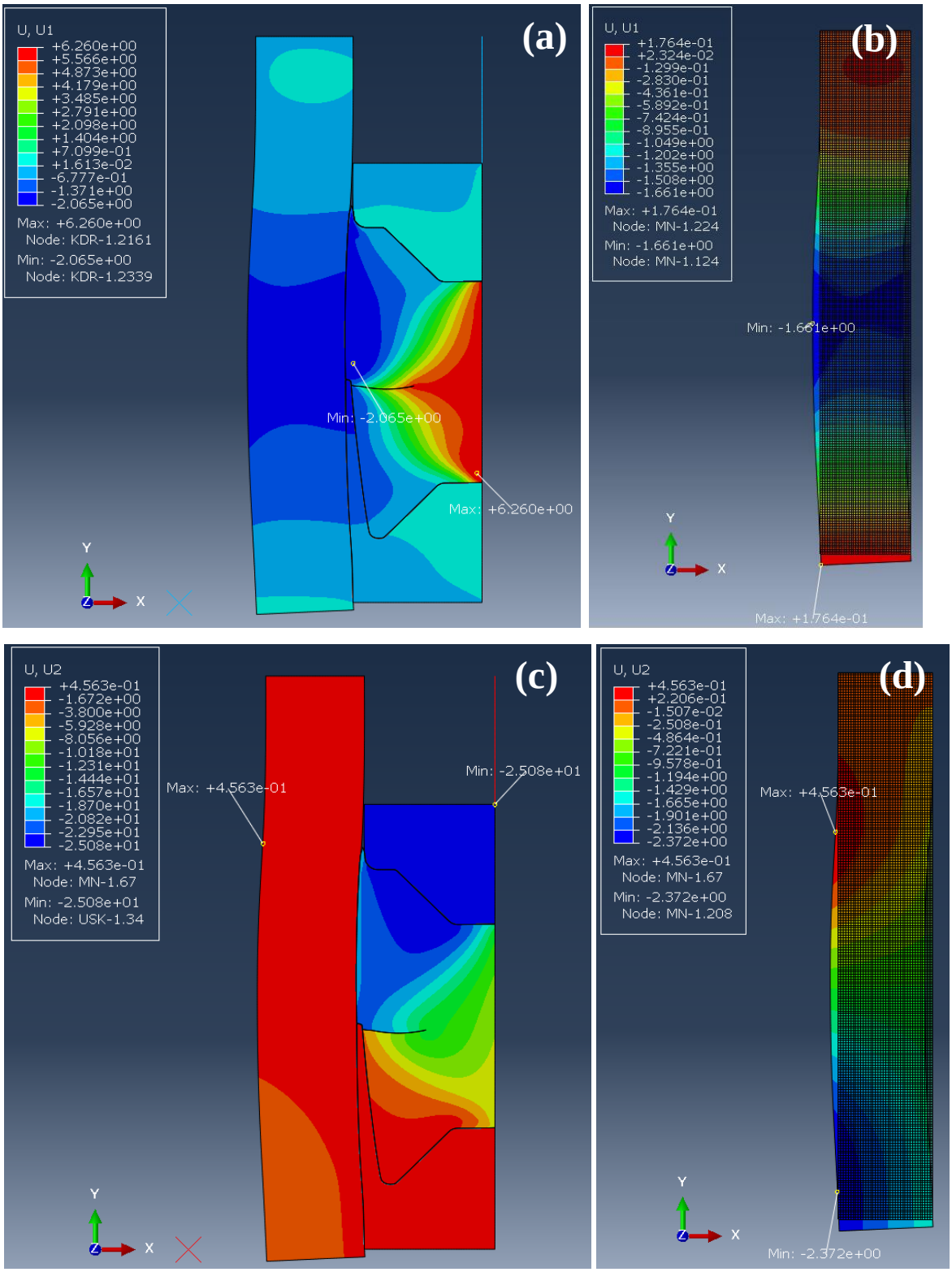

Figure B-50. FEA results of model 9 at 60 MPa of the equivalent pressure: (a) displacement to U1(x-axis) direction of the entire model, (b) displacement to U1(x-axis) direction of the mandrel, (c) displacement to U2(y-axis) direction of the entire model, (d) displacement to U2(y-axis) direction of the mandrel

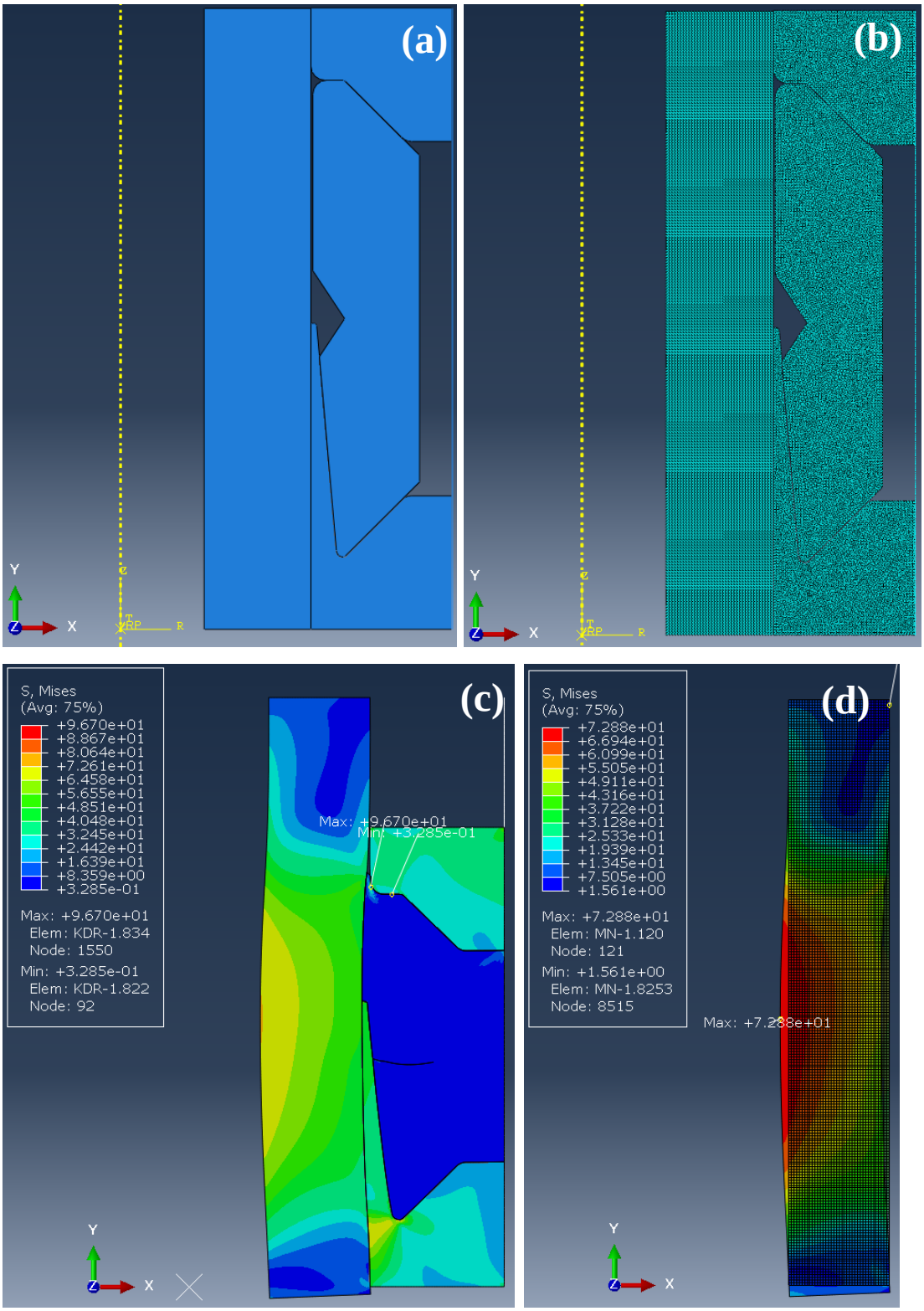

Figure B-51. FEA model and results of model 11 at 60 MPa of the equivalent pressure: (a) Model, (b) FEA model, (c) Mises stress of the entire model, (d) Mises stress of the mandrel

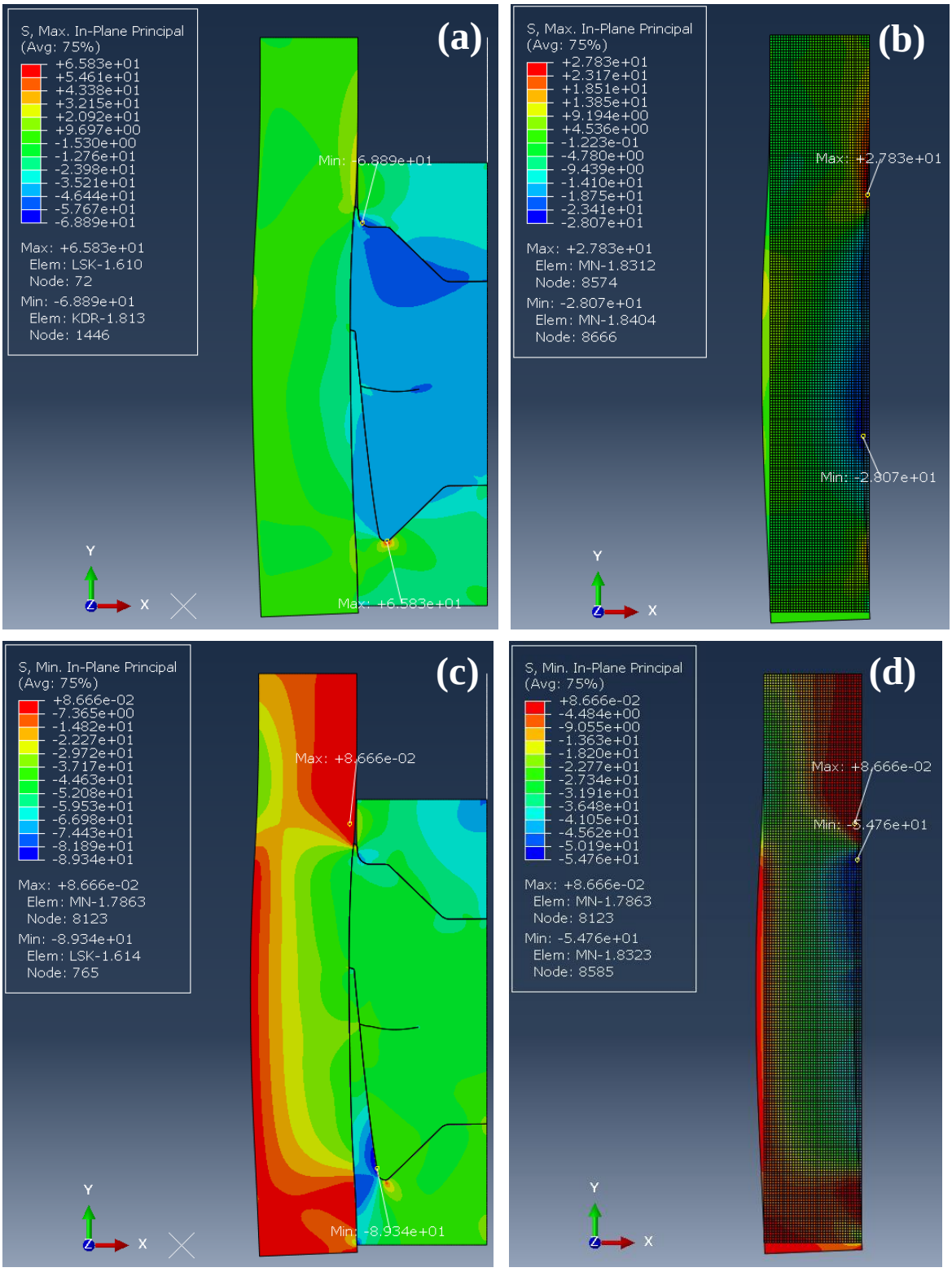

Figure B-52. FEA results of model 11 at 60 MPa of the equivalent pressure: (a) the maximum in-plane principal stress of the entire model, (b) the maximum in-plane principal stress of the mandrel, (c) the minimum in-plane principal stress of the entire model, (d) the minimum in-plane principal stress of the mandrel

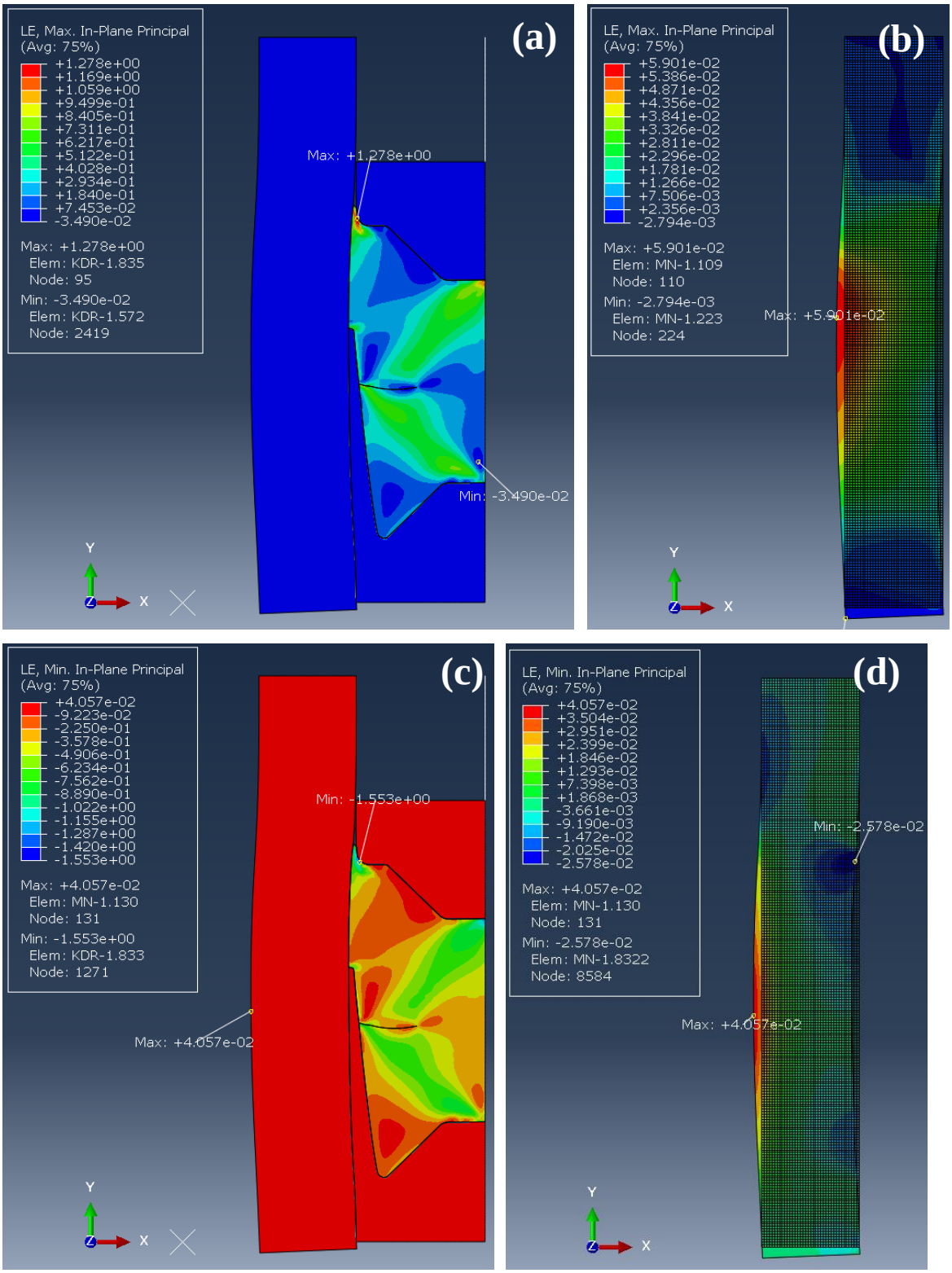

Figure B-53. FEA results of model 11 at 60 MPa of the equivalent pressure: (a) the maximum in-plane principal logarithmic strain of the entire model, (b) the maximum in-plane principal logarithmic strain of the mandrel, (c) the minimum in-plane principal logarithmic strain of the entire model, (d) the minimum in-plane principal logarithmic strain of the mandrel

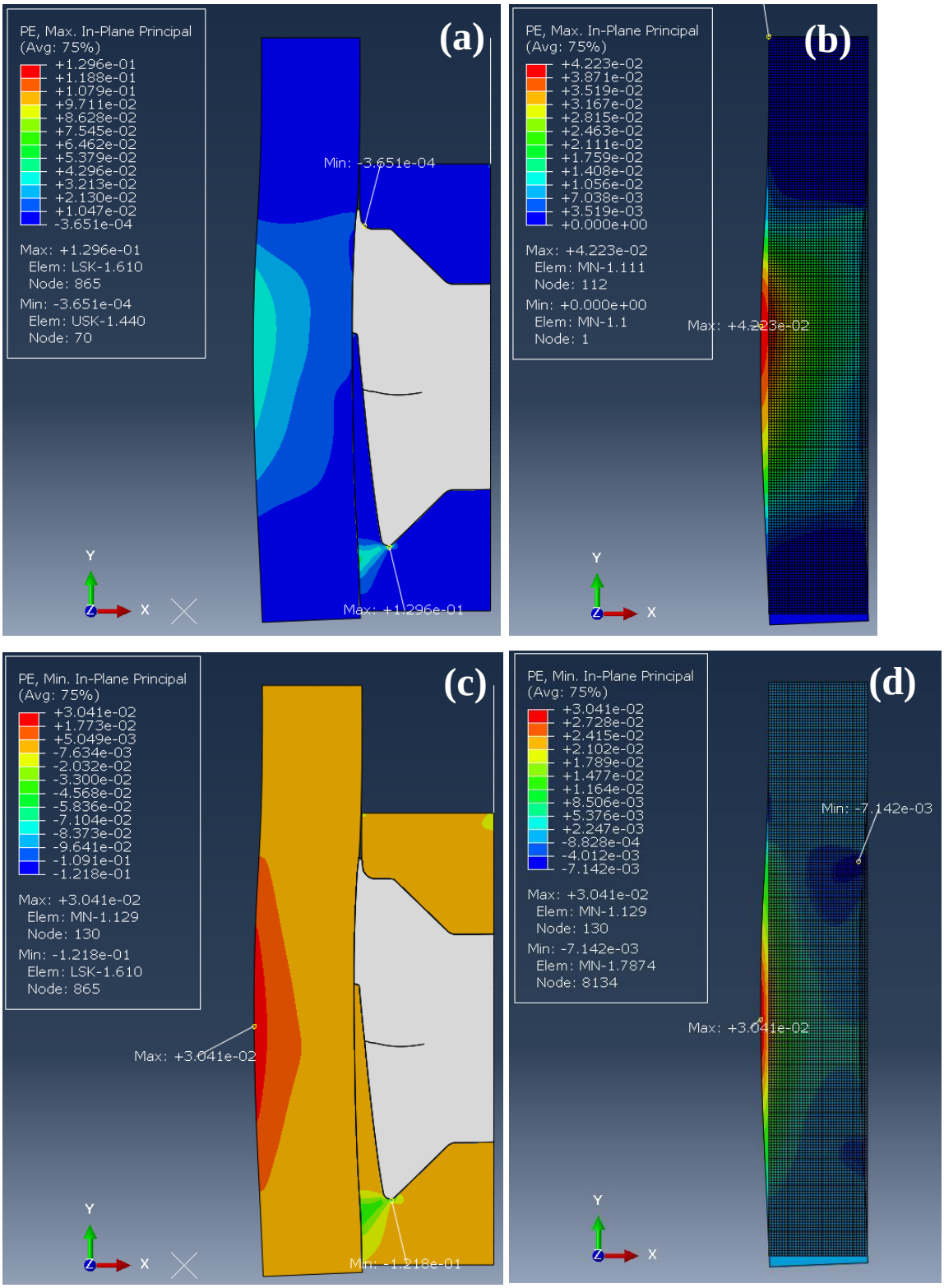

Figure B-54. FEA results of model 11 at 60 MPa of the equivalent pressure: (a) the maximum in-plane principal plastic strain of the entire model, (b) the maximum in-plane principal plastic strain of the mandrel, (c) the minimum in-plane principal plastic strain of the entire model, (d) the minimum in-plane principal plastic strain of the mandrel

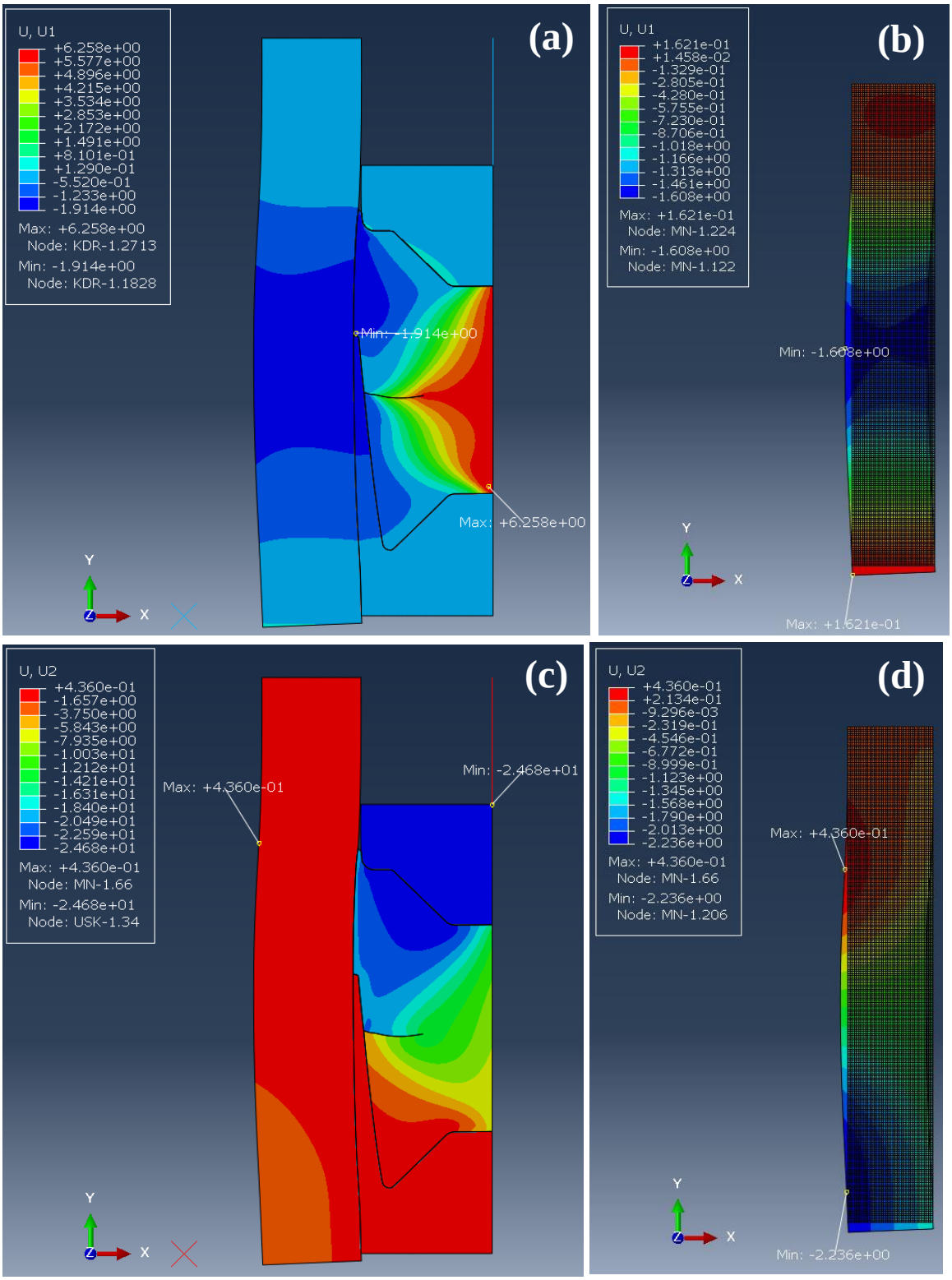

Figure B-55. FEA results of model 11 at 60 MPa of the equivalent pressure: (a) displacement to U1(x-axis) direction of the entire model, (b) displacement to U1(x-axis) direction of the mandrel, (c) displacement to U2(y-axis) direction of the entire model, (d) displacement to U2(y-axis) direction of the mandrel

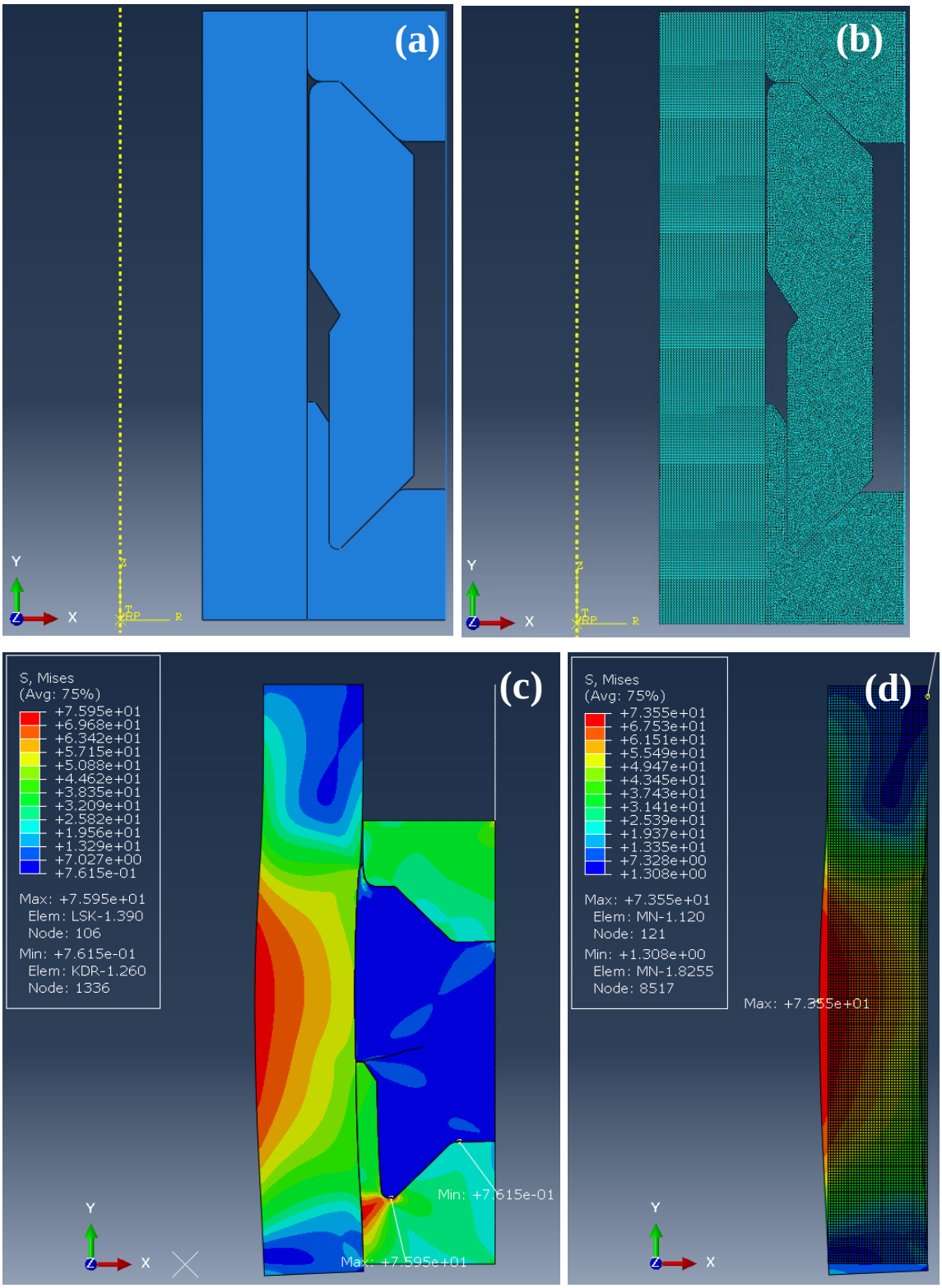

Figure B-56. FEA model and results of model 12 at 60 MPa of the equivalent pressure: (a) Model, (b) FEA model, (c) Mises stress of the entire model, (d) Mises stress of the mandrel

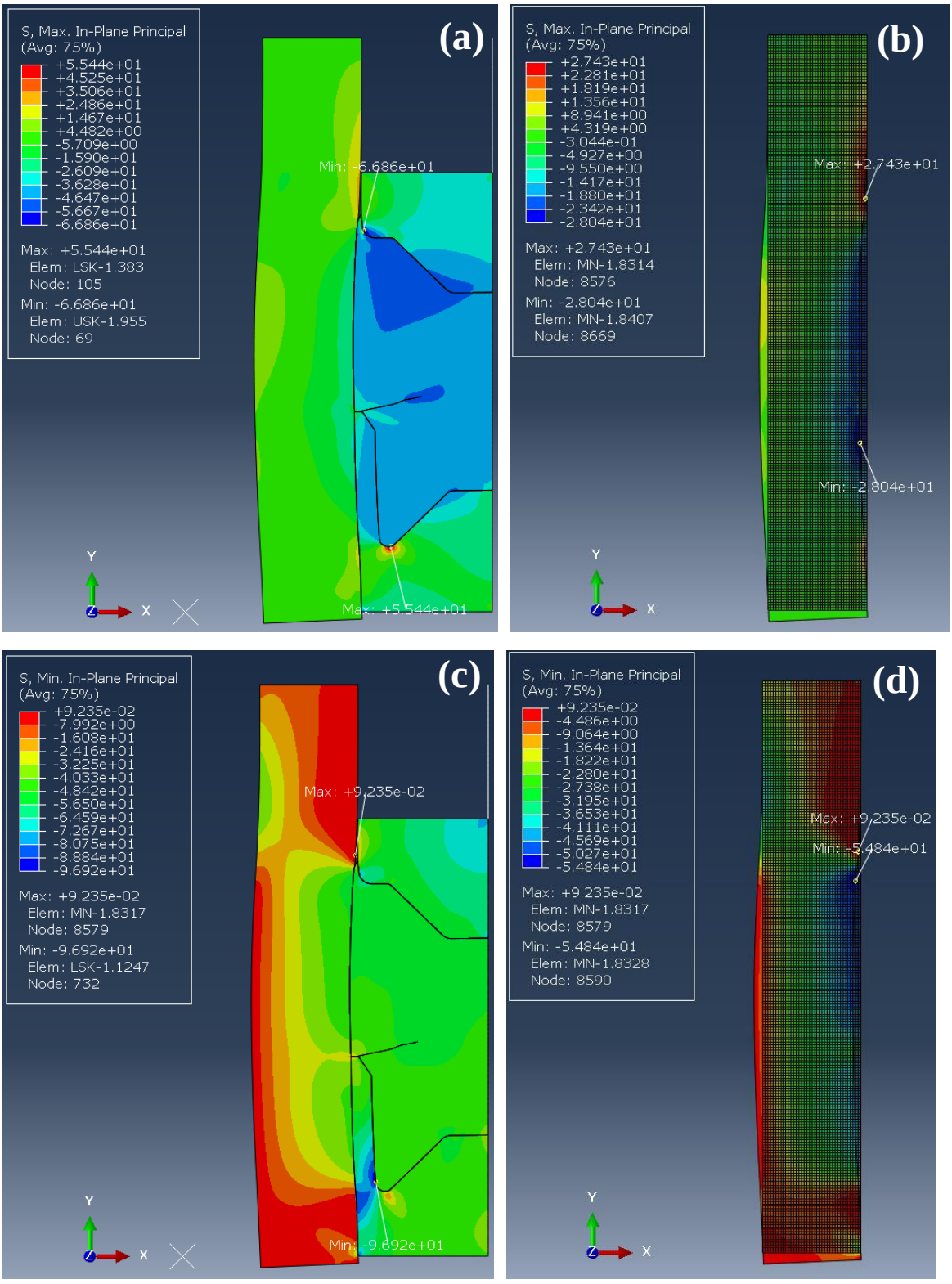

Figure B-57. FEA results of model 12 at 60 MPa of the equivalent pressure: (a) the maximum in-plane principal stress of the entire model, (b) the maximum in-plane principal stress of the mandrel, (c) the minimum in-plane principal stress of the entire model, (d) the minimum in-plane principal stress of the mandrel

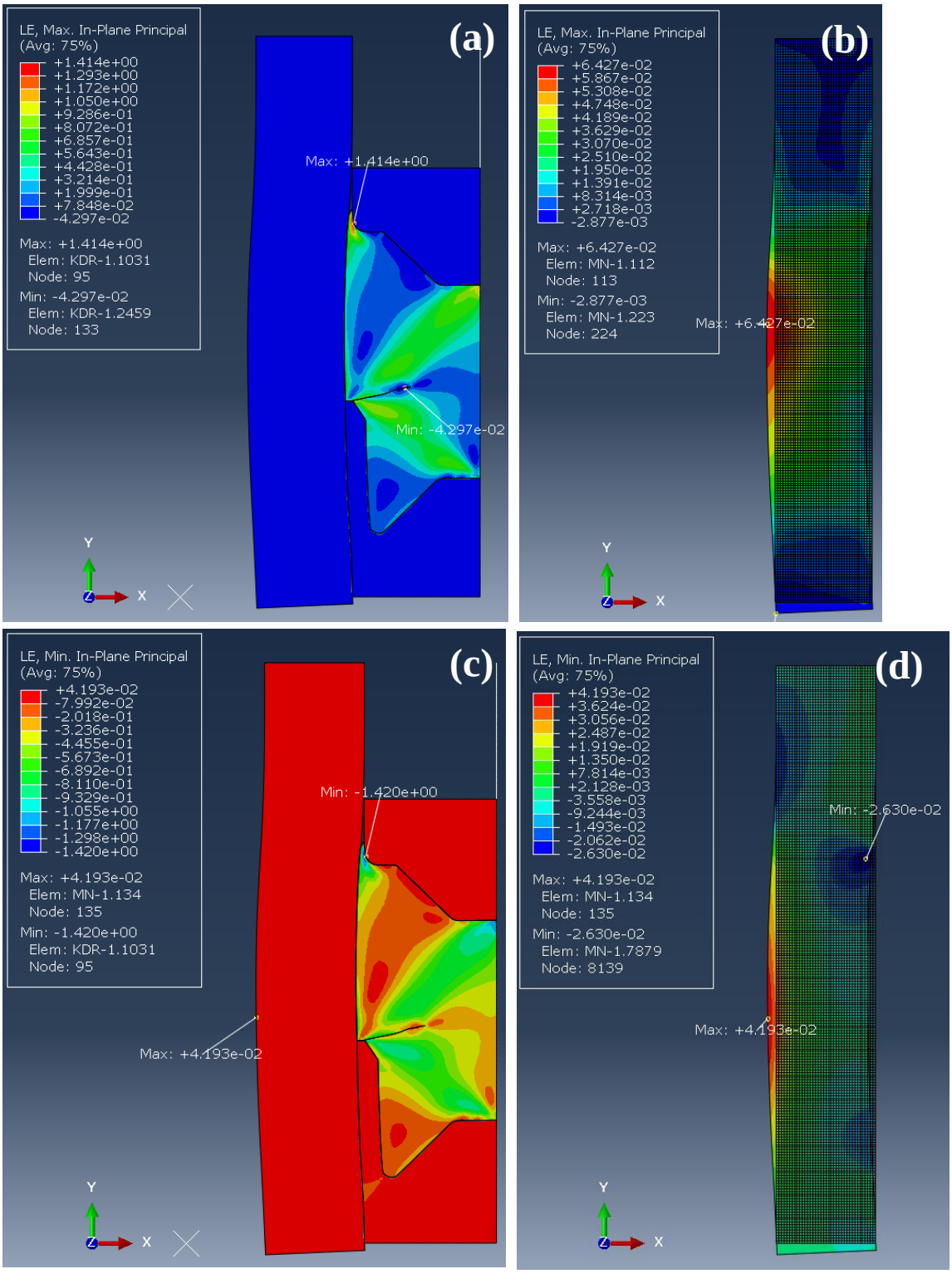

Figure B-58. FEA results of model 12 at 60 MPa of the equivalent pressure: (a) the maximum in-plane principal logarithmic strain of the entire model, (b) the maximum in-plane principal logarithmic strain of the mandrel, (c) the minimum in-plane principal logarithmic strain of the entire model, (d) the minimum in-plane principal logarithmic strain of the mandrel

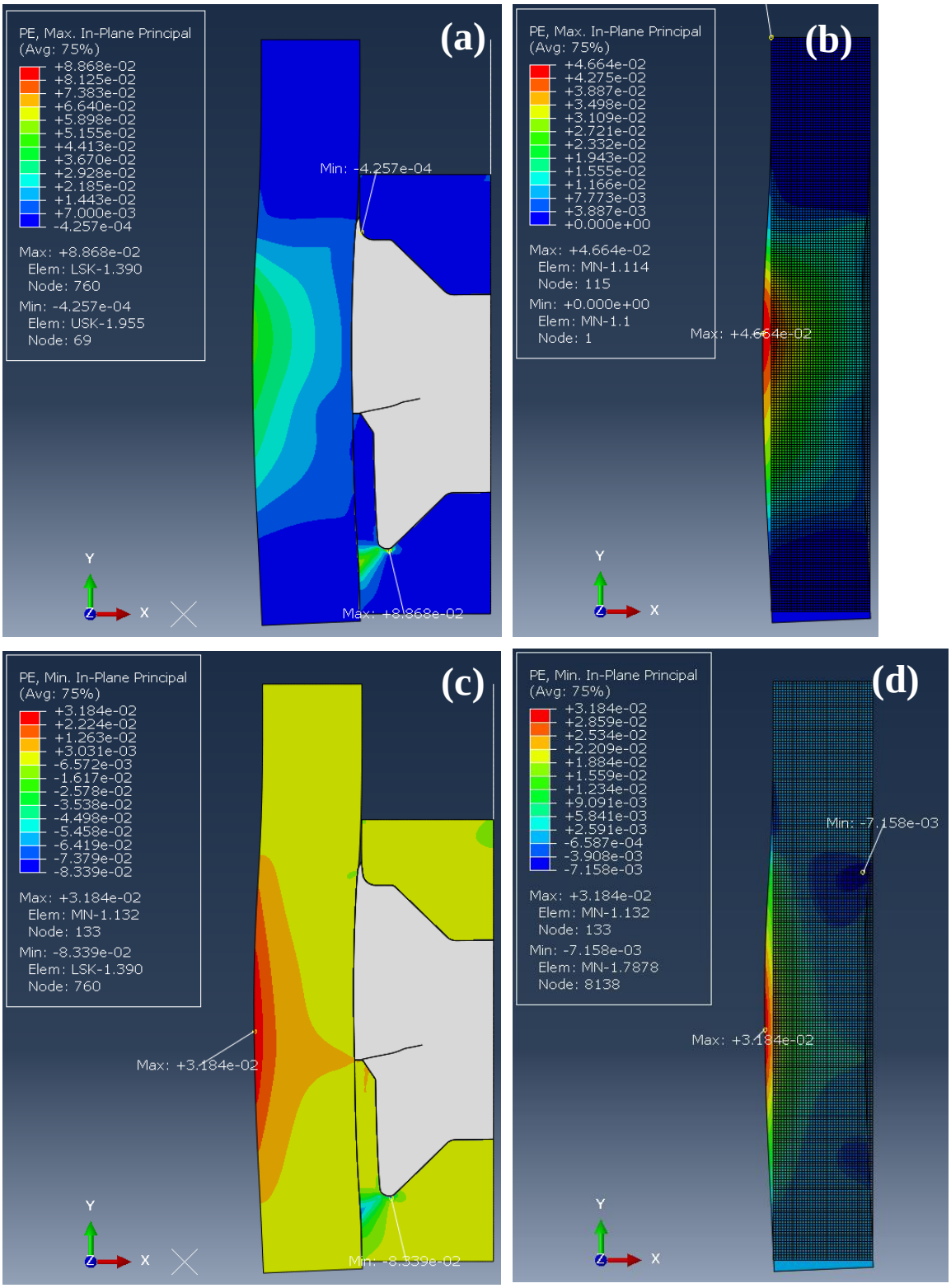

Figure B-59. FEA results of model 12 at 60 MPa of the equivalent pressure: (a) the maximum in-plane principal plastic strain of the entire model, (b) the maximum in-plane principal plastic strain of the mandrel, (c) the minimum in-plane principal plastic strain of the entire model, (d) the minimum in-plane principal plastic strain of the mandrel

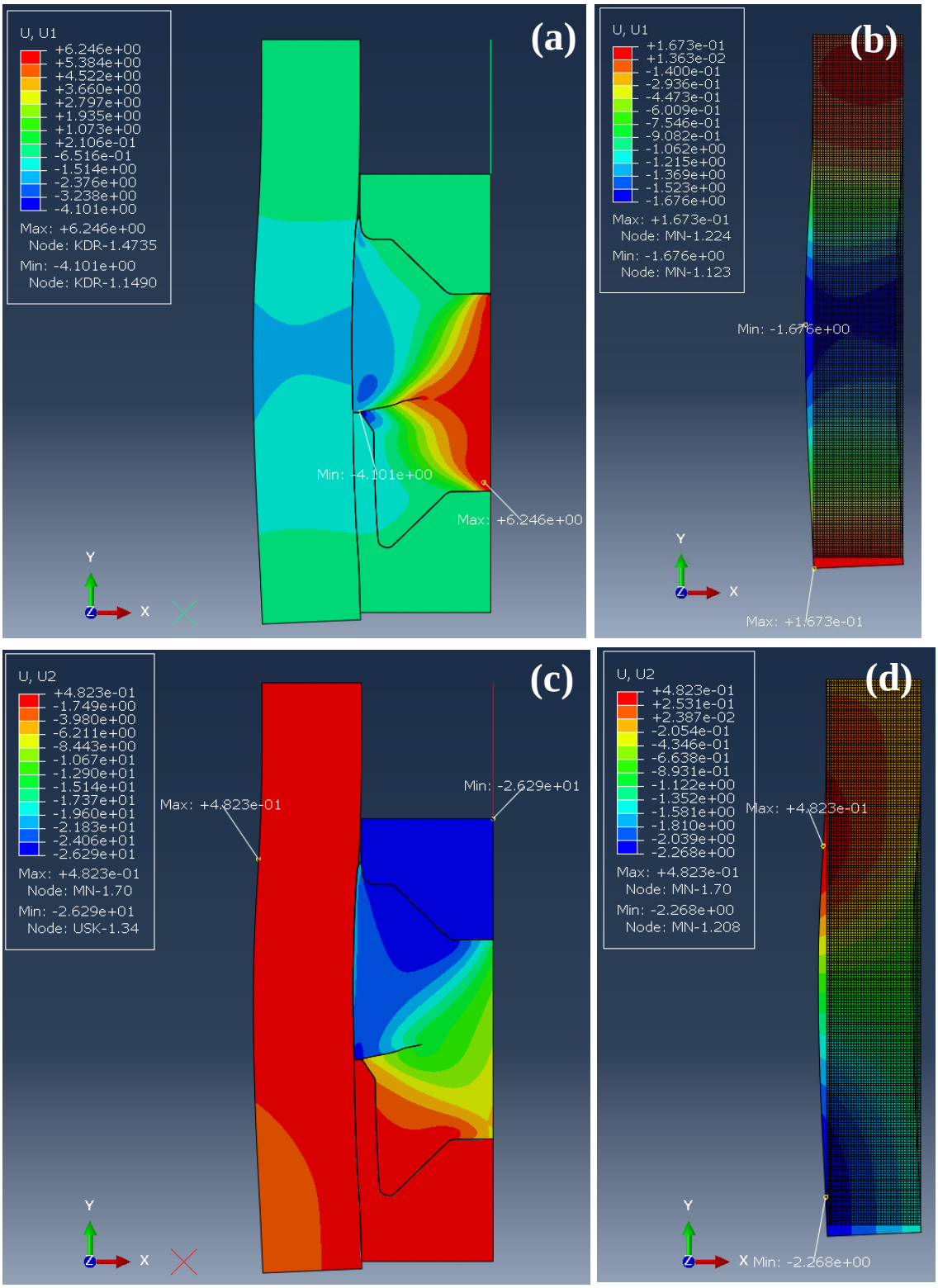

Figure B-60. FEA results of model 12 at 60 MPa of the equivalent pressure: (a) displacement to U1(x-axis) direction of the entire model, (b) displacement to U1(x-axis) direction of the mandrel, (c) displacement to U2(y-axis) direction of the entire model, (d) displacement to U2(y-axis) direction of the mandrel

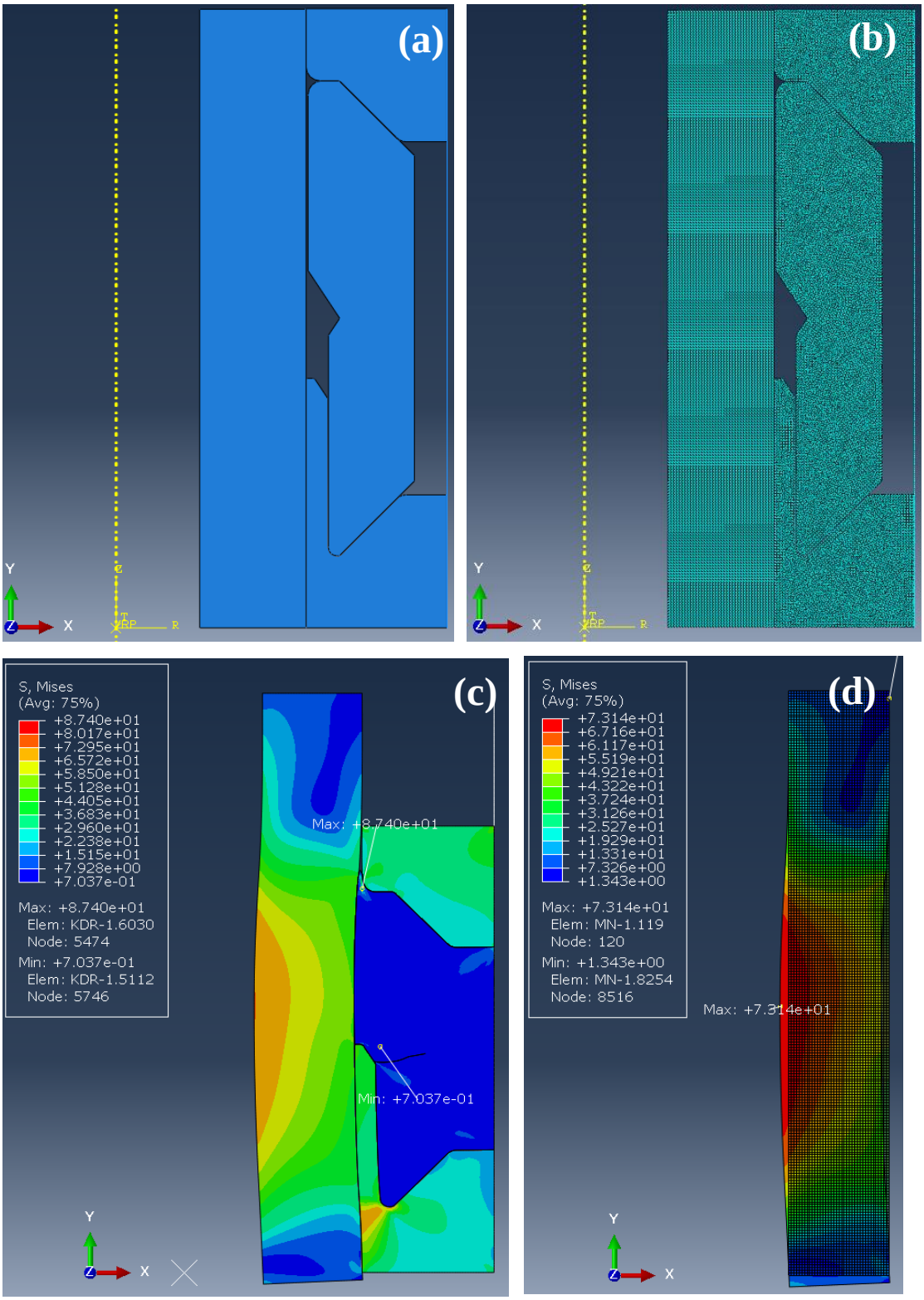

Figure B-61. FEA model and results of model 13 at 60 MPa of the equivalent pressure: (a) Model, (b) FEA model, (c) Mises stress of the entire model, (d) Mises stress of the mandrel

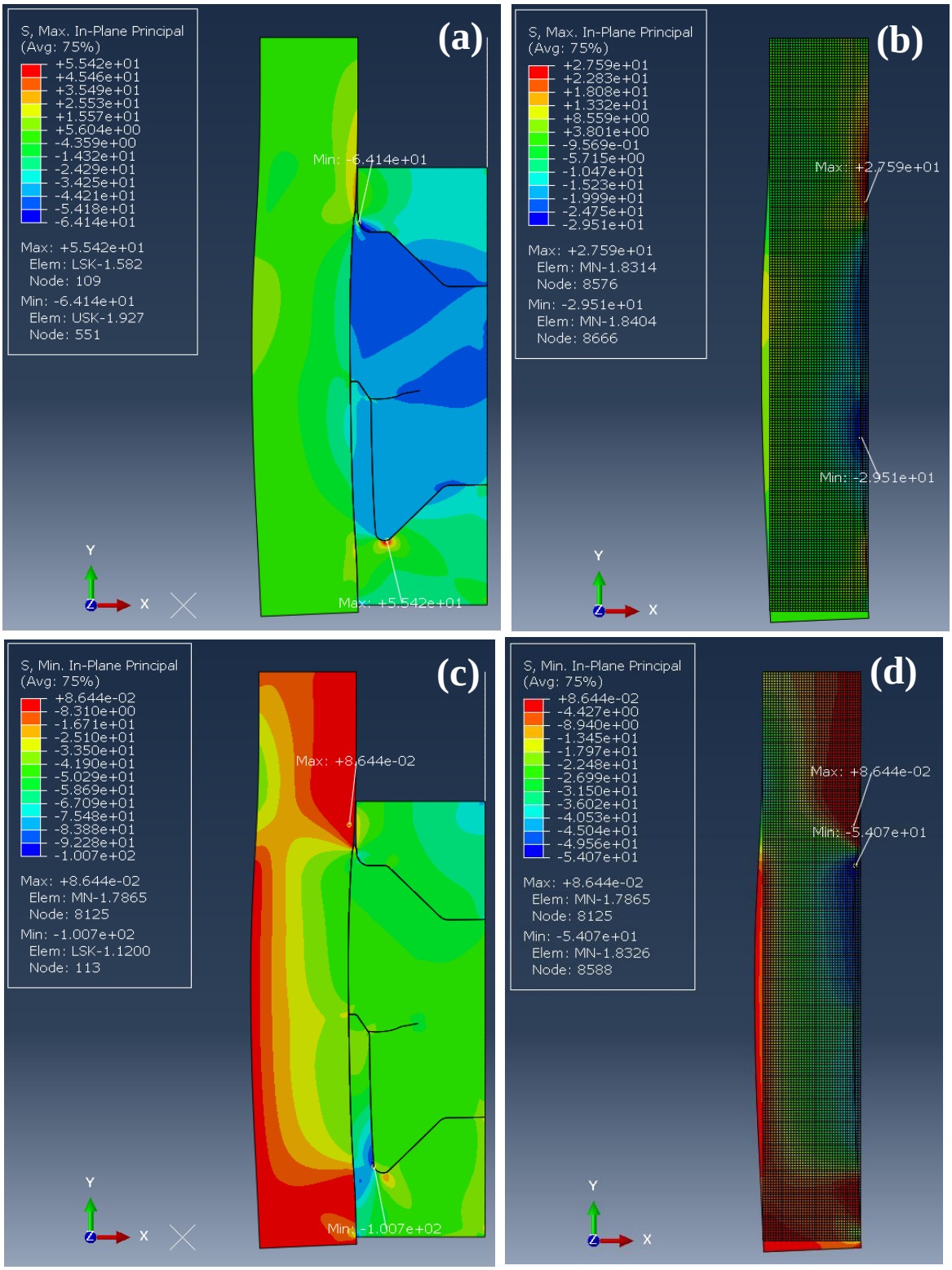

Figure B-62. FEA results of model 13 at 60 MPa of the equivalent pressure: (a) the maximum in-plane principal stress of the entire model, (b) the maximum in-plane principal stress of the mandrel, (c) the minimum in-plane principal stress of the entire model, (d) the minimum in-plane principal stress of the mandrel

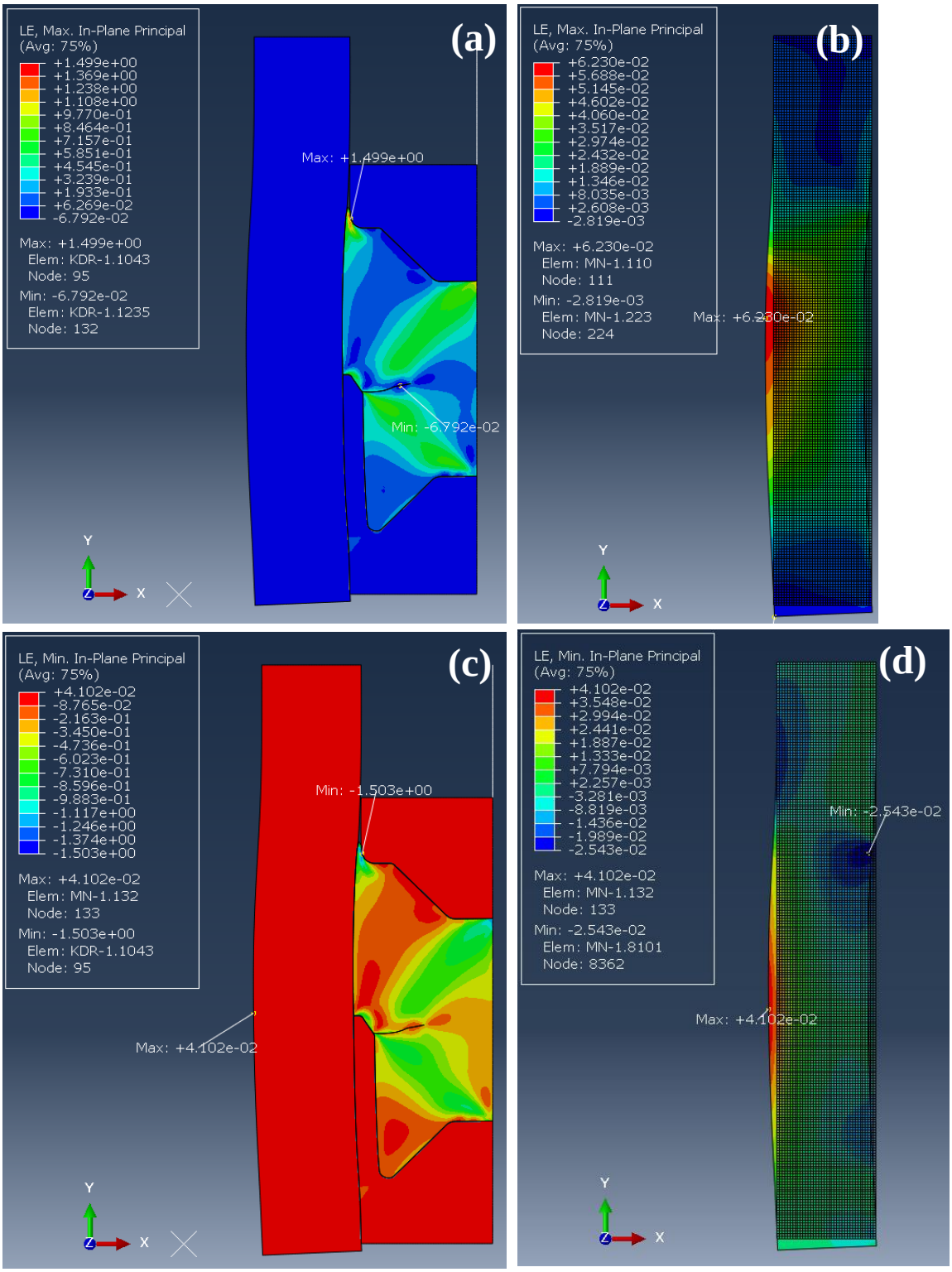

Figure B-63. FEA results of model 13 at 60 MPa of the equivalent pressure: (a) the maximum in-plane principal logarithmic strain of the entire model, (b) the maximum in-plane principal logarithmic strain of the mandrel, (c) the minimum in-plane principal logarithmic strain of the entire model, (d) the minimum in-plane principal logarithmic strain of the mandrel

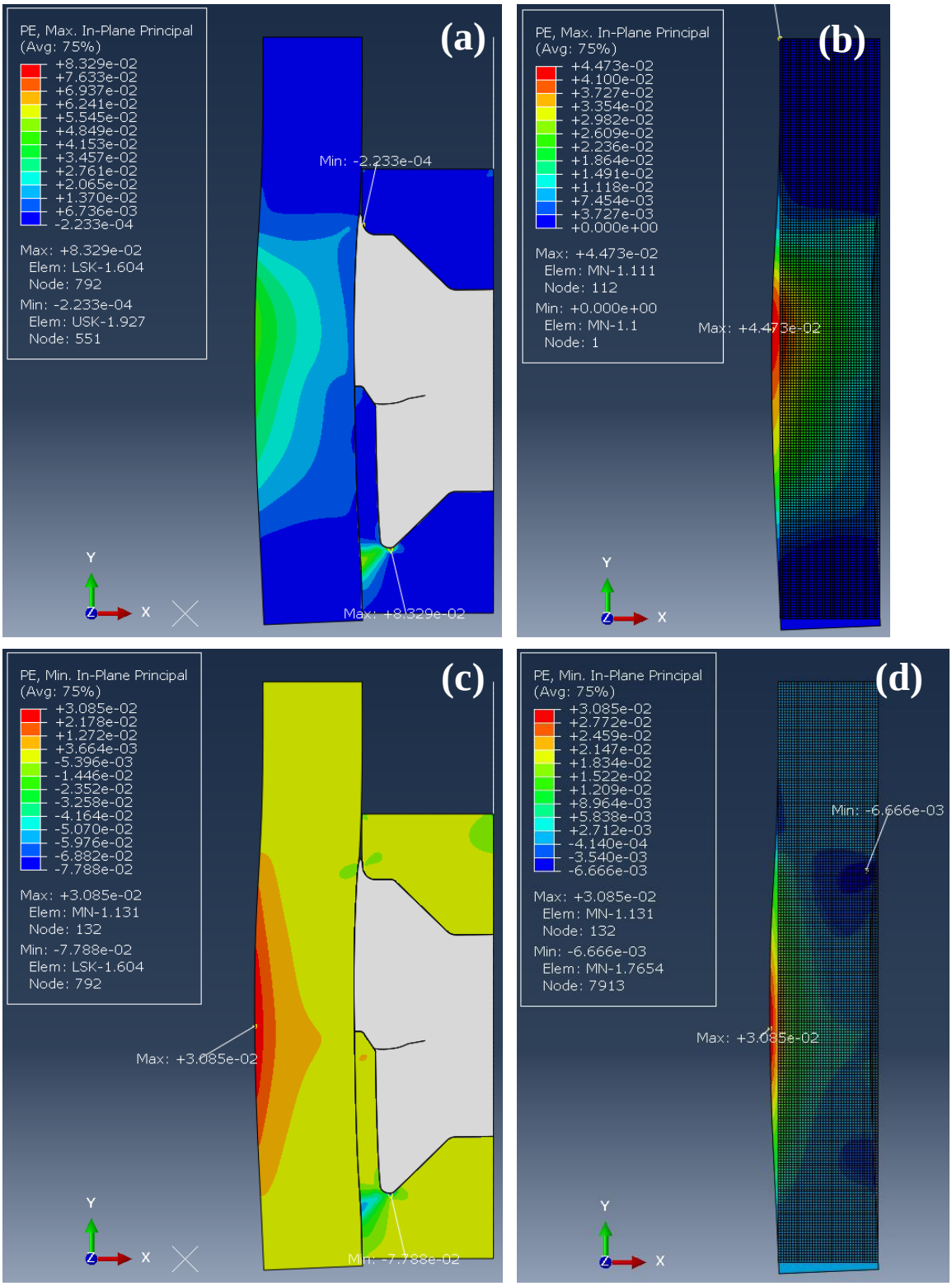

Figure B-64. FEA results of model 13 at 60 MPa of the equivalent pressure: (a) the maximum in-plane principal plastic strain of the entire model, (b) the maximum in-plane principal plastic strain of the mandrel, (c) the minimum in-plane principal plastic strain of the entire model, (d) the minimum in-plane principal plastic strain of the mandrel

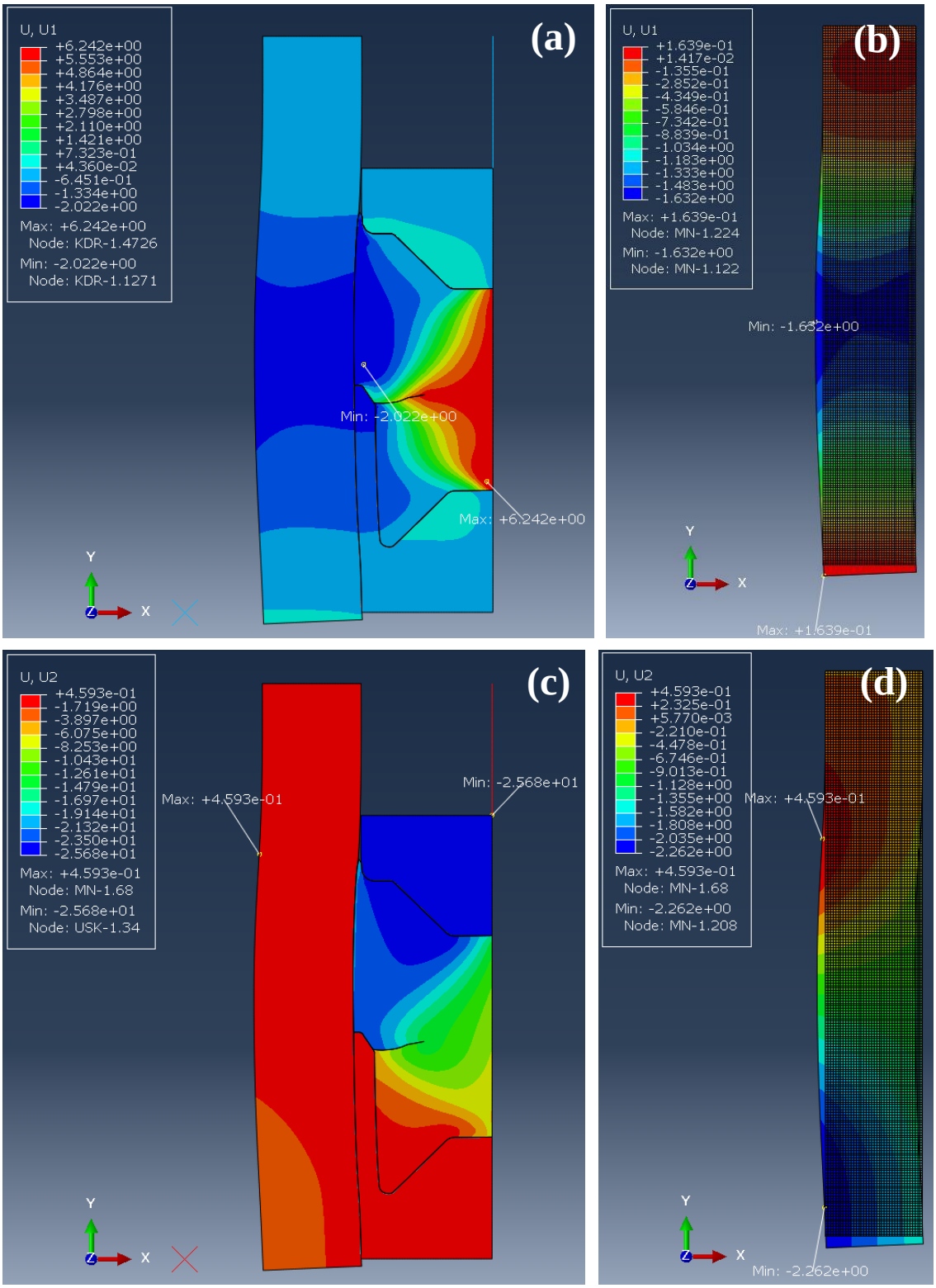

Figure B-65. FEA results of model 13 at 60 MPa of the equivalent pressure: (a) displacement to U1(x-axis) direction of the entire model, (b) displacement to U1(x-axis) direction of the mandrel, (c) displacement to U2(y-axis) direction of the entire model, (d) displacement to U2(y-axis) direction of the mandrel

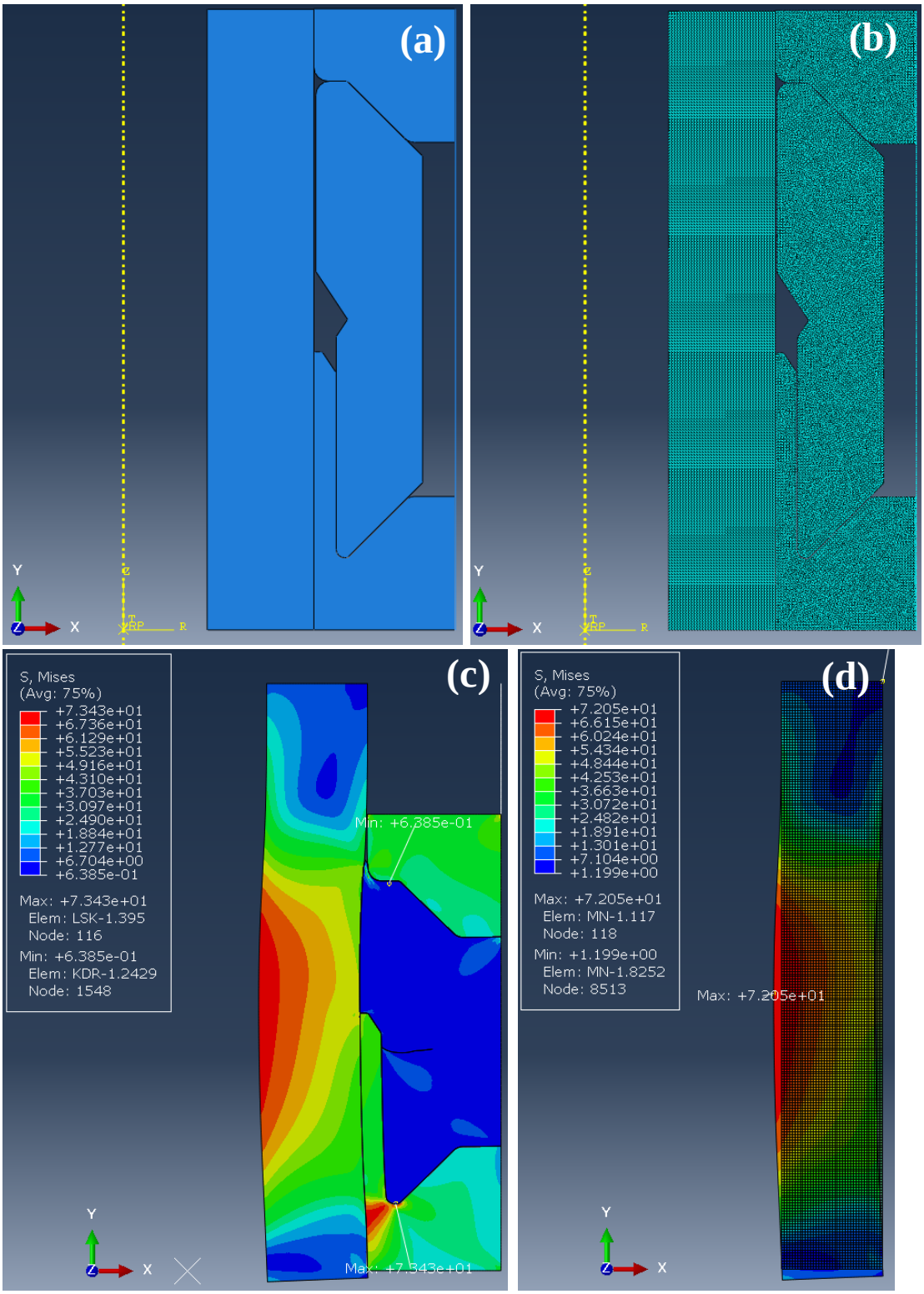

Figure B-66. FEA model and results of model 14 at 60 MPa of the equivalent pressure: (a) Model, (b) FEA model, (c) Mises stress of the entire model, (d) Mises stress of the mandrel

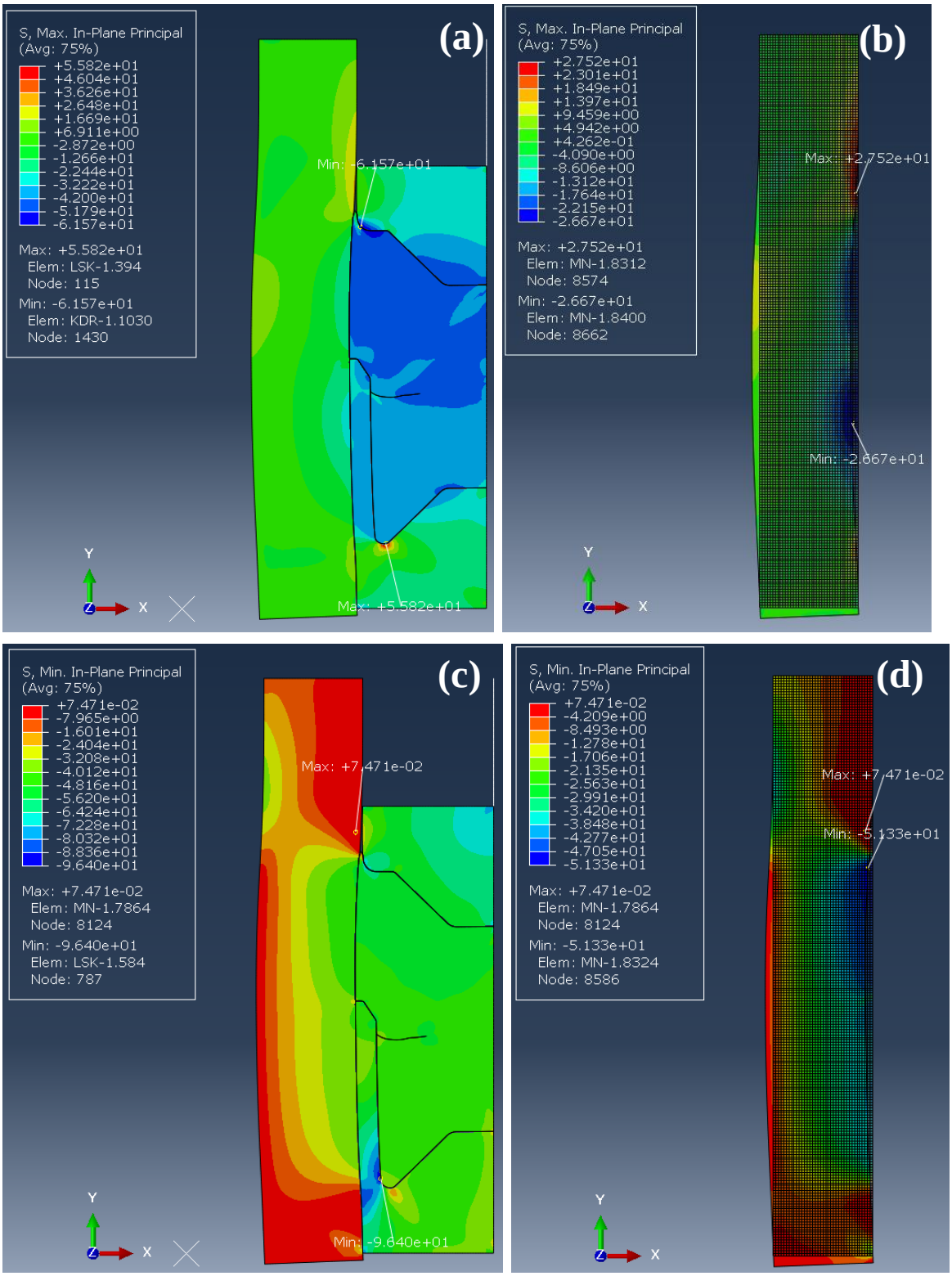

Figure B-67. FEA results of model 14 at 60 MPa of the equivalent pressure: (a) the maximum in-plane principal stress of the entire model, (b) the maximum in-plane principal stress of the mandrel, (c) the minimum in-plane principal stress of the entire model, (d) the minimum in-plane principal stress of the mandrel

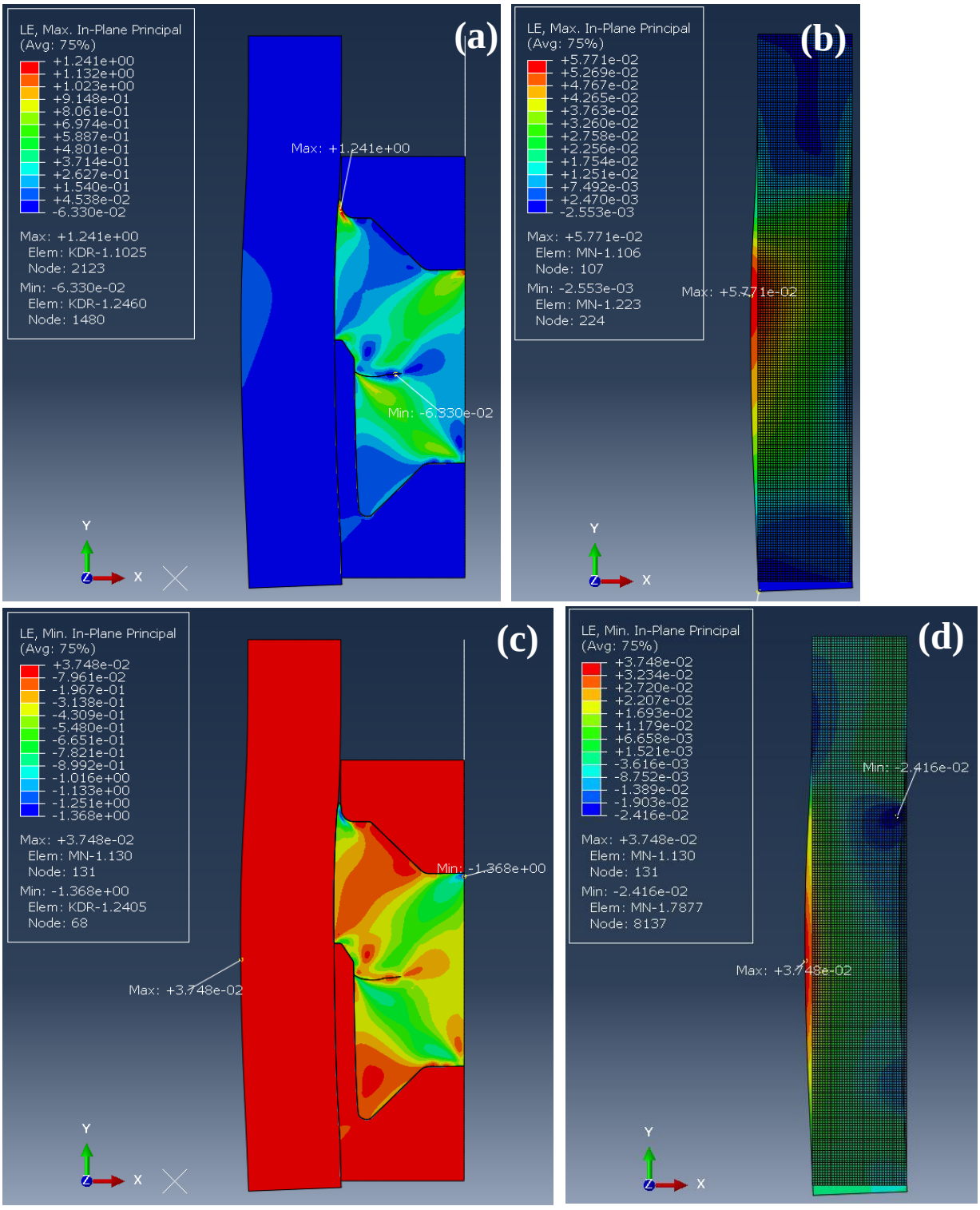

Figure B-68. FEA results of model 14 at 60 MPa of the equivalent pressure: (a) the maximum in-plane principal logarithmic strain of the entire model, (b) the maximum in-plane principal logarithmic strain of the mandrel, (c) the minimum in-plane principal logarithmic strain of the entire model, (d) the minimum in-plane principal logarithmic strain of the mandrel

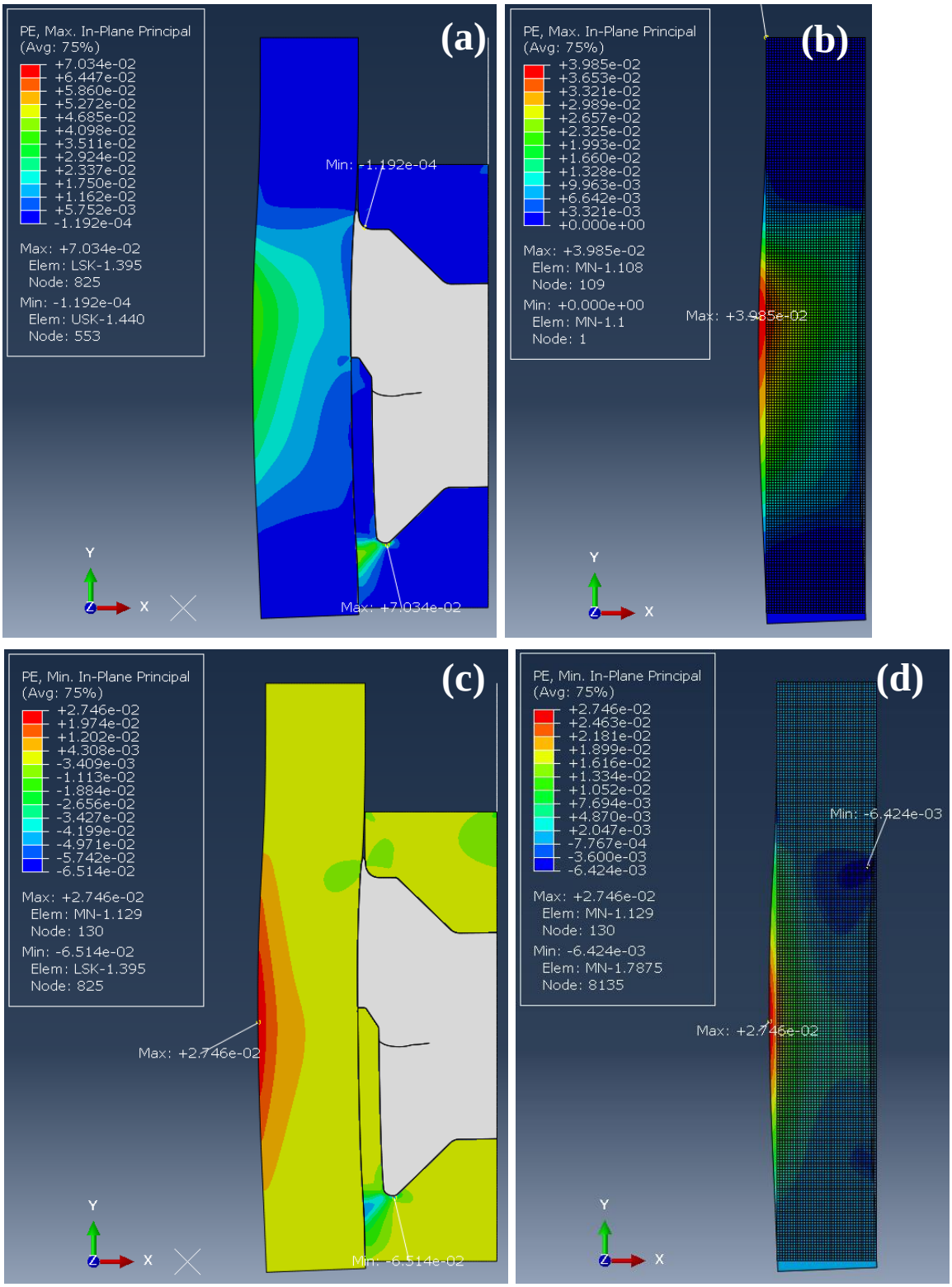

Figure B-69. FEA results of model 14 at 60 MPa of the equivalent pressure: (a) the maximum in-plane principal plastic strain of the entire model, (b) the maximum in-plane principal plastic strain of the mandrel, (c) the minimum in-plane principal plastic strain of the entire model, (d) the minimum in-plane principal plastic strain of the mandrel

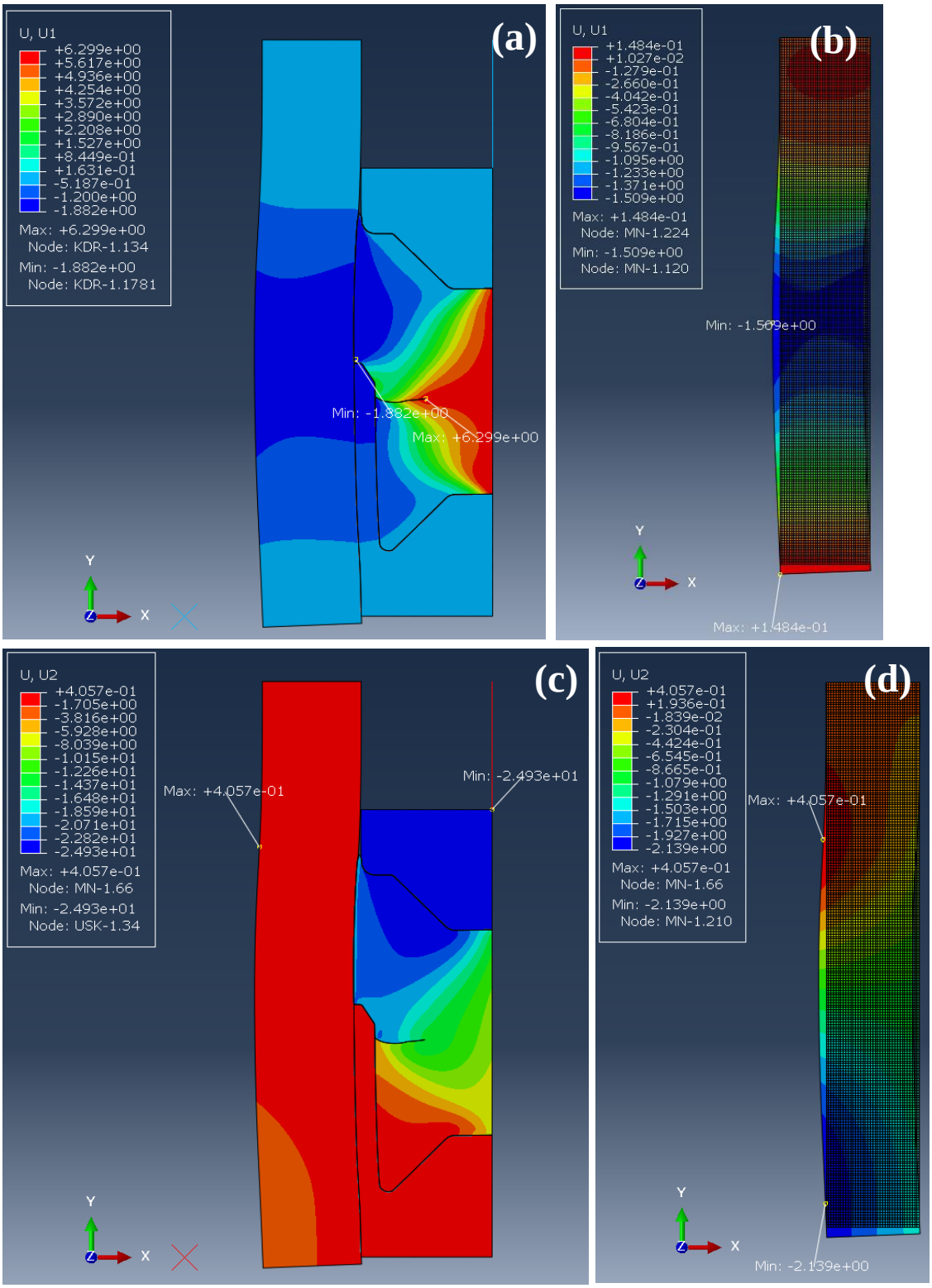

Figure B-70. FEA results of model 14 at 60 MPa of the equivalent pressure: (a) displacement to U1(x-axis) direction of the entire model, (b) displacement to U1(x-axis) direction of the mandrel, (c) displacement to U2(y-axis) direction of the entire model, (d) displacement to U2(y-axis) direction of the mandrel

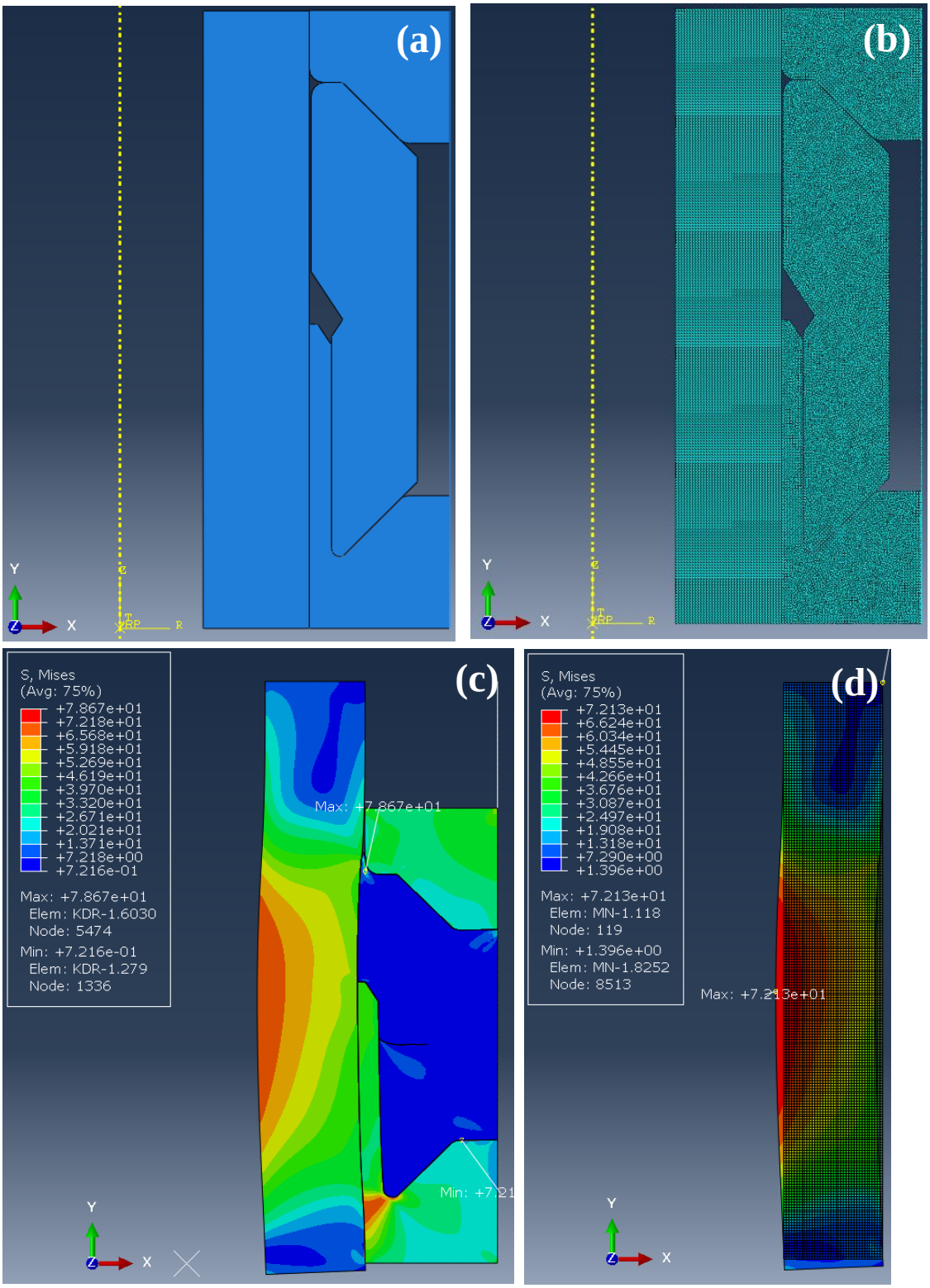

Figure B-71. FEA model and results of model 15 at 60 MPa of the equivalent pressure: (a) Model, (b) FEA model, (c) Mises stress of the entire model, (d) Mises stress of the mandrel

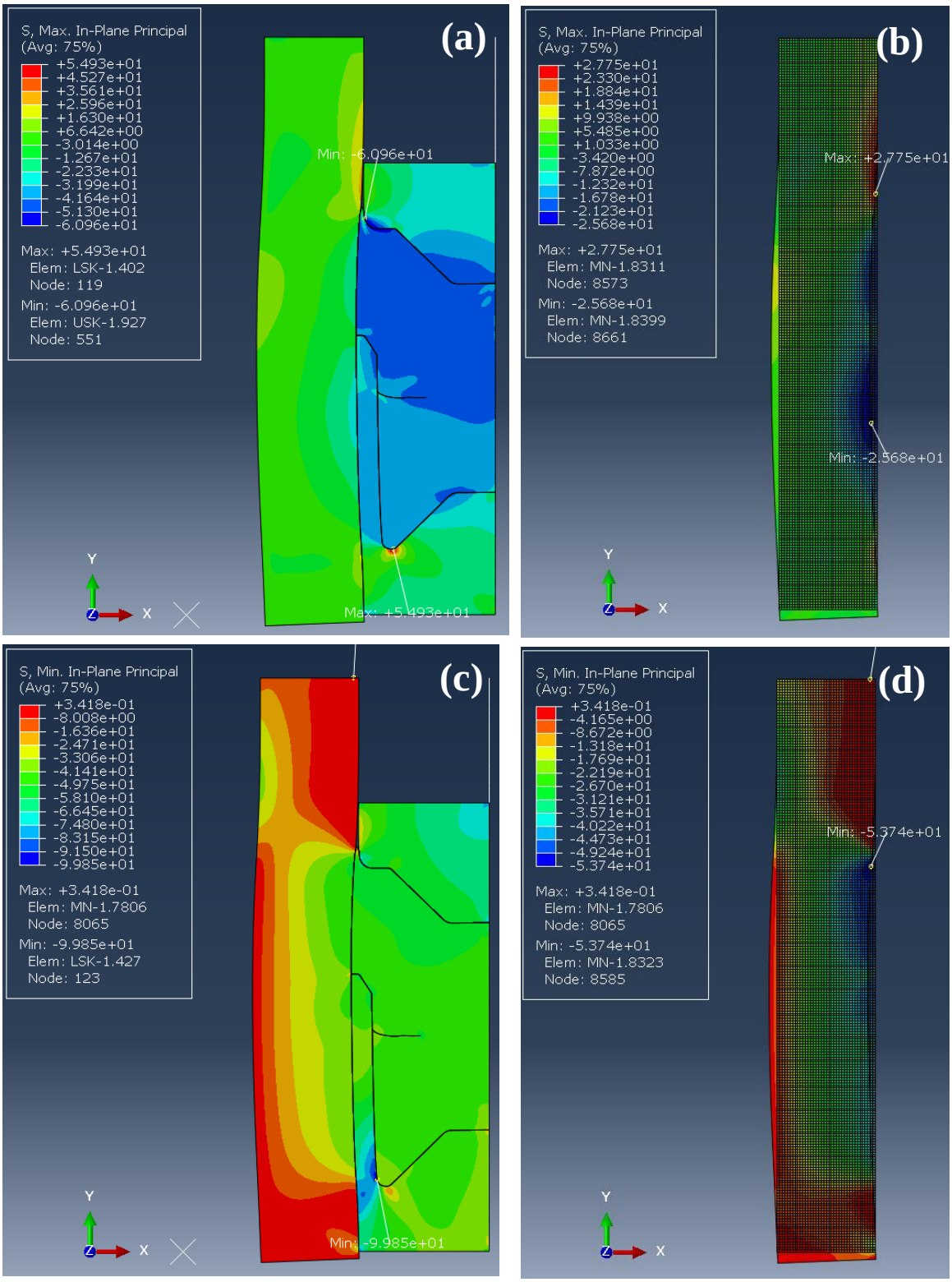

Figure B-72. FEA results of model 15 at 60 MPa of the equivalent pressure: (a) the maximum in-plane principal stress of the entire model, (b) the maximum in-plane principal stress of the mandrel, (c) the minimum in-plane principal stress of the entire model, (d) the minimum in-plane principal stress of the mandrel

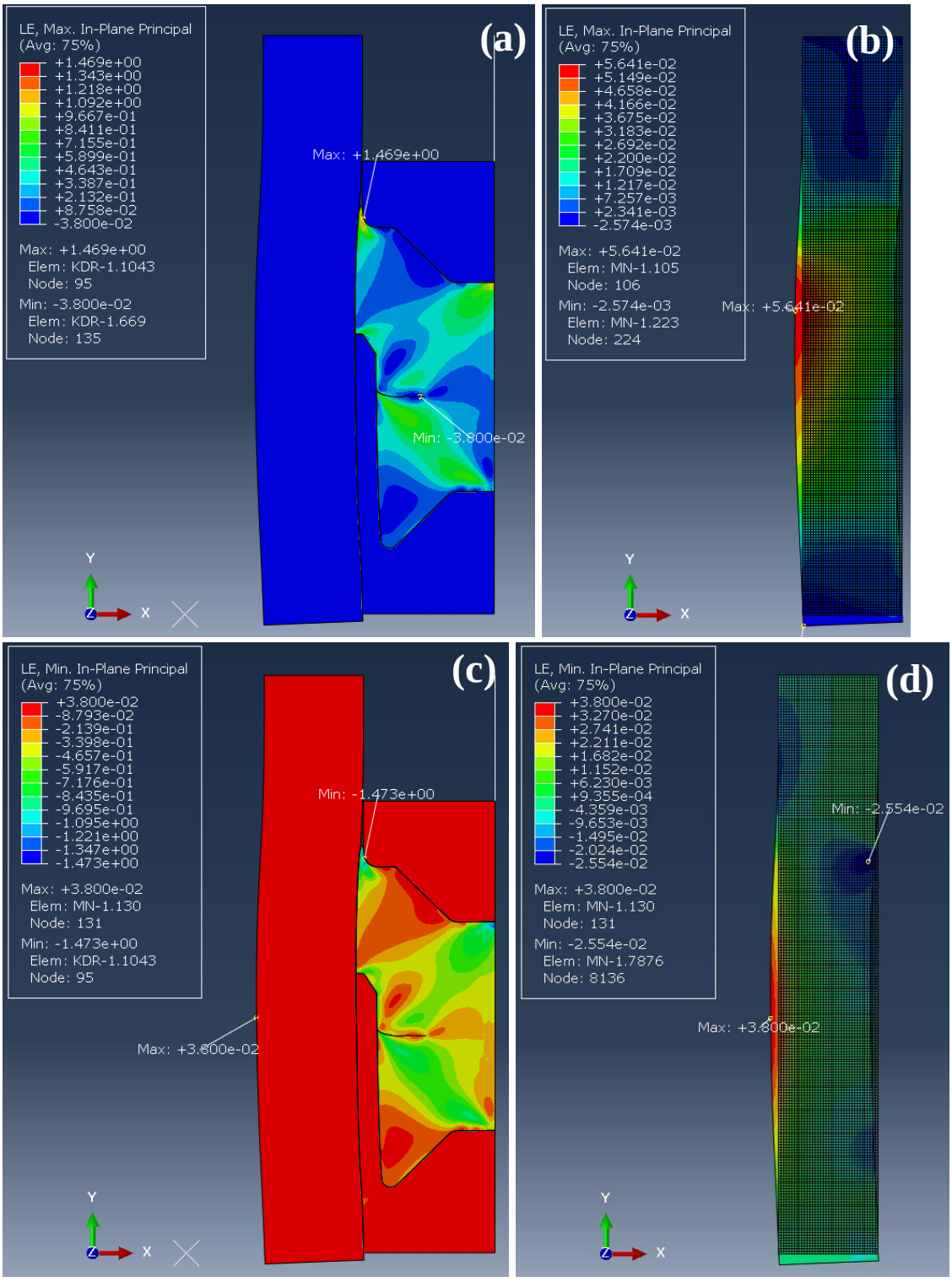

Figure B-73. FEA results of model 15 at 60 MPa of the equivalent pressure: (a) the maximum in-plane principal logarithmic strain of the entire model, (b) the maximum in-plane principal logarithmic strain of the mandrel, (c) the minimum in-plane principal logarithmic strain of the entire model, (d) the minimum in-plane principal logarithmic strain of the mandrel

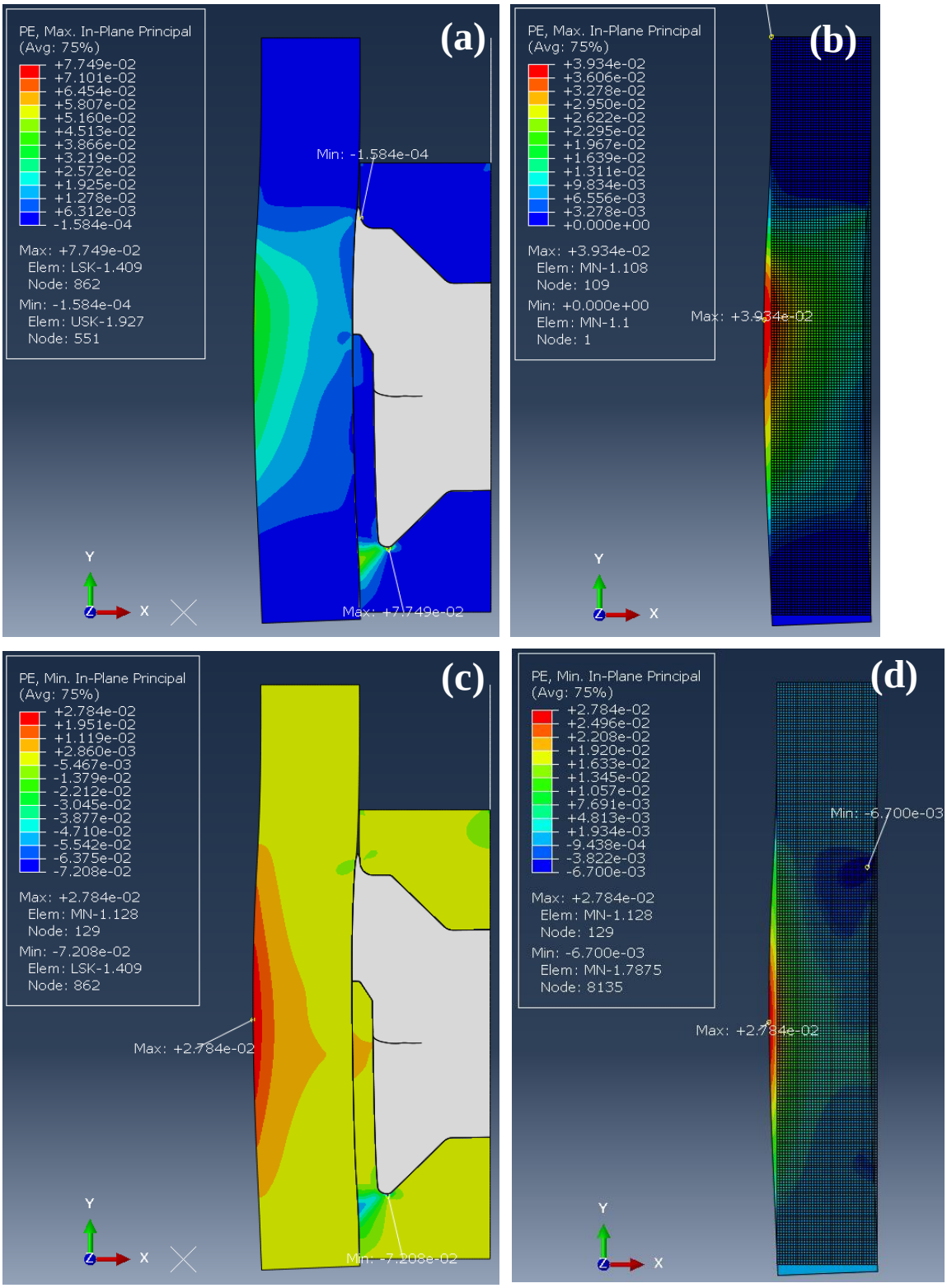

Figure B-74. FEA results of model 15 at 60 MPa of the equivalent pressure: (a) the maximum in-plane principal plastic strain of the entire model, (b) the maximum in-plane principal plastic strain of the mandrel, (c) the minimum in-plane principal plastic strain of the entire model, (d) the minimum in-plane principal plastic strain of the mandrel

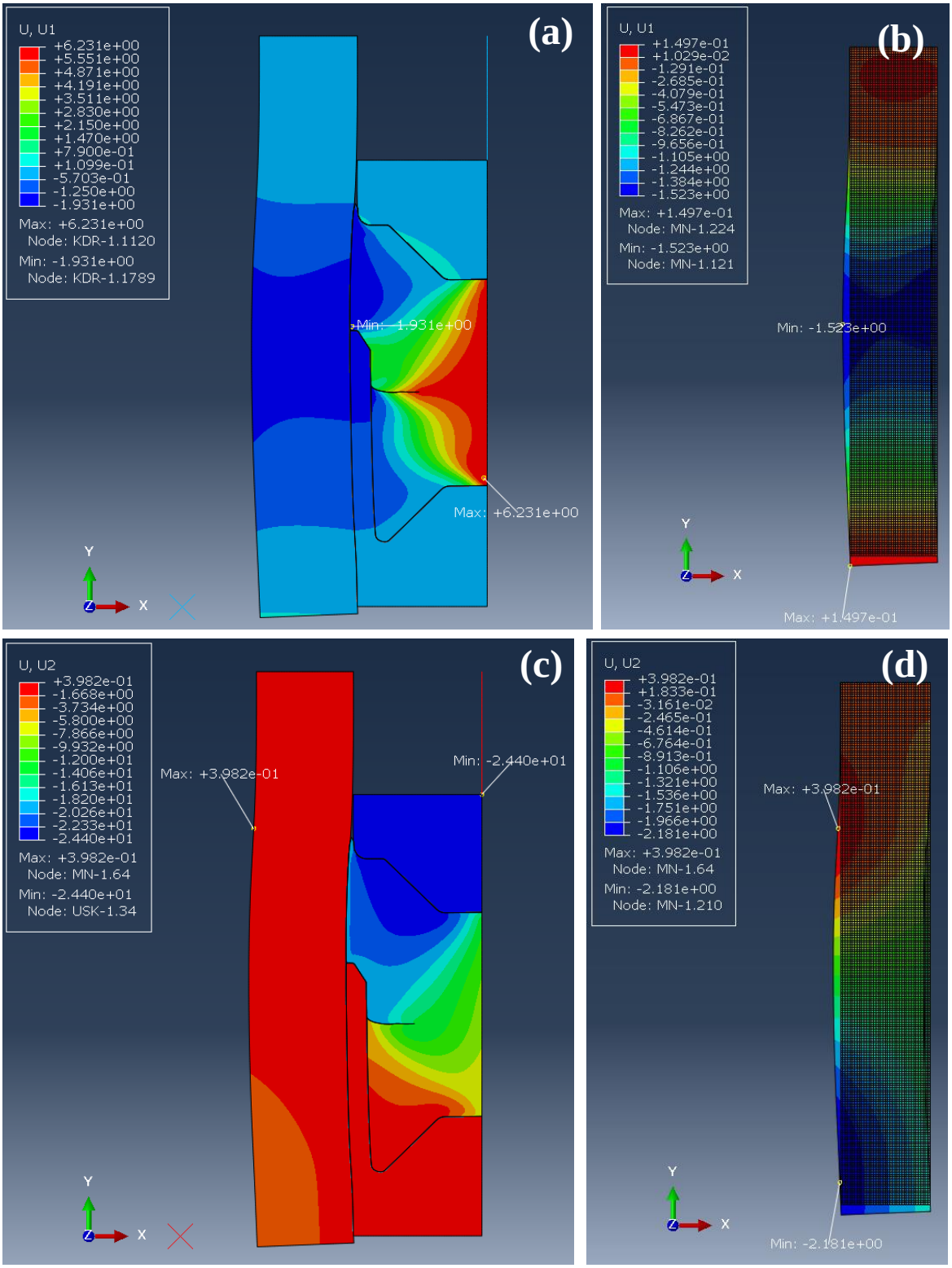

Figure B-75. FEA results of model 15 at 60 MPa of the equivalent pressure: (a) displacement to U1(x-axis) direction of the entire model, (b) displacement to U1(x-axis) direction of the mandrel, (c) displacement to U2(y-axis) direction of the entire model, (d) displacement to U2(y-axis) direction of the mandrel

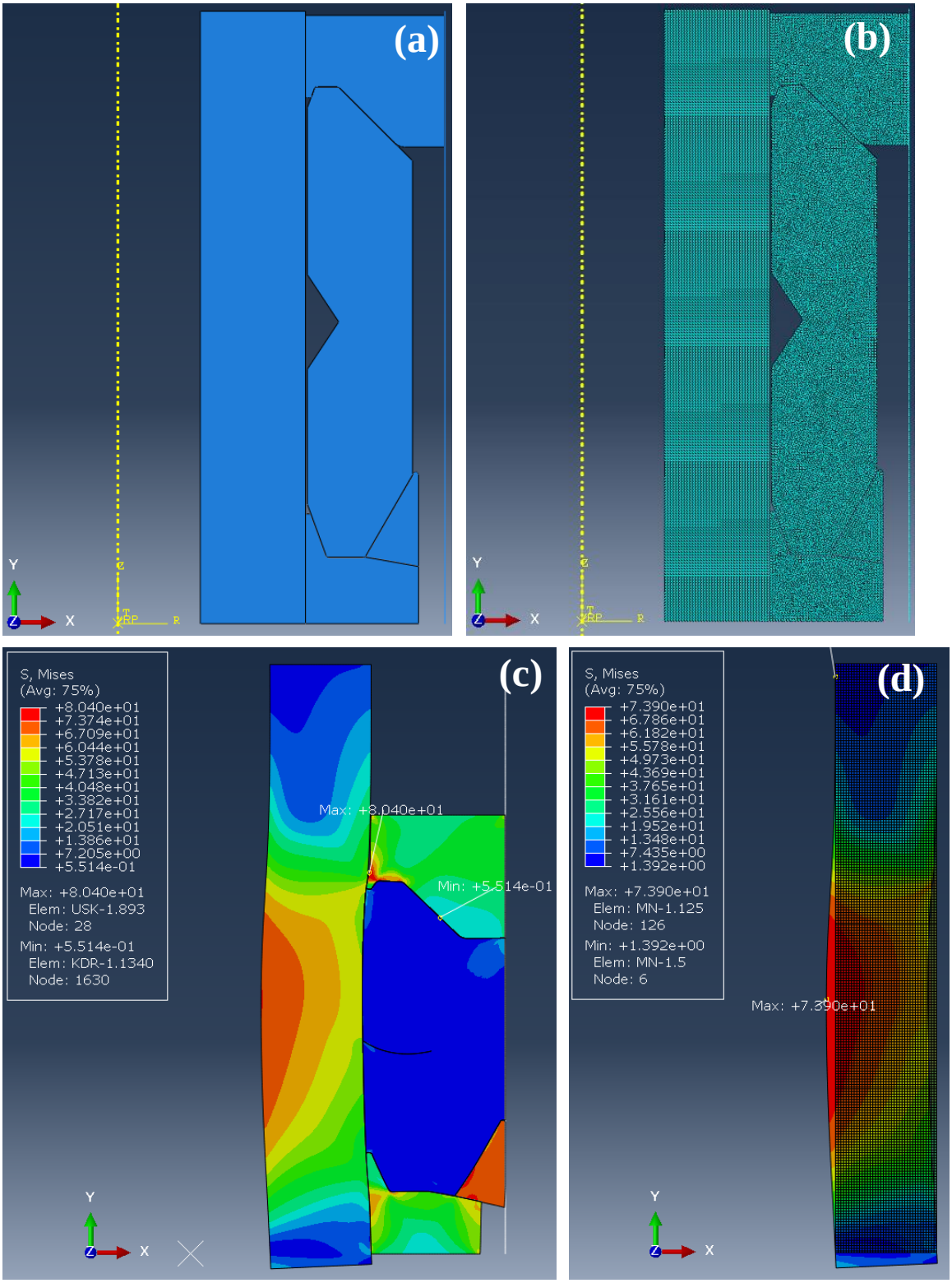

Figure B-76. FEA model and results of model 16 at 60 MPa of the equivalent pressure: (a) Model, (b) FEA model, (c) Mises stress of the entire model, (d) Mises stress of the mandrel

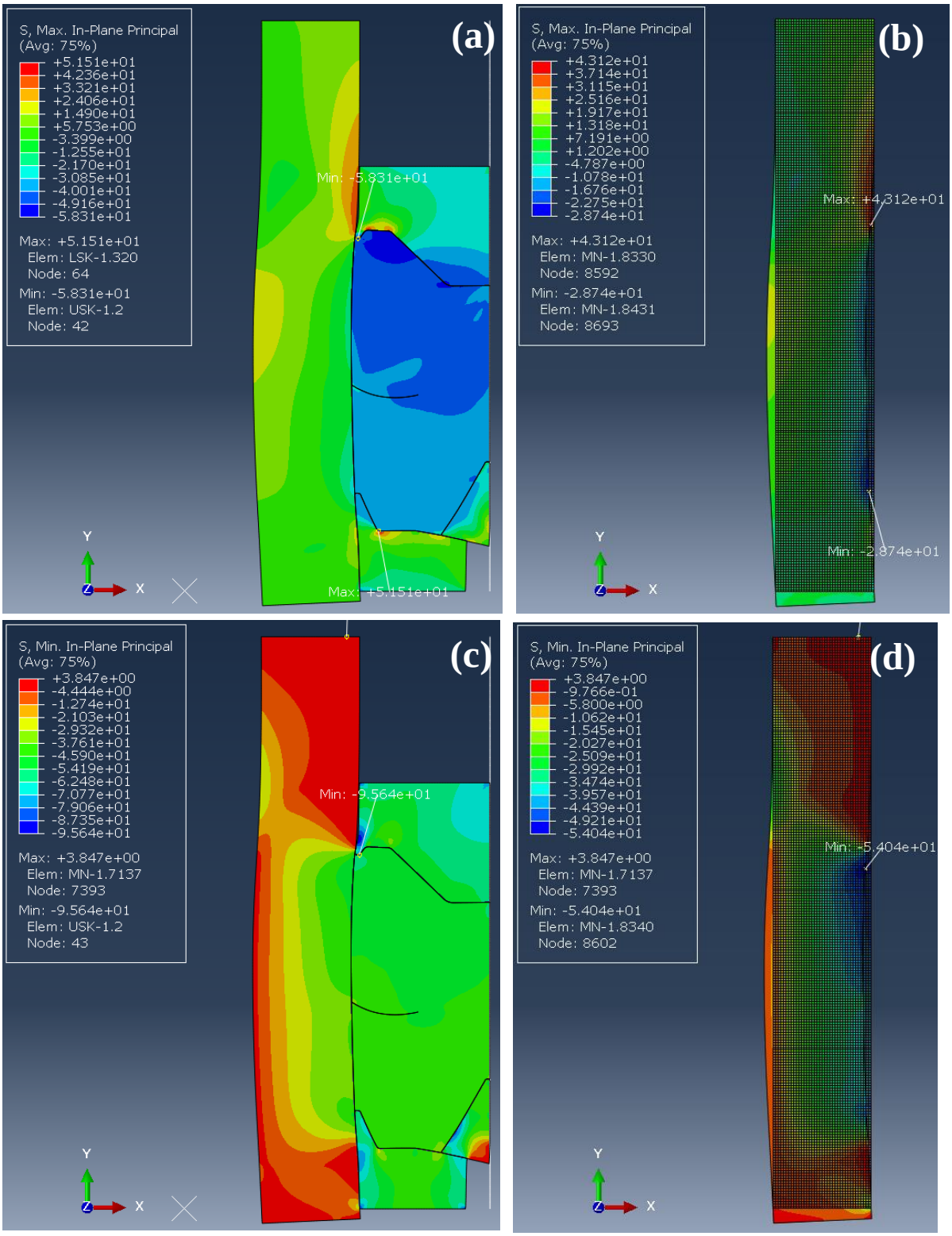

Figure B-77. FEA results of model 16 at 60 MPa of the equivalent pressure: (a) the maximum in-plane principal stress of the entire model, (b) the maximum in-plane principal stress of the mandrel, (c) the minimum in-plane principal stress of the entire model, (d) the minimum in-plane principal stress of the mandrel

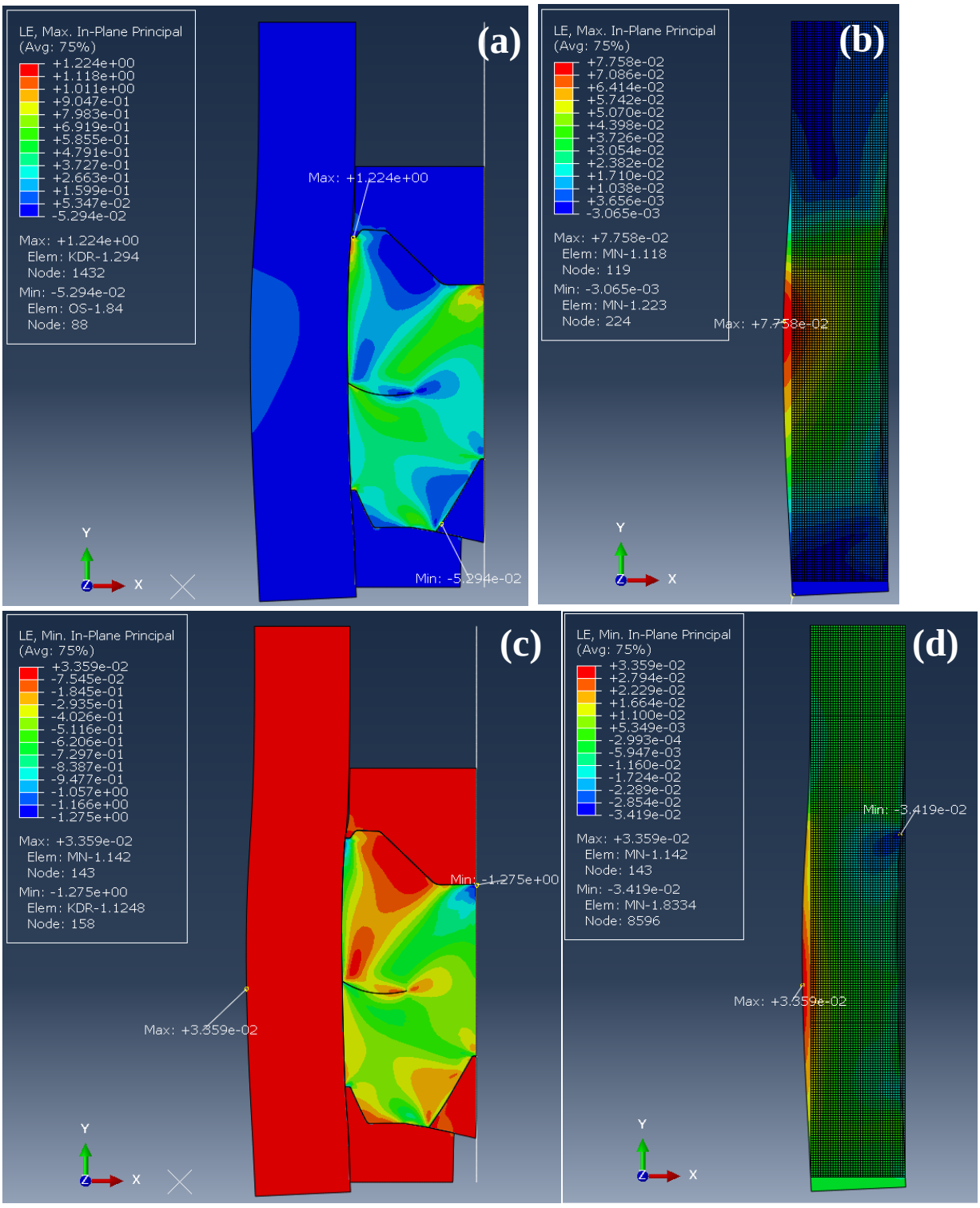

Figure B-78. FEA results of model 16 at 60 MPa of the equivalent pressure: (a) the maximum in-plane principal logarithmic strain of the entire model, (b) the maximum in-plane principal logarithmic strain of the mandrel, (c) the minimum in-plane principal logarithmic strain of the entire model, (d) the minimum in-plane principal logarithmic strain of the mandrel

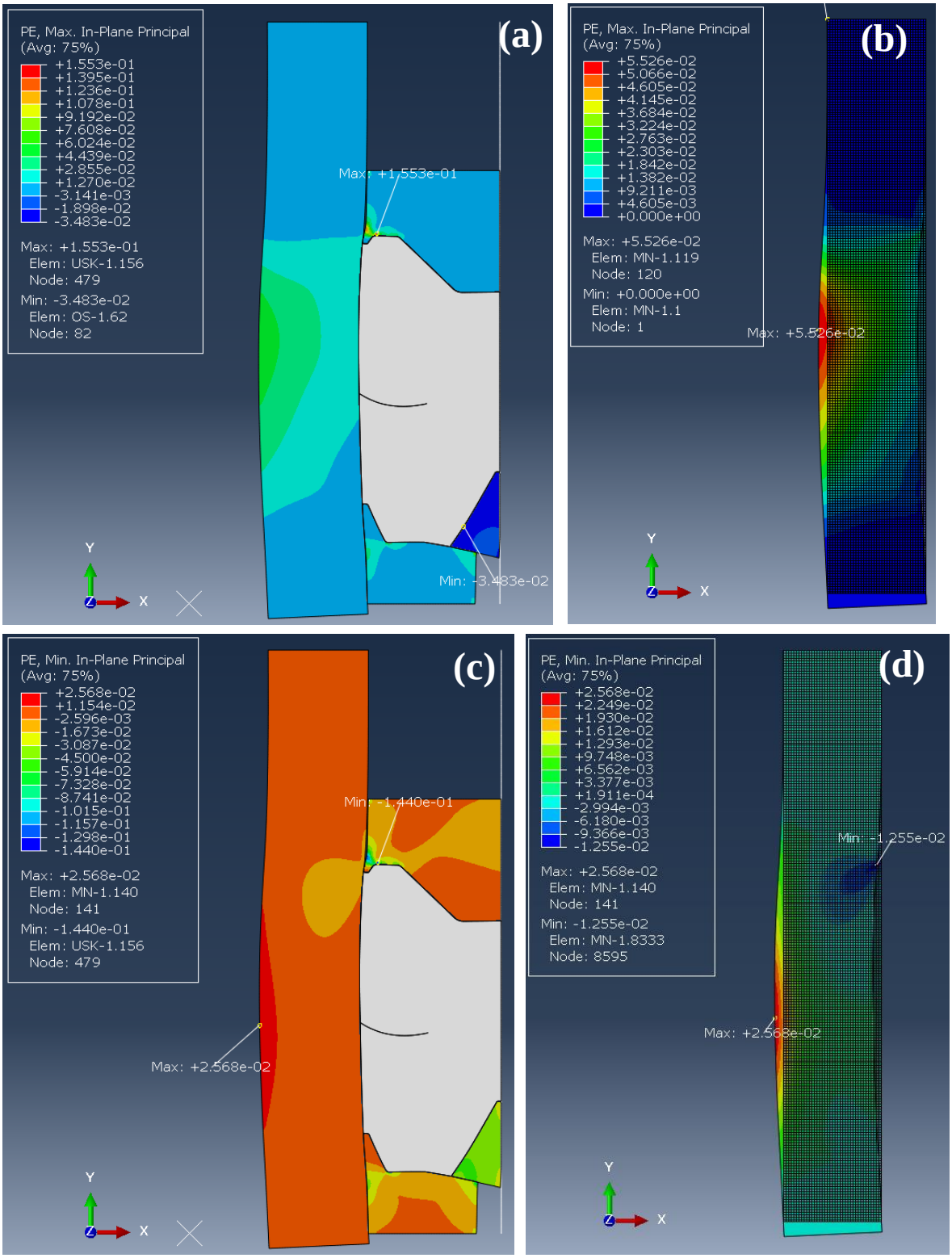

Figure B-79. FEA results of model 16 at 60 MPa of the equivalent pressure: (a) the maximum in-plane principal plastic strain of the entire model, (b) the maximum in-plane principal plastic strain of the mandrel, (c) the minimum in-plane principal plastic strain of the entire model, (d) the minimum in-plane principal plastic strain of the mandrel

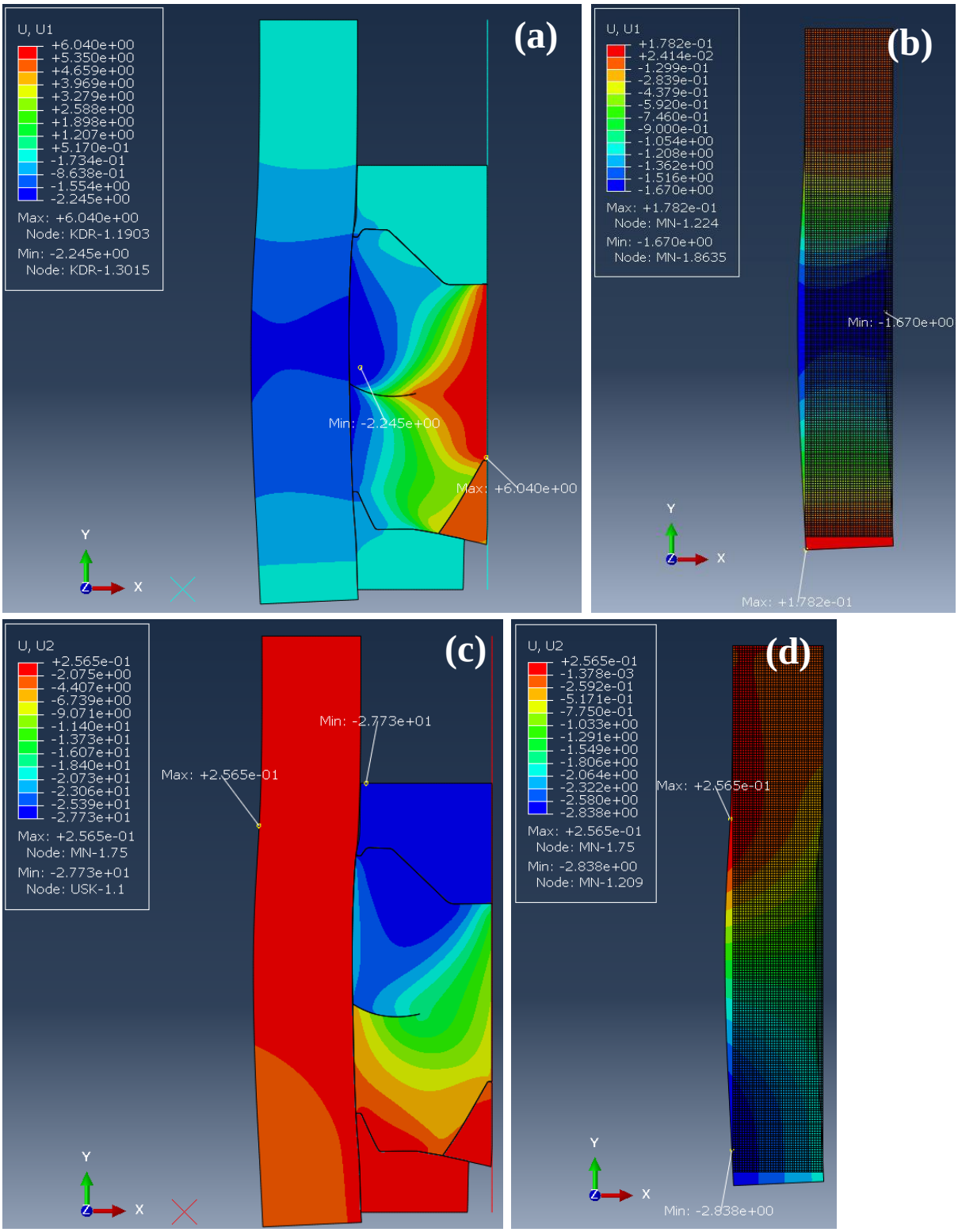

Figure B-80. FEA results of model 16 at 60 MPa of the equivalent pressure: (a) displacement to U1(x-axis) direction of the entire model, (b) displacement to U1(x-axis) direction of the mandrel, (c) displacement to U2(y-axis) direction of the entire model, (d) displacement to U2(y-axis) direction of the mandrel

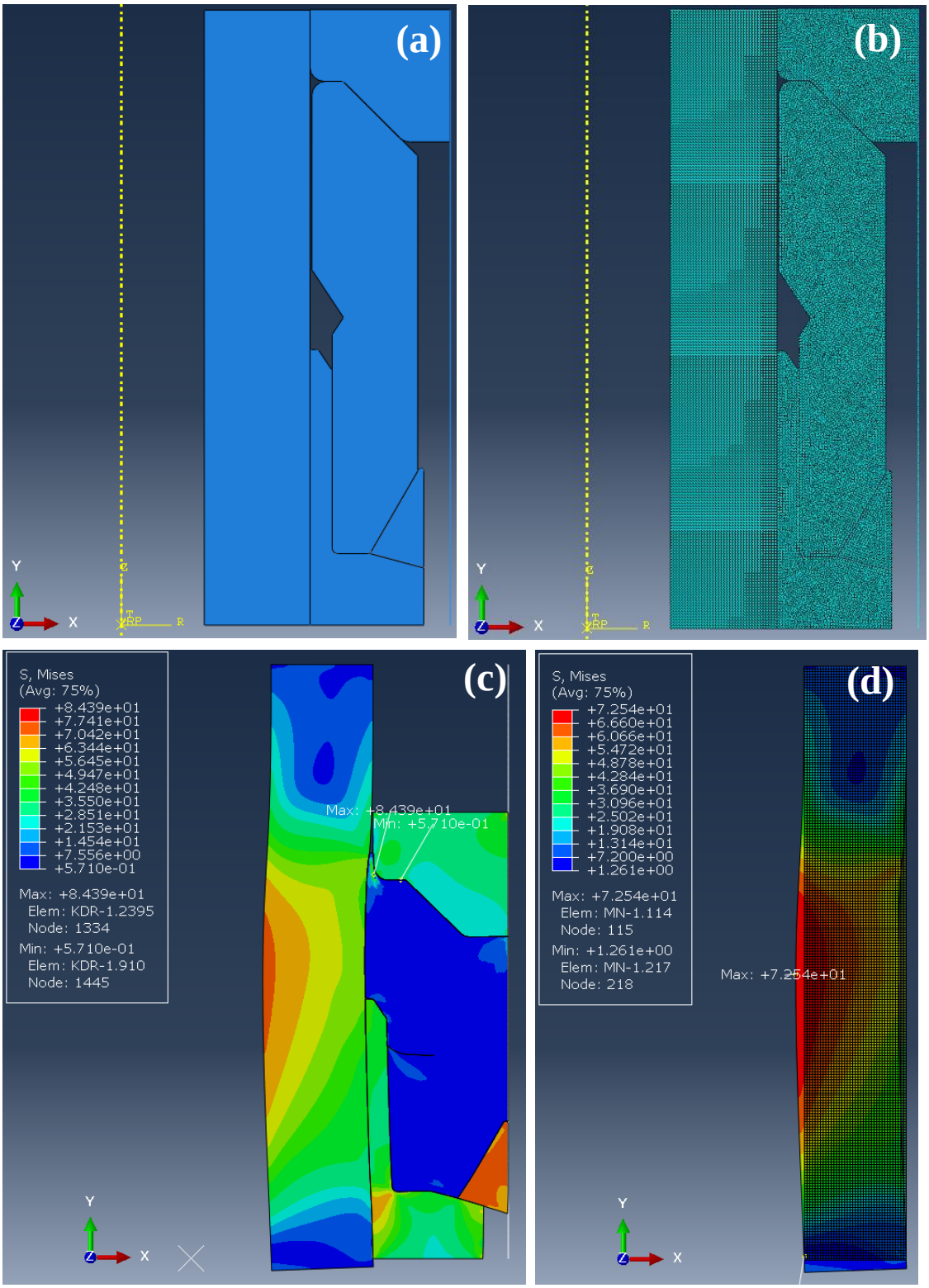

Figure B-81. FEA model and results of model 17 at 60 MPa of the equivalent pressure: (a) Model, (b) FEA model, (c) Mises stress of the entire model, (d) Mises stress of the mandrel

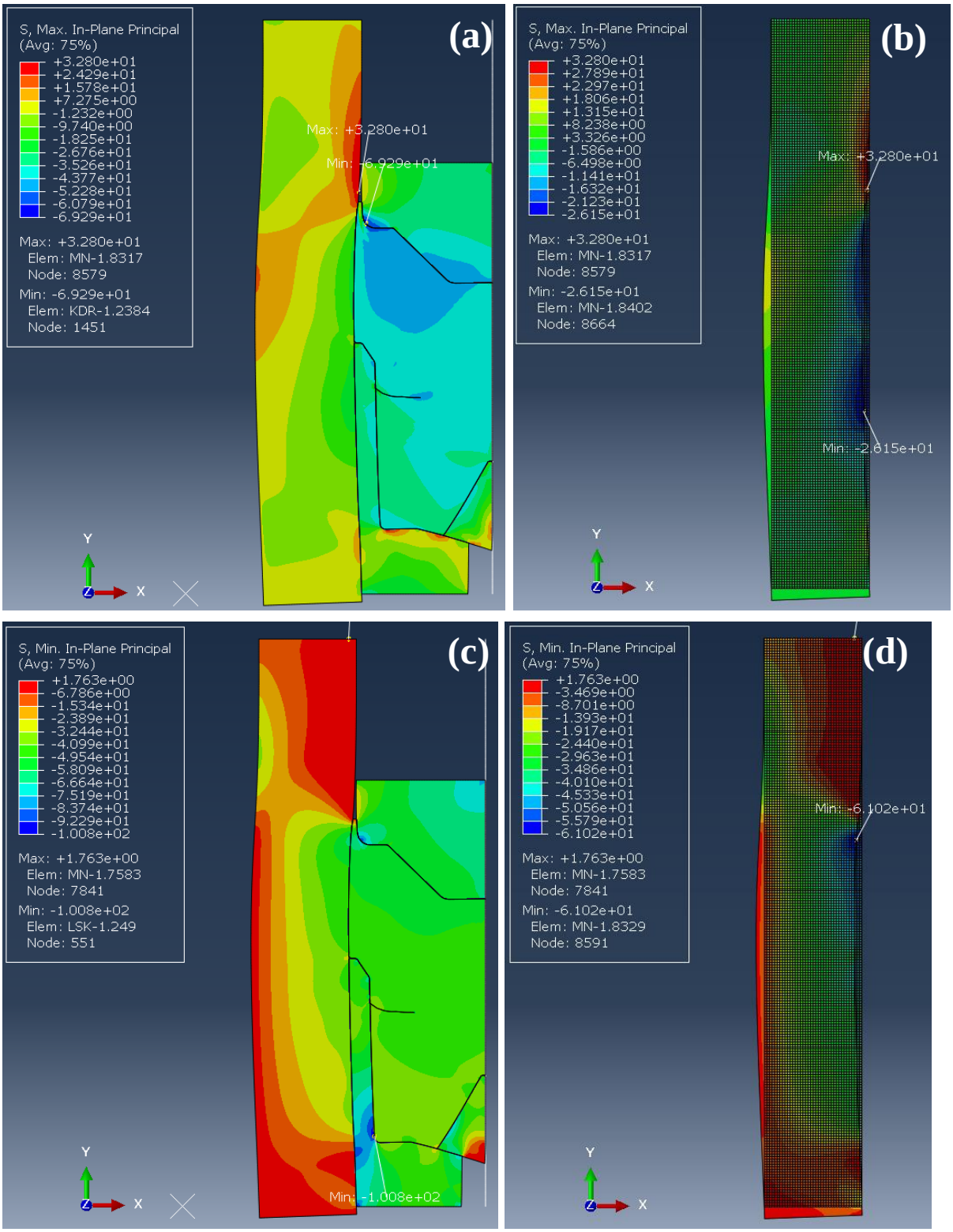

Figure B-82. FEA results of model 17 at 60 MPa of the equivalent pressure: (a) the maximum in-plane principal stress of the entire model, (b) the maximum in-plane principal stress of the mandrel, (c) the minimum in-plane principal stress of the entire model, (d) the minimum in-plane principal stress of the mandrel

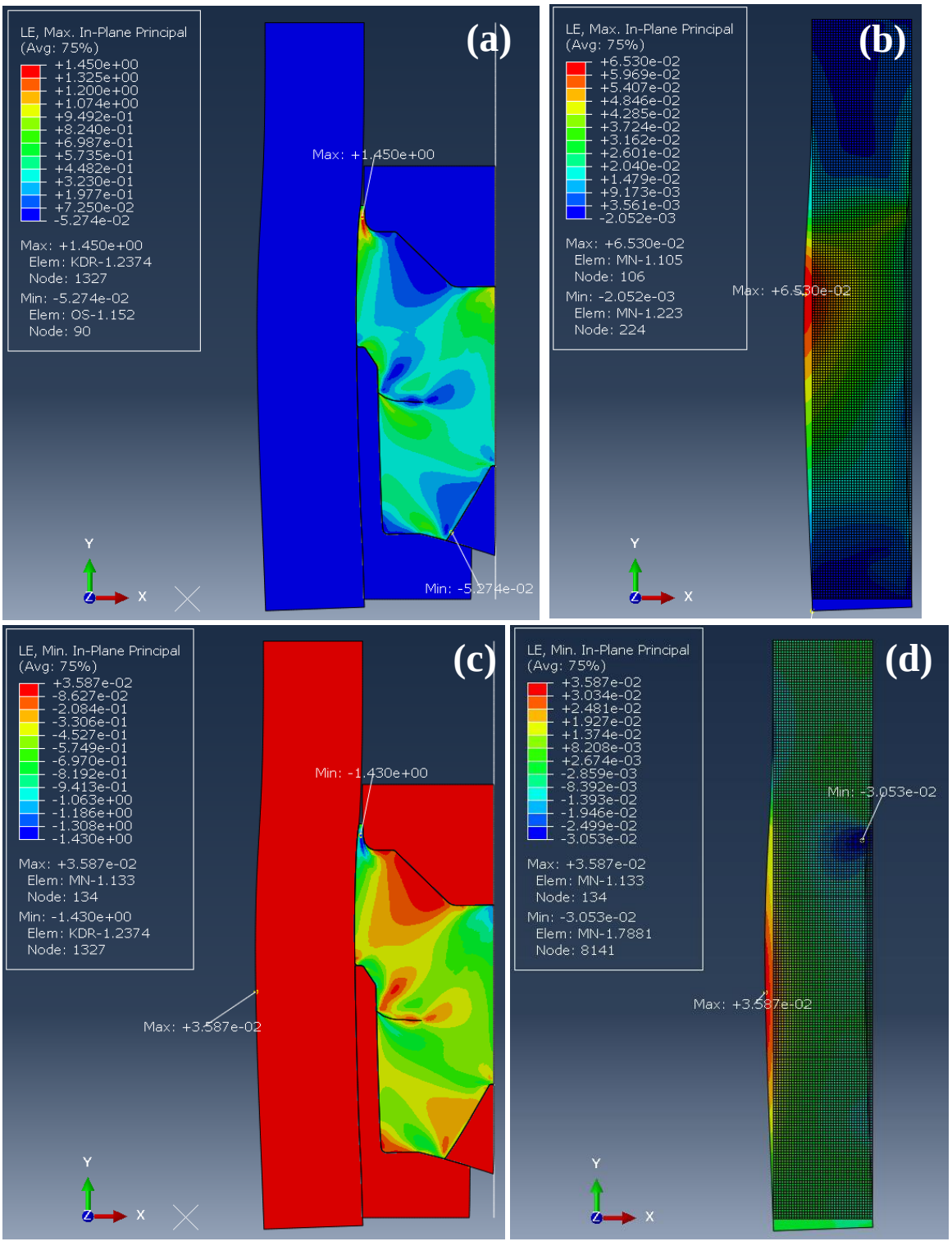

Figure B-83. FEA results of model 17 at 60 MPa of the equivalent pressure: (a) the maximum in-plane principal logarithmic strain of the entire model, (b) the maximum in-plane principal logarithmic strain of the mandrel, (c) the minimum in-plane principal logarithmic strain of the entire model, (d) the minimum in-plane principal logarithmic strain of the mandrel

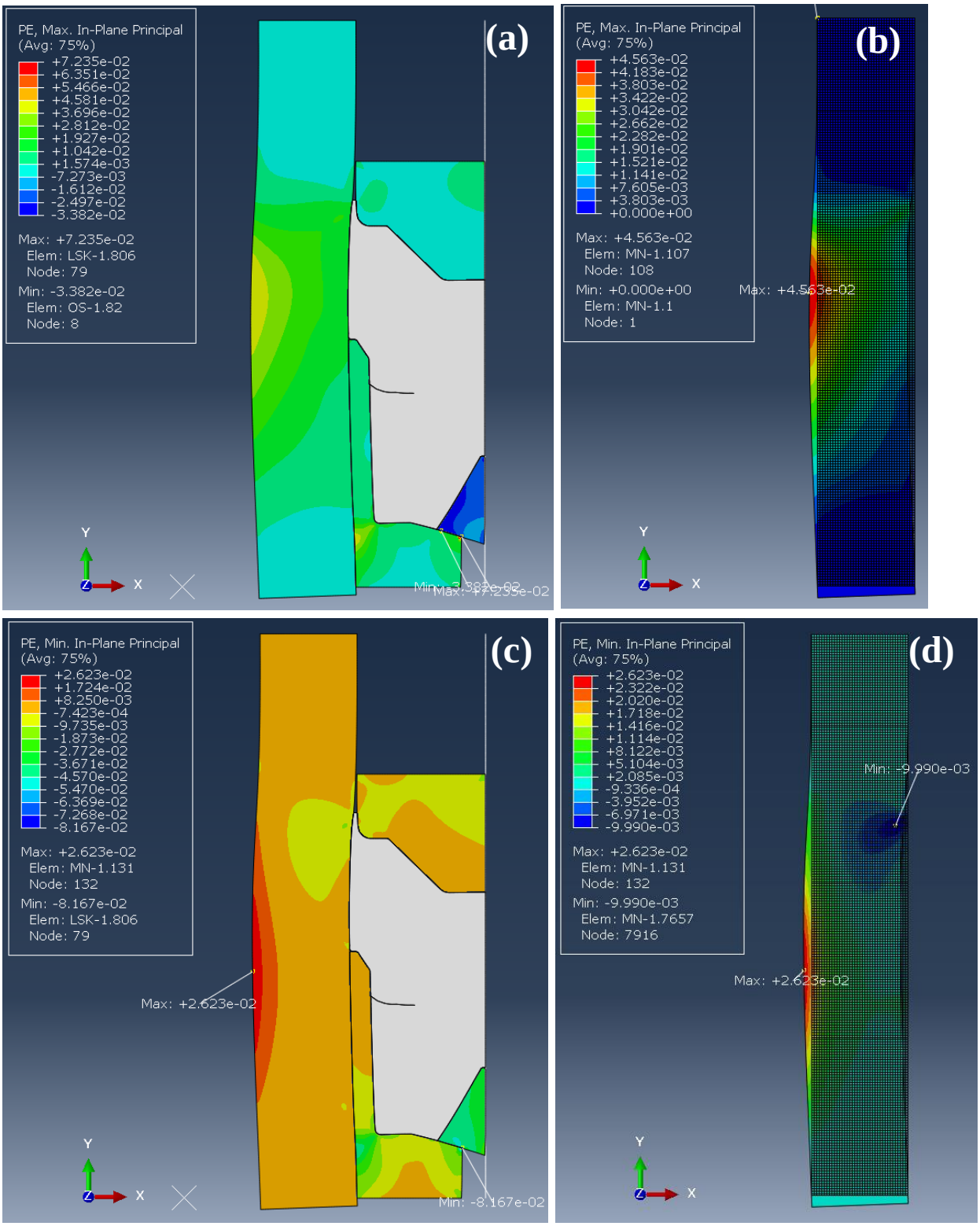

Figure B-84. FEA results of model 17 at 60 MPa of the equivalent pressure: (a) the maximum in-plane principal plastic strain of the entire model, (b) the maximum in-plane principal plastic strain of the mandrel, (c) the minimum in-plane principal plastic strain of the entire model, (d) the minimum in-plane principal plastic strain of the mandrel

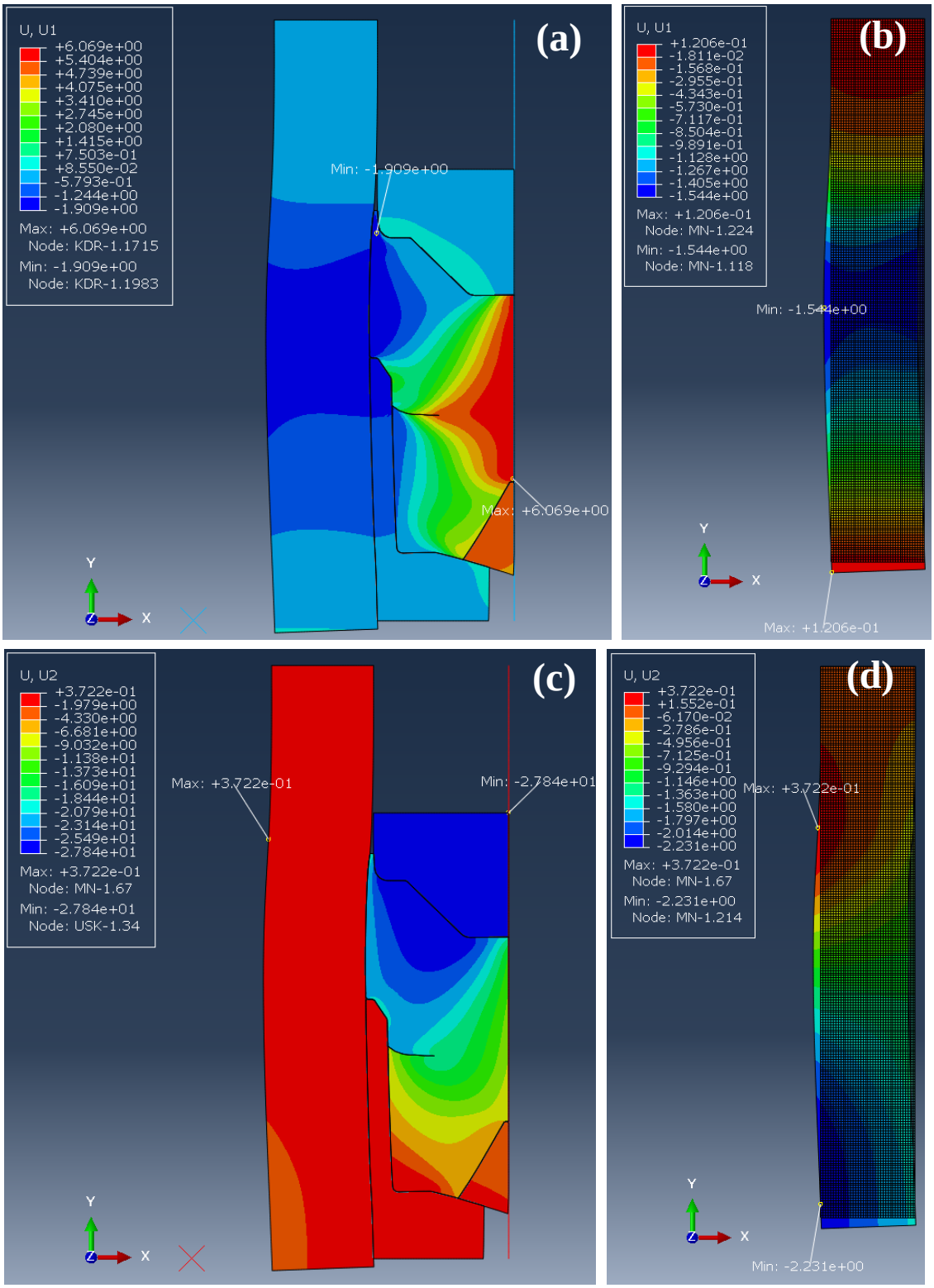

Figure B-85. FEA results of model 17 at 60 MPa of the equivalent pressure: (a) displacement to U1(x-axis) direction of the entire model, (b) displacement to U1(x-axis) direction of the mandrel, (c) displacement to U2(y-axis) direction of the entire model, (d) displacement to U2(y-axis) direction of the mandrel

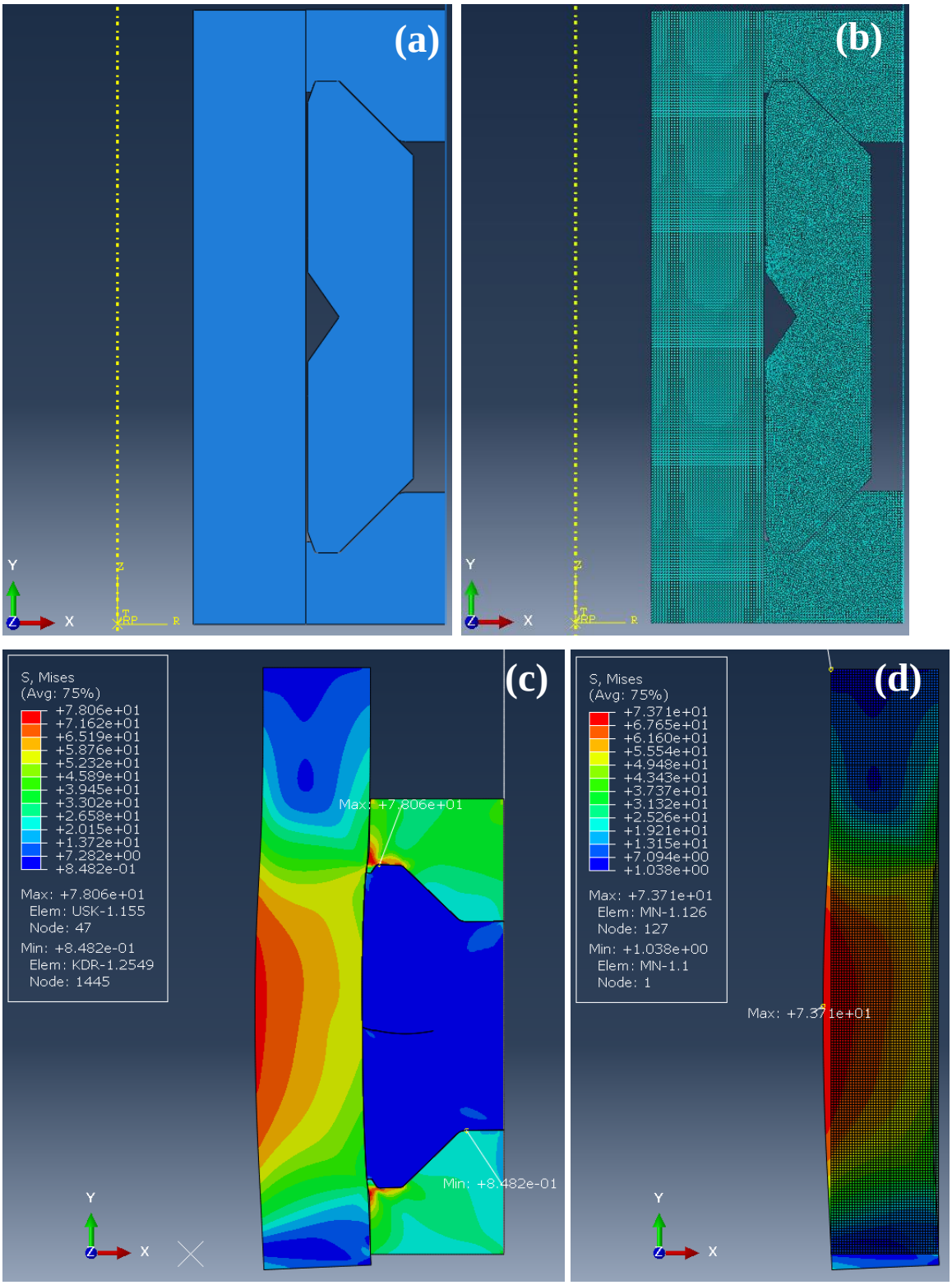

Figure B-86. FEA model and results of the mandrel thickness +1.25 mm model at 60 MPa of the equivalent pressure: (a) Model, (b) FEA model, (c) Mises stress of the entire model, (d) Mises stress of the mandrel

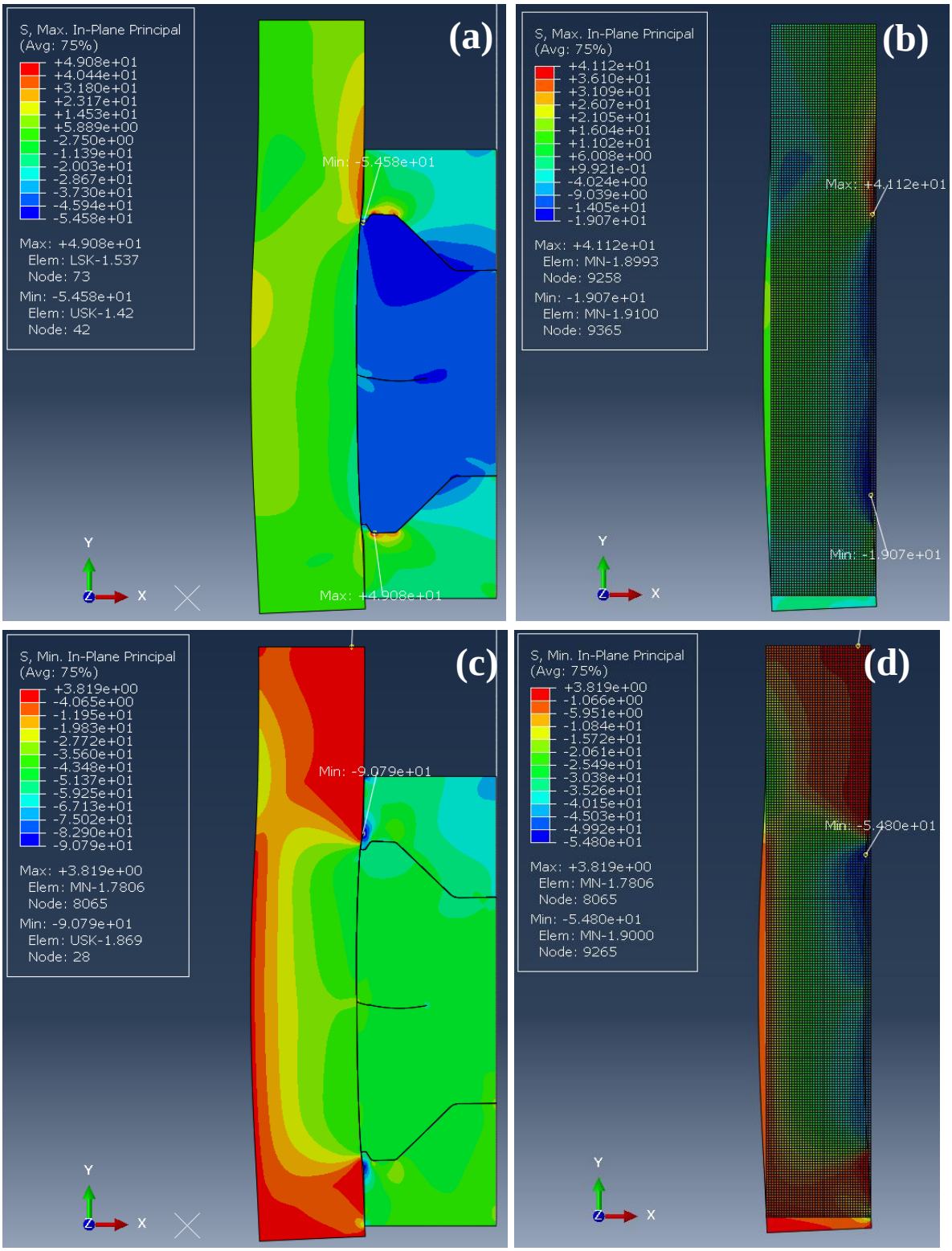

Figure B-87. FEA results of the mandrel thickness +1.25 mm model at 60 MPa of the equivalent pressure: (a) the maximum in-plane principal stress of the entire model, (b) the maximum in-plane principal stress of the mandrel, (c) the minimum in-plane principal stress of the entire model, (d) the minimum in-plane principal stress of the mandrel

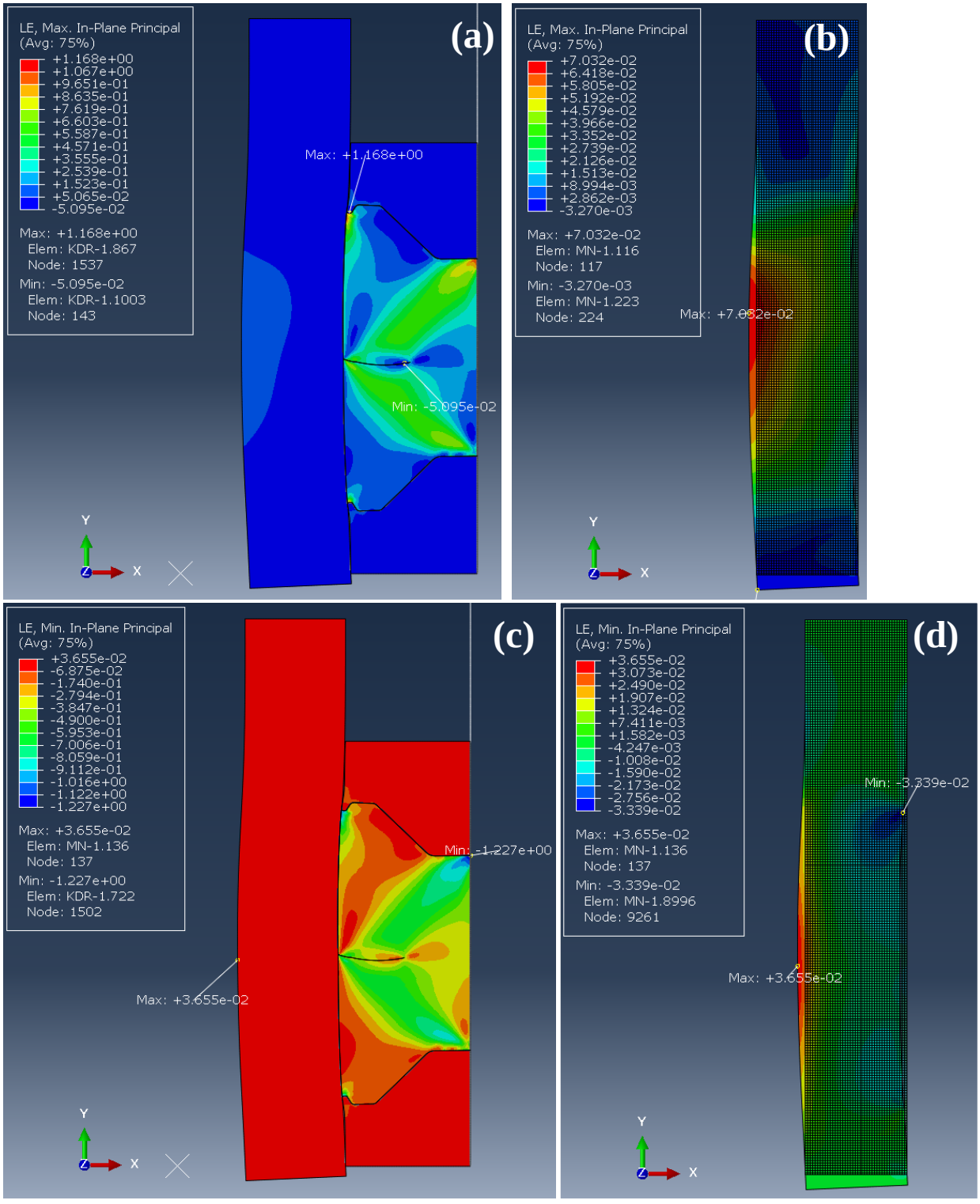

Figure B-88. FEA results of the mandrel thickness +1.25 mm model at 60 MPa of the equivalent pressure: (a) the maximum in-plane principal logarithmic strain of the entire model, (b) the maximum in-plane principal logarithmic strain of the mandrel, (c) the minimum in-plane principal logarithmic strain of the entire model, (d) the minimum in-plane principal logarithmic strain of the mandrel

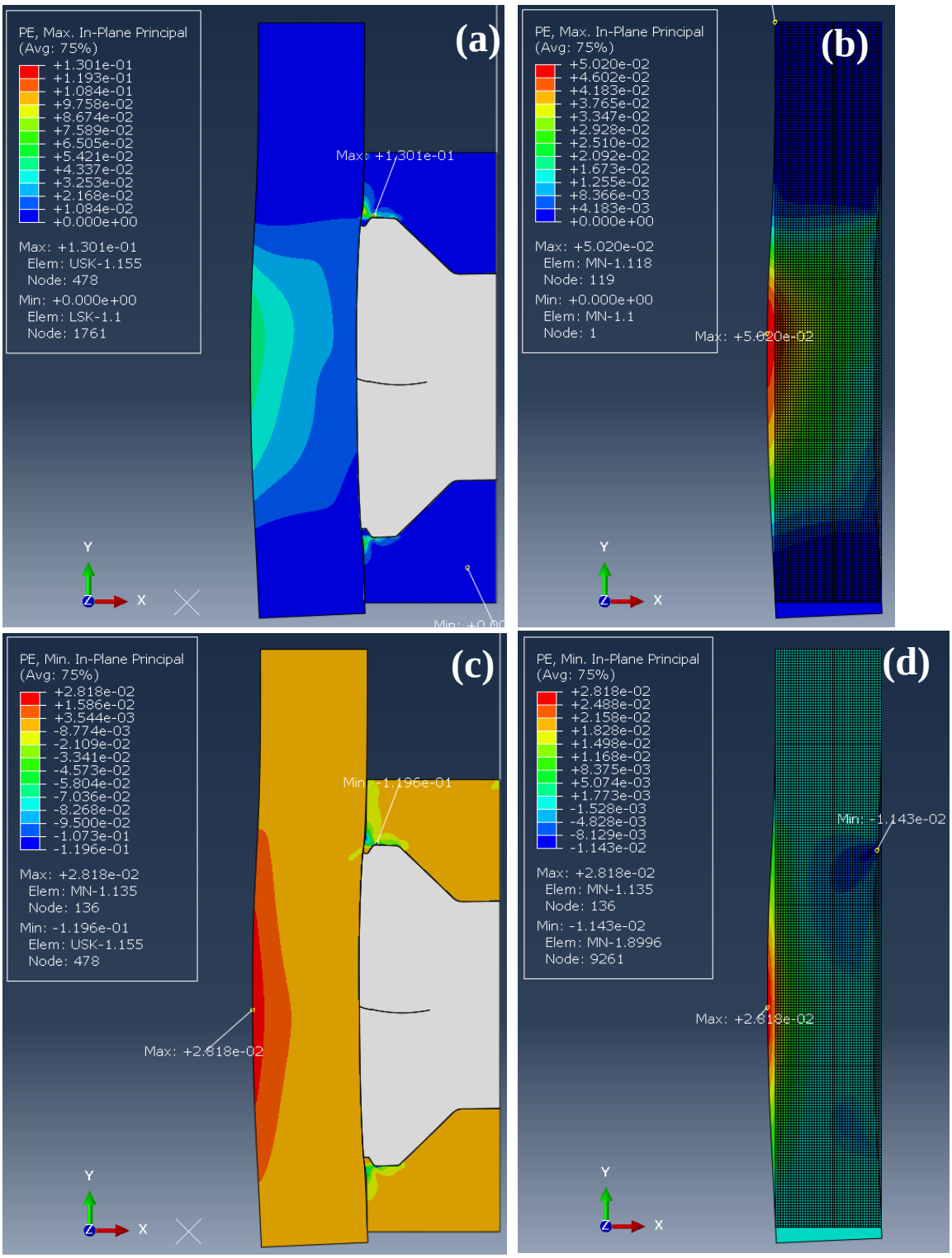

Figure B-89. FEA results of the mandrel thickness +1.25 mm model at 60 MPa of the equivalent pressure: (a) the maximum in-plane principal plastic strain of the entire model, (b) the maximum in-plane principal plastic strain of the mandrel, (c) the minimum in-plane principal plastic strain of the entire model, (d) the minimum in-plane principal plastic strain of the mandrel

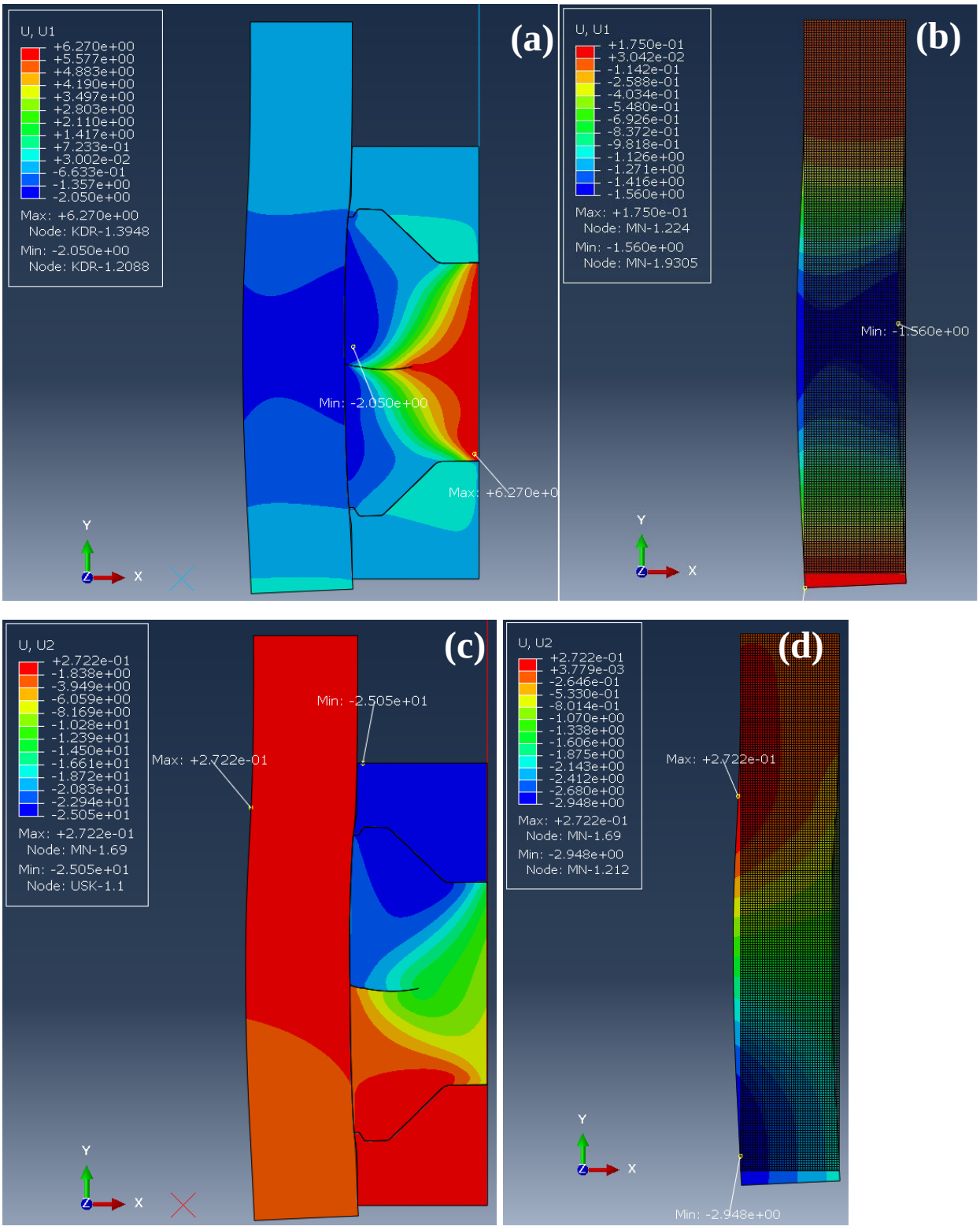

Figure B-90. FEA results of the mandrel thickness +1.25 mm model at 60 MPa of the equivalent pressure: (a) displacement to U1(x-axis) direction of the entire model, (b) displacement to U1(x-axis) direction of the mandrel, (c) displacement to U2(y-axis) direction of the entire model, (d) displacement to U2(y-axis) direction of the mandrel

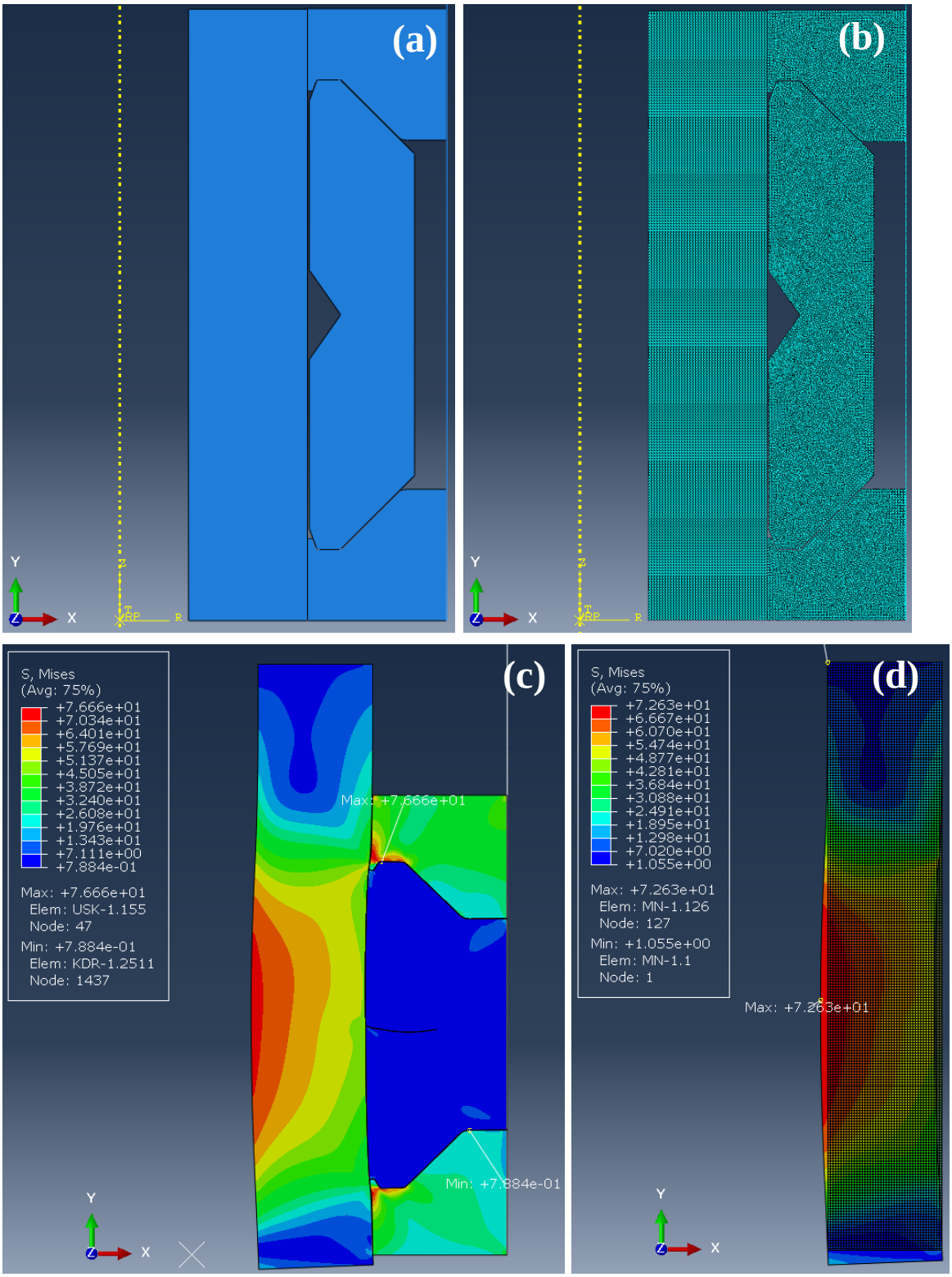

Figure B-91. FEA model and results of the mandrel thickness +2.50 mm model at 60 MPa of the equivalent pressure: (a) Model, (b) FEA model, (c) Mises stress of the entire model, (d) Mises stress of the mandrel

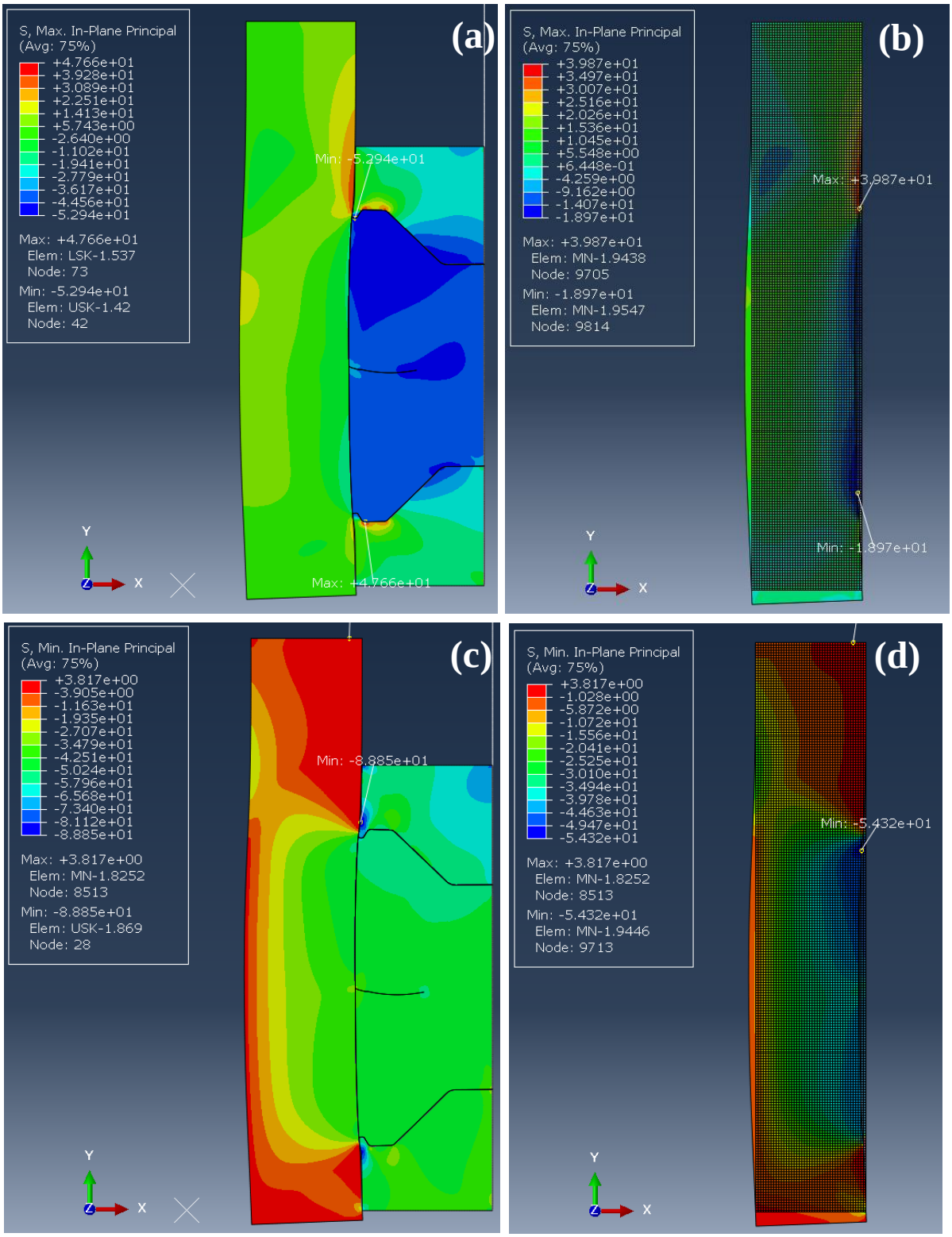

Figure B-92. FEA results of the mandrel thickness +2.50 mm model at 60 MPa of the equivalent pressure: (a) the maximum in-plane principal stress of the entire model, (b) the maximum in-plane principal stress of the mandrel, (c) the minimum in-plane principal stress of the entire model, (d) the minimum in-plane principal stress of the mandrel

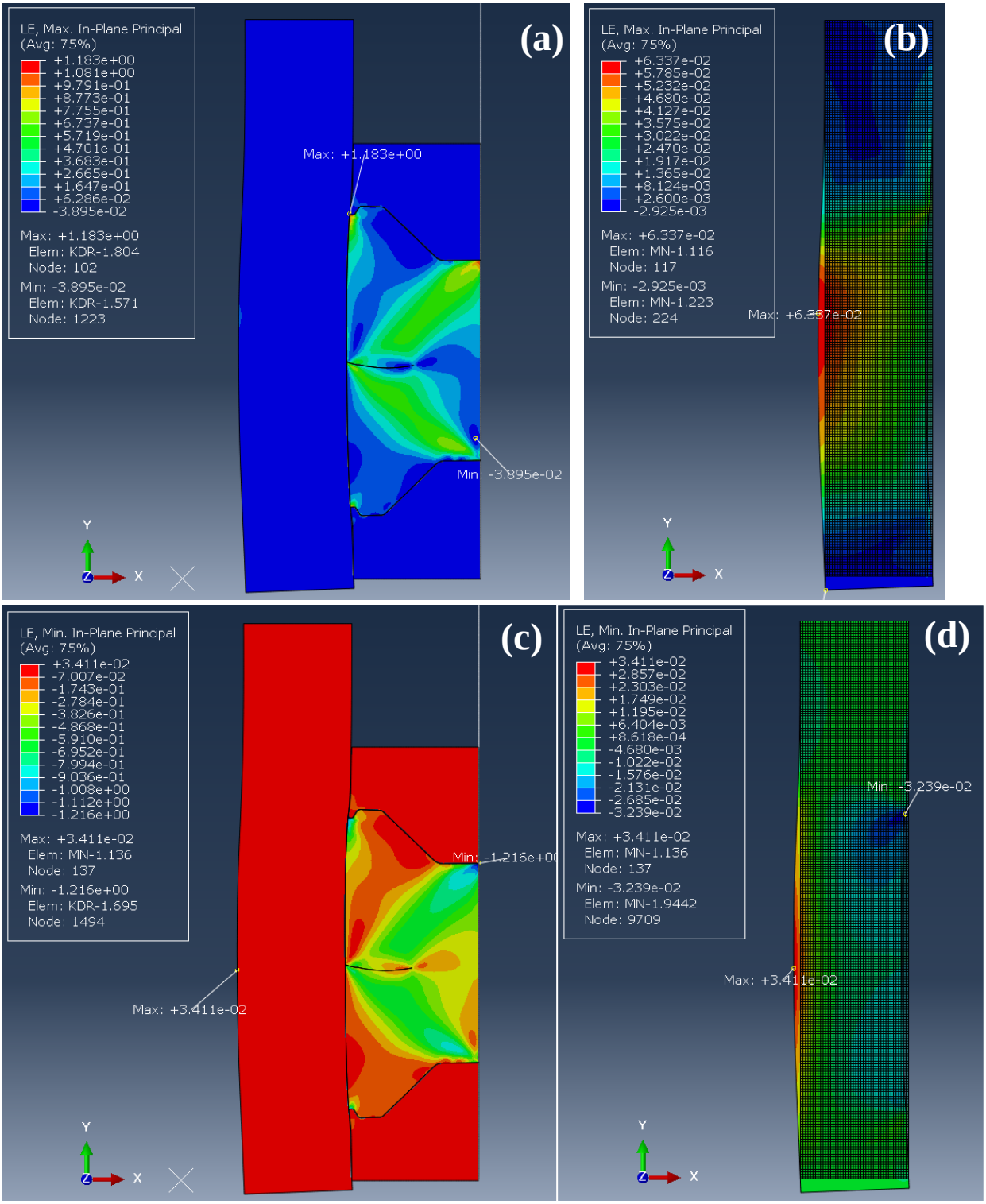

Figure B-93. FEA results of the mandrel thickness +2.50 mm model at 60 MPa of the equivalent pressure: (a) the maximum in-plane principal logarithmic strain of the entire model, (b) the maximum in-plane principal logarithmic strain of the mandrel, (c) the minimum in-plane principal logarithmic strain of the entire model, (d) the minimum in-plane principal logarithmic strain of the mandrel

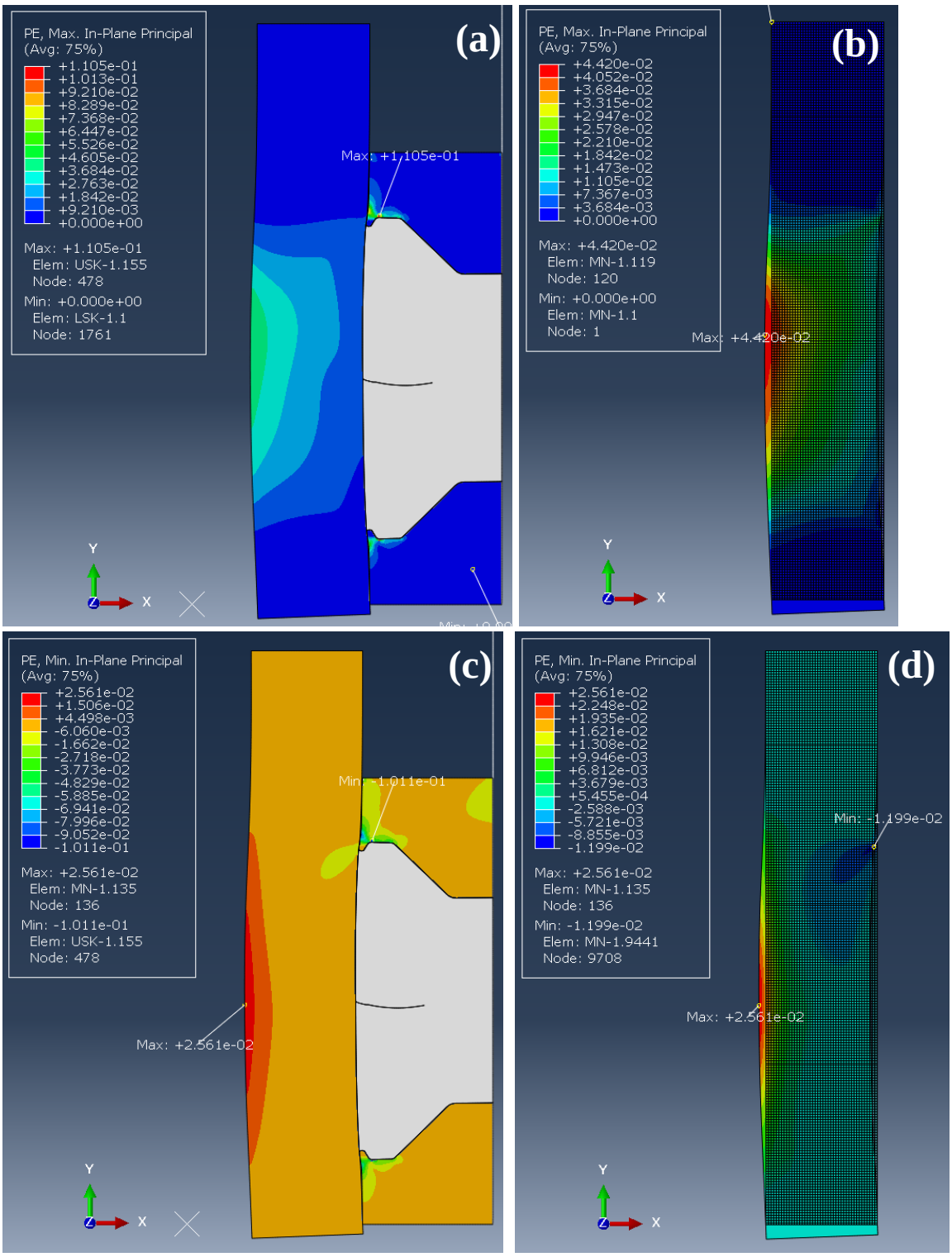

Figure B-94. FEA results of the mandrel thickness +2.50 mm model at 60 MPa of the equivalent pressure: (a) the maximum in-plane principal plastic strain of the entire model, (b) the maximum in-plane principal plastic strain of the mandrel, (c) the minimum in-plane principal plastic strain of the entire model, (d) the minimum in-plane principal plastic strain of the mandrel

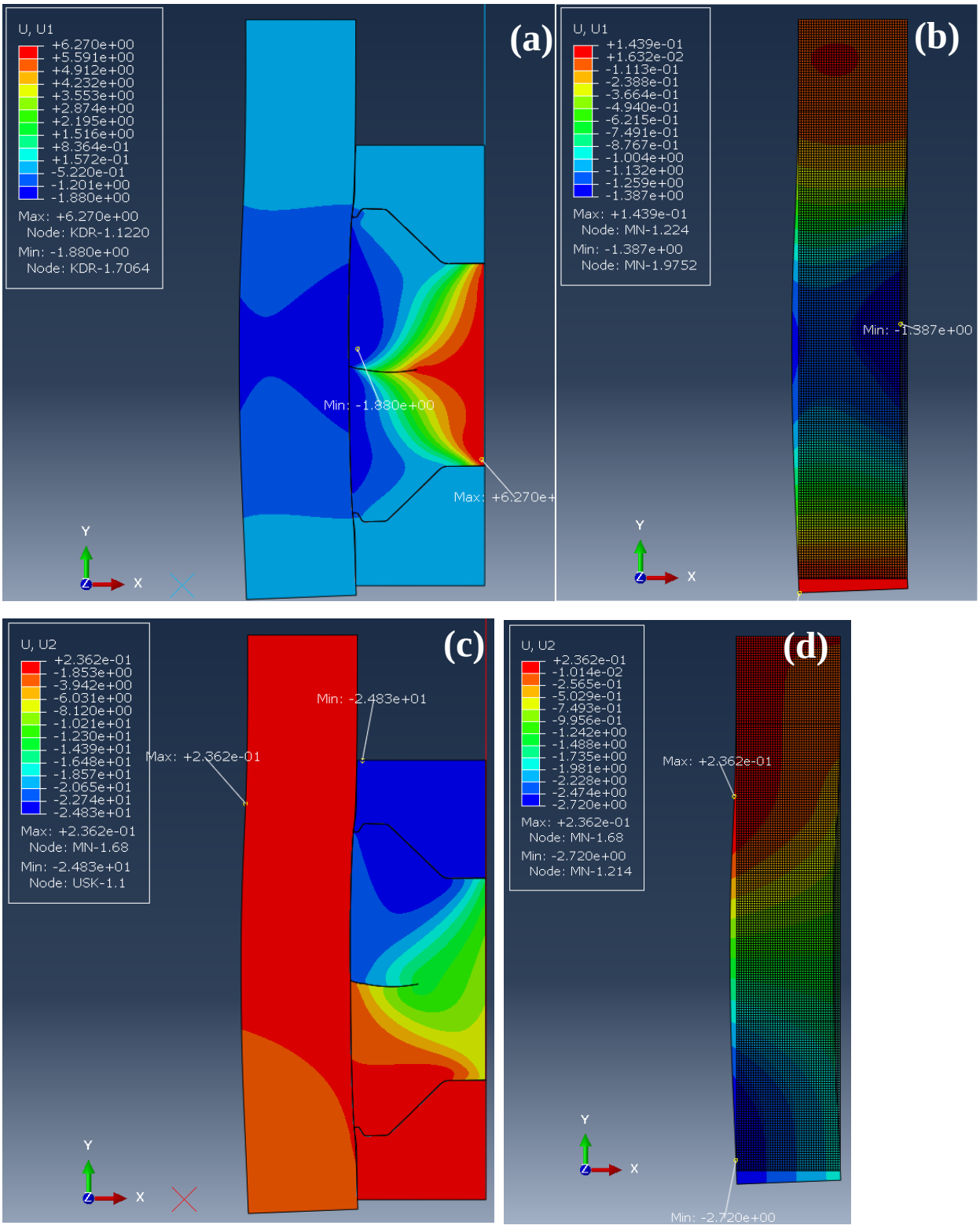

Figure B-95. FEA results of the mandrel thickness +2.50 mm model at 60 MPa of the equivalent pressure: (a) displacement to U1(x-axis) direction of the entire model, (b) displacement to U1(x-axis) direction of the mandrel, (c) displacement to U2(y-axis) direction of the entire model, (d) displacement to U2(y-axis) direction of the mandrel